VNIVERSITAT DE VALÈNCIA

Departament de Física
Atòmica, Molecular i Nuclear

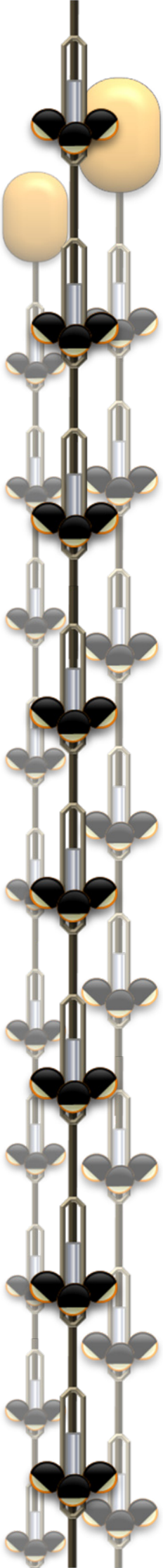

Analysis of the Optical Beacon system and search for point-like sources in the ANTARES neutrino telescope

Memoria presentada por
JUAN ANTONIO AGUILAR SÁNCHEZ
para optar al grado de Doctor en Física
Valencia, 2008

DEPARTAMENT DE FÍSICA ATÒMICA
MOLECULAR I NUCLEAR

VNIVERSITAT DE VALÈNCIA

(ESTUDI GENERAL)

Analysis of the Optical Beacon system and search for point-like sources in the ANTARES neutrino telescope

PhD Thesis

Juan Antonio Aguilar Sánchez

December 2007

D. JUAN JOSÉ HERNÁNDEZ REY, Investigador Científico del C.S.I.C.,

CERTIFICA :

Que la presente memoria, **Analysis of the Optical Beacon system and search for point-like sources in the ANTARES neutrino telescope**, ha sido realizada bajo su dirección en el Departamento de Física Atómica, Molecular y Nuclear de la Universitat de València por D. Juan Antonio Aguilar Sánchez y constituye su Tesis Doctoral, que presenta optar al grado de Doctor en Física.

Y para que conste, en cumplimiento de la legislación vigente, firmo el presente Certificado en Paterna a 10 de Diciembre de 2007.

Fdo.: Juan José Hernández Rey

Visto bueno del tutor: Juan Zuñiga Román

A mis padres

Agradecimientos

Es una tarea difícil condensar en tan pocas líneas las palabras de agradecimiento que merecen todos aquellos que han contribuido de manera tan valiosa al desarrollo de esta tesis. Un gran esfuerzo compensado por el placer que supone comprobar el número de personas que durante estos años han ofrecido desinteresadamente su ayuda. Mucho es lo que he aprendido y más aún lo que he recibido. Sería imposible recompensar toda su generosidad y apoyo, sí puedo darles, aunque valga poco, mi más sincero agradecimiento.

Me gustaría agradecer en primer lugar a mi director de tesis Juan José Hernández-Rey por todo el esfuerzo y la confianza depositada en mí a lo largo de estos cinco años. Su calidad como científico tan sólo es comparable a su valía como persona. De él he aprendido mucho en el terreno profesional y en lo humano y me alegra poder considerarle un amigo.

A Juan Zuñiga, mi tutor, le agradezco su franca disposición siempre que me he presentado con un problema y su esmero en solucionarlo. Sus acertados comentarios han sido esenciales para el desarrollo de esta tesis. Pero sobre todo, le agradezco los libros compartidos y las conversaciones sinceras.

I'm grateful to the whole ANTARES collaboration, specially to Teresa Montaruli for her comments on topics related to fundamental physics. She has a demonstrated a deep knowledge on astroparticle physics and her suggestions have improved the quality of this thesis. Thanks to Maarten de Jong for his support during the development of the Optical Beacon trigger and to Jürguen Brunner for his comments on the attenuation length study. I'd like also to thank Aart Heijboar for many interesting discussions about point-like sources via mail.

Muchas cosas son las que debo agradecer a Juande, muchas y variadas. El confiarme su hogar fue un gesto por el que siempre estaré en deuda. Además de ser una de las mejores personas que he tenido el placer de conocer, le agradezco todas las provechosas conclusiones que he obtenido como fruto de nuestras múltiples discusiones durante estos años. Su valiosa amistad es algo que siempre estimaré.

Deseo dar las gracias también a Paco, Ciro, Víctor, Diego y demás miembros del grupo ANTARES-Valencia por un incomparable entorno de trabajo. También a Emiliano por su amistad y porque sin su labor previa este trabajo no habría visto la luz.

Mi agradecimiento al proyecto GRID de Valencia, en particular a Javi y Alex por su continua disposición a la hora de ayudarme siempre que mis *jobs* así lo han requerido. Dentro del IFIC, tengo un especial recuerdo para Belén, Luis, Carlos, Álvaro, Santi, Esteban, Mari Carmen, Lauren y algunos ya nombrados, que han compartido conmigo no sólo el lugar de trabajo, sino horas de provechosa distracción y una gran amistad.

A todos mis amigos en Albacete, por darle perspectiva a mi vida y permitirme aprender de ellos muchas cosas al margen de la física.

Me gustaría dar las gracias a mi familia, ellos son el mejor apoyo que una persona pueda tener. A mis padres les debo mucho de lo que soy, y les agradezco su confianza absoluta en mí y en mi trabajo. Sin ellos esta tesis no existiría y por tanto les pertenece.

E che posso dire di Simona? Voglio ringraziarla per essere apparsa nel momento in

cui più avevo bisogno di lei. Senza la sua gioia ed il suo entusiasmo non avrei potuto finire questo lavoro. Ma grazie soprattutto per il suo affetto. Ti voglio bene.

Contents

Abstract

High energy neutrino astronomy is a very promising research field that is entering a new stage in which a discovery of a high energy neutrino source seems finally possible. The detection of these high energy neutrinos will shed light to the remaining unresolved questions concerning the nature and origin of the cosmic rays. The cosmic rays are mostly protons and other heavy particles assumed to be accelerated in astrophysical objects. They were first discovered by Victor Hess who measured an increase in the ionizing radiation levels of the atmosphere as a function of the distance from the Earth which is a consequence of the cosmic rays interactions with the upper shells of the atmosphere. Other indirect effects such as the production of showers of secondary charged particles are evidences of the existence of these cosmic particles as well, nonetheless there are also numerous direct measurements provided by satellite and space-borne experiments. However, the accessible information is limited due to the physical nature of these cosmic messengers. During their travel to the Earth, protons can interact with the cosmic microwave background and therefore very energetic protons can not reach distances further than a few tens of Mpc. In addition, the intergalactic magnetic fields deflect charged particles as protons, spoiling any directional information about the origin of the cosmic ray for energies $E_p < 10^{19}$ eV.

Apart from protons, other cosmic messengers also have limitations. Neutrons decay before they can reach long distances. As an example, neutrons with energies $E_n \sim$ EeV will travel less than 10 kpc. Gamma astronomy is becoming an area of fruitful discoveries but the interaction of γ-ray photons with the electromagnetic background light implies that photons with energy $E_\gamma > 10$ TeV coming from sources further than 100 Mpc away are unlikely to be observed.

Neutrinos on the other hand turn out to be the best candidates for cosmic messengers. Accelerated protons in the shock waves of astronomical objects can initiate a high energy neutrino emission due to the decay of the charged pions produced in the interaction of protons with the surrounding matter. Being electrically neutral particles that only interact weakly, they can cross dense regions of the Universe without interacting and without suffering deflection due to magnetic fields. Therefore, the detection of high energy cosmic neutrinos will provide information about the origin of cosmic rays, gamma ray bursts and other topics still not settled.

In order to accomplish the neutrino detection several techniques have been proposed. The optical neutrino detection is based on the measurement of the Cherenkov light induced by secondary leptons produced by neutrino interactions with matter while crossing the Earth. The Cherenkov light is emitted providing that the leptons travel through a suitable optical medium. Therefore two main requirements have to been met

in an optical neutrino telescope. First, the expected atmospheric muon background (6 orders of magnitude larger than the atmospheric neutrino background) constrains the detector location to deep underground infrastructures to escape the backgrounds caused by the unavoidable rain of cosmic rays upon the atmosphere. On the other hand, the low neutrino cross section implies large detection volumes. For that reasons preference locations of a neutrino telescope take advantage of large natural volumes such as under ice or water. The decision whether a neutrino telescope is build underwater or ice implies different aspects concerning the detector performance, such as angular resolution or visibility of the detector, and different technical details to be adopted in the experiment design.

The ANTARES experiment is a high energy neutrino telescope being built in the Mediterranean Sea. The collaboration includes people from 14 European countries. The detector consists in 12 strings spread over the seabed forming a tridimensional array of photomultipliers. Each line has 25 storeys and is equipped with 75 photomultipliers tubes (PMTs) grouped in triplets one per floor amounting a total number of 900 PMTs.

One of the main advantages of underwater neutrino telescopes compared to under-ice telescopes is the better angular resolution that can be achieved. This is possible due to the optical properties of the sea water which compared to the ice allow a more accurate time calibration. This work is divided in two main parts. In the first one it will be proved that the ANTARES time resolution is accurate enough to yield the desirable angular resolution below the 0.3° for muon neutrinos with $E_\nu > 10$ TeV. The second part is devoted to explore the capability of ANTARES in detecting point-like steady neutrino sources. We describe a clustering algorithm to the search for signal excess of neutrinos over the background.

The first chapter is devoted to the problematic of cosmic rays. The cosmic ray spectrum will be described, and a review of their possible origin according to different regions of the spectrum will be given. The basic principles of neutrino astronomy will be described inquiring on the knowledge provided by the γ-ray astronomy and cosmic rays observations.

In the second chapter the detection principle of Cherenkov neutrino telescopes is described. In particular we will focus on the ANTARES neutrino telescope, and a review of its main elements and performance will be introduced.

Chapter 3 explains the first analysis performed in ANTARES with the Optical Beacon system in underwater conditions. First the Optical Beacon system will be described and the study of the time residual distributions will be shown. The conclusion is that the requirements in terms of time resolution in the acquisition system are verified by the Optical Beacons. This chapter is also the subject of a first study about the optical properties of the sea water.

In chapter 4 the point-source analysis is introduced. We will describe a clustering algorithm called the Expectation-Maximization algorithm. A general description of the method is provided, and the particular application to the search for point-like sources is shown.

Chapter 5 contains the analysis of the so-called full *blind* search, in which no assumption about the neutrino source is made. The **discovery potential** and the **average**

upper limits, in the case of no significant evidence for a signal on top of the background is found, are shown. These results are presented both in terms of the average neutrino signal events and the equivalent neutrino or muon flux.

The search analysis described in chapter 6 follows a different approach. In this case, a set of possible candidate neutrino sources are evaluated by introducing the source coordinates in the algorithm. Hence in this case the position of the source is assumed to be known. The sensitivity in this case has an important role since it is the parameter usually selected to compare with other neutrino telescopes. Hence, a comparison with present and the projected performance of future neutrinos telescopes is also shown.

Chapter 1

High energy neutrino astronomy

– Hey professor, what're you teaching this semester?
– Same thing I teach every semester. "The Mathematics of Quantum Neutrino Fields." I made up the title so that no student would dare take it.
– Mathematics... of wonton... burrito meals. I'll be there!
Fry and Professor Farnsworth, Futurama.

In the year 2002 the Nobel Prize in Physics was awarded to Raymond Davis Jr. and Masatoshi Koshiba for pioneering contributions to astrophysics, in particular for the detection of neutrinos from two extra-terrestrial sources, the Sun and the SN1987A supernova [1, 2]. This is usually referred to as the low energy neutrino astronomy since neutrinos are products of nuclear reactions in stars and supernova explosions which are in the few MeV region. High neutrino astronomy, on the contrary, is a very young discipline stemming from the fundamental necessity of extending conventional astronomy beyond the usual cosmic messengers. In this sense, we are witnessing the progress for opening of a new window to explore the extreme Universe. The under-ice neutrino telescope AMANDA located at the South Pole, has already established flux limits being able to rule out some of the most optimistic models of neutrino emission from cosmic accelerators. The AMANDA experiment also represents a proof of concept for the Kilometre-Scale detector, IceCube, which is now under construction at the South Pole. In the Mediterranean sea, the neutrino telescope ANTARES is now being deployed, and it is expected that by the end of 2008 it will provide accurate limits to the neutrino flux in the southern sky. In addition, the technological challenges to build a neutrino telescope in deep sea have been surmounted by experiments like ANTARES, NEMO and NESTOR, which have motivated the approval of the design study of the Kilometre-Scale version in the Mediterranean sea, KM3NeT. This new generation of ambitious neutrino telescope experiments will achieve effective volumes ten times larger than their predecessors and will be able to explore the outer Universe in a way never seen before.

1.1 Cosmic rays

Cosmic rays (CR) are basically high energy non-photon particles (photons are customarily excluded in the definition) which are constantly hitting the upper shells of the Earth's atmosphere. The observation of these CR is mainly performed observing the extensive air showers of secondary charged particles or by means of other effects like the Cherenkov fluorescence of the atmosphere, although direct measurements of CR are experimentally accessible at modest energies (up to about 10^{14} eV). Their composition ranges from nuclei to protons, electrons and neutrinos of all flavours. The energy of these particles can exceed even 10^{20} eV, but their acceleration mechanisms and the sites of origin are still under discussion. The energy spectrum is of non-thermal origin and follows a broken power-law of the form

$$\frac{dI}{dE} \propto E^{-\gamma}, \tag{1.1}$$

where γ is the spectral index. Figure 1.1 shows the CR flux observed at Earth.

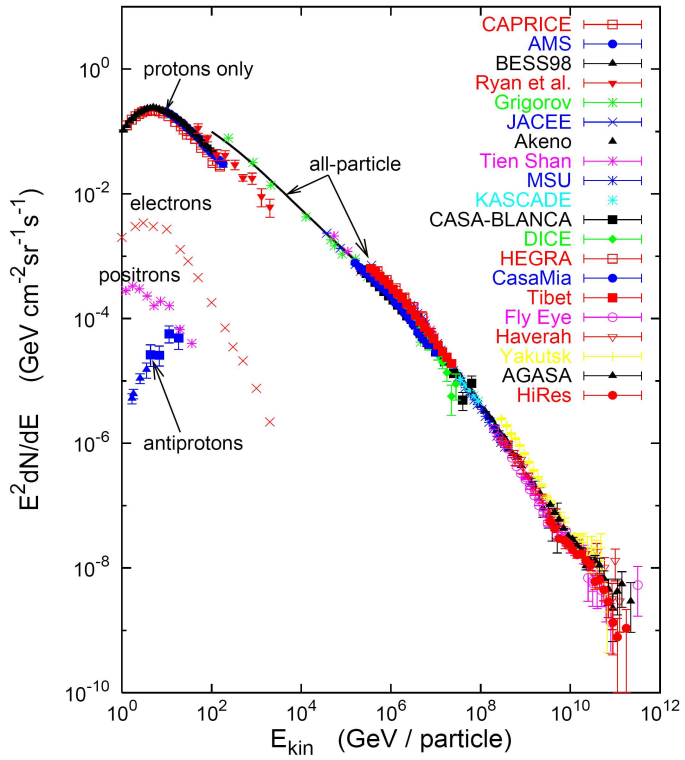

Figure 1.1: *Measurements of the cosmic ray flux over a wide energy range, assembled by Gaisser and taken from [3].*

The CR data have been measured over 13 orders of magnitude in energy and more than 30 orders of magnitude in flux. At the lowest energies, CR are sufficiently plentiful that balloon and satellite experiments can have enough collecting area to directly measure the fluxes of different nuclei being protons the most numerous together with other common nuclei. Above 1 PeV, no measurement of the primary particles can be done, instead secondary particles are measured, produced in high-energy CR interactions in the atmosphere forming an extensive air shower. Although the spectrum of

CR at Earth is mainly characterized by $\gamma \sim 2.7$, it changes to about 3.1 at an energy of roughly 3×10^{15} eV. This feature is referred to as the *knee*. The conventional theory of CR [4] posits that supernova remnants (SNR) in the Galaxy are the site of acceleration of CR for energies up to the *knee*, although this theory is not free from some difficulties as can be seen in [5]. The explanation of the *knee* is still an open question and different models have been proposed to explain this feature in the CR spectrum [6]. Some models invoke astrophysical reasons, arguing that the *knee* is an intrinsic property of the CR spectrum, while others hypothesize new particle processes in the atmosphere [7] as responsible of the steepening in the CR flux. In [8], the author considers a phenomenological model by assigning a cut-off energy to the energy spectra of every individual CR component. This cut-off describes better the data when it is proportional to the nuclear charge. Hence the *knee* at 3 PeV follows from subsequent cut-offs for individual elements at energies $Z \times 3 \times 10^{15}$ eV where Ze is the nuclear charge. This phenomenological model would also explain another feature known as the *second knee* at energies about 4×10^{17} eV where the spectral index increases again due to the end of the Galactic component of the CR spectrum. There is no consensus on a preferred accelerator model for energies above the *knee* up to 10^{19} eV, where there is a flattening in the spectrum dubbed as the *ankle*. The flux above this energy threshold is one 10^{19} eV particle per kilometre square per year per stereoradian, which makes them accessible in large ground-based installations only. The CR above the *ankle* are usually referred to as ultra high energy cosmic rays (UHECR) and are predominantly protons or nuclei, although the possibility that highest cosmic rays to be γ-ray photons has also been discussed [9], although this hypothesis is almost ruled out. It is generally assumed that CR of energies above 3×10^{18} eV are extragalactic in origin, therefore, the *ankle* is usually associated with the appearance of a flatter, extra-galactic CR spectrum [10]. Their sources are presumed to be found in some extreme astrophysical objects such as the Active Galactic Nuclei (AGN). More recently, the Pierre Auger Observatory, still under construction, has reported the first hints of association of CR measured events of energies about 60 EeV[1] and nearby AGN [11]. Although its statistical significance is limited, the results suggest that AGN are the prime source candidates for UHECR acceleration. Above a threshold of 60 EeV, protons from CR interact with the 2.7 K cosmic microwave background radiation (CMB) and lose energy motivating that protons of that energy cannot travel distances further than few tens of Mpc. This phenomena is the so-called Greisen-Zatsepsin-Kuz'min (GZK) cutoff [12, 13].

This cut-off limits the existence of high energy CR emitters to our local super-cluster or other exotic sources of CR to explain events above the GZK cut-off. The GZK cut-off has stimulated further interest since there are two, apparently, contradictory measurements about the CR spectrum in the region between 10^{19} and 10^{20} eV. The AGASA ground array detector [15] reported high energy events ($> 2 \times 10^{20}$ eV) claiming a continuity in the CR spectrum, these observations are in disagreement with the HiRes fluorescence detector [16] whose data seem to be consistent with a boundary in the CR spectrum. The Auger experiment has analysed the first data set collected from 1 January 2004 through 5 June 2005 [14]. The comparison among the data from the

[1] GeV = 10^9 eV, TeV = 10^{12} eV, PeV = 10^{15} eV, EeV = 10^{18} eV

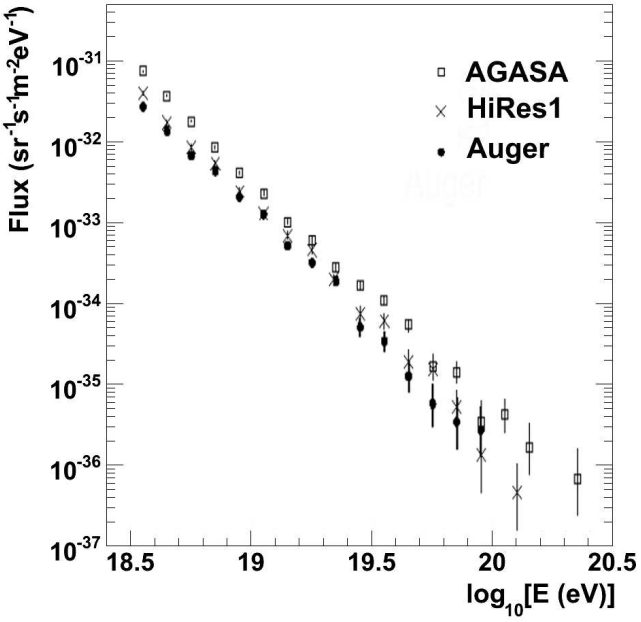

Figure 1.2: *Comparison of the Auger spectrum with those of AGASA and HiRes 1 (mono) [14].*

three experiments can be seen in figure 1.2. Preliminary results coming from Auger indicate that statistical and systematic errors cannot distinguish between a continuing spectrum and one compatible with a GZK suppression. However, the rapidly increasing data set with the exposure time and the expected reduction in systematic uncertainties will improve the precision of this measurement in the near future.

1.1.1 Origin of cosmic rays

The origin of cosmic rays is still an unresolved question. Models for the origin of the highest energy cosmic rays fall into two categories, bottom-up and top-down models.

In the bottom-up scenarios, it is assumed that a charged particle is accelerated in some astrophysical environments. Most likely, the mechanism responsible for the acceleration of particles to high energies is supposed to be the Fermi Mechanism [17,18]. Fermi provided the key for explaining the energization of CR. The Fermi Mechanism explains particle acceleration by the wandering back and forth between the two sides of a shock-wave. These shock-waves are assumed to be originated in environments of exceptional gravitational forces like the vicinity of black holes. This process of acceleration of charged particles is a very appealing scheme for the origin of CR since it explains the power law tendency in the CR spectrum. Figure 1.3 illustrates the particle acceleration by an astrophysical accelerator.

Figure 1.4 shows a diagram first produced by Hillas (1984). Hillas derived the maximum energy at which a particle of a given charge can be accelerated, independently of the mechanism, from the simple argument that the Larmor radius of the particle should be smaller than the size of the acceleration region. This energy is given by the

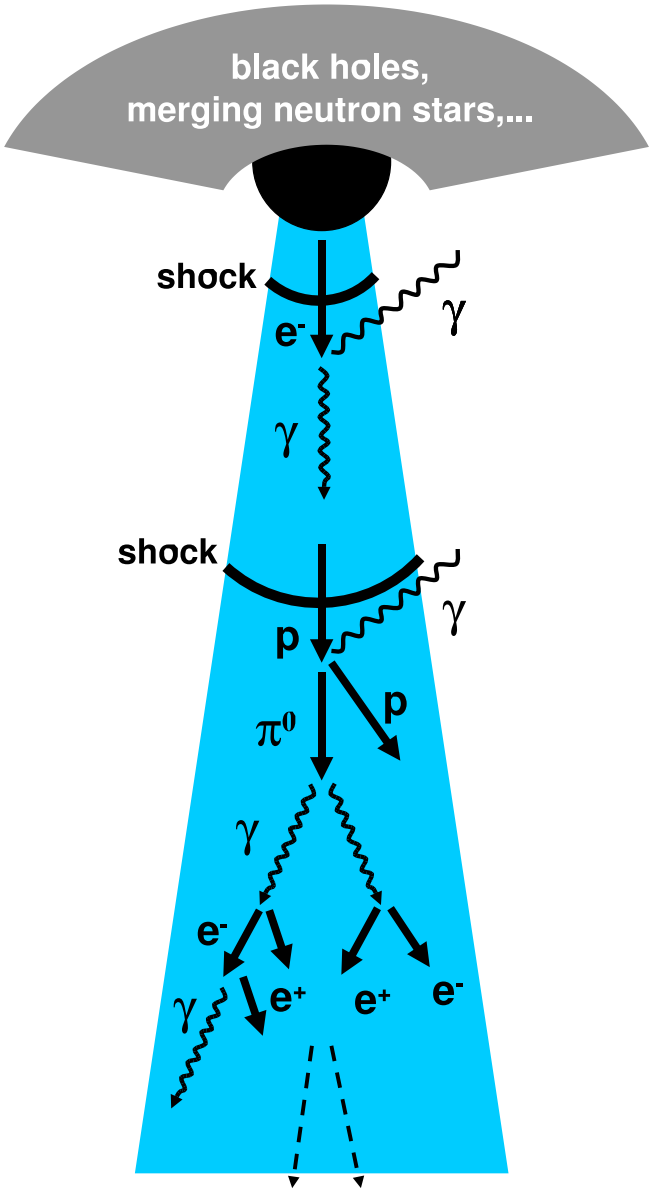

Figure 1.3: *Sketch of a cosmic accelerator producing photons. The charged pions that are inevitably produced along with the neutral pions will decay into neutrinos.*

following relationship:

$$E_{18} \sim \beta Z B_{\mu\mathrm{G}} R_{\mathrm{kpc}}, \tag{1.2}$$

where β is the velocity of the shock wave in the Fermi scheme or other acceleration mechanism efficiency. The plot 1.4 gives the relation between the required magnetic fields to accelerate particles and the dimension of the astrophysical objects needed to contain the accelerating particle through the acceleration process. The lines simple give the magnetic field as function of the gyroradii for protons (solid) and iron (dashed) for a plausible limit of 10^{20} eV CR containment in the sources, indicating the minimum size for scattering centres moving at speeds about c. It is important to mention that the processes of energy losses in the sources are not included in the plot. Above the *ankle* the gyroradius of a proton in the galactic magnetic field exceeds the size of the Galaxy, this is the reason why it is generally assumed that an extra-Galactic component in the CR spectrum is the responsible of the flattening at those energies. As can be seen from the Hillas plot, one of the plausible acceleration sites may be the radio lobes of powerful radio galaxies.

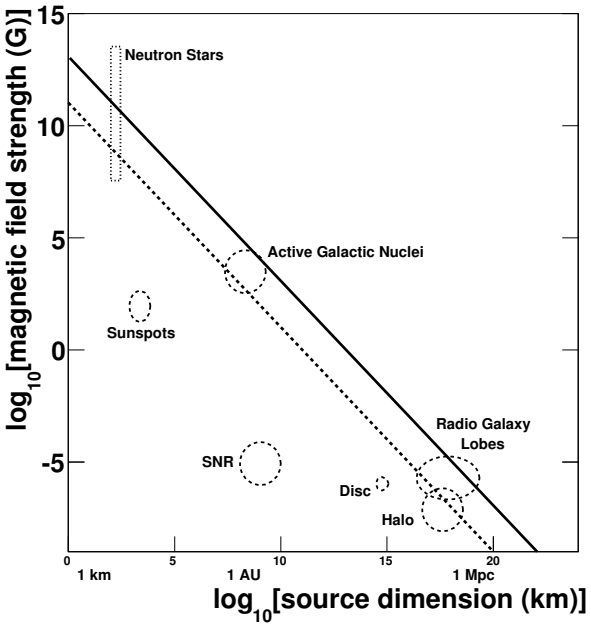

Figure 1.4: *Proposed sites for cosmic ray acceleration related to their likely dimension. The lines shows the magnetic field strength vs. gyroradii for protons (solid) and iron (dashed) for a limit of 10^{20} eV CR containment in the sources.*

There are other approaches to the problem of the origin of high energy cosmic rays. In [19] the authors hypothesize about the *cannonball* mechanism as the only mechanism for the CR acceleration. This model was firstly postulated to explain the origin of γ-ray bursts (see figure 1.5), however, it has been largely discussed and it is controversial [3].

Nevertheless, the explanation of the acceleration of protons to the highest energies above 10^{19} eV is still a challenge. This difficulty is by-passed by means of the top-down models. The top-down mechanisms invoke the decays of super-massive particles mainly relics formed in the post-inflation stage of the early Universe such as primordial black

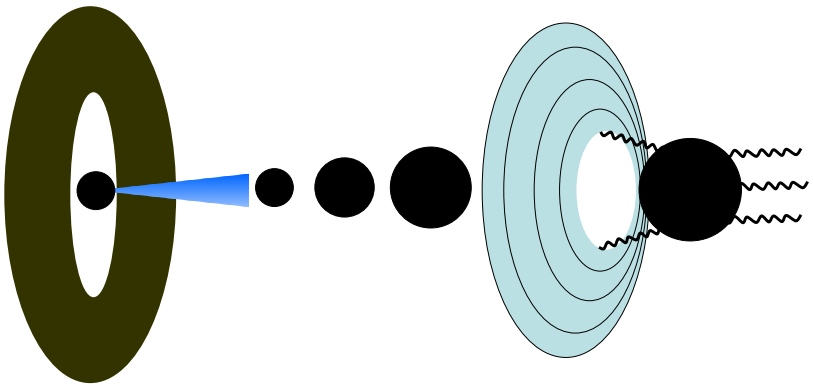

Figure 1.5: *Sketch (not to scale) of the cannonball model of a long duration γ-ray burst.*

holes and topological defects (TDs) associated with Grand Unified Theories. However most of these scenarios predict neutrinos within the observable region of the future Kilometre-Scale neutrino observatories [20]. These neutrinos have not been observed yet [21]. In addition, in [22] the authors showed that the γ-ray flux predicted by many TD models of UHECR exceeds that observed at 100 MeV energies. String theories also predict the existence of other super-heavy metastable particles, *cryptons*, which might form part of the cold Dark Matter clustering in galactic halos. The decay of such particles would also explain the origin of the highest energy CR.

1.1.2 Measurements of cosmic rays

Up to energies of 10^{14} eV, the CR spectrum can be directly detected above the atmosphere, on stratospheric balloons or in outer space by satellites. This kind of experiments, have provided the most relevant information about the composition of CR in the Galaxy and had contributed to establish the standard model of Galactic CR. Among balloon-borne detectors there are two promising experiments, CREAM [23] and TRACER [24]. Both balloons had successful long-duration flights from McMurdo, Antarctica, and data analysis is on-going. These experiments are required to resolve the discrepancies between the Galactic CR model and the measurements when extrapolated to PeV energies.

Satellites, on the other hand, are represented by PAMELA and AMS experiments. PAMELA [25] is a particle identifier using a 20 cm^2sr magnet spectrometer and a variety of specialized detectors. More recently, in June 2006, PAMELA has been put in an elliptical orbit at an altitude between 350 and 600 km on a Russian satellite. The experiment is expected to operate for at least three years. The AMS [26] is a space borne experiment to be placed in the International Space Station. The experiment will be launched with a Space Shuttle, however due to known problems with the Space Shuttle its schedule is still unclear.

Above 10^{14} eV, CR measurements are accessible from ground detection infrastructures. The showers of secondary particles created by interaction of primary CR in the atmosphere are extensive enough to be detected by arrays of scintillation counters or

water tanks. The energy region around the *knee* and shortly above has been explored by different experiments, the most notorious being the KASCADE [27] experiment. Observations of this spectrum region show that the average mass of CR particles increases when passing the *knee* which is directly implied by an acceleration proportional to the charge of the particle. On the contrary, the knowledge about mass composition above a few 10^{16} eV is rudimentary. In order to improve our insight of that region, detectors with an area $\sim$ 1 km^2 are required, but with much smaller spacing than those experiments devoted to extra-Galactic CR detection like AGASA and the Auger Observatory. The future of those experiments will be KASCADE-Grande [28] which is an extension from the original KASCADE array and it is expected to provide important information on the transition from Galactic to extra-Galactic CR. At the South Pole, the future installation IceCube/IceTop, will be able to register simultaneously the electromagnetic and muonic shower components with a 1 km^2 array of ice Cherenkov detector at the surface (IceTop) and a well shielded 1 km^3 ice Cherenkov detector (IceCube).

At energies above 10^{18} eV, the ground array technique is used using grids with $\sim$ 1 km spacing. One of the largest installations was the AGASA [15] experiment which was decommissioned in early 2004. Another technique is the detection of the fluorescence emission due to extensive air showers in the atmosphere. This is the detection principle of Fly's Eye detector and the High Resolution Fly's Eye (HiRes) [16]. At present, the most important of this kind of experiments is the Pierre Auger Observatory [14] which combines both techniques. The Auger Observatory is located in the southern hemisphere in Mendoza, Argentina and will reach its full size, 1600 water Cherenkov tanks covering 3000 km^2, in 2008. The four fluorescence telescopes have already been built. As outlined previously, first results from Auger Observatory, are not in complete agreement with AGASA previous reports concerning the end of the CR spectrum. However, it is expected that forthcoming data from Auger will provide enough information to understand the end of the CR spectrum. Complementary to this observation facility, the construction of the northern Auger site is planned to begin in Colorado, USA, in 2009.

Air showers also emit coherent synchrotron radiation at radio frequencies (20$-$100 MHz) from electrons and positrons deflected in the geomagnetic field. The detection of such radio emission, constitutes a new cost-effective detection principle whose feasibility has been met by work of the CODALEMA [29] collaboration. The Auger Observatory is going to explore these new technique within their program. In addition, ultra high energy cosmic rays might be optically detected from satellites looking downward from orbits. Projects like OWL [30] and EUSO [31] may use this novel detection method and different efforts are being performed to lower the thresholds of this kind of experiments.

1.2 High energy photons and neutrinos

The bottom-up acceleration mechanisms reviewed in the previous section are only valid for charged particles. Particles electrically neutral such as photons or neutrinos are the decay products of accelerated charged particles. As indicated in figure 1.3, both

leptonic and hadronic particles can be accelerated in cosmic accelerators. It is assumed that black holes accelerate electrons, since synchrotron radiation observations indicate so. On the other hand, we know that protons should be accelerated because they are detected as CR. Both models, the leptonic model and the hadronic model should coexist in parallel, but only the hadronic acceleration predicts the neutrino emission. Accelerated protons in *transparent* sources will interact in the surroundings of the CR emitter with photons predominantly via the Δ^+ resonance

$$\begin{aligned} p + \gamma \rightarrow \quad & \Delta^+ \rightarrow \pi^0 + p \\ p + \gamma \rightarrow \quad & \Delta^+ \rightarrow \pi^+ + n. \end{aligned} \tag{1.3}$$

Protons will also interact in *pp* and *pn* interactions. Charged pions and neutral pions will decay into neutrinos and γ-rays respectively. Therefore, the energy escaping from the source is distributed between CR, γ-rays and neutrinos. This implies that the observed CR flux will limit the expected neutrino flux, since the neutrino energy generation rate will never exceed the generation rate of high energy protons. The upper bound derived from a generic transparent CR source is of $E_\nu^2\ \Phi_\nu < 4.5 \times 10^{-8}$ GeV cm^{-2} s^{-1} sr^{-1} which is often referred to as the Waxman-Bahcall flux [32]. Waxman and Bahcall referred to this flux as a bound because, in reality, more energy is transferred to the neutron than to the charged pion in the source.

On the other hand, high energy photons can be produced in both leptonic and hadronic models. The most important processes to produce high energy γ-rays are the Inverse Compton (IC) scattering, and the neutral pion decay following *pp* interaction. IC γ-rays are produced in the interactions of energetic particles with the ambient background fields, the CMB, and the diffuse Galactic radiation of star light. This process is very efficient in producing γ-ray photons since low energy photons are found in all astrophysical objects. Multi-TeV electrons producing γ-ray of TeV energies via IC, produce as well synchrotron radiation of X-ray energies [33]. Therefore, measurements of the synchrotron X-ray flux can derive an IC γ-ray expected flux value.

The relationship between the γ-ray acceleration and the hadronic acceleration model is the meson-decay channel. The most important process is the decay of π^0-mesons, $pp \rightarrow \pi^0 \rightarrow \gamma\gamma$. The γ-ray spectrum in this case, almost repeats the parent proton spectrum. Hence the γ-ray from hadronic models have crucial information about the primary nucleonic CR.

1.3 Gamma ray astronomy

In the last years, astrophysics and astronomy have broadened to encompass the entire electromagnetic spectrum up to γ-ray observations. It was not until the 1990s that photons in the MeV-GeV energy range were detected by the CGRO satellite. This satellite was equipped with the Energetic Gamma-ray Experiment Telescope (EGRET) [34] which covered γ-rays from MeV to GeV. The Third EGRET Catalogue contains 271

detections with high significance, with around 170 yet unidentified sources (see figure 1.6). Presently, the γ-ray astronomy with satellites continues its expansion. The future mission Gamma-ray Large Area Space Telescope (GLAST) [35], which will be launched by the beginning of 2008, is expected to reach the same sensitivity after one week of observation as the EGRET whole operation. However, due to the decreasing energy spectra, γ-rays above 100 GeV are only detectable in ground based detectors.

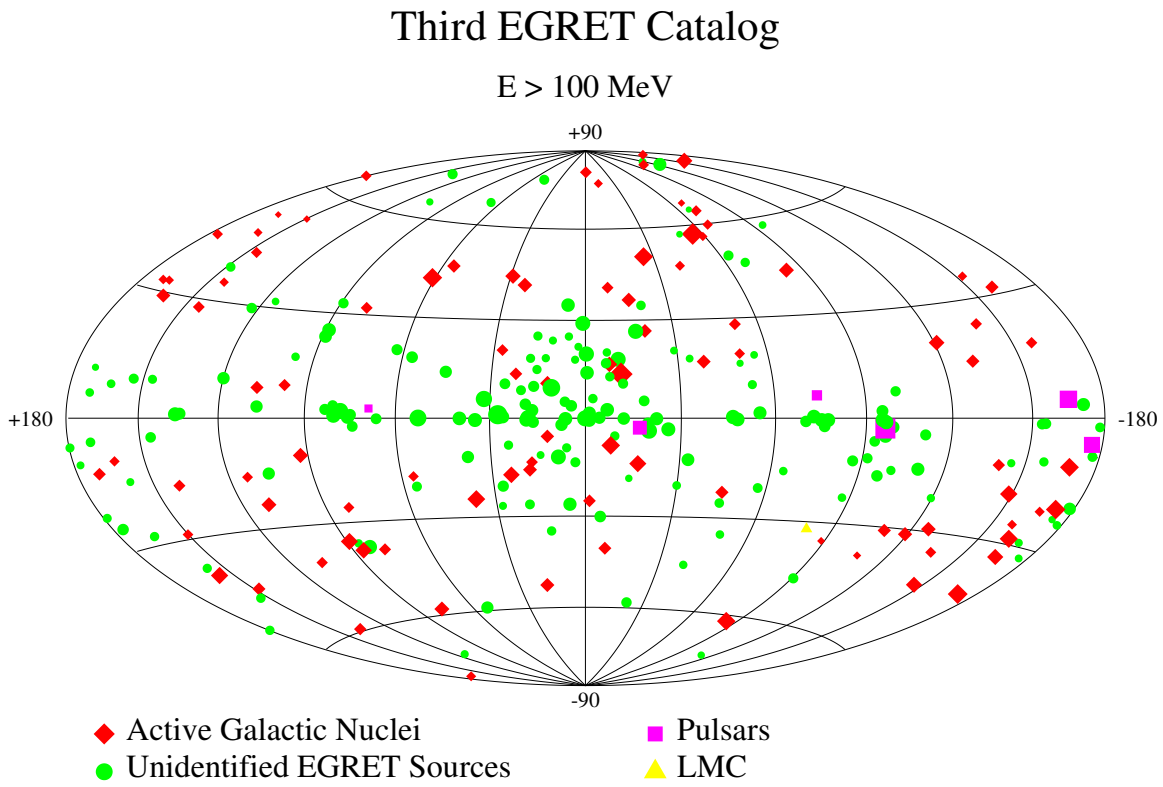

Figure 1.6: *Third EGRET catalogue for sources above 100 MeV in galactic coordinates.*

The pioneer experiment in ground based γ-ray detectors was built by the Whipple collaboration [36]. This was the first of a series of telescopes using a technique known as Imaging Air-Cherenkov Technique (IACT), which basically consists in detecting the images of air showers induced by TeV primaries in the Earth's atmosphere. These images are produced in a camera as the result of the Cherenkov light collection by a suitable mirror. During the past decade, several ground based γ-ray detectors were developed. The HEGRA experiment [37] has pioneered stereoscopic shower imaging by arrays of Cherenkov telescopes. More recently, two new generation telescopes were commissioned: the H.E.S.S. telescope array [38] and the MAGIC telescope [39].

- The H.E.S.S. instrument is an array of 4 twelve-metre telescopes which combines stereoscopic imaging with large light collectors and highly segmented detectors with a wide field of view. The H.E.S.S. telescope has been operational since 2004.

- The MAGIC telescope is a giant seventeen-metre telescope which provides the largest photon collector. It uses photon detectors with enhanced quantum efficiency, and image timing information. One of the particular features of this telescope is the fast positioning to a source when alerted by γ-ray burst trigger from satellite detectors. MAGIC started to take data in 2004. A second telescope is being built.

These IACTs telescopes have made possible to have the first catalogue of γ-ray sources emitting at energies above TeV. The sky map can be seen in figure 1.7. Specially interesting is the great population of new γ-ray sources in the Galactic Centre region discovered by the H.E.S.S. telescope.

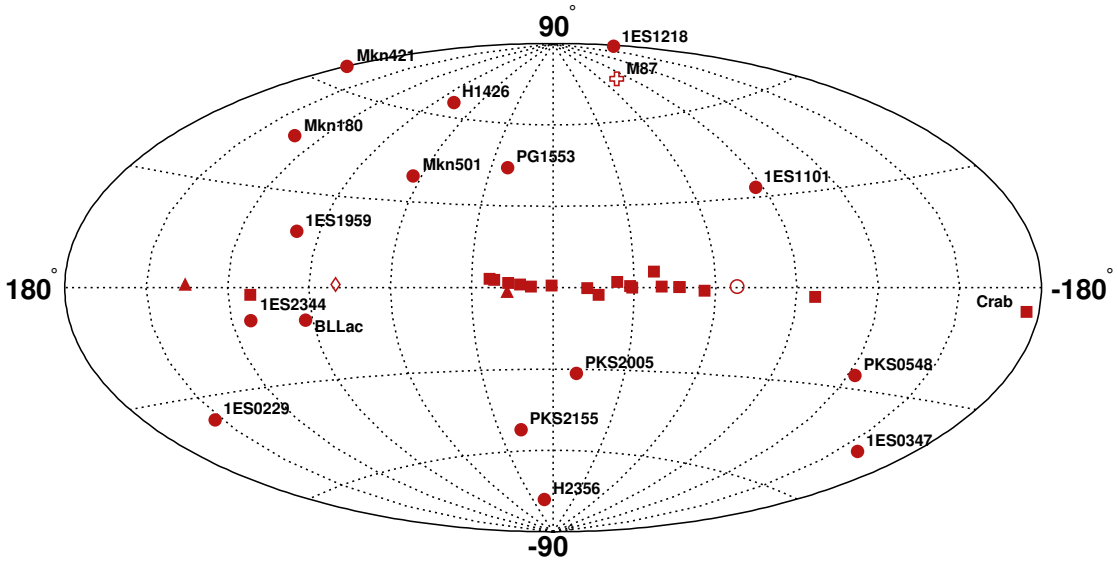

Figure 1.7: *Sky map of γ-rays sources above 100 GeV. The high population of sources in the Galactic range has not been labelled.*

There are also groups participating in missions like the VERITAS array [40] or the upgrade of the existing CANGAROO array [41].

However, although gamma astronomy has provided very exciting results in the recent days, it also has some limitations. Figure 1.8 shows the mean free path travelled by photons as a function of the energy. As can be seen, photons above 10 GeV are attenuated by interactions with the infrared and radio photons of the Extragalactic Background Light (EBL) and the CMB.

1.4 Neutrino astronomy

As mentioned in the previous sections, CR observations are nowadays providing very fruitful and exciting data. However, several important challenges have to be faced. First of all, protons are scrambled by magnetic fields in the Galaxy, which spoils

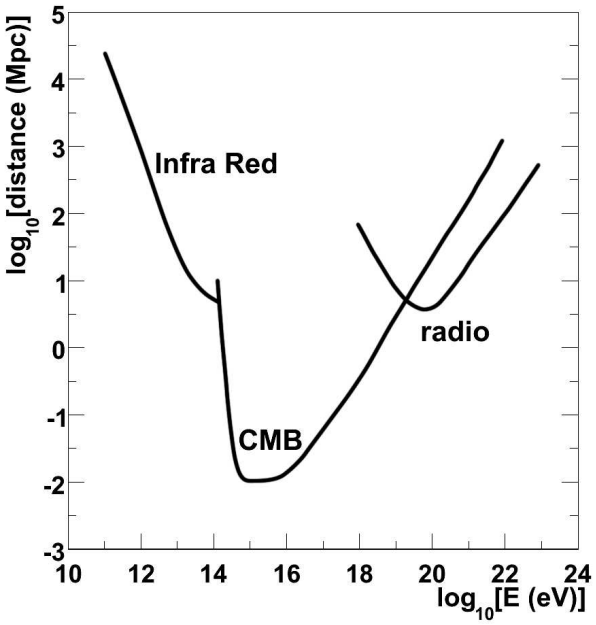

Figure 1.8: *Distance travelled by photons as a function of their energy (log-log scale).*

any position information that may be obtained by observing their arrival directions. Also, neutrons and protons will interact with the CMB (the GZK effect). This implies that high energy protons will not travel distances farther than 50 Mpc. Concerning γ-rays, although they do point back to their sources, they are absorbed on the CMB at an energy above the $\sim$ TeV.

In this scenario, neutrinos turn out to be the best candidate of a cosmic messenger in which we should focus. Neutrino have many advantages repeatedly emphasized in the literature [42], compared to the other cosmic messenger particles. First of all, they are neutral and hence, they do not suffer deflection from magnetic fields. On the other hand, they are stable and interact weakly so they can travel very long distances without decaying or interacting and can bring information from very dense objects even at very high energies. Neutrino astronomy is the natural step in the exploration of the Universe together with the necessity of multi-messenger campaigns, including neutrino observations, for solving some of the outstanding problems of high energy astronomy. On the other hand, their low interaction cross-sections makes the detection of low fluxes an experimental challenge.

1.5 Expected sources of extra-terrestrial neutrinos

In this section, we will review the candidate sources of high energy neutrinos. Many of these sources are guaranteed neutrino sources, since observations of the CR and γ-ray fluxes indicate so. The expected neutrino fluxes at Earth, however, are uncertain and predictions vary orders of magnitude in some cases.

1.5.1 Galactic neutrinos

Galactic sources have been posited to be the source of CR for energies up to the *ankle*. If so, these sources can be potentially interesting for a neutrino telescope. The main advantage with respect to extra-Galactic sources is their shorter distances to the Earth ($\sim 1 - 10$ kpc). The required luminosity for a Galactic source to produce the same event rate than an extra-Galactic source is orders of magnitude smaller. In this section, a list of the most promising sources of neutrinos from a Galactic origin will be reviewed. Many of them are already almost guaranteed neutrino sources in the light of the recent results from γ-ray telescopes such as H.E.S.S., although their neutrino fluxes are uncertain.

- **Shell-type supernova remnants**. After a supernova explosion (SN), particles can be accelerated in the so-called supernova remnants (SNR) in the shock-waves of the expanding shells via Fermi Mechanism. If the final product of the SN is a neutron star, already accelerated particles can also suffer additional acceleration due to its strong magnetic fields. Shell-type SNRs are considered to be the most likely sites of Galactic CR acceleration. This hypothesis is supported by recent observations in the γ-ray spectrum of SNRs. Of particular interest among prospective neutrino sources is the Vela Jr. SNR (RX J0852.0-4622). This SNR is one of the brightest objects in the southern TeV γ-sky which makes it specially appealing for a Mediterranean neutrino telescope. Recent observations of this SNR by H.E.S.S. [43] have concluded that the hadronic acceleration is a good candidate process to explain the hard and intense TeV γ-ray spectrum of Vela Jr. The H.E.S.S. telescope has observed γ-rays exceeding 10 TeV in its spectrum.

  In addition, the morphology of the TeV emission makes this source one of the most interesting astrophysical neutrino sources. The γ-ray TeV emission is observed to originate from several separated regions in a large apparent size of $\sim 2^\circ$. This morphology might allow neutrino telescopes to draw the first *neutrino map* of an astrophysical object. The observation of this extended source would enable a comparison of neutrino emission mechanisms among different regions of the same source. The expected neutrino-induced muon rate has been calculated in [44], leading to the encouraging result that a discovery may be possible in a Mediterranean detector like ANTARES (see figure 1.9).

  Another SNR of paramount importance, from the point of view of neutrino telescopes, is the SNR RX J1713.7-3946. This source has been the subject of endless debates about the nature of the process that originates its γ-ray spectrum [45]. The RX J1713.7-3946 was first observed in the TeV regime by the CANGAROO experiment which firstly claimed a leptonic origin of the observed γ-ray spectrum [46]. The same collaboration, however, disfavours purely electromagnetic processes as the only source of γ-rays from the analysis of later results with CANGAROO-II [47]. This source has been observed twice by the H.E.S.S. telescope improving noticeably the statistics [48]. H.E.S.S. observations support the

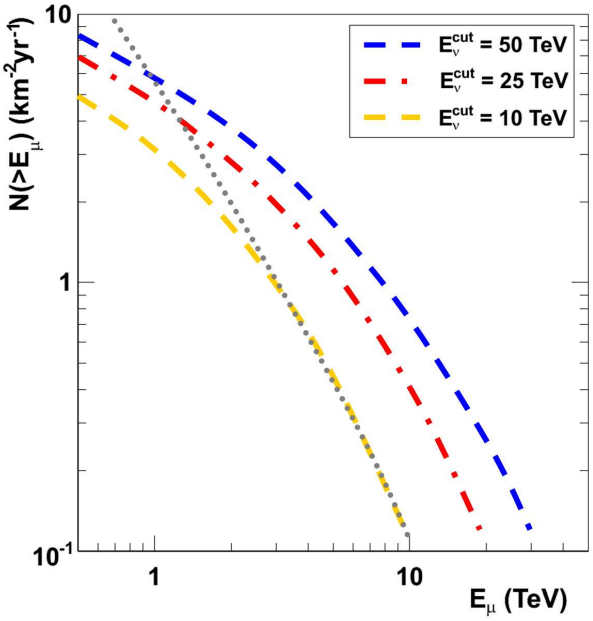

Figure 1.9: *Induced muon rates above a given measured muon energy for the Vela Jr. (RX J0852.0-4622) source. The different curves correspond to different neutrino spectrum exponential cutoffs. The dotted line stands for the atmospheric background in a 7 deg^2 bin. Rates are for one year of a Kilometre-Scale Mediterranean detector [44].*

hadronic origin of the observed γ-ray spectrum of RX J1713.7-3946. Previous neutrino calculations predicted large muon neutrino event rates from this source using the data available from CANGAROO-II [49, 50]. More recent calculations in [44] using the two data sets from H.E.S.S. lead to more realistic results concluding that this SNR should be detectable in a Kilometre-Scale Mediterranean detector.

- **Pulsar wind nebulae (PWNe)**. They are also called Crab-like remnants, since they resemble the Crab Nebula being the youngest and most energetic PWN known. They differ from the shell-type SNRs in the centre pulsar which blows out jets of very fast-moving material into the nebula. The radio, optical and X-ray observations suggest a synchrotron origin for these emissions. H.E.S.S. has also confirmed the TeV γ-ray emission from the Vela PWN, named Vela X. Although the H.E.S.S. collaboration has claimed that this emission is likely produced by the IC mechanism, an independent analysis considered the possibility of an hadronic origin for the observed γ-ray spectrum with the consequent flux of neutrinos [51]. Neutrino fluxes have been calculated in [52] for a few PWNe observed in TeV γ-rays, such as the Crab nebula, the Vela X SNR, the PWN around PSR1706-44 and the nebula surrounding PSR1509-58, concluding that all these PWNe could be detected by a Kilometre-Scale neutrino detector if all γ-rays above 2 TeV are produced in pp collisions via π^0 decays. The Crab nebula will be a special interesting source if neutrinos were emitted. This source is a standard candle in TeV γ-ray astronomy. A bright TeV neutrino source seen from both the northern and southern hemispheres will be of great interest. The predicted event rate in IceCube from the Crab nebula is $N(E_\mu > 1\text{TeV}) \sim 2.8$ yr^{-1} [44]. Unfortunately,

the Crab spectrum is soft and well described by leptonic processes [53], nonetheless AMANDA has reported an excess of a neutrino signal coming from the Crab nebula [54].

- **Galactic Centre (GC)**. The H.E.S.S. telescope has also reported the existence of a diffuse γ-ray emission in the region of the Galactic Centre [55]. The diffuse γ-ray emission of energies greater than 100 GeV is correlated with a complex of giant molecular clouds in the central 200 pc of the Milky Way. Early H.E.S.S. observations of the GC region detected a point-like source of very high energy (VHE) γ-rays at the gravitational centre of the Galaxy (HESS J1745−290 [56]) which coincides in position with the supermassive black hole Sagittarius A* and the SNR Sgr A East. In 2004, a more sensitive campaign revealed a second source, the PWN G 0.9+0.1 [57]. Thanks to the good sensitivity of the H.E.S.S. telescope, it is possible to subtract these sources and search for the diffuse γ-ray emission which spans the Galactic coordinates $|l| < 0.8°$, $|b| < 0.3°$. The reconstructed γ-ray spectrum for this region is well described by a power law with photon index of ~ 2.3. The hardness of this diffuse TeV γ-ray spectrum implies that protons and nuclei, rather than electrons, give rise to the observed γ-rays by π-meson decays induced from interactions of these CR with the ambient material. The photon index of the γ-rays, which closely traces back the spectral index of the CR, indicates a local CR spectrum that is much harder and $3 - 9$ times denser than that of the CR flux as measured at Earth (where an index of 2.75 is measured). The implication of these experimental fact is that there is likely an additional component to the Galactic Centre CR population above the diffuse CR which fills the Galaxy. The proximity of particle accelerators in the CG, and therefore the less propagation effects than in the Galaxy as a whole, gives a natural explanation for the harder spectrum which is closer to the intrinsic CR source spectra. The central source HESS J1745−290 is likely the source of these CR protons as suggested in [55], with two candidates for CR accelerations within it: the SNR Sgr A East, with an estimated age around 10 kyr; and the black hole Sgr A*, which have been more active in the past.

  The expected neutrino flux from these regions should take into account the extent of the GC source. The diffuse Galactic Centre source can be interpreted as a point-like source for a neutrino telescope with a muon angular resolution of $\sim 1°$. The GC is specially appealing for a Mediterranean neutrino telescope since it is within the sky view of a telescope located at such latitude. Using a correct unbinning analysis a discovery could be achieved for the GC in a Kilometre-Scale Mediterranean detector. H.E.S.S. also studied the point-like emission from HESS J1745-290, after subtracting the diffuse γ-ray emission from the GC ridge. These observations have constrained the possibility of Dark Matter annihilation as the origin of the γ-ray emission of this source [58].

- **Microquasars**. They are Galactic X-ray binary systems, which exhibit relativistic radio jets, observed in the radio band [59]. Microquasars present a morphology similar to the AGN, the presence of the jets makes them similar to small quasars,

hence their name microquasars. Furthermore, this resemblance could be more than morphological, it is common thinking that the physical processes that govern the formation of the accretion disk and the plasma ejection in large AGN are the same for microquasars. Microquasars have been proposed as acceleration sites of charged particles up to energies of about 10^{16} eV. These conclusions have been recently boosted by the discovery of the presence of relativistic hadrons in microquasars jets like those of SS 433, as inferred from iron X-ray line observations [60]. Two microquasars have drawn particular attention since they are the only known microquasars listed in the third EGRET Catalogue (see figure 1.6) as γ-ray sources above 100 MeV, and the only two detected so far at higher γ-ray energies [61, 62]. The microquasar LS I +61 303 has been observed by the MAGIC telescope. There is yet uncertainty as to what kind of compact object lies in the system. However, different measurements support the microquasar interpretation of LS I +61 303. MAGIC also reported a variability in the γ-ray emission from LS I +61 303, although a definitive proof (or disproof) of periodicity awaits further MAGIC observations. This source is specially appealing for a neutrino telescope located in the southern hemisphere like AMANDA or IceCube. The muon neutrino flux ($\nu_\mu + \overline{\nu}_\mu$) predicted for this source at Earth (considering neutrino oscillations) is given by

$$\Phi_{\nu_\mu} = 9.73 \times 10^{-13} \left(\frac{E_\nu}{\mathrm{TeV}} \right)^{-2.6} (\mathrm{TeV}^{-1}\mathrm{cm}^{-2}\mathrm{s}^{-1}), \tag{1.4}$$

this flux is below the limit for 4 years of AMANDA II data, at a level of 6×10^{-9} cm^{-2}s^{-1}. When integrating the flux given in equation 1.4 above 10 GeV is about a factor 6 smaller than the AMANDA II upper limit. An equivalent Kilometre-Scale detector like IceCube will be able to detect (or rule out) neutrinos coming from LS I +61 303 [63].

In the other hemisphere, the H.E.S.S. telescope has detected TeV γ-rays from microquasar LS 5039 and similar to LS I +61 303, the observed flux does not allow so far an unequivocal conclusion about the variability of the TeV source. In this regard, different astrophysical scenarios with involvement of both leptonic and hadronic interactions have been proposed to explain the TeV γ-ray emission. However, in [64] the authors show that electrons hardly explain the observed TeV γ-ray signal, and therefore, the parent particles of γ-rays should be protons or nuclei. Table 1.1 summarizes the numbers of predicted neutrinos per year for the ANTARES Mediterranean detector coming from the LS 5039 assuming a power-law neutrino spectrum with two different spectral index, $\gamma = 1.5$ and $\gamma = 2.0$, and two energy cutoffs, $E_{max} = 10$ TeV and 100 TeV [64].

- **Known unknowns and unknown unknowns**. In addition to SNR, PWNe and microquasars, there are other theoretical environments in which hadronic acceleration processes could take place, and therefore, a neutrino flux may be expected. Neutron stars in binary systems and magnetars [65] are candidates to yield and observable neutrino flux. From an experimental point of view, it is

E_{max} (TeV)	$\gamma = 1.5$	$\gamma = 2.0$
10	0.20	0.11
100	0.26	0.15

Table 1.1: *Number of ν_μ events with E_ν >1 TeV expected in 1 yr of observation of ANTARES (taking into account neutrino oscillations). See text and [64] for further details.*

reasonable to expect numerous discoveries of new γ-ray sources from the H.E.S.S., MAGIC and VERITAS air Cherenkov telescopes and the GLAST satellite. It is also worth remarking that a non-negligible number of VHE γ-ray sources detected by H.E.S.S. do not have a known counterpart in other wavelengths. The origin of such sources is a theoretical challenge in which neutrino astronomy may yield an insight.

1.5.2 Extra-Galactic neutrinos

The extension of the CR spectrum above the *ankle* is assumed to be the result of an extra-Galactic contribution in the CR components. Therefore, the existence of extra-Galactic high energy neutrino sources is directly implied by the CR observations. If hadronic particles (protons or any other nuclei) are accelerated in extra-Galactic objects it is reasonable to think that a neutrino flux will be also produced in such environments. As already mentioned there is an upper bound to the expected neutrino flux coming from optical thin sources, the so-called Waxman-Bahcall limit (WB). Although this limit may be surpassed by *hidden* or optically thick sources for protons to $p\gamma$ or $pp(n)$ interactions [66] as we will describe later, it is a reasonable limit to the predicted neutrino flux coming from different extra-Galactic sources of UHECR. The most plausible sources of UHECR are Active Galactic Nuclei (AGN) and γ-ray bursts (GRBs). In addition, in this section we review two guarantee sources of cosmic neutrinos, GZK neutrinos and the high energy neutrino background from starburst galaxies.

- **Active Galactic Nuclei**. Galaxies with a very bright core of emission embedded in their centre are called Active Galactic Nuclei. Models of AGN concentrate on the possibility of a supermassive black hole which lies at the centre of the galaxy. This supermassive black hole ($10^6 - 10^9$ $M_\odot$) would produce material accretion onto it releasing a large amount of gravitational energy. AGN are the brightest steady sources. According to equation 1.2 and taking into account the relativistic nature of the jets outflow and a Lorentz factor $\Gamma \sim 3-10$ for AGN, the estimation of the energy rate generated by the source is $L > 10^{47}$ erg s^{-1}, which may be satisfied by the brightest AGN [67]. Early models [68, 69, 70] postulating the hadronic acceleration in the AGN cores predicted an intensity well above the WB bound. The neutrino flux prediction from some of these models has been experimentally disproved by AMANDA. More recent models [71], however, predict fluxes close to the WB bound. Figure 1.10 presents a comparison of

various model predictions for the diffuse neutrino flux produced by AGN together with the WB bound.

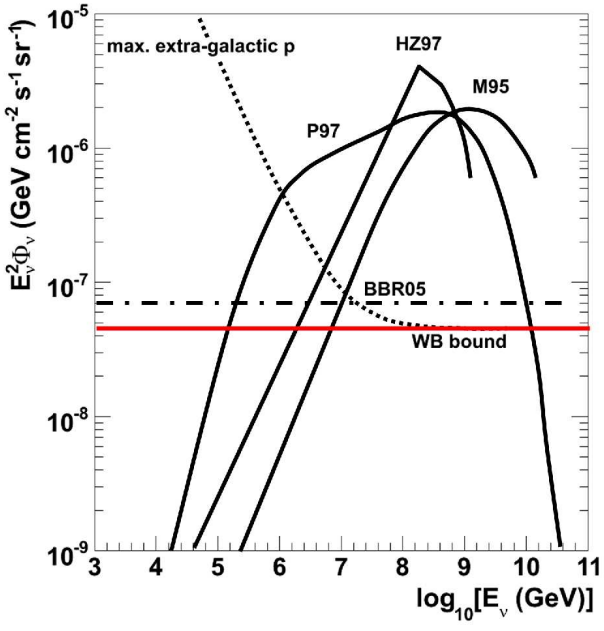

Figure 1.10: *The WB bound and various AGN predictions for the diffuse neutrino flux. Early models (M95 = Mannheim 1995 [68], HZ97 = Halzen & Zas 1997 [69], P97 = Protheroe 1997 [70]) yielded a neutrino flux above the WB bound. A more recent model (BBR05 = Becker, Biermann & Rhode 2005 [71]) predicts fluxes close to the WB bound.*

As outlined before, the Auger observatory has reported the first hints of correlation between CR directions and nearby AGN. Although the results do not exclude any other CR sources distributed among the nearby galaxies (in a similar way to AGN), the data suggest that AGN are the most promising candidates for CR emission and therefore an accompanying neutrino flux is expected.

- **Gamma ray burst**. They are perhaps the best motivated sources of high energy neutrinos. GRBs are short flashes of γ-rays –typically from milliseconds to tens of seconds long– carrying most of their energy in > 1 MeV photons. The collapse of massive stars to a black hole has emerged as the likely origin of the *long* GRBs with duration of tens of seconds. Recent observations suggest that the formation of the central compact object is associated with Ib/c supernovae [72, 73, 74]. GRBs also produce X-ray, optical and radio emission subsequent to the initial burst. This issue is referred to as the *afterglow* of the GRB. The detection of the afterglow is performed with more sensitive instruments that detect photons at wavelengths other than MeV γ-rays. The leading models assumed that a *fireball* is produced in the collapse which expands with a highly relativistic velocity ($\Gamma \sim 10^{2.5}$) powered by radiation pressure. The emission of γ-rays is assumed to be due to internal collisionless shocks within the *fireball*. Protons accelerated in the *fireball* internal shocks lose energy through photo-meson interaction with *fireball* photons. This interaction takes place via the Δ^+ resonance. In the

observer frame,

$$E_\gamma E_p = 0.2 \text{ GeV}^2\Gamma^2, \tag{1.5}$$

for $\Gamma \sim 10^{2.5}$ and $E_\gamma = 1$ MeV, characteristic proton energies of $\sim 10^{16}$ eV are required to produce pions. The interaction rate between photons and protons is high due to the high density photons yielding a significant production of pions. Neutrinos produced by pion decay typically carry 5% of the proton energy, hence, $\sim 10^{14}$ eV neutrinos are expected [75]. Less energetic neutrinos can also be originated in different regions or stages where GRB γ-rays are produced. The GRB afterglow arises as the jet *fireball* runs into the ambient medium, which could be the interstellar medium (ISM) or the pre-ejected stellar wind. Depending on this, a different contribution of neutrinos is expected at every time stage of the GRB. Figure 1.11 shows the expected muon neutrino flux at Earth from GRB 030329 and the associated supernova SN 2003dh taken from [76]. Different neutrino contributions from different stages of the GRB are indicated.

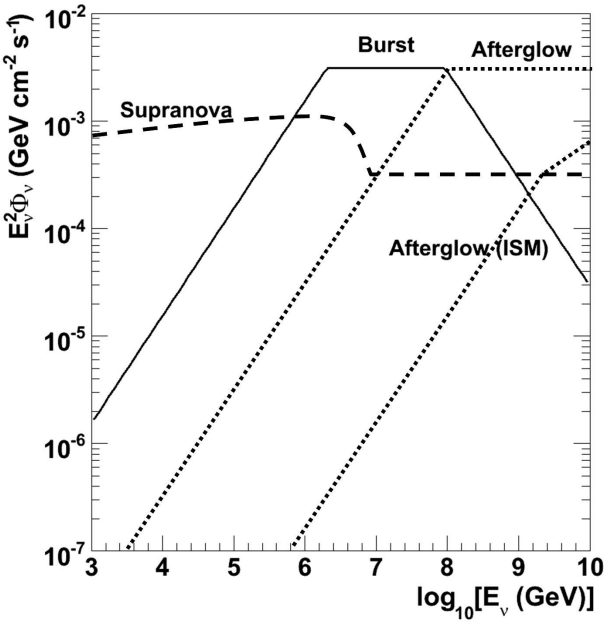

Figure 1.11: *Estimated muon neutrino flux from GRB 030329 and the associated SN 2003dh. Indicated are the possible supranova component, neutrinos coming in the internal shock burst component and the two afterglow contributions; flux coming from an early stage and the afterglow neutrino spectrum in the ISM case.*

Further estimates of the neutrino flux [77] lead to the conclusion that a Kilometre-Scale neutrino telescope detector will be necessary to detect neutrinos from GRBs. Nonetheless, being transient sources, GRBs detection has the advantage to be practically background free since neutrino events coming from GRB are correlated both in time and direction with γ-rays.

- **GZK neutrinos**. CR protons exceeding the threshold for pion production, $\sim 5 \times 10^{19}$ eV, will lose most of their energy in a relatively short time compared to the age of the Universe by interactions with the low energy photons

of the CMB [78]. This produces the well-known GZK cut-off already mentioned. Assuming the CR rate from the observations, the proton energy loss to pion production will produce a neutrino flux similar to the WB bound above $\sim 5\times10^{18}$ eV [79], since neutrinos from the Δ^+ resonance photomeson production approximately carry 5% of the proton energy.

- **Starburst or neutrino factories**. As we have mentioned, the WB bound is computed assuming that CR sources are optically thin for protons. However, radio observations of starburst galaxies have motivated the idea of the existence of such *hidden* sources of CR or purely-neutrino accelerators, since only neutrinos will be able to escape from these dense regions. A substantial fraction of the cosmic star formation activity at redshift ~ 2 occurs in transient starburst episodes. Supernovae are expected to enrich the dense star forming region of the starburst galaxy with relativistic protons and electrons. In addition, external relativistic particles injected by an outflow, in cases where quasar activity accompanies the starburst phase [80, 81], can contribute to the CR population. These relativistic protons, injected along with electrons into the starburst interstellar medium, would lose energy through pion production. Part of the proton energy will, therefore, be converted into neutrinos by π-meson decays. This neutrino flux, will act as a background high energy neutrino flux. The cumulative flux of GeV neutrinos calculated in [66] is

$$E_\nu^2\Phi_\nu \approx 10^{-7}\ \text{GeV cm}^{-2}\ \text{s}^{-1}\ \text{sr}^{-1}, \tag{1.6}$$

  which is of the order of the WB bound at the energy range $\sim$ 1 GeV to $\sim$ 300 TeV, and possibly extending also to higher energies which makes this neutrino background potentially detectable by forthcoming Kilometre-Scale neutrino telescopes.

1.5.3 Neutrinos from exotic models

The origin of CR at the highest energies ($E > 10^{19}$ eV) is a mystery. It has been suggested that modification of the basic laws of physics, or other exotic scenarios are necessary in order to account for the existence of UHECRs. These *exotic* models suggest non-acceleration or top-down mechanisms to explain the origin of extremely high energy CR (EHECR). According to the Hillas plot (see figure 1.4) by the simple criterion of Larmor containment there is a relationship between the size of the cosmic accelerator and the maximum energy up to which the particle can be accelerated. Advocates of the top-down scenario argue that the most energetic CR observed can barely be achieved in even the most powerful astrophysical objects. Moreover, the problem becomes more acute when the energy loss during the CR propagation is taken into account. In the top-down scenarios, massive particles called X particles, decay to quarks and leptons. The hadronization of quarks will produce light mesons, baryons and the subsequent flux of photons, neutrinos and electrons. These X particles should satisfy the following conditions: 1) they must decay in recent cosmological epochs, 2) the X particles must be

sufficiently massive, with masses $m_X \gg 10^{11}$ GeV, and 3) the density and decay rate of X particles must be large enough to produce detectable flux of UHECRs. The particular realization of the top-down scenario identifies the X particles with the supermassive gauge bosons, Higgs bosons and/or superheavy fermions produced by cosmic TDs like cosmic strings, magnetic monopoles, superconducting cosmic strings and alike. These TDs could be formed in symmetry-breaking phase transitions associated with Grand Unified Theories (GUTs) in the early Universe. For an extensive review of top-down models see [22].

1.6 Other physics topics

Apart from neutrino fluxes related to the CR spectrum, there are further estimates of neutrino signals coming from other sources, like for instance, neutrinos coming from Dark Matter annihilation. In addition, a neutrino telescope will be able to detect other non-neutrino signals, being the magnetic monopoles one of these candidates.

- **Neutrinos from Dark Matter annihilation**. There is a variety of observations that indicate that a large fraction of the matter in the Universe must be non-baryonic. In fact, only about 4% of the total energy density in the Universe can be observed directly. About 22% is thought to be composed of Dark Matter, and the remaining 74% is thought to consist in Dark Energy. It has been proposed that Dark Matter is made up of low interacting particles with masses around the GeV-TeV scales. These so-called weakly interactive massive particles (WIMPs), are predicted by supersymmetric extensions of the Standard Model. If WIMPs contribute to Dark Matter, they would also populate the galactic halo of our Galaxy. These WIMPs would suffer gravitational interaction and would accumulate in the core of massive objects such as the Sun, the Earth and the GC where they would annihilate pairwise, producing high energy neutrinos that can be searched by neutrino telescopes. In the minimal standard supersymmetric model (MSSM), the favourite WIMP candidate is the lightest supersymmetric particle (LSP) which is generally assumed to be the lightest neutralino.

- **Magnetic Monopoles**. Extrapolation to sufficiently high energies of the coupling constants, suggests that strong, weak and electromagnetic interactions could be unified in one single force. GUTs assumed that these forces can be described at high energies with a single simple gauge group in which only gauge couplings appears. The existence of magnetic monopoles is a generic prediction of these GUT models according to [82, 83]. Monopoles appeared as TD in the transition phases of the early Universe. One property of monopoles is that they are accelerated along the magnetic field lines as charged particles are accelerated in electric fields. Since there is not an unique model of magnetic monopoles, best estimations about the fluxes are derived without depending on specific models. The upper limit on the monopole flux can be reasoned from cosmological constrains, like the monopole mass density which cannot exceed the mass density of

the Universe. The expected limit on the monopole flux is [84]

$$\langle F \rangle \lesssim 10^5 \beta \frac{1}{M} \ \ \mathrm{cm}^{-2}\mathrm{s}^{-1}\mathrm{sr}^{-1}, \tag{1.7}$$

where β is the typical monopole velocity and M stands for the monopole mass in GeV. There is a mass-independent upper limit of approximately 10^{-15} cm^{-2} sr^{-1}s^{-1}, the so-called Parker bound [85], which is derived from the requirements in the Galactic magnetic field.

Monopoles energy loss is dominated by ionization processes, when passing through matter, for Lorentz factors $\Gamma \lesssim 10^4$. At those velocities, monopoles emit very intense Cherenkov light in transparent media. With a specific trigger in an underwater neutrino telescope like ANTARES, monopoles can be distinguished from PeV muons.

- **Nuclearities**. They are, together with slow monopoles ($\beta < 0.1$), the best candidates for slowly moving and bright particles that might be detected with a neutrino telescope. Alike some models of monopoles, these nuclearities (strange quark matter) will catalyse nucleon decays yielding Cherenkov light signals generated by the nucleon decay products along their path. Nuclearities could have been produced in the primordial Universe or in violent astrophysical processes [86,87].

- **Quantum gravity and violation of Lorentz invariance**. For many years, the search for a quantum theory of gravity has been a theoretical quest solely, since scales at which gravitational effects become important were far beyond from those achieved in experiments. Recently, two of the most promising theories of quantum gravity; string theory [88,89] and loop quantum gravity [90] imply consequences of quantum gravity phenomenology that may arise as modifications of standard physics at present or near future experiments. Two particular effects are the quantum decoherence, in which particles travelling large distances may interact with *virtual* black-holes or quantum fluctuations of space-time. As a result, particles may change their flavour. This effect will have special implications in neutrino oscillations. The second effect is the violation of the Lorentz invariance [91] which is directly implied by the assumption of a fundamental length scale. In both cases, neutrino will play a major role and modifications of neutrino oscillations will be a test of this quantum gravity phenomenology.

1.7 Neutrino oscillations

Neutrino oscillations are a well known phenomenon that will affect logically the cosmic neutrino flux. As already mentioned, high energy neutrinos are believed to be produced in astrophysical sources mainly through the decay of charged pions, $\pi^+ \rightarrow \mu^+ + \nu_\mu \rightarrow e^+ + \nu_\mu + \nu_e + \overline{\nu}_\mu$ or $\pi^- \rightarrow \mu^- + \overline{\nu}_\mu \rightarrow e^- + \nu_\mu + \overline{\nu}_e + \overline{\nu}_\mu$ produced in $p\gamma$ or nucleons pp, pn. Therefore, neutrino fluxes of the different flavours are expected to be at the source in the ratio $\nu_e : \nu_\mu : \nu_\tau = 1 : 2 : 0$. Neutrino oscillations will induce

flavour changes while neutrinos propagate through the Universe. A complete review about neutrino oscillations can be found in [92]. According to neutrino oscillations parameters, the ratio of the fluxes of neutrinos changes to an observed flux ratio at Earth of $\nu_e : \nu_\mu : \nu_\tau = 1 : 1 : 1$ [93]. There are, however, some modifications to this scenario. Since the pion lifetime is shorter than that of the muons, at sufficiently high energy the probability for pion decay is higher than the corresponding probability for muon decay. That yields a flux ratio at source of $\nu_e : \nu_\mu : \nu_\tau = 0 : 1 : 0$ [94], which implies a $\nu_e : \nu_\mu : \nu_\tau = 1 : 1.8 : 1.8$ ratio on Earth at high energies [95]. The observation of such energy dependence in cosmological neutrino oscillations by future neutrino telescopes will provide a unique information about astrophysical neutrino sources. On the other hand, this energy dependence of the flavour ratio will make difficult the study of variations of the neutrino oscillation pattern due to new exotic physics like the quantum decoherence and the violation of the Lorentz invariance.

1.8 Neutrino telescopes

In this section we will discuss different neutrino experiments which are presently operating or will be soon commissioned. The energy region between TeV and PeV is dominated by Cherenkov neutrino telescopes in open water or ice. ANTARES is one these Cherenkov telescopes but it will be reviewed in detail in the following chapter, as well as, a detailed description of the detection principle followed by these neutrino telescopes.

- **NT-200**. It is the full configuration of the pioneering Baikal detector located in the Siberian lake Baikal at a depth of 1300 m [96,97]. The Baikal experiment has been running since 1993, and in 2005 it was expanded in a configuration known as the NT-200+ stage (192 photomultiplier at eight strings and 36 additional photomultipliers in three separated strings). The NT-200 telescope is one of the first to demonstrate the feasibility of optical detection underwater or ice. In [98] the collaboration presented the latest results based on data taken in 1998-2003. For an E^{-2} behaviour of the neutrino spectrum, the limit set by the Baikal collaboration for a diffuse neutrino flux of all flavours (assuming a flavour ratio of $\nu_e : \nu_\mu : \nu_\tau = 1 : 1 : 1$) and for 1038 days is $E^2\Phi_\nu(E) < 8.1\times10^{-7}\mathrm{cm}^{-2}\mathrm{s}^{-1}\mathrm{sr}^{-1}\mathrm{GeV}$ over an neutrino energy range $2 \times 10^4 \div 5 \times 10^7$ GeV.

- **AMANDA/IceCube**. AMANDA [54] is a neutrino telescope located at the South Pole using the antarctic ice as the Cherenkov medium. AMANDA started in 1992 and its current stage, AMANDA-II, has a total of 677 photomultipliers in 19 strings. AMANDA effective area is 0.02 km^2, about one order of magnitude below the size suggested by flux estimations from astrophysical sources. Figure 1.12 shows the 4382 up-going neutrino candidate events collected with AMANDA-II between 2000 and 2004 [99]. Unfortunately, even with this high statistics, no evidence of a point source signal has been identified. Accumulation of events in clusters in the sample have significances consistent with background expectations. The highest significance seen was 3.7σ and the probability of seeing

something this significant or higher was found to be 69%. This has motivated the construction of detectors more than one order of magnitude beyond AMANDA size. Therefore, based on the acquired experience at the South Pole operations, a Kilometre-Scale detector, IceCube [100, 42, 54], is being deployed at the South Pole. IceCube will be considerably more sensitive than AMANDA consisting in 80 strings with 60 photomultipliers per string. The project, whose completion is foreseen in 2010/11, also includes a surface air shower detector array, IceTop, composed of 160 tanks of frozen water with two photomultipliers each, which will enable correlations with the IceCube events, and therefore will enhance the physics capabilities of the deep ice detector.

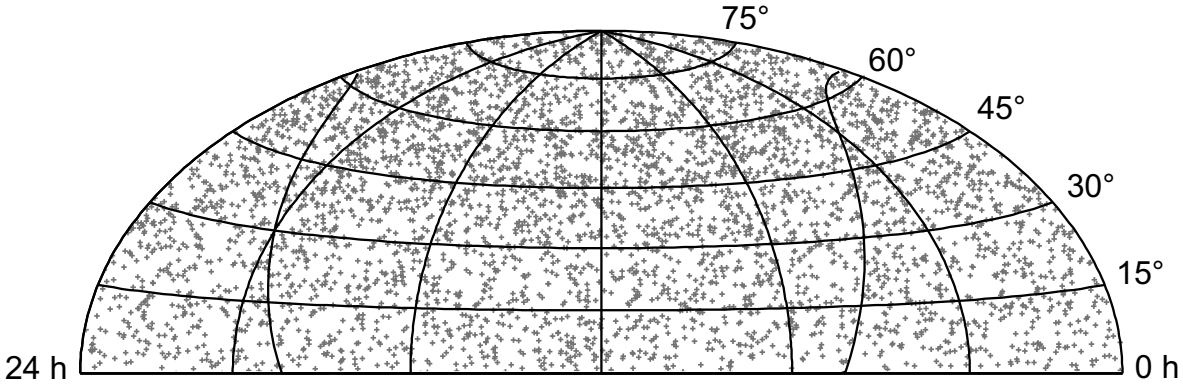

Figure 1.12: *Sky map of 4282 neutrino events candidates recorded by AMANDA in 2000-2004 in equatorial coordinates. The black line marks the location of the galactic plane. Figure taken from [99].*

The projected upper limit to muon neutrinos diffuse flux for the full IceCube detector is $E^2\Phi_\nu(E) < 4.2 \times 10^{-9}\mathrm{cm}^{-2}\mathrm{s}^{-1}\mathrm{sr}^{-1}\mathrm{GeV}$. The current limit set by AMANDA for muon neutrino diffuse flux using the period of 2000-2003 as given in [101] is $E^2\Phi_\nu(E) < 8.8 \times 10^{-8}\mathrm{cm}^{-2}\mathrm{s}^{-1}\mathrm{sr}^{-1}\mathrm{GeV}$ over an neutrino energy range $10^{4.2} \div 10^{6.4}$ GeV. Since the point-like analysis is one of the main topics of this thesis, the results of AMANDA and the expected sensitivity of IceCube concerning the point-like search will be reviewed and compared with ANTARES capabilities in chapter 6.

- **KM3NeT (ANTARES+NEMO+NESTOR)**. The Galactic Centre is of particular interest and only telescopes in the northern hemisphere will be able to observe this region. Since IceCube essentially observes the northern sky, that calls for the construction of a neutrino telescope counterpart to IceCube in the Mediterranean sea. KM3NeT [102] is the Design Study that is addressing different issues linked to the construction of a cost-effective, Kilometre-Scale deep-sea neutrino telescope. Three Mediterranean experiments have joined activities in order to participate in the KM3NeT project using the experience and expertise gained in the underwater operation and sea campaigns. These experiments are: NEMO [103], NESTOR [104] and ANTARES [105]. The NEMO collaboration

activities have been focused mainly on the search and evaluation of an optimal site for an underwater neutrino telescope installation, and on the development of different solution to various detector components for a Kilometre-Scale telescope. During 7 years and 30 sea campaigns, the proposed site located at a depth of 3400 m about 80 km from Capo Passero near the Italian coast of Sicily, was evaluated within the NEMO Phase-2 which included a long term monitoring of the site. More recently, on December 18, 2006 two of the key components of the detector apparatus have been deployed at a depth of 2100 m at the Catania Underwater Test Site in the so-called NEMO Phase-1. A junction box and a four storey tower have been validated in real underwater conditions together with the data acquisition system. This milestone proves the fully functionality of the main components of a Kilometre-Scale detector. The NESTOR project, with mainly Greek participation, intends to build a Mediterranean detector with approximately the same effective volume as AMANDA. The selected site for the NESTOR collaboration to build the detector is the Ionian sea (Greece) near the West Coast of the Peloponnese at 4 km depth. On 29 March 2003 the NESTOR collaboration successfully deployed the first floor of a detector tower recording the first atmospheric muons. In the future, NESTOR collaboration will participate in the KM3NeT project, but also they will construct a more specialized sparse neutrino telescope for high energy neutrinos in coincidence with GRBs, the so-called NuBE experiment. The third one, ANTARES, is the subject of this work, and it will be discussed in detail in the following chapter. KM3NeT has been included in the *List of Opportunities* by the *European Strategy Forum for Research Infrastructures (ESFRI)* [106, 107]. KM3NeT will be a pan-European and multidisciplinary facility, with a novel working philosophy, giving open access to the neutrino telescope data, and allowing external users to ask for *observation time* by adapting the online trigger algorithm to specific directions in the sky.

Neutrinos with energies above 100 PeV are difficult to detect by the Cherenkov based optical telescopes. New techniques are used to detect the very high energy neutrinos. Higher energy detection will be covered by experiments recording radio emission in terrestrial ice masses or in the moon crust, by searching for fluorescence light from neutrino-induce air showers. Here these novel techniques and the experiments to survey the highest energies of the cosmic neutrino spectrum are briefly summarized.

- **Air shower optical detection**. This detection principle is followed in large air shower detectors such as the Pierre Auger Observatory. As already mentioned, Auger is devoted to CR observation through their induced air showers. However, almost horizontal air showers can only be produced by high energy neutrino interactions nearly skimming the Earth atmosphere. The expected Auger sensitivity for this kind of neutrino-induced air showers is $E^2\Phi_\nu(E) \leq 10^{-8}\mathrm{cm}^{-2}\mathrm{s}^{-1}\mathrm{sr}^{-1}\mathrm{GeV}$ within an energy window of $0.1 \div 10$ EeV. The EUSO satellite will intend to use large mirrors looking down upon the atmosphere searching for nitrogen fluorescence signals due to CR or neutrino interactions.

- **Air shower radio detection**. This detection principle exploits a property of electron-magnetic cascades known as the Askaryan effect [108]. The method is

based on the radio detection of the coherent Cherenkov radiation emitted by electromagnetic cascades generated by electron-neutrino interactions. For energies above PeV, this radio detection in ice or salt domes is even more competitive than the standard optical Cherenkov detection. The RICE detector [109] uses an array of radio receivers deployed within holes drilled in the antarctic ice cap at the South Pole. The model dependent limit set by RICE is $E^2\Phi_\nu(E) \leq 10^{-6}\text{cm}^{-2}\text{s}^{-1}\text{sr}^{-1}\text{GeV}$ in the energy range of $0.1 \div 10^2$ EeV, ruling out the most intense flux predictions at a 95% confidence level. When a high energy neutrino showers in ice sheet, the resulting impulses can easily propagate up through the surface to a balloon-borne detector. This is the concept of the ANITA experiment which uses an array of radio detectors assembled in a balloon in an antarctic circumpolar flight on December 15, 2006. The limit set by a completed 18.4 day flight of a prototype long-duration balloon payload called ANITA-lite in early 2004 in the energy range of $10^{0.5} \div 10^{5.5}$ EeV is $E^2\Phi_\nu(E) \leq 1.6 \times 10^{-6}\text{cm}^{-2}\text{s}^{-1}\text{sr}^{-1}\text{GeV}$ [110]. Extremely high energy cascades can also be induced by neutrinos skimming the moon's surface. This detection principle is followed by GLUE using two NASA radio antennas which has set a limit of $E^2\Phi_\nu(E) \leq 10^{-3.14}\text{cm}^{-2}\text{s}^{-1}\text{sr}^{-1}\text{GeV}$ at 10 EeV [111]. LOFAR, the Low Frequency Array, is a radio telescope under construction design to operate between 30 and 240 MHz although still not reaching the GLUE sensitivity.

- **Acoustic detection**. This novel technique is still in its R&D phase. It is based on the heat released by the ionization loss in high energy induced cascades. The following fast expansion of the medium results in a short acoustic pulse. Due to the large attenuation length this technique turns out to be very promising for high energies. European groups play a major role in the development of the acoustic detection of neutrinos. The KM3NeT project includes the realization of an acoustic detector surrounding the optical detector to extend its sensitivity to much higher energies.

Figure 1.13 shows an overall picture of the present and future situation in the neutrino astronomy field. The prospective sensitivities to diffuse neutrino fluxes of future detection experiments, and the limits already set by present experiments are shown together with the estimated fluxes from different models and sources of neutrinos. These limits are referred to a diffuse neutrino fluxes (due to the combination of several unresolvable neutrino sources) and differ from the sensitivities to the point-like sources search analysis. A summary of the upper limits and sensitivities of present and future experiment within the point-like source analysis context will be provided in chapter 6.

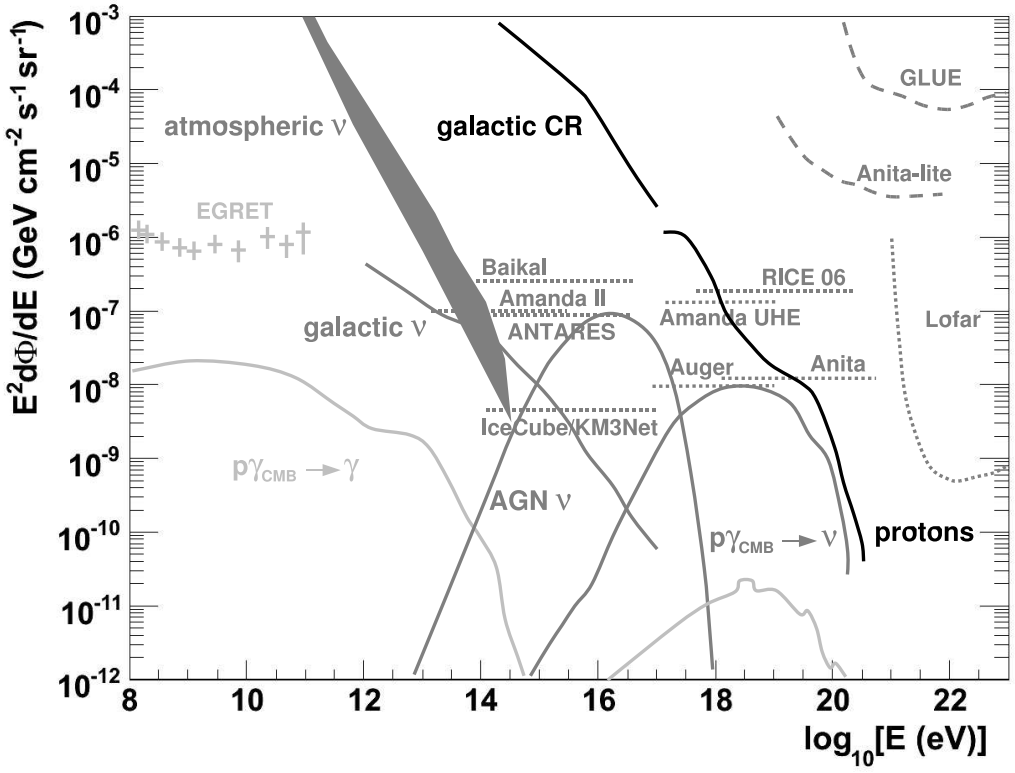

Figure 1.13: *Estimated fluxes (full lines) and sensitivities for present and projected neutrino detectors (dashed lines and crosses). Cosmic rays and γ-rays fluxes are also indicated for the sake of comparison. The primary CR spectrum is shown in black. The secondary γ-ray spectrum stemming from proton interactions with the CMB is shown light grey, as well as the instrumental sensitivity for γ-ray from EGRET. In grey are indicated the estimated neutrino fluxes (cosmic and atmospheric fluxes), the present upper limits set by AMANDA-II, Baikal and the expected limits of different future neutrino detectors, like the expected 1 year limit of ANTARES.*

Chapter 2

The ANTARES neutrino telescope

– It's a little experiment that might win me the Nobel Prize.
– In which field?
– I don't care, they all pay the same.
Professor Farnsworth and Leela, Futurama.

In this chapter, we will review the detection principle of the so-called Cherenkov neutrino telescopes. Cherenkov neutrino telescopes consist in arrays of photomultipliers deployed in natural water or ice. These telescopes cover the region between $\sim 10^{11} - 10^{16}$ eV. Detection at higher energies is tackled by experiments recording radio emission in terrestrial ice masses or in the moon crust, or by searching for fluorescence light from neutrino-induced air showers. A technical description of the ANTARES neutrino telescope and its expected performance will be presented.

2.1 Neutrino interactions

Neutrinos are neutral weakly interactive particles. Interaction with matter is severely dominated by the inelastic scattering of the neutrino on a target nucleon. Neutrino interactions with electrons in Earth can generally be neglected in comparison with nucleons over the energy range of interest for neutrino astronomy. The exception is, however, the Glashow resonance [112] that appears in $\overline{\nu}_e e$ interactions in the neighbourhood of 6.3 PeV of neutrino energy, which may offer a detectable signal. The neutrino interaction with an isoscalar target nucleon N can be either through charged current (CC) or neutral current (NC) weak interactions depending on whether they exchange a charged $W^{\pm}$ or a neutral Z^0

$$\begin{aligned} \nu_l + N &\rightarrow l + X \\ \nu_l + N &\rightarrow \nu_l + N, \end{aligned} \tag{2.1}$$

where the final products are a $\nu_l(l)$ in NC(CC) and a hadronic shower. For high energy neutrinos, interactions are *deep inelastic* and a large fraction of the neutrino energy

goes into the hadronic shower. At the energies of interest for neutrino astronomy, perturbative QCD corrections to the neutrino cross section are insignificant, therefore, the leading order differential cross section for the CC interactions is given by [113]

$$\frac{d^2\sigma_{\nu N}}{dxdy} = \frac{2G_F^2 m_N E_\nu}{\pi} \frac{M_W^4}{(Q^2+M_W^2)^2}[xq(x,Q^2) + x(1-y)^2\overline{q}(x,Q^2)], \tag{2.2}$$

where $x = Q^2/2m_N(E_\nu - E_l)$ and $y = (E_\nu - E_l)/E_\nu$ are the so-called *scale variables* or *Feyman-Björken variables*, Q^2 is the square of the momentum transferred between the neutrino and the lepton, m_N is the isoscalar nucleon mass ($N = (n+p)/2$), M_W is the mass of the W boson, and G_F is the Fermi coupling constant ($G_F = 1.17\times10^{-5}$ GeV^{-2}). The functions $q(x,Q^2)$ and $\bar{q}(x,Q^2)$ are the parton distributions for quarks and anti-quarks. The Björken variable x is a measure of the inelasticity of the interaction. Therefore, the high energy *deep inelastic* neutrino interactions are characterized by $x \ll 1$. Figure 2.1 shows the $\nu_\mu N$ and $\overline{\nu}_\mu N$ cross sections as a function of the neutrino energy. As can be seen, at low energies the neutrino cross section rises linearly with E_ν up to $E_\nu \sim 10^4$ GeV. For higher energies, the invariant mass $Q^2 = 2m_N E_\nu xy$ could be larger than the W rest mass, reducing the increase of the total cross section.

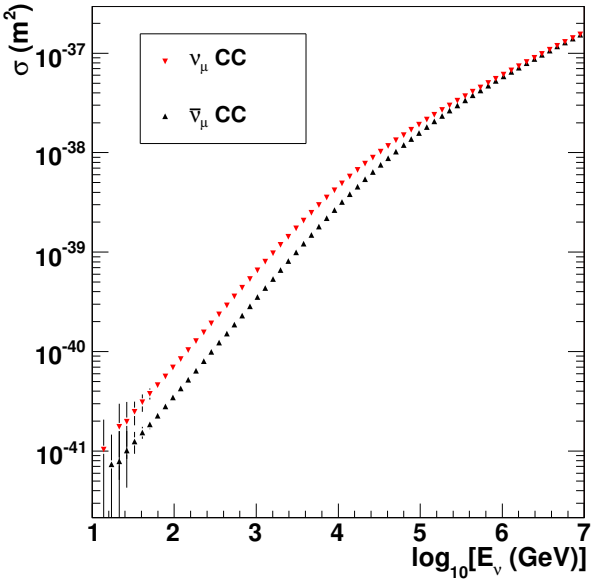

Figure 2.1: *Cross section for ν_μ and $\overline{\nu}_\mu$ as a function of the neutrino energy according to CTEQ6-DIS [114] parton distributions.*

The direction of the produced lepton after CC neutrino interactions is on average the same as the direction of the parent neutrino. The lepton and neutrino tracks are almost collinear specially at high energies ($E_\nu > 10$ TeV). Figure 2.2 shows the scattering angle between the incident neutrino and the outgoing muon as a function of the neutrino energy in ANTARES using the simulation tools described in appendix A. Also indicated in the figure is a functional formula [105] describing this energy dependence.

Consequently from this formula, the scattered angle for $E_\nu > 10$ TeV is less than $0.1°$, which justifies the name *telescope* applied to the ANTARES neutrino detector.

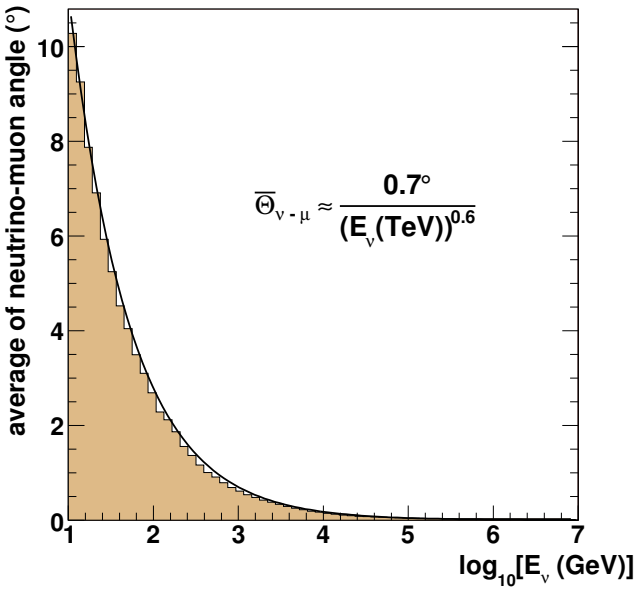

Figure 2.2: *Median angular difference between the initial neutrino direction and that of the muon track at the detector; the functional form shown (solid line) reproduces well the simulated energy dependence average angle (histogram).*

2.2 Cherenkov radiation

Cherenkov radiation is emitted when charged particles cross through an insulator exceeding the speed of light in this medium [115]. The charged particle polarizes the molecules along the particle trajectory, but only when the particle moves faster than the speed of light in that medium, the overall dipole moment is not null. Light is emitted as the insulator's electrons restore themselves to equilibrium after the disruption has passed, creating a coherent radiation emitted in a cone with a characteristic angle θ_C given by

$$\cos\theta_C = \frac{c/n}{\beta c} = \frac{1}{\beta n}, \tag{2.3}$$

where n is the refractive index of the medium and β is the particle speed in units of c. Figure 2.3 schematically shows the Cherenkov light cone and the wave front radiation.

This phenomenon is similar to the sonic shock-wave of supersonic bodies. For relativistic particles ($\beta \approx 1$) and taking the refractive index of sea water as $n = 1.364$ the Cherenkov angle is $\theta_C \simeq 43°$. The number of Cherenkov photons, N_γ, emitted per unit wavelength interval, $d\lambda$, and unit distance travelled, dx, by a charged particle of charge e is given by

$$\frac{d^2N_\gamma}{dxd\lambda} = \frac{2\pi}{137\lambda^2}\left(1 - \frac{1}{n^2\beta^2}\right), \tag{2.4}$$

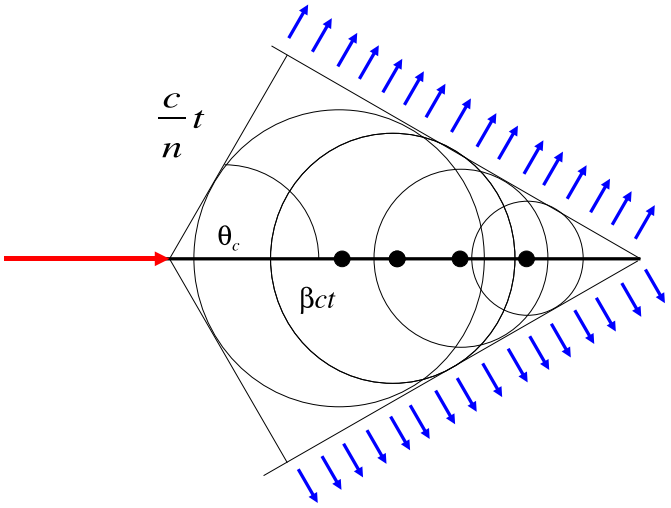

Figure 2.3: *Scheme of the Cherenkov radiation. The Cherenkov angle, θ_C, for a moving particle with speed β, is indicated.*

where λ is the wavelength of the light radiation. From this formula it can be seen that shorter wavelengths contribute more significantly to the Cherenkov radiation. For an underwater neutrino telescope like ANTARES, the light absorption by water and the photomultiplier response will strongly suppress some wavelengths. For the wavelength range of the photomultiplier tubes in ANTARES (300-600 nm) the number of Cherenkov photons emitted per meter travelled by the charged particle is about 3.5×10^4.

2.3 Detection principle

Neutrinos can be detected when product particles released by neutrino interactions with matter nucleons induce Cherenkov radiation when crossing at relativistic velocities a suitable optical medium such as ice or water.

The neutrino detector has to be placed under water or under ice, also benefiting of the shielding against secondary CR. The actual neutrino detection strongly depends on the low expected fluxes and neutrino interaction cross section, therefore, large detectors ($\sim$ GTon) are required. The problem is overcome using large volumes of sea water or ice as the detection medium [116]. Figure 2.4 depicts the detection principle for under water/ice Cherenkov telescopes for muon neutrinos.

The detector operates by collecting the Cherenkov light on a three-dimensional array of photomultiplier tubes (PMTs). The information provided by the number of photons detected and their arrival times is used to infer the neutrino track direction and energy. The most common neutrino detection in the ANTARES telescope will take place through the muon neutrino interaction with nuclei by charged currents ($(\nu_\mu(\overline{\nu}_\mu)+N \rightarrow \mu^-(\mu^+)+X)$. Nevertheless, neutrinos can also be detected by identifying other signatures. Figure 2.5 summarizes the possible event signatures observed in a Cherenkov neutrino telescope.

In this work we will explore the potential of ANTARES as a neutrino telescope,

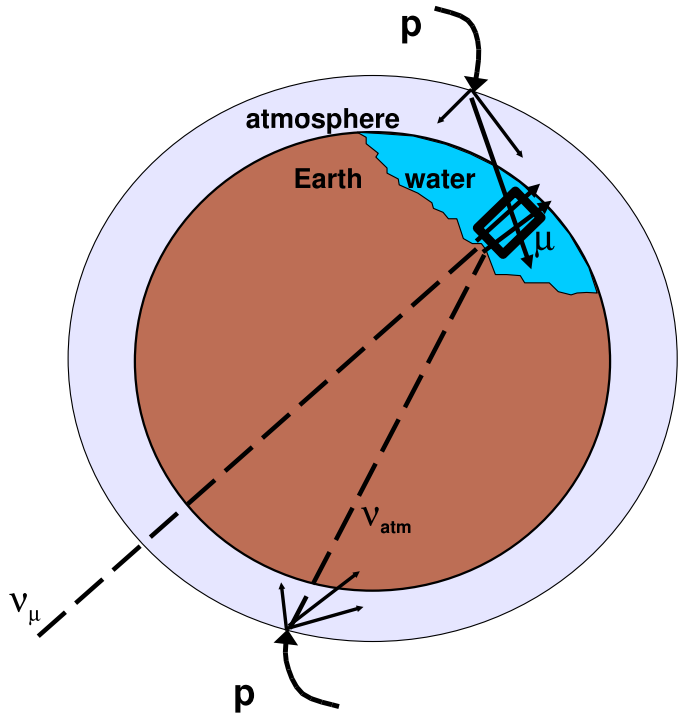

Figure 2.4: *Scheme showing the detection principle. Physical background due to CR interactions with the upper shells of the atmosphere is also depicted.*

therefore, only topologies including a long range particle track that enables a good pointing performance are interesting for our analysis, that is, only those signatures coming from ν_μ and ν_τ interactions. In the case of ν_τ, the produced τ travels only a few meters before decaying, which invalidates the track reconstruction of the τ trajectory. Only at energies larger than $E_\tau \approx 2 \times 10^6$ GeV, the τ range become of the order of the ANTARES typical dimension. Unfortunately, this kind of high ν_τ events are indistinguishable from a ν_μ with a muon track of $\sim 6 - 11$ times lower energy [117]. Other signatures coming from ν_τ clearly identify the ν_τ events in the detector. About 35% of τ decays result in a new ν_τ appearance. This feature will draw an event signature dubbed as the *double bang* (see fig. 2.5) or the *lollipop* events proposed in [93]. If we are able to distinguish between the hadronic cascade at the first $\nu_\tau N$ CC interaction and the second hadronic or electromagnetic cascade due to lepton decay, we will be able to detect a *double bang* signature. Alternatively, if the first cascade lies outside the instrumentation volume of the detector, a *lollipop* event is detected. On the other hand, if it is the hadronic or electromagnetic cascade of the τ decay the one that is not contained in the detector, we will not be able to distinguish it from a muon neutrino signal. Although these signatures are potentially *background free* events, the expected rate per year for a Kilometre-Scale detector is of the order of $1-3$ events [117], hence for a smaller detector like ANTARES, they are practically negligible. In 17% of the cases, the τ decay channel produces a muon (the second cascade is absent). Unfortunately, this signature is once again indistinguishable from a ν_μ event.

As already said, the most common signature detection in ANTARES is via $\nu_\mu N$ CC interactions. In a Cherenkov detector no distinction between ν_μ and $\overline{\nu}_\mu$ can be

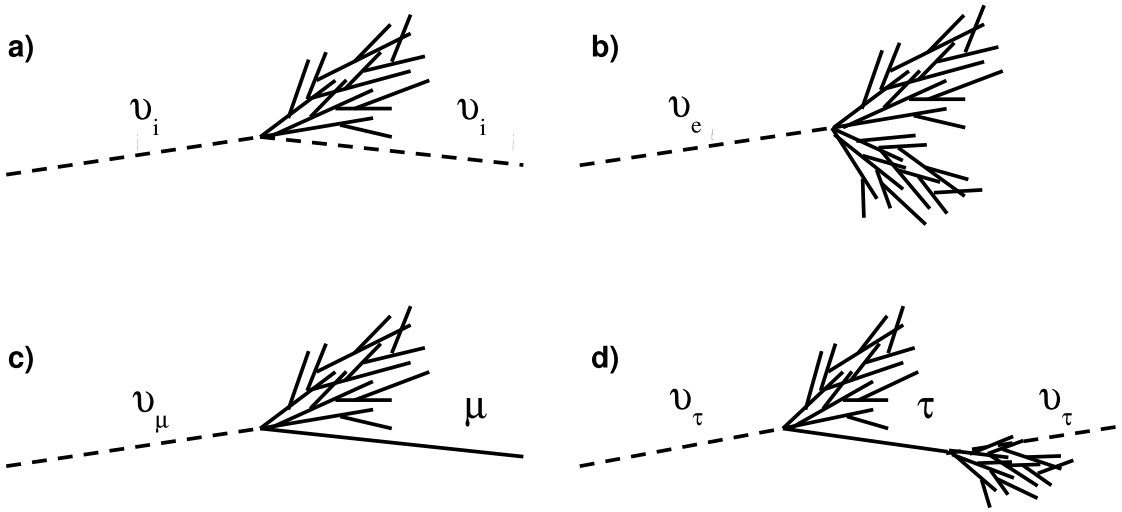

Figure 2.5: *Event signature topologies for different neutrino flavours and interactions: a) NC interaction producing a hadronic shower; b) CC interaction of ν_e producing both an EM and a hadronic shower; c) CC interaction of ν_μ producing a muon and a hadronic shower; 4) CC interaction of ν_τ producing a τ that decays into a ν_τ tracing the double bang event signature. Particles and anti-particles cannot be distinguish in neutrino telescopes.*

made. Although the hadronic cascade created in the neutrino interaction vertex could be reconstructed using the suitable reconstruction strategy, the muon track is sufficient to clearly evidence the ν_μ detection. Figure 2.6 shows the effective muon range through a general combination of rock and water as a function of the parent neutrino energy. As can be seen, for energies larger than 10 TeV the produced muon can travel more than 5 km, therefore the event will be well detected even if the neutrino interaction vertex happened outside the instrumented detector volume.

The muon energy losses are due to several processes such as ionization, pair production, *bremsstrahlung* and photonuclear interactions. Hence the total energy loss per unit length can be written in a parametrized formula as

$$-\left\langle \frac{dE_\mu}{dx} \right\rangle = \alpha(E_\mu) + \beta(E_\mu)E_\mu, \tag{2.5}$$

where $\alpha(E_\mu)$ is an almost constant term that accounts for ionization, and $\beta(E_\mu)$ stands for the radiative losses which, in first approximation, can be considered as energy independent. Figure 2.7 shows the energy loss per distance as a function of the muon energy due to different interactions in water and standard rock (Z = 11, A = 22) [118].

In a neutrino telescope, the neutrino energy is in general unmeasurable since only an unknown fraction of its energy goes to the muon. In addition, only for the small

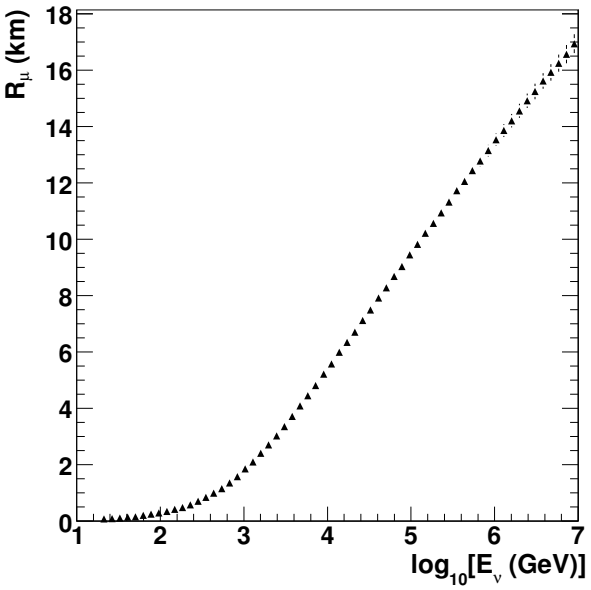

Figure 2.6: *Average effective muon range as a function of the parent neutrino energy through a general combination of rock and water where the water is at the end of the muon path.*

fraction of contained events (those where the neutrino interaction vertex is inside the detector volume), an estimate of the total neutrino energy can be made by detecting the hadronic cascade. Therefore, the only reasonable approach is to estimate the muon energy by energy loss processes, although only part of the muon track is inside the detector volume. Despite these difficulties, there is a correlation between the parent neutrino energy and the muon energy which can be used to estimate the former. In ANTARES, extensive work has been carried out to perform the energy reconstruction of the events [119, 120]. The energy reconstruction of the neutrino events together with the capability of pointing neutrino sources are key issues in a Cherenkov neutrino telescope.

2.4 Physical background

As depicted in figure 2.4, the detection principle for Cherenkov neutrino telescopes entails some physical backgrounds. We call them physical background opposed to other sources of background originating in the environment such as bioluminescence or, for the case of underwater neutrino telescopes, the decay of radioactive salts. This physical background is produced by the interactions of CR in the higher shells of the atmosphere depicted in formula 2.6. When a cosmic proton interacts with an atmospheric nucleus it gives rise to a hadronic cascade composed, among others, of π^+ and π^- that can decay giving both muons and neutrinos. These atmospheric muons and neutrinos constitute the two sources of physical background for a neutrino telescope.

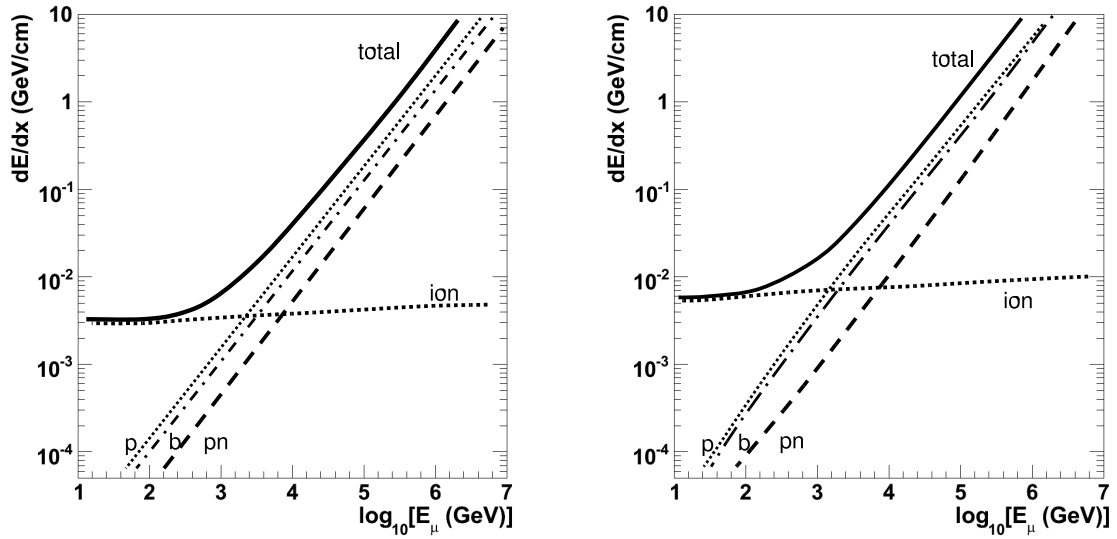

(a) Water **(b)** Standard rock

Figure 2.7: *Energy loss per distance of a muon in water and standard rock: p, pair production; b, bremsstrahlung; pn, photo-nuclear interactions; ion, ionization.*

$$
\begin{aligned}
p \longrightarrow \pi^+(+K^+\cdots) \longrightarrow \quad & \mu^+ + \nu_\mu \\
& \downarrow \\
& e^+ + \bar{\nu}_\mu + \nu_e
\end{aligned}
\tag{2.6}
$$

$$
\begin{aligned}
n \longrightarrow \pi^-(+K^-\cdots) \longrightarrow \quad & \mu^- + \bar{\nu}_\mu \\
& \downarrow \\
& e^- + \nu_\mu + \bar{\nu}_e
\end{aligned}
$$

Atmospheric muons can cross the atmosphere and reach the Earth where they are absorbed after several kilometres. As a consequence, the expected background is solely constituted of down-going muons and, therefore, they can be in principle rejected if we restrict the search for signal exclusively to up-going reconstructed events since up-going muons can only be produced by interaction of up-going neutrinos. A group of parallel muons coming from the same atmospheric cascade and arriving together at the detector, a so-called *muon bundle*, may induce errors in the track reconstruction algorithm, and they can be wrongly identified as a single up-going muon event. These are removed

by tight requirements on the fitted track. The atmospheric muon background is one of the main motivations to build neutrino telescopes at very deep sites, in order to have the largest possible shielding.

On the other hand, there are also up-going muons produced by atmospheric neutrinos that have partially or fully crossed the Earth. Atmospheric neutrinos are an irreducible background component, since they cannot be distinguished from extraterrestrial neutrinos. At high energies, however, we expect that the cosmic neutrino diffuse flux (due to the combination of several unresolvable neutrino sources) may dominate over the atmospheric neutrino background, since the flux of the latter is lower due to its softer energy spectrum compared to the cosmic neutrino spectrum. However, specially dangerous for the diffuse cosmic neutrino flux analysis, are the so-called *prompt neutrinos*, which are neutrinos coming from the semileptonic decays of very short-lived charmed particles like D mesons. These neutrinos have a spectrum that follows the primary CR spectrum. In the search of point-like sources, on the other hand, atmospheric neutrinos do not suppose an important drawback since the probability of atmospheric neutrinos to mimic a cluster signal from a neutrino source is low.

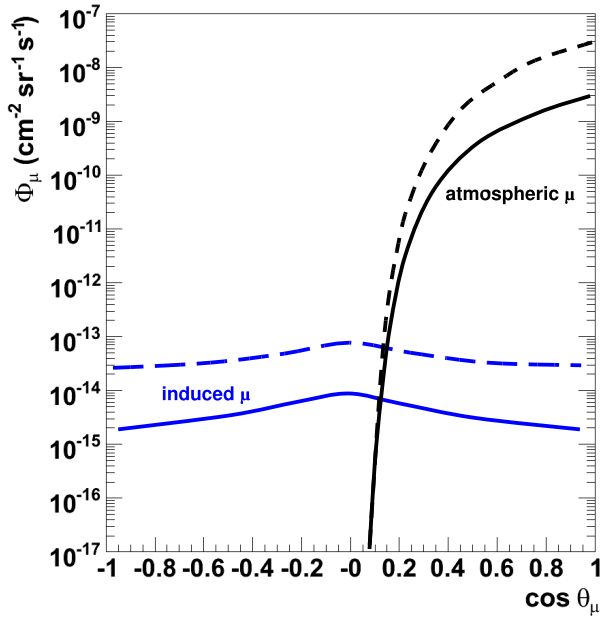

Figure 2.8: *Different contributions to muon background as a function of the zenith angle: atmospheric muons (from [121]) and atmospheric neutrino induced muons (from [122]). The solid lines stand for $E_\mu > 1$ TeV and the dashed lines for $E_\mu > 100$ GeV.*

Figure 2.8 shows the muon flux induced by atmospheric neutrinos and the direct atmospheric muon flux as a function of the zenith angle. The atmospheric muon flux exceeds that of muons induced by atmospheric neutrinos by six orders of magnitude, although it is completely suppressed for the up-going direction. The peak in the atmospheric neutrino induced muon flux at the horizon is due to the *secant theta effect*. This effect occurs because pions and kaons that are produced nearly skimming the Earth have more flight time in less dense atmosphere, so they have more chance to decay and produce neutrinos.

2.5 The ANTARES neutrino telescope

The ANTARES collaboration (*Astronomy with a Neutrino Telescope and Abyss environmental RESearch*) [105] is deploying an underwater neutrino telescope in the Mediterranean Sea, at a depth of about 2.5 km. The telescope design had to face different challenges most of them derived from the extreme conditions of deep oceanic environments. Nevertheless, extensive studies have been carried out and all the technical requirements have been met, which concluded with the deployment in 2006 of the first two lines of ANTARES and the reconstruction of the first atmospheric muons proving the feasibility of the detection principle and the design of an underwater neutrino telescope[1].

2.5.1 Detector architecture

The ANTARES detector is located on the seabed of the Mediterranean Sea at a depth of 2475 m and a distance of about 40 km from the coast. The detector [123] consists of an array of twelve identical independent and flexible lines (also called strings) separated by a distance of $\sim$ 74 m. These lines are anchored to the seabed and stay vertical and taut by a buoy located in the upper end of the strings. Each line has 25 storeys holding a triplet of photomultiplier tubes (PMTs) that are used to collect the Cherenkov light induced by charged particles crossing the sea water coming from neutrino interactions in the surrounding vicinities of the detector. Figure 2.9 shows a schematic view of the detector. The detector is operated from a control room, the *shore station*, located in La Seyne sur Mer (France). Here we will review the main components of the ANTARES detector.

- **The Optical Modules**. The detector is equipped with 900 photomultiplier tubes housed in a glass sphere capable to withstand the water pressure up to 700 bars. The sphere with a diameter of 43 cm and a thickness of 1.5 cm together with the enclosed PMT and the accompanying electronics make up the basic optical unit of ANTARES dubbed the *Optical Module* (OM) [124]. Figure 2.10 shows a schematic view of the OM. An exhaustive study about the suitable PMT for ANTARES was carried out during the R&D phase which led to the selection of the 14-stage, 10" Hamamatsu R7081-20 model [125]. The binding between the PMT photocathode and one of the hemispheres of the pressure-resistant sphere is done with a silicon gel that ensures the proper optical coupling ($n_{gel} = 1.40$, $n_{glass} = 1.48$, $n_{water} = 1.35$). Among the associated electronics, there is also an internal LED placed so that it can illuminate the PMT photocathode. This internal LED is one of the timing calibration devices, as they will be described later on, and it is used to monitor the variation of the PMT transit time. The inner surface of the back hemisphere of the glass container is covered with black paint, which absorbs induced photons and reduces the risk of inner reflexions. Each PMT is also shielded from magnetic fields by means of a μ-metal cage, an iron and nickel alloy of high magnetic permeability which avoids the deviation

[1] For the present status of the ANTARES detector see section 2.10.

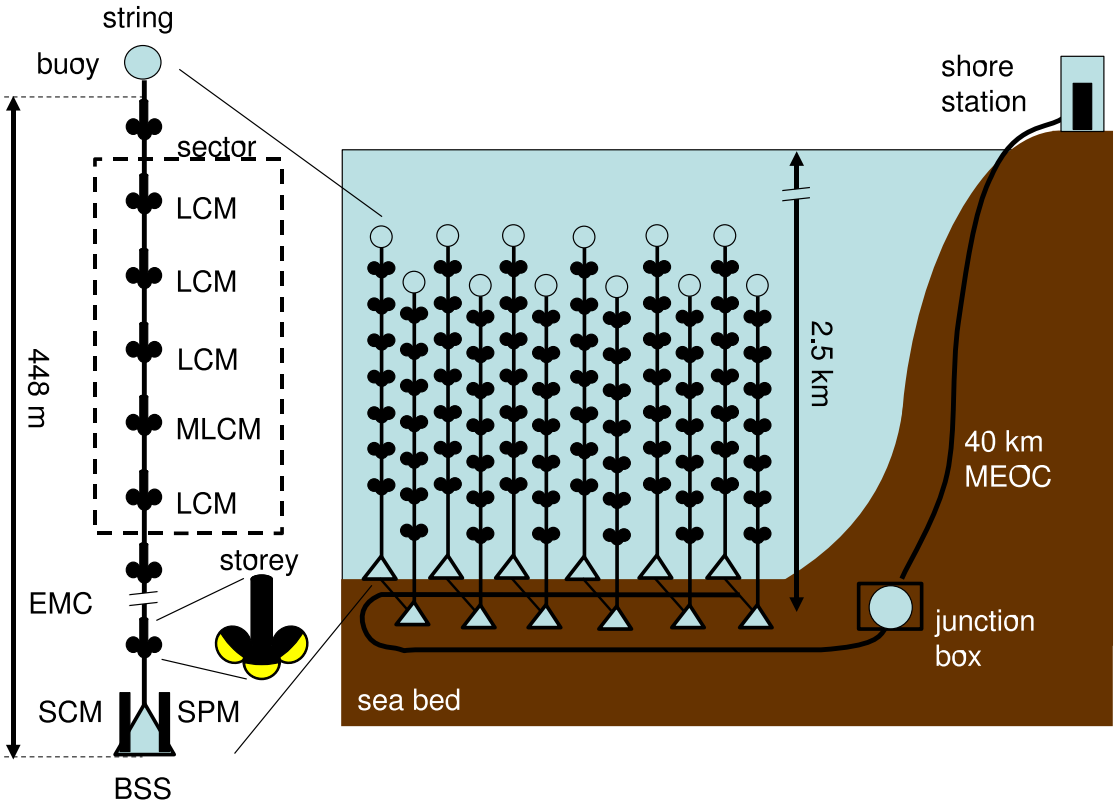

Figure 2.9: *A schematic view of the ANTARES detector layout. The site is about 2.5 km from the sea level and at 40 km from the shore station. The main elements of the ANTARES detector are outlined in the figure. The active part of the detector are the photomultiplier tubes (PMTs) grouped in triplets in each storey. Each of the 12 lines of the detector has 25 storeys.*

of the trajectory of low energy electrons inside the photomultiplier by Earth's magnetic fields (~ 0.5 G).

- **Storeys and Local Control Module**. The OMs are grouped in triplets of modules in a *storey* (also called floor) and mechanically fixed to the lines. The three OMs within the same group are equally spaced at 120°, and pointing downward with an angle of 45° with respect to the horizontal (see fig. 2.11). The accompanying electronics is contained in the so-called *Local Control Module* (LCM). The LCM container is a titanium cylinder housing the electronics boards for all the functionalities at the storey level. As can be seen in figure 2.10, OMs have a cable penetrator that links the OMs to the LCM. Five storeys make up a sector, which is a stand-alone unit concerning the power distribution and the data acquisition system (DAQ). One out of the five storeys of a sector has a *Master Local Control Module* (MLCM), which contains different elements not present in standard LCMs. It has an Ethernet switch, a bidirectional concentrator and a Dense Wavelength Division Multiplexing board (DWDM) which multiplexes the

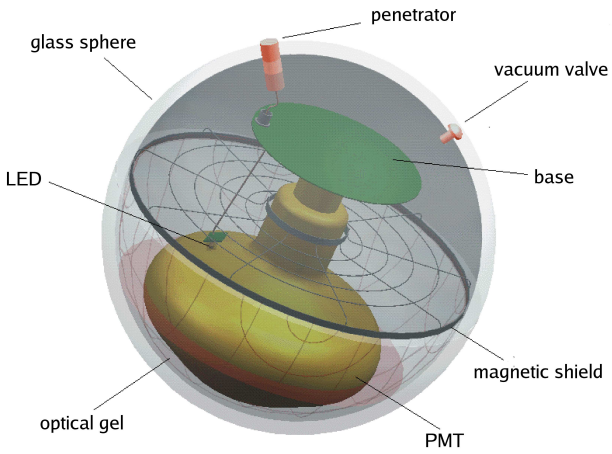

Figure 2.10: *A schematic 3D view an Optical Module. Indicated in the figure are the main elements of the OM, such as the water-pressure resistant glass sphere and the photomultiplier tube, taken from [124].*

signal information from the five storeys onto one optical fibre at a wavelength unique for that storey. In all senses, the MLCM contains all the electronic boards for all the functionalities at the sector level.

- **The lines**. A full string or line consists of five sectors (25 floors). The study of the detector layout and different line geometries can be found in [126]. In the final configuration the distance between storeys is 14.5 m and $\sim$ 74 m between lines. The detector layout (see fig. 2.12) follows an octagonal shape, which ensures the flat response of the detector in azimuth angles.

  The strings are flexible to prevent their breaking due to mechanic tension during their deployment. They are held vertically by means of a buoy located in the upper end of the line, and are anchored to the seabed by a dead weight located in the bottom string socket (BSS). Lines can be recovered by releasing this weight from the BSS by issuing an acoustic command from a ship on the surface. The active part of the lines starts at about 100 metres above the seabed in order to avoid the sea mud and dirt that can be spread out due to underwater currents. Apart from the LCMs, each string is instrumented with an electronics container in the base called *String Control Module* (SCM).

  In addition to the standard strings, there is also an additional line referred to as *Instrumentations Line* (IL). This line is equipped with different instrumentation devices to perform detailed oceanographic and water properties measurements: an Acoustic Doppler Current Profiler (ADCP) is used to trace a profile of underwater currents; the CTD measures the conductivity, temperature and density; the CSTAR transmissometer is used to measure the variation of the light attenuation coefficient along 25 cm using light of wavelength $\lambda = 470$ nm and the acoustic velocimetres determine the water temperature and the sound velocity.

- **The Junction Box and the MEOC**. Each SCM is connected to the *Junction Box* (JB) which provides power and control signals and receives the data from the

Figure 2.11: *Drawing of the ANTARES storey showing the OM triplet and the LCM titanium cylinder placed in the centre of the storey. The glass cylinder at upper part of the storey is an LED Beacon (see section 2.8.1).*

lines. The JB is connected to the shore station through the *Main Electro-Optical Cable* (MEOC) sketched in figure 2.9.

The internal elements of the JB are protected from the water pressure and corrosion by a titanium egg-shaped structure. In order to provide stability on the seabed, this structure is housed in a parallelepiped frame. This frame is equipped with two front panels with the 16 connectors for the 12 lines, the instrumentation line and the spares. The undersea connections are made using a submarine vehicle. The front panels of the JB offer a safe interface for submarine vehicle operation.

The MEOC links the JB to the *power hut*. This power hut houses the power feed system and is the first infrastructure on shore reached by the cables. The MEOC must withstand the external water pressure, and resist the corrosion during a live time of at least 10 years. It contains an internal steel tube and 48 monomode optical fibres. The cable is a standard telecommunication cable and is protected and insulated by a set of external layers of copper and steel, satisfying a series of mechanical and environmental criteria such as temperature tolerance, bending

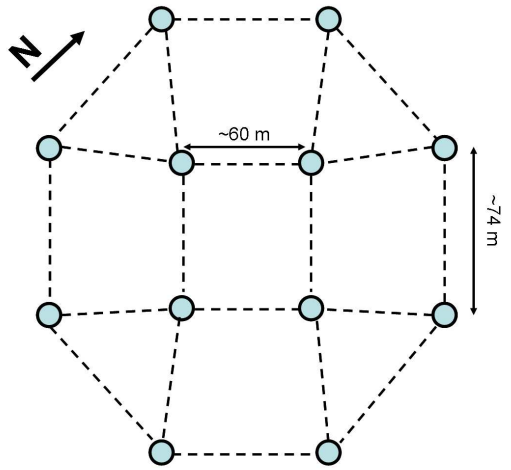

Figure 2.12: *Octagonal detector layout on the seabed, dots represent the position of each detector string.*

radius, etc.

2.6 Site evaluation

The selected emplacement of the ANTARES detector is located at a distance of about 40 km from Toulon (see fig. 2.13), at coordinates 42°50′ N, 6°10′ E. This location ensures a 3.5π sr sky coverage, and also the observation of the Galactic Centre 65% of the time.

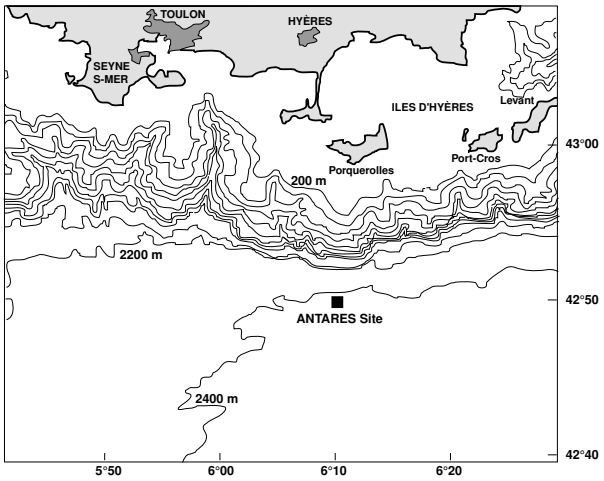

Figure 2.13: *Location of the ANTARES site near the south of France. The detector will be located at 2475 m deep, 40 kilometres away from the shore station.*

During the R&D phase of the experiment, a comprehensive study of the site evaluation was carried out. Different environment parameters and the optical water properties were measured. In this section we will review the main aspects of the ANTARES selected location that affect the performance of the detector with sound implications in the technical design of the telescope.

- **Optical background**. As explained in section 2.4, there is an optical background contribution with an environmental origin [127]. This optical background is responsible of the constant count rate in the PMTs (see fig. 2.14). This count rate can be decomposed into a continuous component, the baseline rate, which varies between 60 kHz and 90 kHz in a 10" PMT, and a discontinuous and rapid ($\sim$ 1 s) component of bursts of several MHz. The baseline rate has three components: the PMT dark noise ($\sim$ 3 kHz), light from radioactive salts decays and bioluminescence from bacteria. The β-decay of the ^{40}K isotope present in the oceanic salt produces an electron with a maximum energy of 1.3 MeV, enough to produce Cherenkov emission. Taking into account the salinity in the ANTARES vicinity (S = 38.47 per mil), the disintegration rate of ^{40}K in water yields a counting rate of $\sim$ 30 kHz in a 10" PMT. Together with the dark noise rate, that leaves a contribution of about 30 kHz due to light produced by bacteria or other micro-organisms. Bacteria emit light continuously and without external stimulation. Large baseline variations observed during sea campaigns are due to variation in bioluminescent bacteria activity, which are not correlated to the water current speed.

  Unlike bacteria, multi-cellular organisms emit light in short flashes which originate the discontinuous burst component superimposed on the baseline rate. This contribution is extremely high and positively correlated to the water current. Figure 2.15 shows the number of burst per minute versus the underwater current velocity.

  The data collected with the final detector lines have supplied additional information about the time evolution of the optical backgrounds in the ANTARES site. Figure 2.16 shows the complementary of the baseline rate cumulative distribution for different periods of data-taking. This distribution does not show a seasonal variation. The high baseline rates of the different periods in 2006 decrease with time, so that in the first half of 2007 the activity is particularly moderate or even low. The effect of a high optical background is to decrease the duty cycle of the data-taking. Successful efforts have been made to increase the useful data by adapting the trigger and reconstruction tools to cope with moderately high rates.

- **Biofouling and sedimentation**. Underwater sedimentation and biofouling is the accumulation of micro-organisms, mostly bacteria, on the outer surfaces and the subsequent adherence of falling sediments to artificial surfaces. The fouling by deposits of light-absorbing particles has direct implication in the light transmission in the OM modules of the ANTARES detector. In order to measure the average loss of light transmission in the ANTARES site, an experimental setup was deployed during the R&D phase of the experiment [128]. Direct measurements were made during immersions of several months and extrapolated to longer periods of time.

  The setup consisted in two resistant glass spheres similar to those used for the OMs. One of them was equipped with two blue light LEDs and the other con-

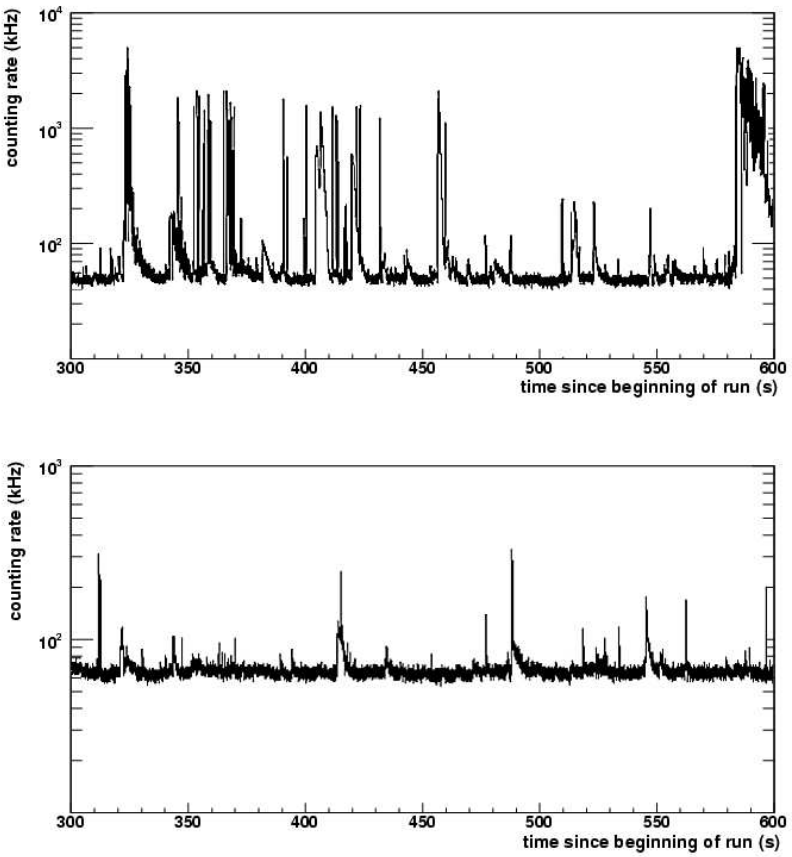

Figure 2.14: *The count rate recorded by one PMT for two different periods of time. The upper plot shows the count rate for an active period with frequent light flashes compared to a quieter period shown in the lower plot.*

tained five photodetectors glued to the inner surface of the sphere at different inclinations (zenith angles θ). The relevant quantity is the variation of the measured light transmission relative to the value measured immediately after immersion. Figure 2.17 shows the evolution of the light transmission since the immersion day for the different photodiodes inclinations.

As can be seen there is a tendency in the fouling to decrease when the zenith angle on the glass sphere increases. Sporadic transmission recoveries seem to be in partial correlation with an increase in the measured water current velocity. This is easily understood when the surfaces are being fouled by sediments rather than microbial adhesion, which can be washed off by flowing water. The measured loss in transmission at a zenith angle of 90° after 8 months is 2.7%, and it seems to saturate with time. Extrapolations indicate a global loss after 1 year of $\sim 2\%$ (taking into account the two glass spheres used in the setup). In the final design the OMs in the storeys are oriented downward at zenith angles of 135° (45° from the horizontal), the average loss in sensitivity of the OMs is expected to be small during the live time of ANTARES. In the present deployed lines, biofouling

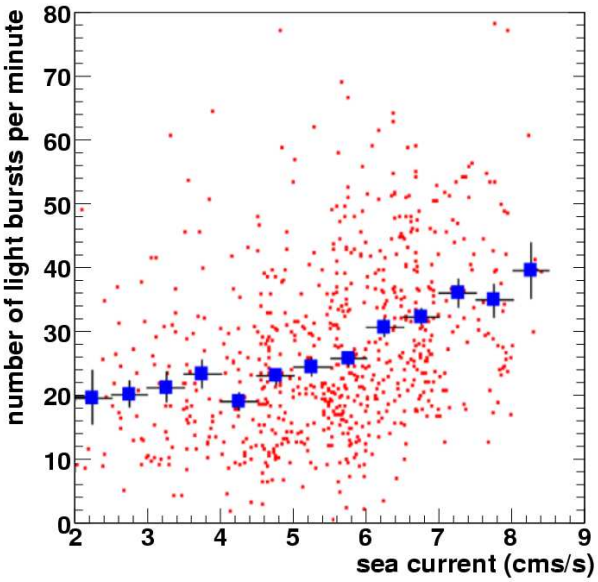

Figure 2.15: *Number of burst per minute versus the underwater current velocity.*

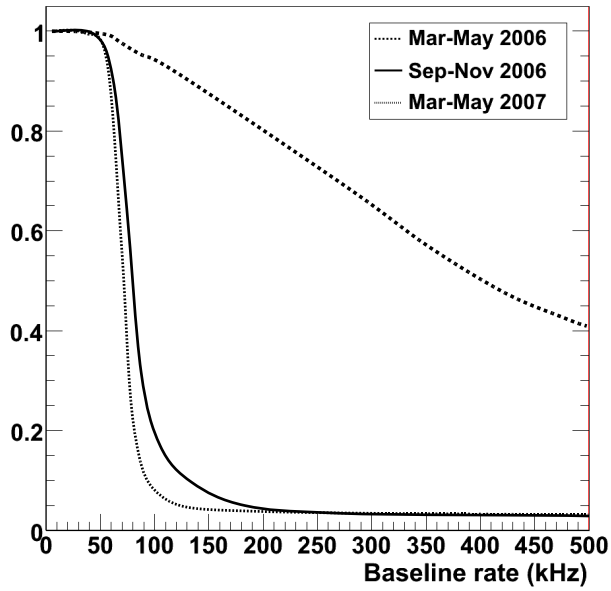

Figure 2.16: *Anticumulative cumulative distribution for the baseline rate for different periods of time.*

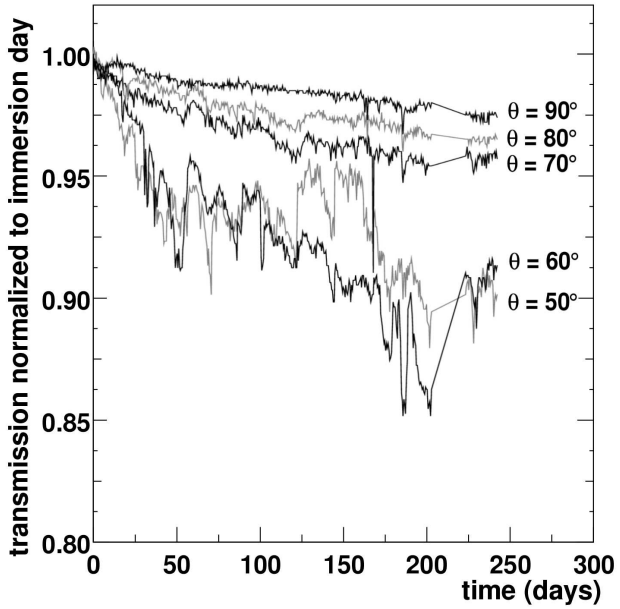

Figure 2.17: *Light transmission as a function of time since the immersion day. Curves are labelled according to the photodiode zenith angle θ. Taken from [128].*

can be partially monitored using the time evolution of the rates of coincidences on two different OMs of ^{40}K events. A few OMs show a moderate decrease of the coincidence rate. If this decrease is indeed due to biofouling is still under investigation.

- **Water properties**. Knowledge of the underwater photon propagation is of utter importance in an underwater Cherenkov neutrino telescope. This photon propagation is defined by the optical properties of water such as the absorption and the scattering of light in water and the group velocity of light. The absorption and scattering are described mainly by the absorption length (λ_{abs}) and the scattering length (λ_{scat}), respectively. These parameters have been studied in the ANTARES site during several sea campaigns from 1997 to 2000, using different *in situ* autonomous lines [128]. The attenuation effective length gives an indication of the fraction of photons emitted by the source that are detected. The attenuation effective length results from the combination of the absorption length and the effective scattering length

$$\frac{1}{\lambda_{att}^{eff}} = \frac{1}{\lambda_{abs}} + \frac{1}{\lambda_{scat}^{eff}}, \tag{2.7}$$

where λ_{scat}^{eff} is defined as $\lambda_{scat}/1 - \langle cos\theta \rangle$ being $\langle cos\theta \rangle$ the average cosine of the total scattering angular distribution[2]. The attenuation length was measured for

[2]The definition is justified since scattering is dominantly at small angle in natural waters and hence $\langle cos\theta \rangle \simeq 1$.

a setup deployed in December 1997 using a continuous collimated source. This measurement yields an effective attenuation length of

$$\lambda_{att}^{eff}(\text{Blue, collimated}) = 41 \pm 1(\text{stat.}) \pm 1(\text{syst.}) \text{ m}. \tag{2.8}$$

The absorptions and scattering lengths were measured separately using a different experimental setup. A set of measurements for different epochs were recorded and are shown in figure 2.18. These results can also be seen in section 3.7.2 when a first study of the attenuation length parameter with the Optical Beacon system is shown and the result compared with these measurements.

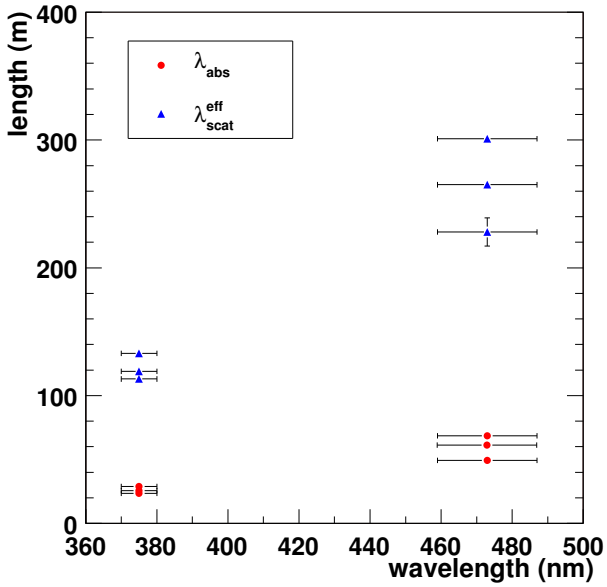

Figure 2.18: *Absorption and effective scattering lengths measured at ANTARES site at different periods for two wavelengths (UV, Blue) [128]. Horizontal error bars represent the source spectral resolution.*

The isotropic setup prevents the direct comparison of values given in figure 2.18 with equation 2.8 which was measured using a collimated source. Values of the absorption and effective scattering lengths measured are obtained after a fit procedure where the other parameter of the fit, the group velocity of light, is directly introduced from model estimations. This can be computed from

$$v_g = \frac{c}{n}\left(1 + \frac{dn/n}{d\lambda/\lambda}\right), \tag{2.9}$$

where n is the refractive index that can be evaluated from different empirical models using the ANTARES site parameters (pressure $p = 230$ atm, salinity $S = 38.47$ per mil and temperature $T = 13.2°\text{C}$). Figure 2.19 shows the comparison of measurements of the group velocity of light with respect to the model predictions. Measured values are used as an experimental verification of the model estimations. As can be seen from the figure, the experimental and analytical values are in quite good agreement. As already stated, absorption and effective

scattering measurements are obtained using the analytical estimates described above for the group velocity.

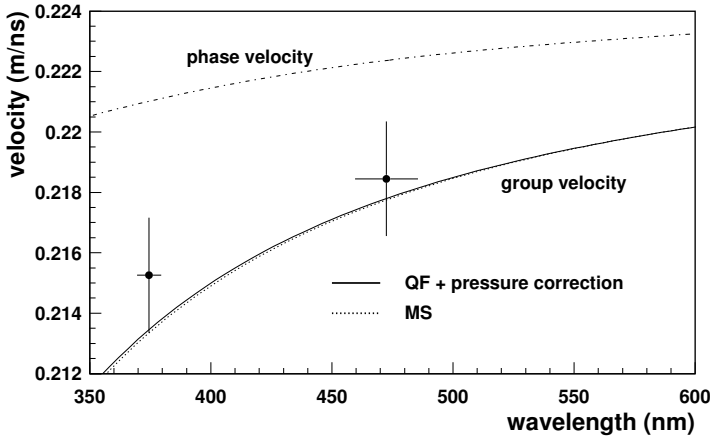

Figure 2.19: *Measured group velocity of light for two wavelengths (Blue, UV). Model predictions (MS, Millard and Seaver [129] and QF, Quan and Fry [130]) of the group velocity and phase velocity as a function of wavelength are also shown [128].*

2.7 Data acquisition system

The data acquisition system (DAQ) of the ANTARES telescope comprises various aspects of the data processing, ranging from digitization of the PMT signals to data transport filtering and storage. In this section we will review briefly the design and implementation of the DAQ system. For further information see [131].

2.7.1 Signal digitization

The distortion and attenuation of the analogical signal provided by the photomultipliers tubes through a 40 km long cable led the collaboration to the decision to digitize the signals before sending them to shore. To this end an Application Specific Integrated Circuit (ASIC) was designed to match the telescope requirements. This front-end chip is the Analogue Ring Sampler (ARS) [132]. One of the four inputs of the ARS reads the PMT anode signal, the other two read the same attenuated signal and the signal of the last dynode and the fourth input is connected to the 20 MHz master clock signal. This master clock signal is generated at the shore and is used to time-stamp the PMT signals (further details about the master clock signal will be discussed in section 2.8.1). The digitization of the signal is triggered when the voltage crosses a certain threshold L0 set to a fraction of the single photo-electron average amplitude (typically 0.3 p.e.). The ARS then separates simple pulses for which the time and integrated charge are measured from complex pulse shapes which are sampled at up to a frequency of 1 GHz. This selection is carried out by means of an analogue pulse shape discriminator (PSD) in which the signal from the PMT is compared to a standard photo-electron profile. This criterion is illustrated in figure 2.20.

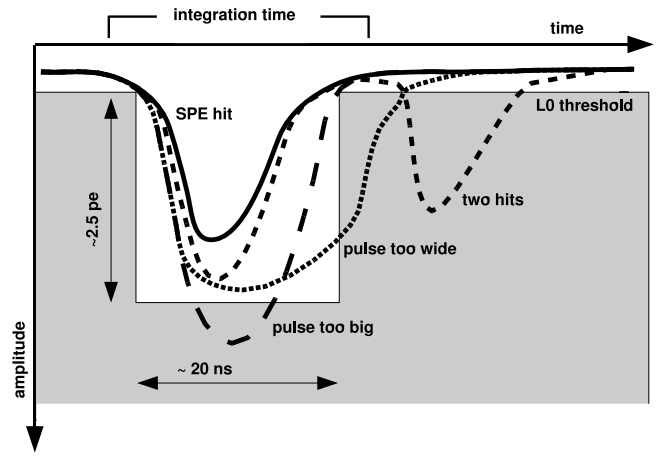

Figure 2.20: *Pulse shape discriminator using three different criteria: time width, pulse height and multiple hit during integration.*

About 99% of the signals are essentially due to optical background with a charge corresponding to one photo-electron. If the PSD profile contains the signal then it is called a single photo-electron (SPE) pulse and the charged is integrated during a time window of 35 ns and digitized by a 8-bit ADC Analog-to-Voltage Converter (AVC). The conversion from AVC units to photo-electrons has been computed in the laboratory for each ARS and is given by the following transfer formula

$$Q_{pe} = \frac{AVC - AVC_0}{AVC_1 - AVC_0}, \tag{2.10}$$

where AVC_0 and AVC_1 are the charge calibrated values coinciding with the pedestal and the photo-electron peaks, respectively. These values are stored and form part of the calibration settings of ANTARES.

After the integration time, the ARS chip is idle for about 200 ns. To limit the dead-time in the data acquisition, two ARSs that work in flip-flop mode are connected to each PMT. If the signal has a more complex structure, the waveform mode is used (WF). In this mode, the signal is sampled together with the clock signal. The sampling is performed with a set of 128 switched capacitors running at a selectable frequency between 150 MHz and 1 GHz. In practice, during the standard operation of the detector, the ARSs are forced to digitize every signal as SPE, independently of the PSD, and the WF mode is not used. The WF feature is used for calibration and tuning of detector parameters.

During the digitization, the signal is time-stamped assigning the time with respect to the master clock at which the L0 threshold is crossed. To measure the L0 time within the 50 ns interval between two subsequent clock pulses, a linear voltage ramp is generated and stopped by the L0 signal. This Time-to-Voltage Converter (TVC) provides a voltage which is digitized with an eight-bit analogue-to-digital converter. The TVC procedure is illustrated in figure 2.21. Since the fall back to the base voltage is not immediate, there are two TVC ramps working alternatively in order to avoid dead-times. These two ramps are labelled **A** and **B** in the figure.

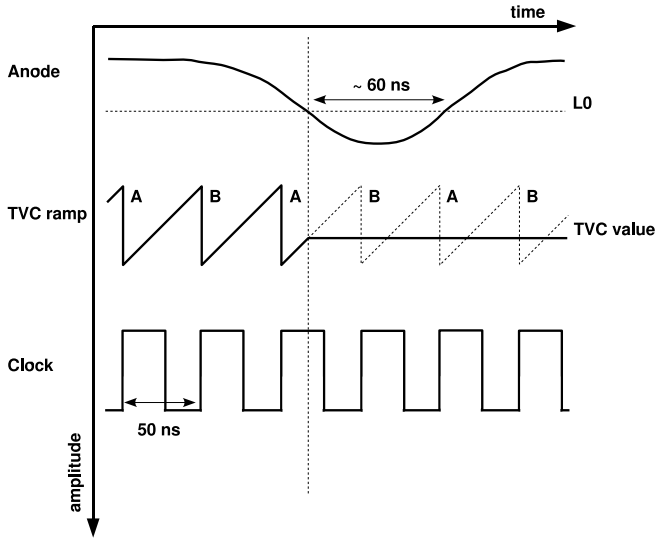

Figure 2.21: *Scheme of operation of the Time-to-Voltage converter used to interpolate interpolate between two clock cycles. Two independent ramps,* **A** *and* **B**, *are used to avoid dead-time effects.*

The TVC of the two ARSs must be calibrated independently. To this end, a uniform time distributed signal is induced in the ARSs and the TVC values are stored in a histogram. As can be seen from figure 2.22, only part of the full dynamic range of the TVCs is used. The calibration of the TVC consists in assigning to each TVC channel a time within the 50 ns time window. The minimal (TVC_{min}) and maximal (TVC_{max}) channel values are estimated, respectively, as the first and last bin that exceeds the 10% of the average bin occupancy. The TVC is considered linear between these two limits. The transfer formula from TVC channels to time in nanoseconds is given by

$$t = 50 \times \frac{TVC - TVC_{min}}{TVC_{max} - TVC_{min}}. \tag{2.11}$$

This calibration procedure assumes that the ADC channels in the ARS are equal in size. For a TVC of equal binning and events randomly distributed in time the resolution is given by $\sigma = \Delta t/\sqrt{12}$ where Δt is the bin size. However, it is known that the ADC channels are different in size as can be seen in the different bin occupancy in the TVC histogram of figure 2.22. This unequal binning is known as *Differential Non Linearity* (DNL). This effect has implications in the time resolution as well as in the shape of the time difference distributions, as we will see in chapter 3. The theoretical resolution expected considering this effect is $\sigma^2 = \frac{\Delta t^2}{12}\frac{\sum x_i^3}{\sum x_i}$ where $\Delta t \cdot x_i$ is the width of bin i. An analysis of the influence of the DNLs shows that improvements in the relative time accuracy of up to 80 ps can be achieved if we correct for this effect [133]. Nonetheless the trade-off is an increase in the number of calibration values that have to be stored. For that reason, the linear calibration of the TVC is a reasonable approximation.

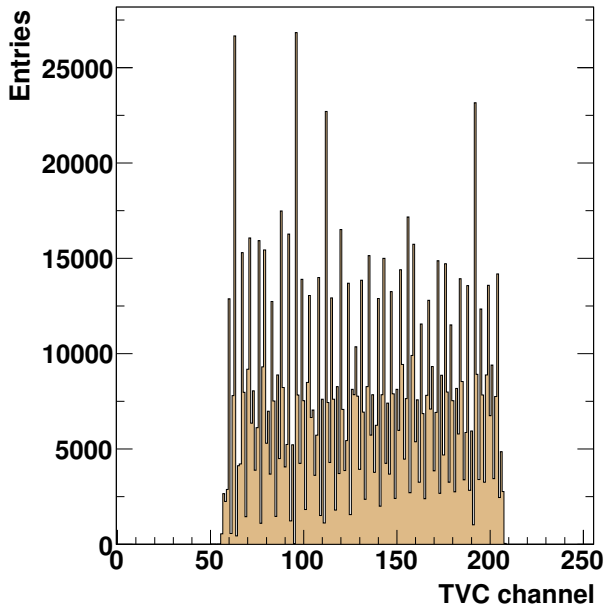

Figure 2.22: *TVC histogram with 255 channels, only part of the full dynamic range of the TVC is used. The different bin occupancy for this uniform time distribution is due to the DNL.*

2.7.2 Data transport and processing

The basic unit in the DAQ system is the group of 5 LCMs that constitutes a sector. In each sector there is an MLCM containing an Ethernet switch that merges the links from the five storeys into a single Gb/s Ethernet link. For the data transport to shore the dense wavelength division multiplexing (DWDM) technique is used. This DWDM network enables the transmission of different streams of data along a single fibre using different wavelengths.

The MLCMs of all sectors transfer the signals through the SCM to the shore station. The SCM collects the data from all the MLCMs and from the SCM itself and combines the 5+1 signals onto one fibre with a passive optical multiplexer. The SCM is also used for the slow control of the electrical power and calibration systems and also for the clock signal distribution and has an additional 100 Mb/s link to shore. An illustration of the DAQ system is shown in figure 2.23.

Except for the L0 threshold selection in the ARSs, no further filtering of the PMT signal is done offshore. All hits are sent to shore which is commonly referred to as *all-data-to-shore* implementation. After the signal digitization, the result of the ARS is buffered in a 64 MB SDRAM and separated in frames covering a certain period of time. The length of this time window can be set to values between 10 and 100 ms. Each frame is sent as a single packet to shore. A set of PCs in the shore station handles all the raw data sent. All frames that belong to the same time window are processed by the same PC. This collection of frames belonging to the same time window is called a time slice. A time slice contains all data digitized by all ARS in the detector in a given time window. Depending on the PMT signal rate, the frame sampling (sampling mode) has to be adapted in order not to saturate the DAQ system. The nominal procedure

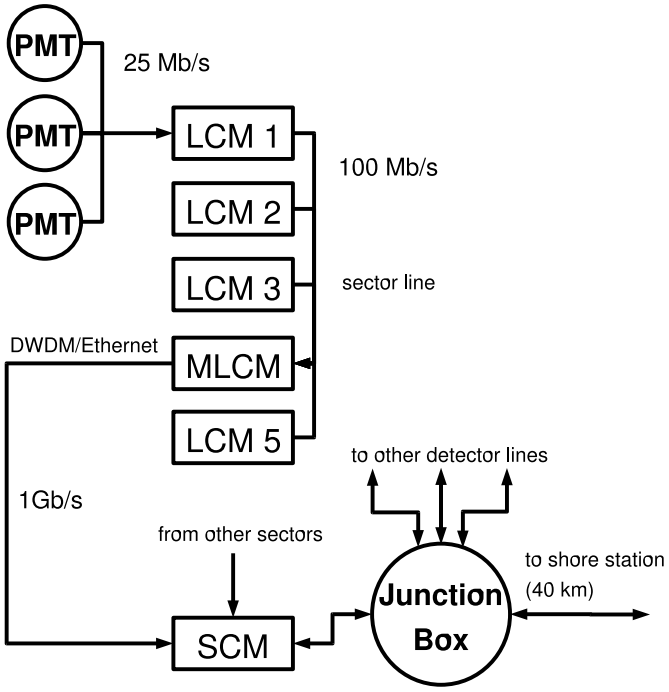

Figure 2.23: *Schematic picture of the DAQ system. The signal path from (to) the OMs to (from) shore is indicated. The digitized signal from the PMTs are transmitted to shore via the MLCM.*

is dubbed as sampling 1, which means that every frame is sent to shore. In periods where a high bioluminosity activity is present ($>$ 140 kHz), the system is constrained to work in sampling modes higher than one like sampling 2, where only one frame out of two is sent to shore. Higher sampling modes are used depending on the PMT rates.

The amount of raw data sent to shore is too large to be fully stored, so it is first analysed by the so-called DataFilter program. The DataFilter looks for correlated SPE hits consistent with a specific physics signal, if so, data are considered as a physics event and stored on disk in ROOT format [134]. The DataFilter runs on multiple processors and incorporates different algorithms depending on the specific physics signal being searched. Apart from the standard muon filter, there is a magnetic monopole filter, an optical beacon filter (as it will be explained in the following chapter) and a directional filter to look for spatial correlated sources (GRBs, flares, and so on).

The main user interface to the DAQ software is the RunControl program. It has a graphical user interface from which the operator of the detector controls all processes in the system. The detector configuration and initialization settings, such as DAQ and filtering parameters, are stored in a relational Oracle database system from where only the RunControl can retrieve the data. The organization of the data transfer and communication between processes in the DAQ system is based on the ControlHost package [135]. The ControlHost server running on different PCs enables transparent communication between all processes in the DAQ system.

2.8 Calibration

ANTARES is expected to achieve very good angular resolution ($< 0.3°$ for muon events above 10 TeV). This pointing accuracy is closely related to the precision in the determination of the arrival time of the Cherenkov photons at the PMTs. As already mentioned, lines are not rigid but move slowly due to underwater currents, hence the second essential element is a good knowledge of the position in 3D space of the OMs. Different calibration systems for timing and positioning have been devised in ANTARES. In this section we will discuss the main properties of these systems. Next chapter will be devoted to the Optical Beacon system, which is one of the time calibration systems used in ANTARES.

2.8.1 Time calibration systems

The precise measurement of the arrival time of the Cherenkov photons on the photocathode of the PMTs is of the utmost importance to accurately reconstruct the tracks and showers and their direction of arrival. A good absolute time determination is required to correlate the tracks with astrophysical events and a high relative timing between OMs is needed to reach the desired reconstruction efficiency and angular resolution. A precision of around 1 ms in the absolute time is enough to correlate events with any conceivable variation of an astrophysical phenomenon, while the relative timing is limited by the transit time spread of the signal in the PMTs ($\sigma \sim 1.3$ ns) and the optical properties of the seawater as the light scattering and chromatic dispersion ($\sigma \sim 1.5$ ns for a light propagation of 40 metres) [128,136]. As a consequence, the electronics of the ANTARES detector is designed in order to contribute less than 0.5 ns to the overall time resolution. To determine the absolute and the relative time between OMs, several complementary time calibration systems have been implemented in the ANTARES detector:

1. The **internal clock** calibration system. A very precise time reference clock distribution system has been implemented in the ANTARES detector. It consists of a 20 MHz clock generator on shore, a clock distribution system and a clock signal transceiver board placed in each LCM. A common clock signal is provided to the ARSs. Synchronized data commands can be superimposed on the clock signal, in particular *start* and *stop* commands, which together with a high precision Time-to-Digital Converter (TDC) make up the essential components of the system. This system also includes an echo-based time calibration whereby each LCM clock electronics board is able to send back a return signal through the same optical path as the outgoing clock signals. This system allows the time offsets between all LCM clock boards to be measured by recording the propagation delays of the return signals of each storey with respect to the original clock signal emission time. Measurements in real conditions show a resolution of ~ 0.1 ns, well within the specifications. The system also allows the synchronization with respect to Universal Time by assigning the GPS timestamp to the data with a precision of some tens of microseconds, much better than the required precision of

$\sim$ 1 ms. The clock signals are distributed across all detector components from the shore up to the clock boards. The remaining path between these boards and the PMT photocathodes however requires a different timing calibration mechanism.

2. The **internal Optical Module LEDs**. Inside each OM there is a blue LED attached to the back of the PMT capable of illuminating the photocathode. The LED is an HLMP-CB15 from Agilent whose light intensity is peaked at around 470 nm with a FWHM of 15 nm. These LEDs are used to measure the relative variation of the PMT transit time and dedicated runs of this LED calibration system are customarily taken in the sea [137]. This system calibrates the path travelled by the signal starting at the PMT photocathode up to the read-out electronics. The effect of the transmission of the light in the water is, however, not addressed by this calibration method.

3. The **Optical Beacons**. The Optical Beacons (OB), LED and Laser, enable the relative time calibration of different OMs to be determined by means of independent and well-controlled pulsed light sources. This system also makes possible to monitor the influence of the water on the light propagation. These Optical Beacons will be described in detail in chapter 3.

4. Several thousand down-going *muon tracks* will be detected per day. The hit time residuals of the reconstructed muon tracks can be used to monitor the time offsets of the OM. In principle, this can provide an overall space-time alignment and calibration cross-checks.

Prior to the deployment of the lines, all line elements are verified as functioning correctly in a dedicated *dark-setup* where a time calibration is carried out after the integration of each sector of the line. An optical signal is sent to each OM of every storey. The signal is provided by a Nd-YAG solid state laser that emits intense, short duration light pulses. The light pulse is attenuated before being sent to the OMs and guided through an optical fibre to a 1-to-16 optical splitter. Each of the outgoing fibres is connected to one of the 15 OMs of the sector. The 16^{th} signal is sent to a control module that is used to create a time reference signal. The resulting information from timing calibration in the dark-setup is used as the reference for the validation of the *in situ* timing calibrations. This system is also used to determine the time offsets of the Optical Beacons with respect to the OMs.

2.8.2 Position calibration

The quality in track muon reconstruction depends on the knowledge of the position of the OMs. To guarantee the projected angular resolution of ANTARES, the position measurements should be done with an accuracy of $\sim$ 10 cm. An acoustic positioning system has been designed to obtain distance measurements and the subsequent triangulation of some of the storeys of the detector. The full acoustic positioning system consists of emitting transducers (RxTx modules) attached to the BSS of the lines, receiving hydrophones (Rx modules) located on one every five storeys, and it is completed by four autonomous pyramids transponders fixed in the sea bed surrounding

the detector site. Timed acoustic signals are exchanged between the emitting transducers and the hydrophones in the 40-60 kHz frequency range. This system has been already tested in real conditions showing a resolution of a few mm and a stability of $\sim$ 1 cm on a distance of 175 m during two months of monitoring [137]. Absolute positioning is also provided by this system which shows a quite good agreement with the measurements of the long base line acoustic navigation system used on-board the boats during the deployment of the lines and other marine operations. The obtained precision of $\sim$ 10 cm on the spatial reconstruction achieved by this system is well within the specifications. In addition, a set of compasses and tiltmetres located inside each LCM container provide the orientation angles (pitch, roll and heading) of the OM frame. This information enables a line shape fit, which together with the acoustic system triangulation, provides a measurement of the relative position of the OMs with an accuracy of a few centimetres.

2.9 Detector performance

The ANTARES telescope is foreseen to be fully deployed and commissioned in 2008. In this section we will review the expected detector performance for the complete detector. To this end, the main magnitudes and parameters that better describe the telescope efficiency are introduced.

- **Effective area**. It is defined as the size of a 100% efficient surface that detects the same number of through-going neutrinos (or muons) than the ANTARES detector. This quantity reflects the ANTARES efficiency. Obviously, the ratio of selected events with respect to the incident flux could also be used to express the detector efficiency, however it is more convenient to express the parameter as an effective area. This effective area can be expressed both in terms of muons and neutrinos, depending on the incident flux we are considering. The neutrino effective area is computed from the number of events selected with respect to the total incident neutrino flux arriving at the Earth. The effective area depends on the neutrino energy (E_ν) and direction (θ_ν, ϕ_ν) and is given by the following expression:

$$A_\nu^{eff}(E_\nu, \theta_\nu, \phi_\nu) = \frac{N_{sel}(E_\nu, \theta_\nu, \phi_\nu)}{N_{gen}(E_\nu, \theta_\nu, \phi_\nu)} \times V_{gen} \times (\rho N_A) \times \sigma(E_\nu) \times P_{Earth}(E_\nu, \theta_\nu), \quad (2.12)$$

  where N_{gen} is the number of generated events in the generation (or *can*) volume, V_{gen}, and N_{sel} is the number of events that meet the selection criteria after muon track reconstruction. The neutrino cross section is given by $\sigma(E_\nu)$ which together with the term ρN_A, the target nucleon density of Earth, gives the number of neutrino interactions. The factor P_{Earth}, which also depends on the Earth density and neutrino cross section, accounts for the Earth absorption for a given neutrino flux. This absorption factor is a function of the neutrino energy and direction. Figure 2.24 shows the effective area as a function of the neutrino energy. When

an isotropic upward neutrino flux is assumed, the effective area can be averaged over ϕ_ν and $\cos\theta_\nu$, and be expressed only as a function of the neutrino energy.

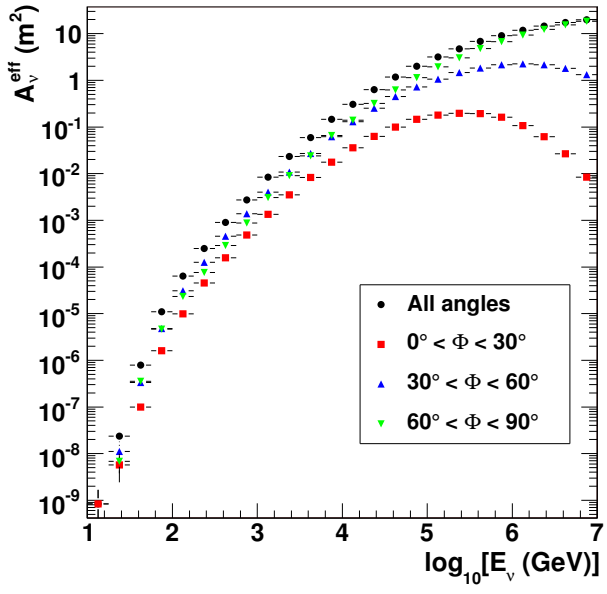

Figure 2.24: *Neutrino effective area, averaged over the neutrino angle direction, as a function of the neutrino energy. Different nadir angles (Φ) have been selected which evidences the Earth opacity at high energies.*

The muon effective area is defined in the same way as the neutrino effective area, considering now the muon flux that crosses a flat, totally efficient ideal surface. The muon effective area is given by

$$A_\mu^{eff}(E_\nu,\theta_\nu,\phi_\nu) = \frac{N_{sel}(E_\nu,\theta_\nu,\phi_\nu)}{N_{gen}(E_\nu,\theta_\nu,\phi_\nu)} \times \frac{V_{gen}}{\langle R^\mu_{eff}(E_\nu)\rangle}, \tag{2.13}$$

where $\langle R^\mu_{eff}(E_\nu)\rangle$ is the average muon range defined as

$$\langle R^\mu_{eff}(E_\nu)\rangle = \int \frac{dP_\mu}{dE_\mu} R_{eff}(E_\mu) dE_\mu, \tag{2.14}$$

being $\frac{dP_\mu}{dE_\mu}$ the probability of a neutrino to produce a muon in the interval dE_μ, and $R^\mu_{eff}(E_\nu)$ is the effective range, that is, the average distance travelled by muons with a given starting energy up to the point where their energy goes below a given threshold. Although it is a muon effective area, it is commonly expressed as a function of the neutrino energy, being the muon energy not a suitable magnitude due to the continuous energy loss during the muon flight.

- **Angular resolution**. The angular resolution is one of the main features of a neutrino telescope. In ANTARES the muon angular resolution is defined as the median of the angle between the true muon track and the fitted track. There is also a neutrino angular resolution which includes in addition the angle between

the true neutrino and the estimated muon track. This neutrino angular resolution is dominated by the kinematics for energies lower than 10 TeV. Figure 2.25 shows both the muon and the neutrino angular resolutions. As can be seen, the projected angular resolution for ANTARES is less than 0.3° for energies above a few TeV. This magnitude is of paramount importance in the search of point-like sources as we will discuss later. The angular resolution, on the other hand, is constrained by different aspects such as the nature of light propagation in the sea water, the knowledge of the OMs positions and the accuracy in the determination of the arrival photons to the PMTs.

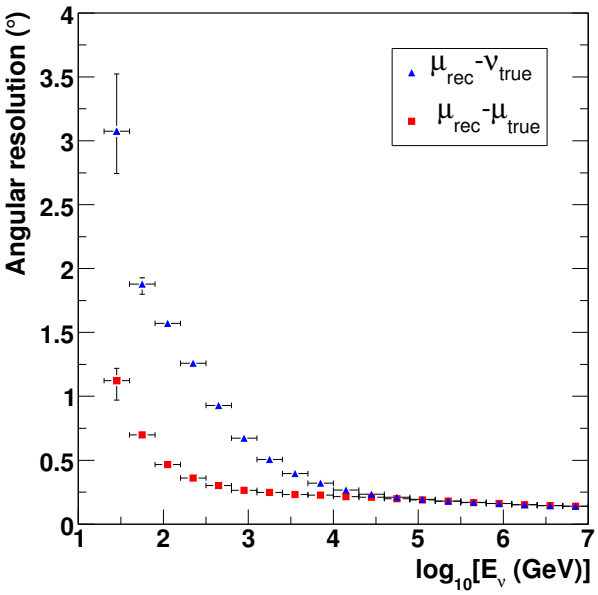

Figure 2.25: *Distribution of the medians of the angular error distributions for muons (angle between the true muon and the reconstructed one) and neutrinos (angle between the true neutrino and the reconstructed muon) as a function of the neutrino energy. The angular resolution is better than 0.3° at high energies ($E_\nu > 10$ TeV).*

2.10 ANTARES status and milestones

The ANTARES collaboration has accomplished very important milestones during the years 2006 and 2007. The first complete line of the neutrino telescope was deployed on the 14th of February, 2006. The connection to the Junction Box –in the sea since December 8, 2002– was done by means of an underwater *Remote Operated Vehicle* (ROV). This first line is the so-called *Line 1* and is taking data since the connection day. Together with the standard line the *Mini-Instrumentation Line with Optical Modules* (MILOM) was already deployed and in operation from April 2005 to April 2006. The second full line (*Line 2*) was deployed in July 27, 2006 and connected a few months later. Right after, three additional lines were connected in early 2007 and connected during that year. Currently, the detector consists of 10 full lines already deployed and connected in December 2007. The first atmospheric muons were detected during the first months of operation with the 5-line configuration and the first atmospheric neutrino candidates have been observed. The pace of line deployment and connection

operations has been remarkably high during the last months. In this thesis we constrained the analysis of the Optical Beacon system to the data available from the first two lines. Oncoming lines are expected to be connected by 2008 when the ANTARES detector is scheduled to be fully commissioned.

Chapter 3

The Optical Beacon system

– That's impossible. You can't go faster than the speed of light.
– Of course not. That's why scientists increased the speed of light in 2208.
Cubert and Professor Farnsworth, Futurama.

High energy neutrino telescopes are expected to achieve good angular resolution making possible the identification of point neutrino sources. This is particularly true in underwater telescopes, where the optical properties of water used as the detection medium, enable a good precision in the determination of the arrival time of the muon induced Cherenkov photons on the PMTs surfaces. In this context, the timing calibration is a key issue in the reconstruction of the muon tracks as mentioned in section 2.8.1 and therefore the verification of the time resolution with different calibration devices is of utmost importance to guarantee a good track reconstruction angular resolution.

The Optical Beacon (OB) system [138] consists of a series of pulsed and well-controlled light sources distributed throughout the detector used for timing calibration *in situ*. In this chapter, a brief description of the design adopted by ANTARES will be presented, as well as the analysis of the first data of the Optical Beacon system in underwater conditions.

3.1 The Optical Beacons

There are two different Optical Beacons, the LED Beacons and the Laser Beacons. An LED Beacon is composed of 36 LEDs pulsed by dedicated electronic circuits and arranged on the surface of hexagonal cylinders. The LED Beacons are located, almost, uniformly along the lines so that their light can illuminate all storeys on the neighbouring strings. The Laser Beacons are much powerful devices that use a solid state pulsed laser whose light is spread out by a diffuser, they are located in a stationary position at the BSS of the lines 7 and 8 and illuminate mainly the bottom of the lines.

3.1.1 The LED Beacon

An LED Optical Beacon (LOB) is a device made up by 36 individual LEDs arranged in groups of six on six vertical boards (henceforth called *faces*) which are placed side

by side forming an hexagonal cylinder. The selected LED is the Agilent HLMP-CB15-RSC00 model[1] whose emission peak is at a wavelength of 472 nm and with a spectral half-width of 35 nm according to the specification sheet. These LEDs have also a fast risetime measured to be between 1.9 and 2.2 ns. On each face of the LED Beacons, one LED is placed pointing upward (*top LED*) to illuminate the storeys higher above in the same string. The *central LED* and the surrounding group of four LEDs point horizontally outward to illuminate radially the nearby strings. The LED Beacon is housed in a pressure resistant glass vessel. This is a cylindrical borosilicate glass container commercially available[2] consisting of a cylinder and two end-caps, one of them detachable. The overall dimensions of the cylinder plus end-caps are 210 mm outer diameter and 443 mm in length. Figure 3.1 shows a picture of the LED Beacon dismantled together with its main components, one of the faces and the upper cap of the container.

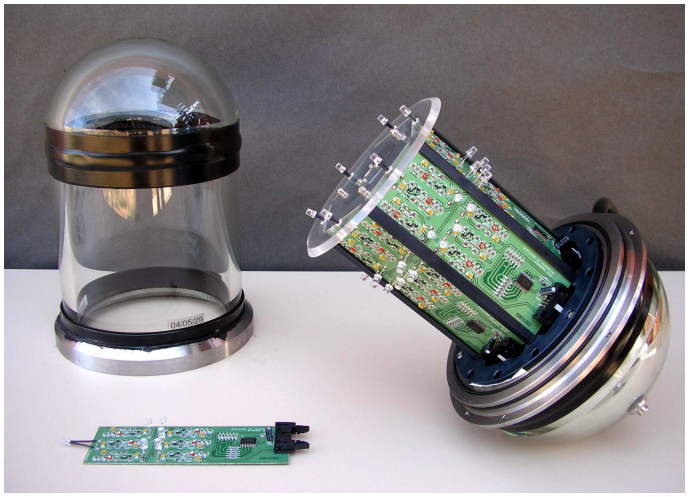

Figure 3.1: *An LED Beacon without the upper cap of the borosilicate container (visible on the left side). One of the face circuits that form the LED Beacon is also shown.*

The faces are mechanically fixed to a nylon structure whose outer surface forms the hexagonal cylinder and whose inner part houses a small Hamamatsu H6780-03 photomultiplier tube. This PMT has a risetime of 0.8 ns and a transit time of 5.4 ns and is used to provide the precise time of emission of the light flash independently of the triggering signal. A flat acrylic disk is fixed to the upper part of the nylon mounting and acts as a light-guide collecting the light emitted by the LEDs. A conical depression was machined in the centre of the collecting disk following Fields and Janowski [139], to guide the light directly into the PMT. The lower part of the LED Beacon houses the electronic boards that provide the required operating voltages and enable the actual LED flashing according to externally supplied slow control commands.

Each of the six faces can be flashed independently or in combination. Within a face, the top, central and group of four LEDs can be triggered independently or in combination. The possibility of flashing certain faces allows the monitoring of the uncertainty in the time calibration arising from the non-uniformity of the angular

[1] Agilent Technologies, Inc. Headquarters 395 Page Mill Rd. Palo Alto, CA 94306 United States.
[2] Nautilus Marine Service GmbH, Blumenthalstrasse 15 D-28209 Bremen Germany.

distribution of the emitted light and other dedicated studies. This layout allows a distribution close to uniform in the azimuth angle when all the LEDs are flashing. The top LEDs enable the calibration of the OMs in those storeys of the same line above that of the beacon. The amount of light can be further controlled changing the number of LEDs flashing at a given time as well as the intensity of the LEDs. The pulser circuit is based on an original design from Kapustinsky et al. [140] that has been modified for ANTARES to include a variable capacitor that enables the synchronization of the pulses produced by several different circuits [141]. The selection of the LEDs combination and intensities are performed through the general RunControl program [131], in which the user can select among different configurations (a run *set-up*) before the start of the run. In addition, a graphical user interface written in Java enables a direct communication between the expert user and the beacons and allows to request their status or change their configuration. This method is rarely used and is employed mainly in the laboratory for test or debugging purposes.

Like any active instrument in ANTARES, the Optical Beacons have to be calibrated before the immersion in a dedicated dark-setup. The PMT of the LED Beacon is calibrated simultaneously with the OMs. This calibration enables the measurement of the relative shifts in the arrival times between the LED Beacon and the PMTs of the OMs.

3.1.2 The Laser Beacon

The Laser Beacons (LB) emit high intensity, short duration pulses of light and are located at the bottom of lines 7 and 8, attached to their BSS, the mechanical structure that anchors the line to the seabed. Figure 3.2 shows a general view of the Laser Beacon and its components. The Laser Beacon points upward so that the emitted light can reach nearby lines.

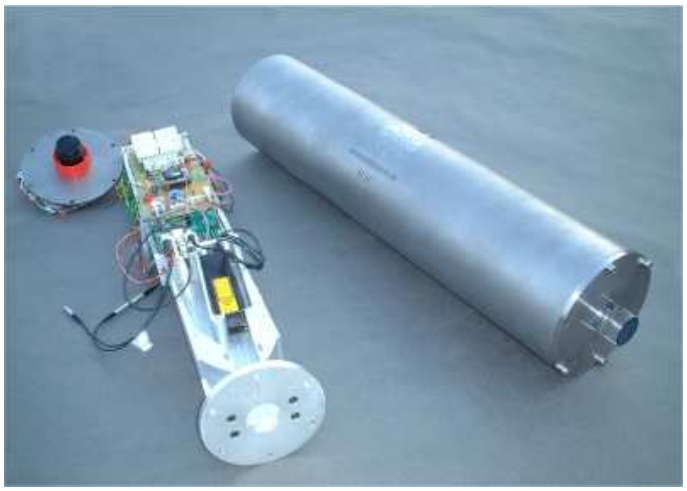

Figure 3.2: *A Laser Beacon dismantled: On the left of the picture, the inner mechanics holding the laser head and its associated electronics. On the right, the pressure-resistant titanium container that houses the equipment. On the top end plate of the container (right part of the picture) the quartz cylinder that prevents sedimentation effects.*

The main component of the Laser Beacon is a diode pumped Q-switched Nd-YAG laser which produces short pulses with a time duration less than 1 ns (FWHM) and a

total energy of $\sim$1 μJ. The laser model selected is the NG-10120-120[3] which emits at 532 nm after frequency doubling of the original Nd-YAG wavelength of 1064 nm. It is very compact, with head dimensions of $144 \times 37.4 \times 30$ mm. The laser can be operated in a non-triggered mode at a fixed frequency (around 15 kHz) or in a triggered mode with a variable trigger frequency. In the latter mode, which is the one being used in ANTARES, the laser is triggered when a TTL signal arrives at the device through a connection in the rear panel of the power supply. Since the laser is passively Q-switched, the delay between the trigger signal and the light pulse emission is of the order of microseconds and the pulse to pulse jitter is of the order of a few hundred nanoseconds.

The actual time of laser emission is obtained using a fast photodiode integrated in the laser head. Once the laser shot is produced, the built-in photodiode sends back a signal which is passed on to an ARS chip located in the String Control Module (SCM) –the electronics container similar to the LCM located on the BSS– the current that feeds the pumping diode is switched off and the system waits for the next trigger signal.

The laser is housed in a cylindrical titanium container with 705 mm in length and 170 mm in diameter (see figure 3.2)[4]. Inside the container, an aluminium inner frame holds the laser and its associated electronics. In the upper end-cap there is an opening with an optical flat disk diffuser[5] with a thickness of 2.2 mm and a diameter of 25 mm that spreads the light beam out following a cosine distribution, so that the light can reach the surrounding lines. Since the Laser Beacon is pointing upward, is more affected by the transmission losses due to underwater sedimentation and biofouling (the accumulation of micro-organism on the outer surfaces). In order to minimize this effect, a quartz cylinder was bonded to the upper surface of the diffuser as can be seen in figure 3.3 left. The upper surface of this cylinder is coated with a black, water resistant epoxy layer. The light then leaves the cylinder through the vertical wall where biofouling is negligible (see scheme on figure 3.3 right). The cylinder dimensions where chosen accordingly with the refractive index of quartz to conserve the cosine distribution, due to Snell's law, when light leaves the cylinder through its vertical walls.

3.2 Data format and Optical Beacon trigger

When acquiring data in SPE mode, a *hit* (a pulse in one OM processed by one of its ARS) is also dubbed as an *spe_item*. Each *spe_item* carries all the information required for the processing and analysis:

- Each hit can be unambiguously identified by the *header*. The *header* contains the information about the origin of the hit addressed by a pair of identification numbers. One of these numbers is the `LCM_ID` label which identifies the storey

[3]Nanolase, presently part of JDS Uniphase Corp., 430 N. McCarthy Blvd. Milpitas, CA 95035 United States.

[4]The new laser design dimensions for lines 7 and 8 are smaller.

[5]ORIEL model 48010, Newport Corporation-Oriel 150 Long Beach blvd. Stratford, CT 06615 United States.

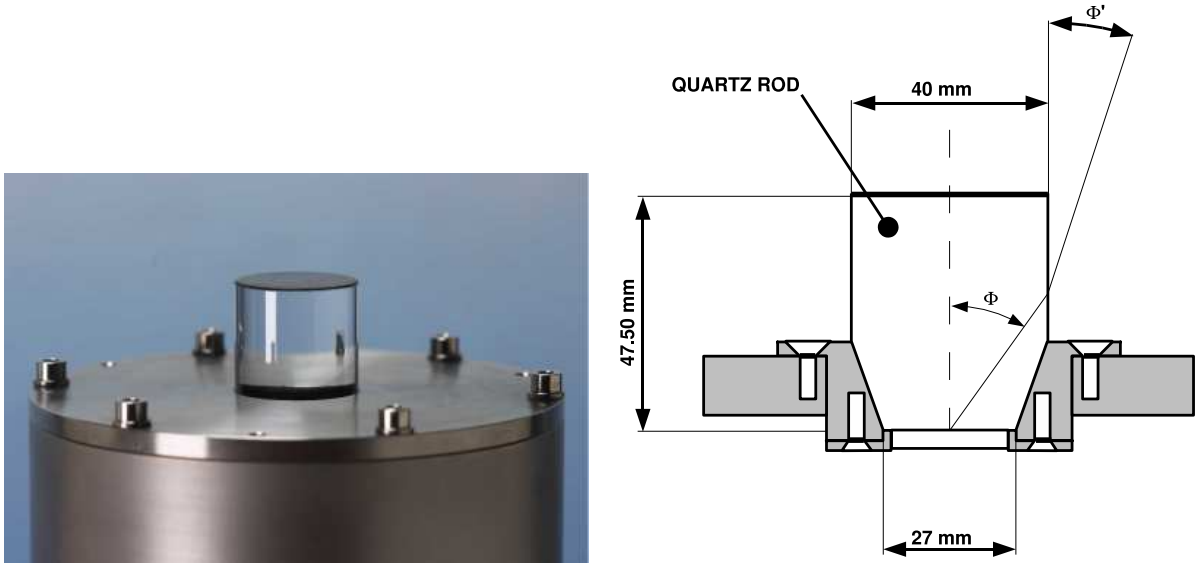

Figure 3.3: *Left: Upper end-plate of the Laser Beacon container with the quartz cylinder used to avoid losses due to biofouling. Right: Schematic path of the outgoing light.*

(or the LCM) from where the hit was originated. The second one is the `ars_link` which takes values from 0 to 6, indicating which ARS processed the signal. Values 0/1 are for the optical module labelled as OM 0, values 2/3 for OM 1 and 4/5 for OM 2. When the `ars_link` equals 6 the origin of this hit is an Optical Beacon.

- The *timestamp* gives the impression time of the hit referred to the internal clock with a precision of 25 ns.

- The TVC value gives the arrival time of the hit in the interval between two clock cycles.

- The charge of the *spe_item* is digitized and stored in the AVC value.

As mentioned in section 2.7.2, there are different filtering algorithms depending on which kind of event we are interested in. The standard muon filter looks for correlation in the *spe_item* consistent with a specific physics signal like a muon crossing the detector. With the **Optical Beacon trigger** (`triggerOB`) we devised an algorithm to filter and process events coming from the Optical Beacon system [142]. This software takes advantage of the peculiarities of Optical Beacon events: for instance, the origin in time and space of the event is well known since it corresponds to the flash of an Optical Beacon device. The algorithm seeks for signals with an `ars_link` equal to 6 corresponding to the small photomultiplier tube, in the case of an LED Beacon, or the built-in photodiode, in the case of the Laser Beacon. This *spe_item* is then used as a reference and is considered as the *root hit* of the event. Correlations between this *root*

hit and the rest of hits can be inferred directly from causality relations. Only hits that satisfy the following equation are considered:

$$\frac{|\Delta\bar{x}|}{c/n} - t_E \leq |\Delta t| \leq \frac{|\Delta\bar{x}|}{c/n} + t_E, \tag{3.1}$$

where value t_E stands for the parameter `maxExtraTime`, that defines the time window within which the Optical Beacon hits are considered. Another parameter taken into account in order to speed up the triggering is the `maxDistance`. Once the *root hit* is found from a given Optical Beacon, hits located at distances greater than `maxDistance` are excluded from the computation. A reasonable value for `maxDistance` is three times the absorption length of light in water, since photons will hardly travel such distances.

3.3 Timing calibration with the Optical Beacons

As of February 2007, five complete lines were installed and started operation in the ANTARES site. In addition, one *Mini-Instrumentation Line with Optical Modules* (MILOM) was in operation from Spring 2005 to Spring 2007 [137]. This MILOM was equipped with two LED Beacons (one of which suffered from a water leakage and stayed nonoperational) and a Laser Beacon located at the BSS of the line. In this section, we will present the first results of the Optical Beacon system in underwater conditions. To this end, dedicated Optical Beacon runs are regularly taken. The current procedure is that one run per Optical Beacon is taken. In the so-called **nominal run**, the duration is set to about 10 minutes flashing with a trigger rate of a few Hz, and LED Beacons are flashed at high intensity. The LED Beacons are distributed more or less uniformly along the line. More precisely they are located in storeys 2, 9, 15 and 21. With this distribution we ensure that all parts of the lines are illuminated and that each OM receives light from at least two different Optical Beacons. Figure 3.4 shows an schematic view of a standard line of ANTARES with the position of the LED Beacons indicated. The figure is separated in line sectors (a group of 5 storeys) for the sake of representation. It can be seen that there is an LED Beacon in each sector except in the fourth sector.

A Laser Beacon was deployed located at the bottom of the MILOM. Two additional Laser Beacons with a newer design that enables the adjustment of the light pulse intensity, are located in lines 7 and 8. At the moment of writing this thesis, lines 7 and 8 were deployed but not still connected to the Junction Box. Hence the results presented here concerning the Laser Beacon, correspond only to that laser housed in the MILOM.

3.3.1 LED Beacon and OM signals

In every storey there are six ARSs numbered from 0 to 5. If in the storey there is also an LED Beacon a seventh ARS is present and is labelled as ARS_6. An example of a signal processed in this ARS coming from the internal PMT of an LED Beacon can be seen in figure 3.5. This is an example of the WF mode acquisition. However,

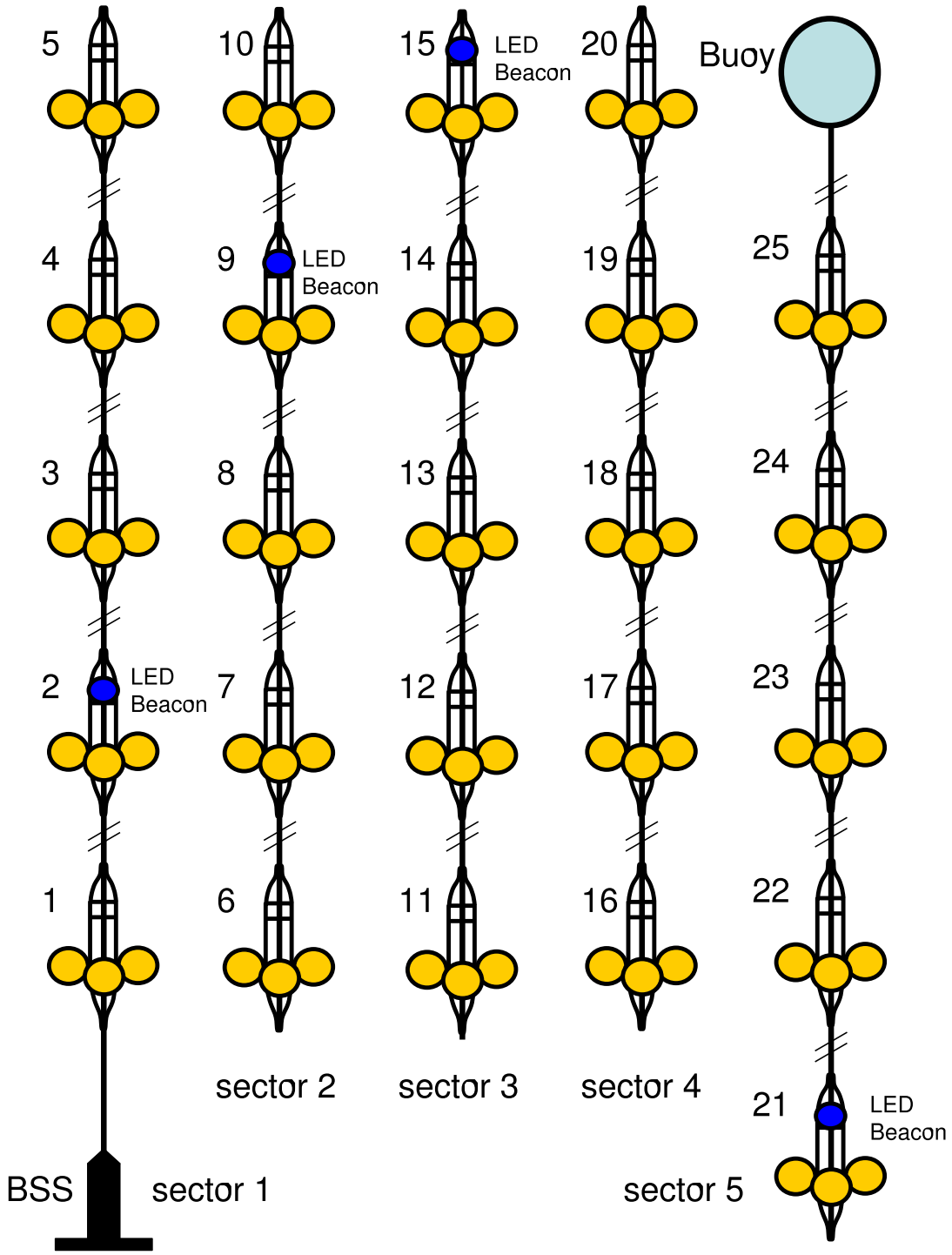

Figure 3.4: *Schematic view of a standard ANTARES line with 25 storeys. The string is shown separated in sectors (groups of five storeys) to show in a handy way the LED Beacon positions. As indicated in the figure, Optical Beacons are located in all sectors (storeys 2, 9, 15 and 21) except Sector 4.*

as mentioned before, the standard procedure in ANTARES is to take all data in SPE mode. The WF mode is mainly used during pre-integration of the different detector components and the assembly test.

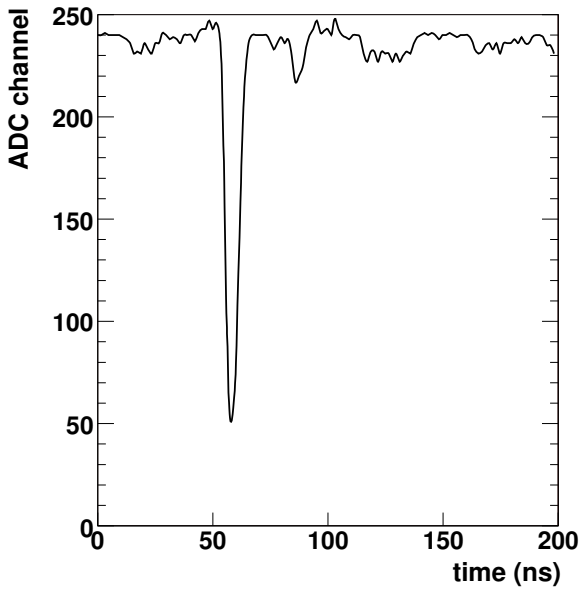

Figure 3.5: *Signal from the small PMT of an LED Beacon recorded by the ARS in WF mode.*

As already explained, during the SPE mode acquisition, every SPE hit is described by the values obtained by the AVC and TVC. Figure 3.6 shows the distribution of these two magnitudes for a nominal LED Beacon calibration run recorded by the internal PMT of the LED Beacon. As can be seen, the TVC distribution shows a narrow peak, since the LED Beacon is flashed synchronized with the internal clock. In the figure the two distributions of the two TVC ramps are shown. The AVC distribution depends on the gain in the internal photomultiplier tube and on the intensity selected for the LEDs of the beacon.

The TVC and AVC distributions from the signal recorded by the PMTs during a LED Beacon run differ dramatically from those during the standard operation of the detector. During an LED Beacon run all hits processes in the OMs have the same values of the TVC, since the LED Beacons are flashed synchronized with the master clock signal. Therefore the TVC distribution (see fig. 3.7 right) is peaked at the same value of the TVC. As can be seen in the figure, together with the narrow peak there is also a small broader peak in the distribution. This second peak is customarily called *after-pulse*, although its origin has nothing to do with the after-pulses due to the photon emission in the last dynode of the amplification stage in the PMTs [143]. Instead, these after-pulses are originated when the analogical signal is too large to be processed by only one ARS. When the token ring is passed on to the second ARS, about 10 ns after the SPE integration (33 ns), the tail of the analogical signal is processed as a new hit. Therefore, the after-pulse hit in one ARS is delayed $\sim$ 43 ns with respect to the true saturated hit processed by the second ARS. In the TVC distribution of figure 3.7 right, the contribution of true hits populates the narrow peak in the histogram, whereas the

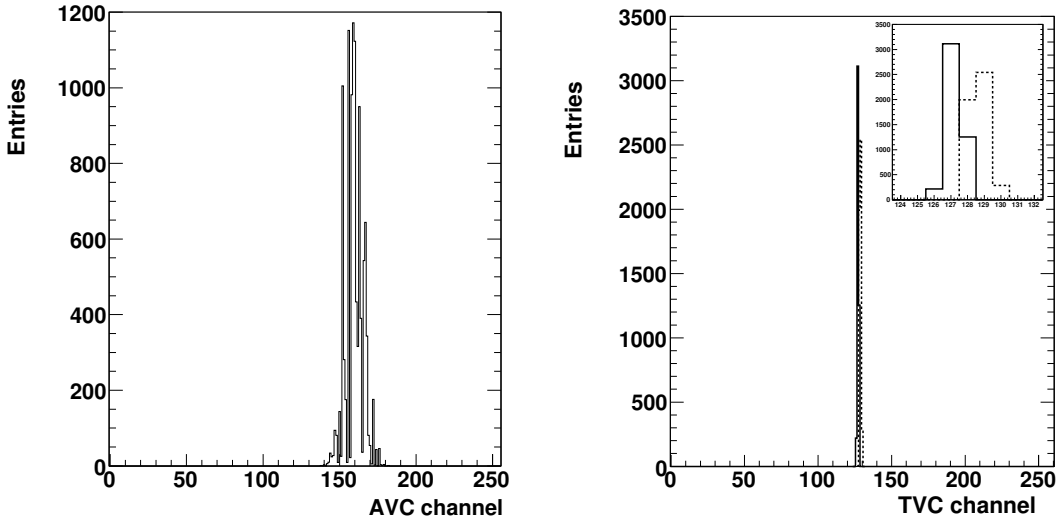

Figure 3.6: *Left: Distribution of the AVC value for the internal PMT of an LED Beacon for a nominal calibration run. Right: TVC distribution for the same signal, both ramps are indicated by the solid/dashed lines. The inset shows a blow-up of the TVC distributions.*

after-pulses hits derived from the signal processed by the second ARS gives rise to the second small peak, which in fact is one clock cycle later. Since the TVC cycle is of 50 ns, this small peak of after-pulses appears almost superimposed on the true hits.

The AVC distribution depends on the PMT gain, the intensity and number of LEDs that are emitting and also on the distance of the OM with respect to the flashing LED Beacon. Figure 3.7 left, shows the AVC distribution corresponding to one ARS of one OM located near the LED Beacon. Due to the proximity of this OM with respect to the LED Beacon the majority of hits are in the saturated bin (AVC = 255) while the rest are basically noise.

3.4 Time correlations OM-OB

In this section we will evaluate the time difference distribution between the OMs signal and the Optical Beacon. The plots in figure 3.8, show the distributions of $\Delta t = t_{\mathrm{ARS_{DEST}}} - t_{\mathrm{ARS_{REF}}} - d/c$, where ARS_{DEST} is the ARS_5 of the OM 2 of the third storey of *Line 2*, and ARS_{REF} is the ARS_6 of the LED Beacon in the second storey of the same

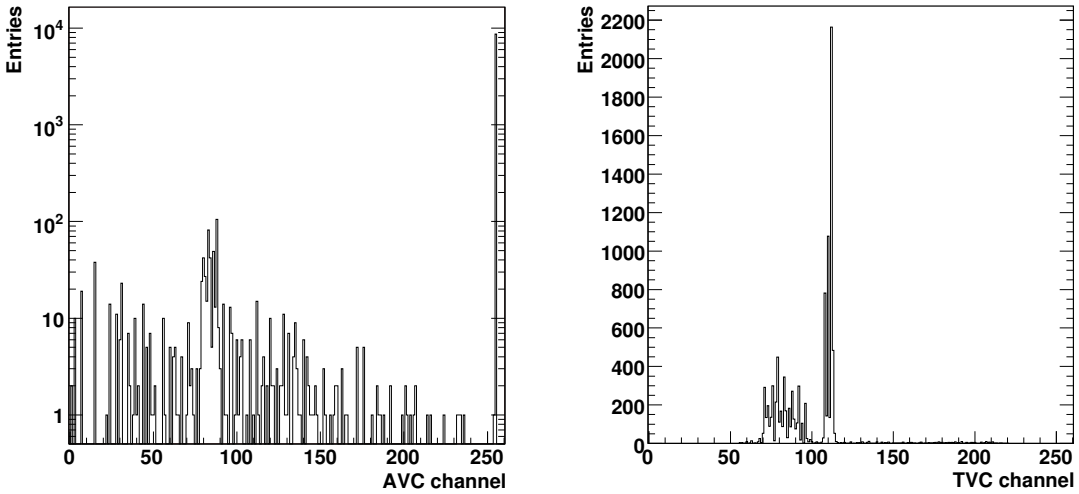

Figure 3.7: *Left: Distribution of the AVC value recorded by one of the two ARSs of an OM during an LED Beacon calibration run. Right: TVC distribution for the same signal and ARS.*

line. The term d/c is the theoretical travel time computed as the ratio of the OM-OB distance and the speed of light in water. In this work we use a value of 0.21722 m/ns as the speed of light in water according to [128]. In this sense, Δt is a *time residual* which indicates the difference between the observed hit time and the expected time for a direct photon. In order to compute the factor d/c in this particular measurement, the on-line information about the position of the detector elements given by the alignment and geometry has been used. This alignment information is provided by the set of compasses and tiltmetres located along the detector, as described previously, which enable a line shape reconstruction.

In order to determine the time-offsets and possible deviations from the values measured in the dark-setups it is important to provide a time based on the arrival time of the first photons on the OMs. A fit procedure to the early photons (left part of the distributions) are useful for the time calibration since the rest might be distorted by scattering and other effects such as the token ring process. The plots in figure 3.8 show schematically the fit procedure. A double fit procedure is performed. First, the most populated bin is selected and the rising-edge (from 20% to 90% of the maximum occupancy) is fitted to a Gaussian function. The mean (also designated by T^{100}) obtained by this first fit is used to re-define the new fit range (from 10% to 80% of the bin corresponding to T^{100}). The binning in the histograms was selected so as to have at least 4 bins from the most populated bin to the bin with 10% of the maximum. This selection constrains the fit region to the most stable part of the distributions and the double fit prevents as much as possible the problem of the *Differential Non Linearities* as explained later in this section. The final estimated T^{100} gives a measurement of the time-offset, while the resolution is given by the width of the Gaussian fit.

These time-offset measurements enable the monitoring of possible deviations from

the values previously measured off-shore in the dedicated dark-setups, and the updating of the corresponding values in the calibration database in those exceptional cases when time-offsets have changed during the operation of the detector.

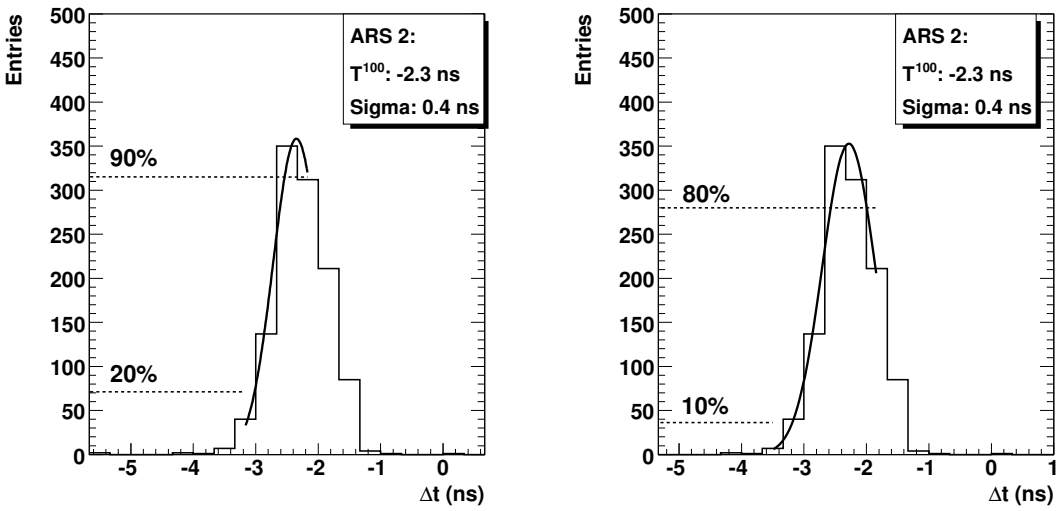

Figure 3.8: *Left: Time difference distribution fitted to a Gaussian in the rising-edge. Right: Same distribution with an Gaussian fit to the early-photon region.*

The standard deviation of the fit is a measurement of the time resolution achieved by the ANTARES telescope. This resolution has several contributions, namely

$$\sigma^2 = \frac{\sigma^2_{TTS}}{N_{pe}} + \frac{\sigma^2_{water}}{N_\gamma} + \sigma^2_{OB} + \sigma^2_{elec}. \tag{3.2}$$

The transit time spread of the PMT gives a contribution to the time resolution which is indicated by σ_{TTS}, this contribution, however, depends on the number of photoelectrons induced in the photocathode and at high intensity it becomes negligible. The second contribution comes from the water influence in the photon dispersion in water (σ_{water}). The arrival time will be dominated by the first photons that reach the PMT photocathode, hence when many photons are produced, the uncertainty given by the transmission of light in water is negligible since the arrival time will be provided by the direct photons. The source time spread, σ_{OB}, is in fact very small due to the fast rise time of the internal PMT of the LED Beacon (0.8 ns). The final resolution comes from the intrinsic electronics resolution which has been estimated to be about 0.3 ns [132]. In the example shown before, due to the short distance between the beacon and the OMs ($\sim$ 13.4 m) and to the high intensity at which the beacon was operated, contributions to the width of the time distribution from the transit time spread in the PMT, from light scattering in the water and any other contribution arising from line movements are all negligible. Therefore, the width of the distribution is a direct measurement of the read-out electronics resolution. Figure 3.9 shows different measurements of time resolutions using the LED Beacons at high intensity level (nominal runs) and the next storey above. As can be seen, the averaged resolution measured with the Optical

Beacon system is about 0.3 ns which is in agreement with the expected value due to the intrinsic electronics resolution.

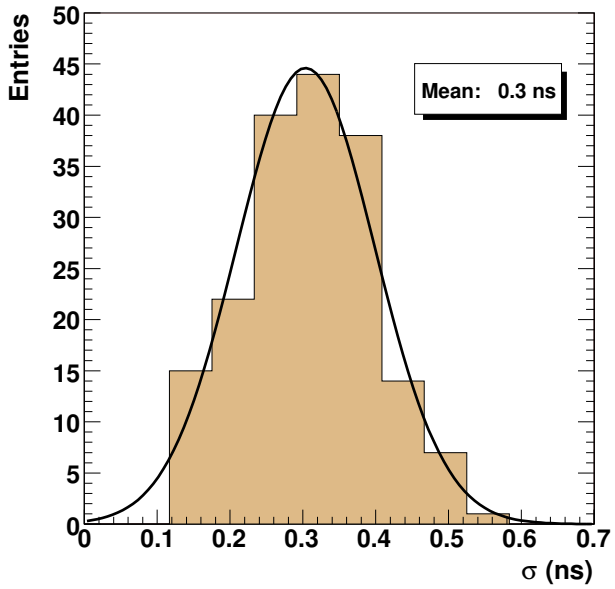

Figure 3.9: *Distribution of the standard deviations of the distributions of time differences between the LED Beacon signal and the OMs.*

As can be seen, the resolution achieved in ANTARES by the electronics is below the nanosecond level, **about 0.3 ns** well within the specifications. This is a very important result since it is the first time that the requirements in the time resolution of ANTARES have been completely verified in underwater conditions. Figure 3.10 shows an example of these time differences distributions. Each distribution corresponds to one ARS in storey 3 of *Line 2*. The LED Beacon flashing in this case is the one located in storey 2 of the same line.

Most of the distributions shown in this figure have a Gaussian-like shape. However, the distribution computed for ARS_2 presents a slight deviation from this shape. In this case, the contribution to the less populated bin next to the peak is a result of the *Differential Non Linearities* (DNLs) mentioned in section 2.7.1. This DNL effect was originated from a non uniformity in the TVC bins of the ARSs. Considering a time calibration run this non-uniformity becomes problematic being the signal digitized with the approximately always the same value of the TVC, since the LED Beacons are flashed synchronously with the master clock. If the PMT processed signal is often stored in a narrower TVC bin, the effect will be transferred to the time distribution. Nonetheless, as the TVC is evenly distributed during the standard acquisition of the detector, the DNLs are washed-out and can be neglected.

Figure 3.11 shows the TVC distribution of one of the ramps for the considered ARS_2 in two different situations. The upper histogram shows the TVC peak in an LED Beacon run, the lower plot is the measurement in the dark-setup of the TVC distribution where the non-uniformity in the occupancy of the bins reflects the DNL effect. For this particular ARS and TVC ramp, bins 109 and 111 of the TVC are narrow bins that cause the appearance of false peaks in the TVC distribution during

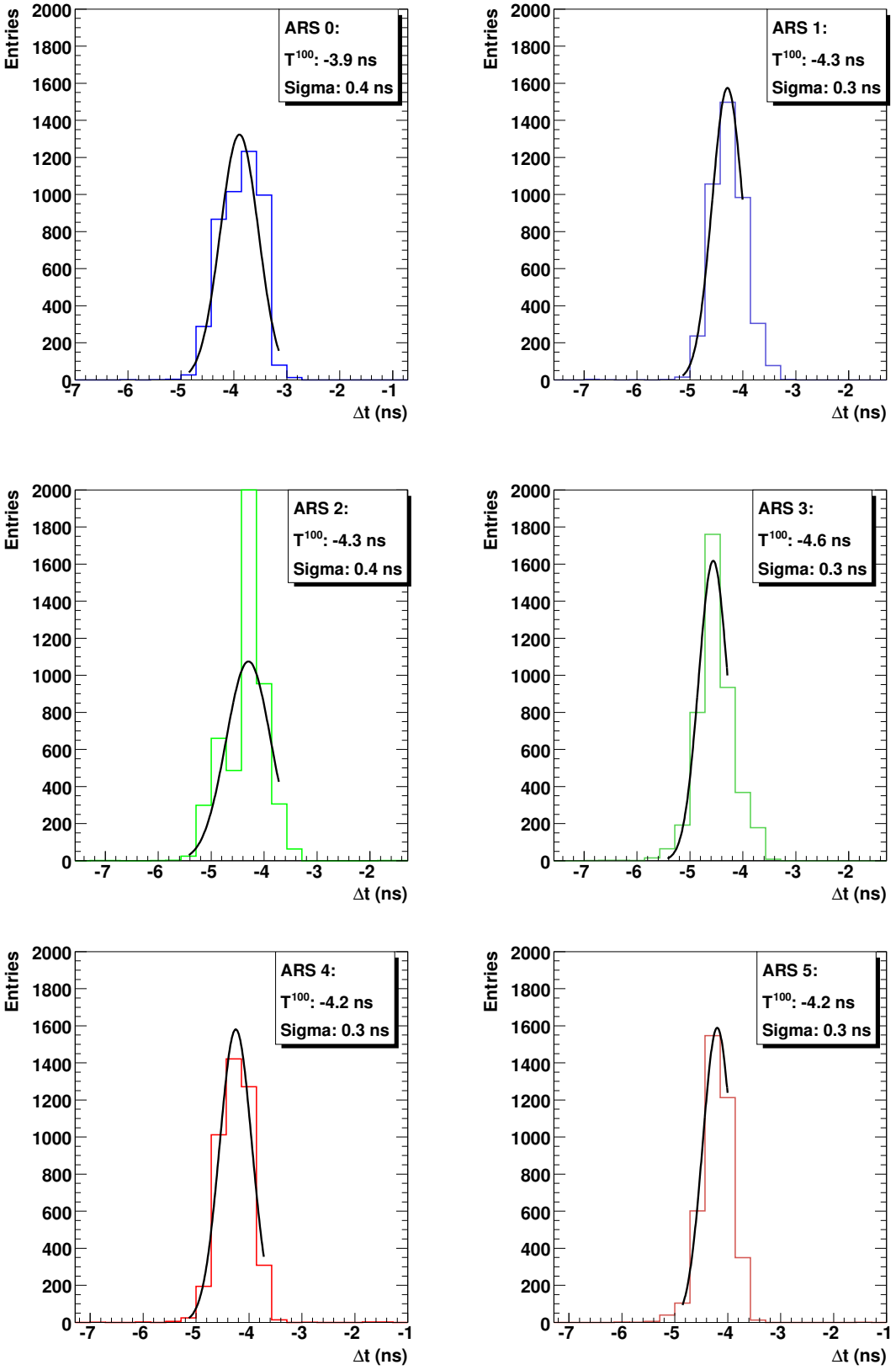

Figure 3.10: *Distributions of the time difference between the signal recorded by the internal PMT of the LED Beacon in storey 2 of Line 2 and the signal in each of the ARS of the OMs of storey 3 of the same line.*

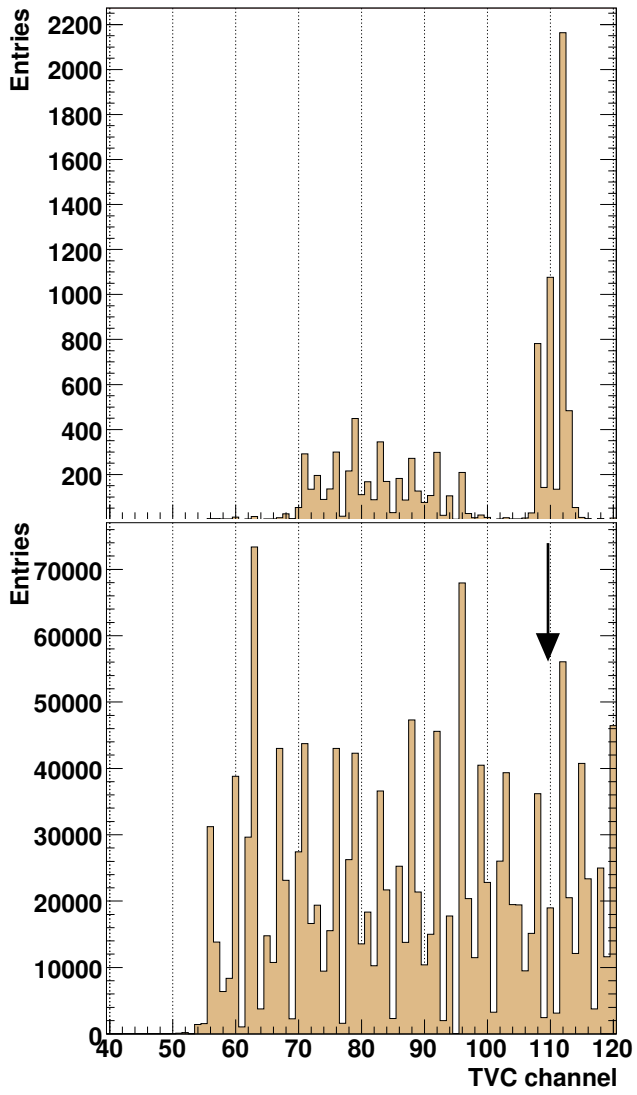

Figure 3.11: *Top: TVC distribution of one of the ramps in ARS_2 in an LED Beacon run. Bottom: Uniform distributed events for the same ARS and TVC ramp measured in the dark-setup. Bins 109 and 111 with low occupancy (arrow) generate the fake peaks in the TVC distribution during the Optical Beacon run.*

an LED Beacon run. These fake peaks in the TVC distribution distort the Gaussian shape of the final time difference distributions.

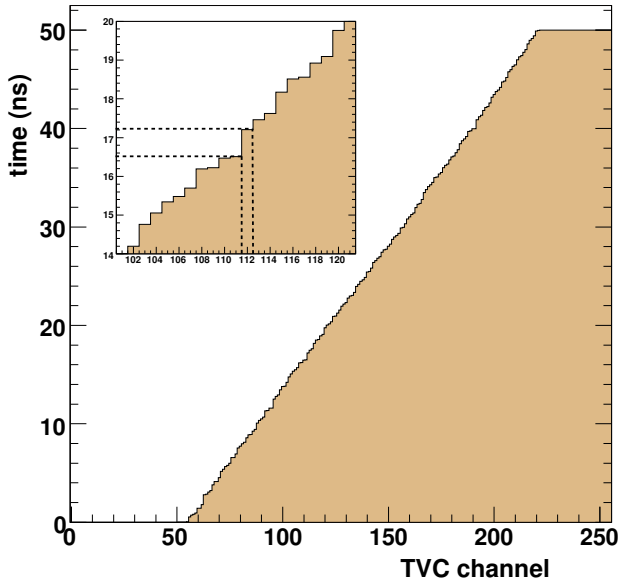

Figure 3.12: *Cumulative distribution of the ramp 0 of the TVC in the ARS_2. The inset plot shows a blow-up of the distribution illustrating how low occupancy bins correspond to small bins in time and vice versa.*

In order to correct by the DNLs, instead of assuming a linear behaviour between the dynamic range $[TVC_{min}, TVC_{max}]$ as given by the expression 2.11, the time assigned to each ADC channel should depend on the bin size. Since the bin size can be inferred by the bin occupancy when randomly distributed hits are generated, a straightforward assignment is to compute the cumulative distribution of the uniform TVC distribution normalized to 50 ns as shown in figure 3.12. For each ADC channel in the horizontal axis, a different bin size in time –the vertical axis– is assigned. The inset in figure 3.12 shows a blow-up of the cumulative distribution where the calibration procedure is graphically represented.

With this correction, we are able to avoid the fake peaks appearing in the TVC distribution. As an example, figure 3.13 shows the distributions of time differences for the ARS_2 using the standard lineal TVC calibration (left) and the calibration corrected for the DNLs (right). However, as mentioned before, this calibration has the main drawback that 256 values will have to be stored in the database for each TVC ramp of each ARS in the whole detector, the total number of entries to insert in the database will be greater than $9{\times}10^5$ which makes this calibration an unpractical solution. Moreover, in the future, when the Optical Beacon will be flashed asynchronously with the clock, the effect of the DNL will be washed-out. As can be seen, the width of the distribution does not change, but the distribution becomes more Gaussian-like and the T^{100} parameter changes slightly.

Time difference distributions can also be computed for each OM combining the information provided by both ARSs of the same OM. These distributions are shown in figure 3.14 for the three corresponding OMs of the storey 3 of *Line 2* with respect to the LED Beacon signal in storey 2 of the same line. The widths of these distributions

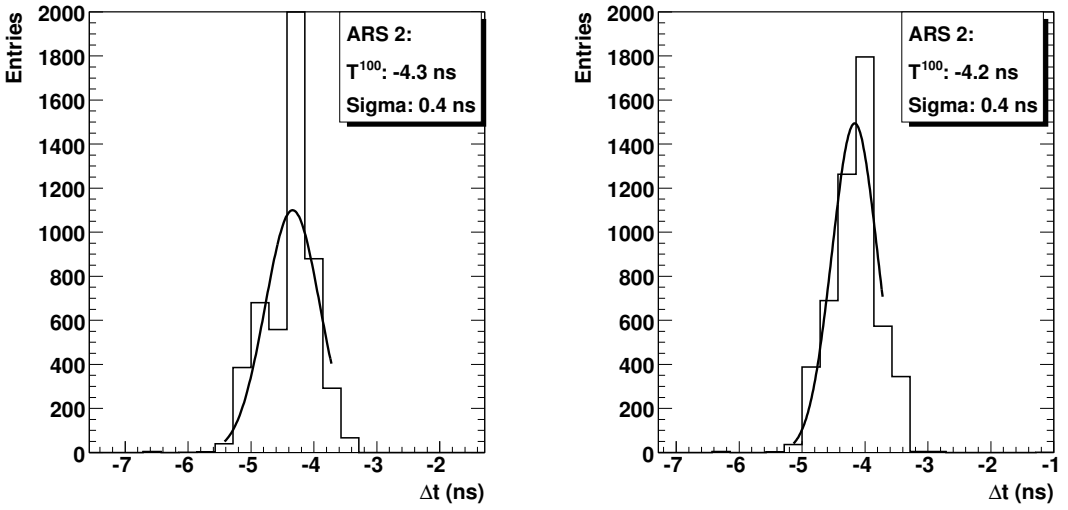

(a) Linear calibration **(b)** DNL correction

Figure 3.13: *Distributions of time difference for the ARS_2 of the third storey in Line 2 with respect to the LED Beacon located in Line 2 storey 2, for two different TVC calibration procedures.*

are measurements of the timing resolution achieved per OMs since as noted before, contributions to the time resolution coming from effects other than the pure electronics resolution are all negligible. Taking into account several distributions, it can be seen that the global time resolution per OM in the ANTARES detector is **about 0.4 ns** which is in agreement with the electronic resolution mentioned above.

Up to now, all time difference distributions have been done using an LED Beacon as the source of the light pulses. The Laser Beacons are more powerful devices with the advantage that are located at the anchor and therefore not suffering the line movements due to underwater currents. Being an intense source of light, the first design deployed in ANTARES of the Laser Beacon was equipped with a light filter which attenuated the emitted light. This solution was decided in order to prevent any damage in the PMTs stemming for the high light level. Unfortunately, the selected filter was too absorbing and the Laser Beacon in the MILOM was able to illuminate only a few number of storeys of the nearby strings. Figure 3.15 shows the time difference distributions for the first storey of *line 2* and the Laser Beacon located in the MILOM. Although the light scattering corresponding to laser wavelength is less marked, a long tail due to scattering is clearly visible in the distributions due to the distance between the Laser Beacon and the OMs ($\sim$ 109 m).

In this case, the time-offset of the Laser Beacon was not correctly computed in the dark-setup. Hence the value of the parameter T^{100} is not well-defined. Nonetheless, it should be stressed that the Laser Beacon faced several challenges ranging from technical and mechanical issues and environmental constrains like the upward emission of the laser. The results presented in this section, constitute a verification of all the different

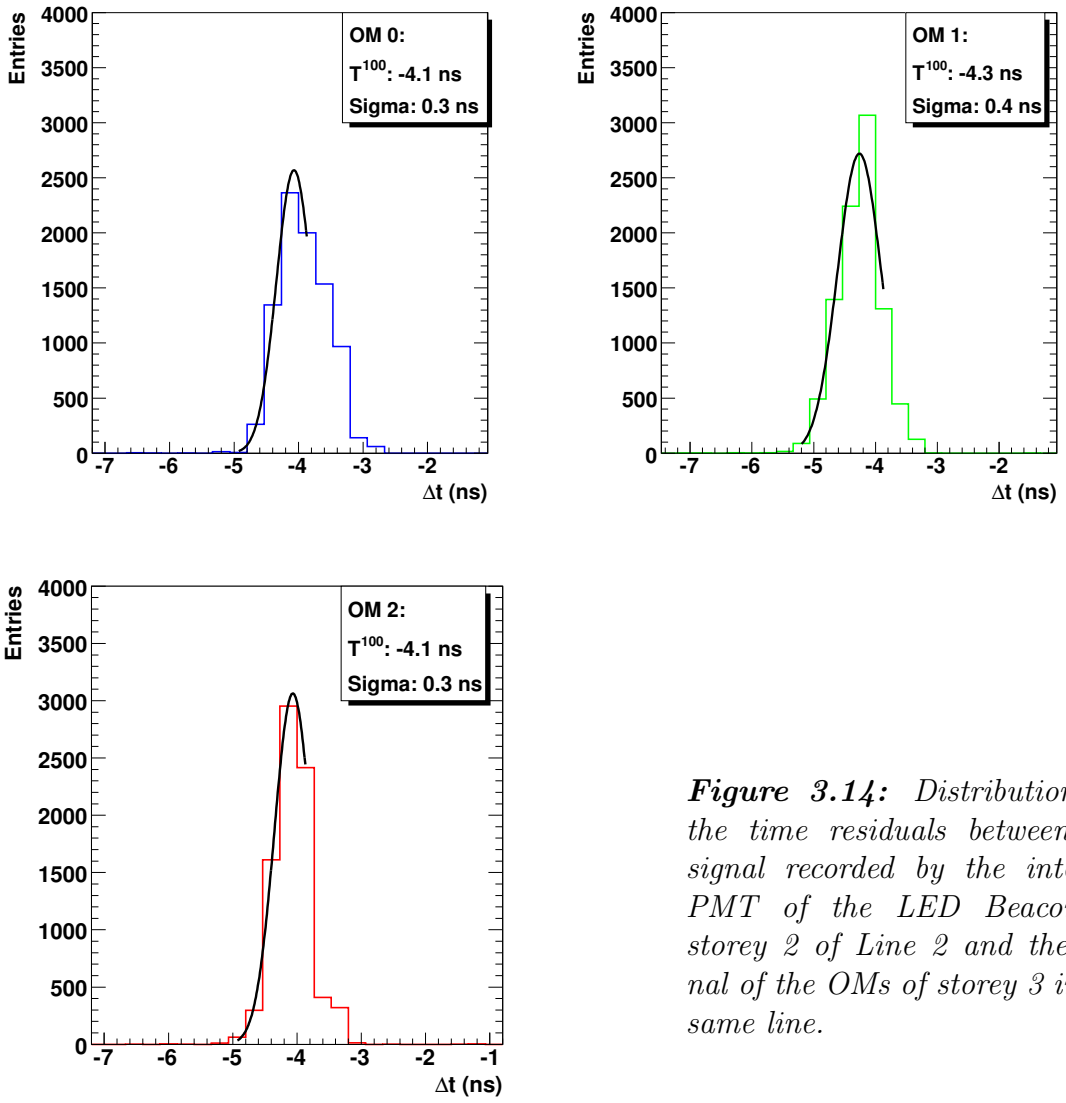

Figure 3.14: *Distributions of the time residuals between the signal recorded by the internal PMT of the LED Beacon in storey 2 of Line 2 and the signal of the OMs of storey 3 in the same line.*

details adopted in the Laser Beacon design. In particular, it is specially remarkable that the scheme proposed for the upward emission consisting of the light diffuser and the quartz rod has turned to be a practical and good solution.

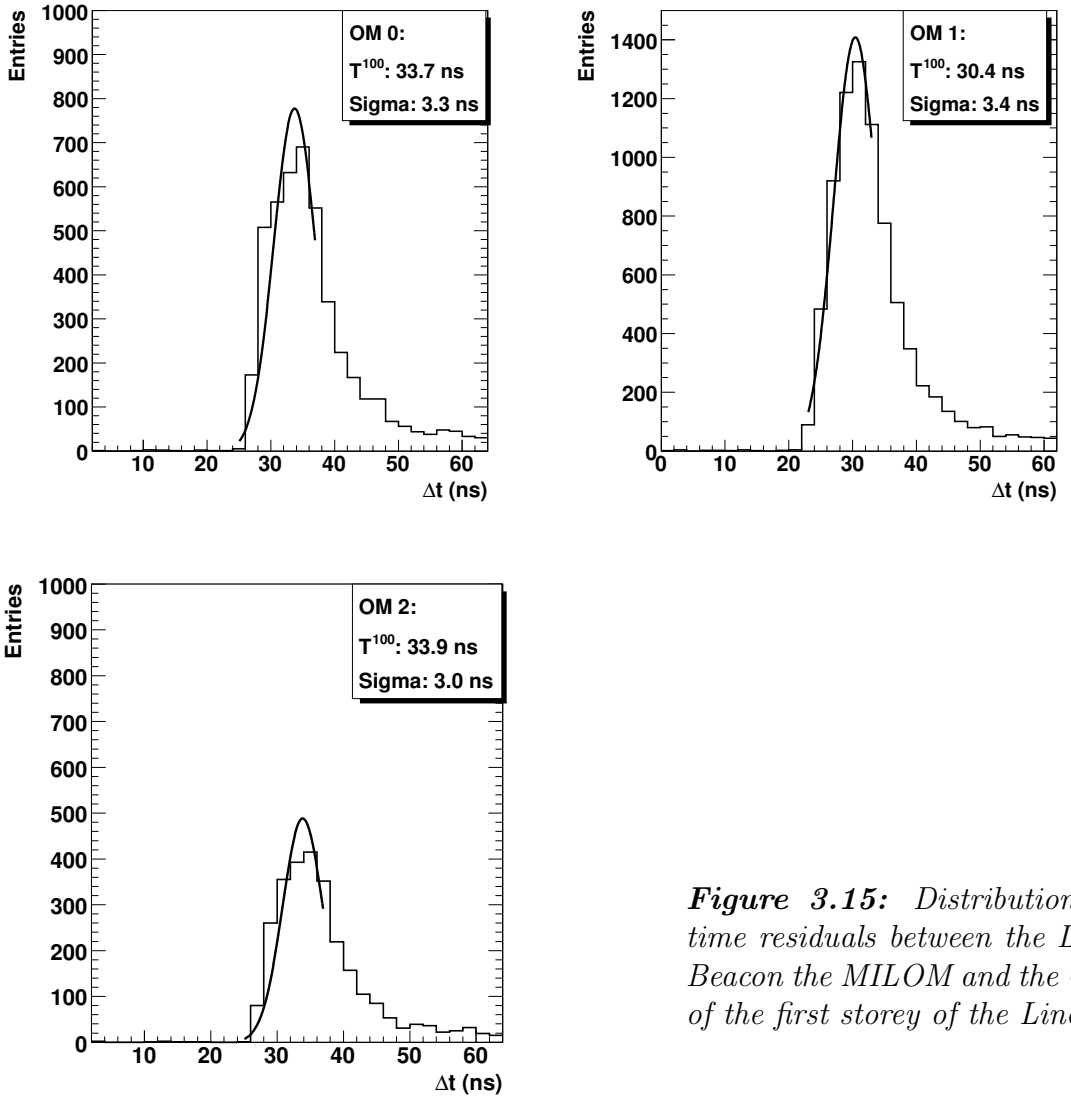

Figure 3.15: *Distributions of time residuals between the Laser Beacon the MILOM and the OMs of the first storey of the Line 2.*

3.5 Parameter dependence with distance

In this section we review how the estimate of the time-offsets and resolution depends on the distance of the PMTs with respect to the flashing Optical Beacon. We will study the evolution of the T^{100} parameter as a function of the distance between OM-OB once this distance is corrected as defined in Δt. The error in the determination of the T^{100} has two different components. A first contribution was assumed to be related to the fit procedure and the binning selected in the time difference distribution. Other source of accidental errors have been inferred by acquiring several calibration runs with identical

run-setup, during a short period of time and therefore with the same detector and environmental conditions. The deviations from the first measured value of a series of measurements of the T^{100} parameter can be seen in figure 3.16.

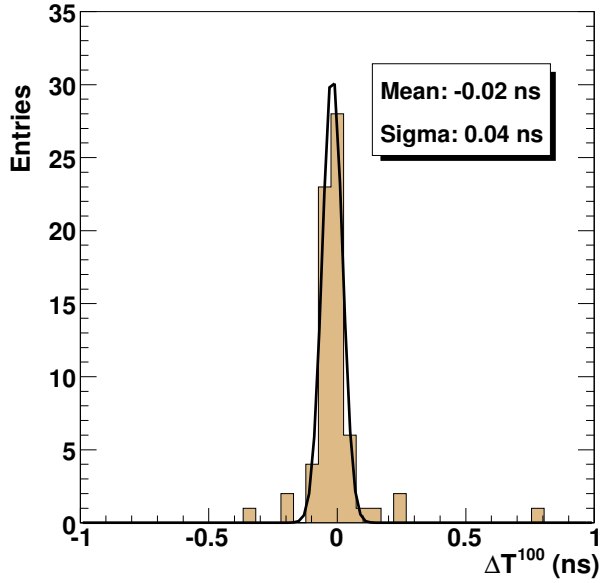

Figure 3.16: *Deviation from the first measured T^{100} value in a series of measurements. The standard deviation of the fit is assumed to be the accidental error in estimating the T^{100}.*

The error in the T^{100} parameter can be expressed therefore as

$$\sigma^2 = \sigma_{acc}^2 + \sigma_{bin}^2, \tag{3.3}$$

where $\sigma_{bin} = \Delta_{bin}/\sqrt{12}$ is the contribution from the binning in the time difference distributions and σ_{acc} is the error estimated to be due to an accidental origin. As already mentioned, the information from the positioning system together with the speed of light in water are used to correct the time difference between the signal provided by the LED Beacon and the signal recorded in the different OMs. An example of the T^{100} parameter computed for the LED Beacon on the second storey of *Line 2* and the PMTs in the same line can be seen in figure 3.17. It is important to remark that in order to show the results in an orderly way we have grouped the data according to the OM that recorded the signal, even though there is no physical relation between OMs of the same label in different storeys. This is particularly true when the LED Beacon is illuminating its own line. However, when illuminating the nearby strings we assumed that all OM 0 are aligned along the string. Although during the assembly of the line, shifts from one storey to another are expected, these shifts are not considered significant.

As can be seen, the T^{100} parameter increases as a function of the distance of the LED Beacon and the storeys ($\sim$ 14.5 m within a line). Hence there is a delay in the expected arrival time of the photons derived, at first sight, from purely geometrical considerations when increasing the distance between the light source and the PMTs. It is also important to remark that this increase seems to follow a linear trend. This

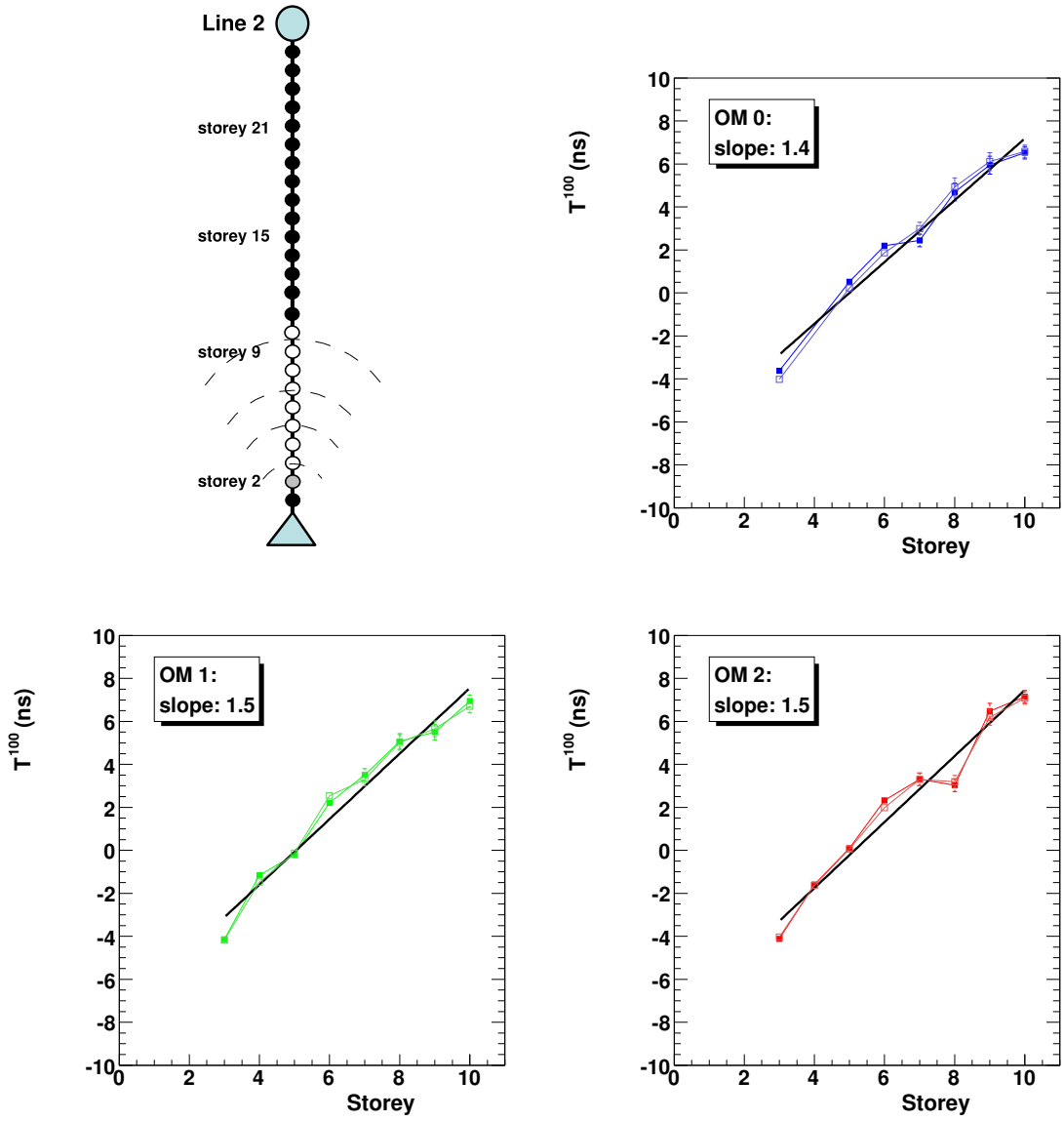

Figure 3.17: *The upper left drawing illustrates the way in which Line 2 is illuminated. The remaining three plots show the evolution of T^{100} as a function of the LOB–OM distance for OM 0 (ARS_0 and ARS_1), OM 1 (ARS_2 and ARS_3) and OM 2 (ARS_4 and ARS_5) of the different storeys of Line 2.*

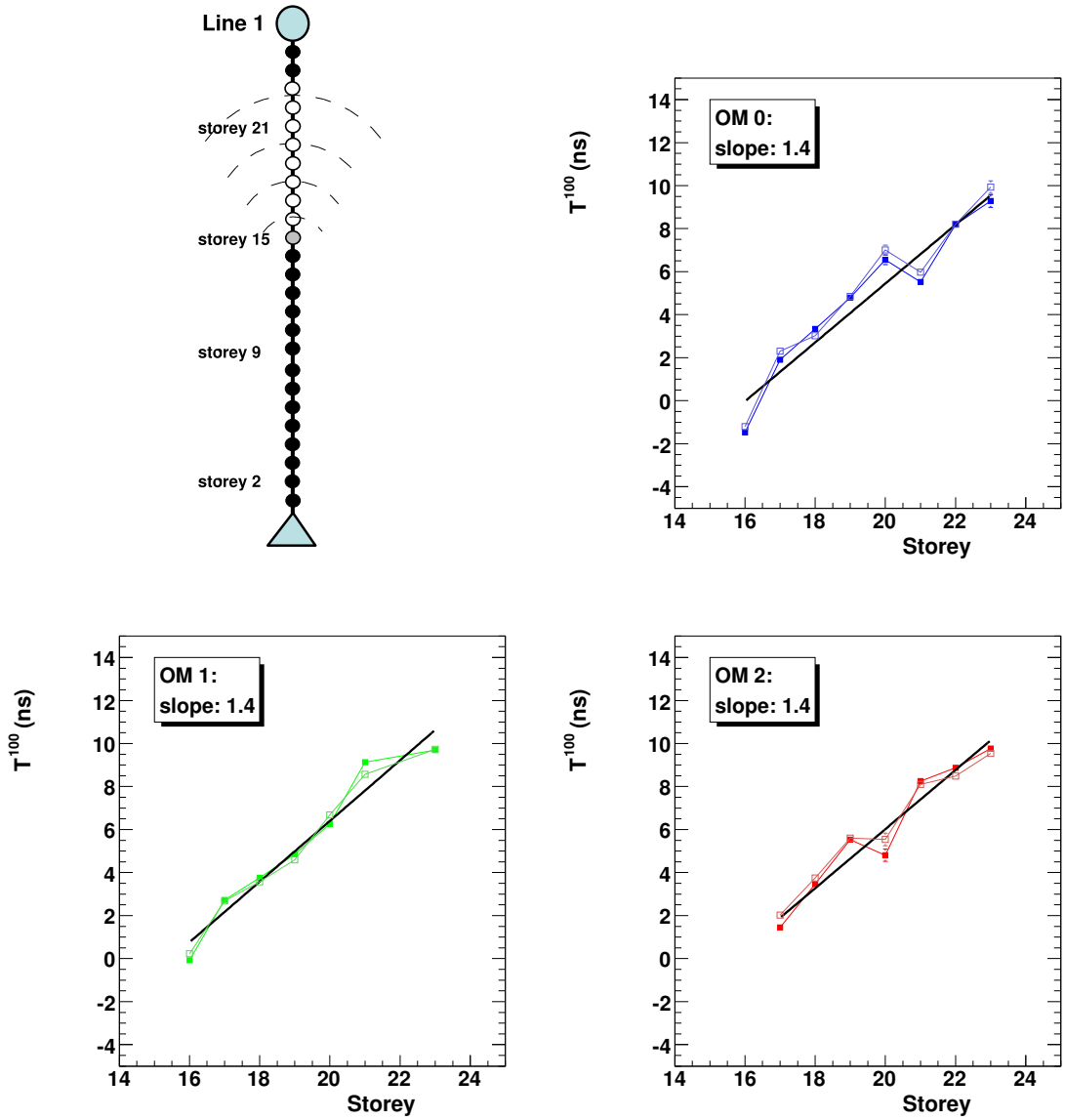

Figure 3.18: *The upper left drawing illustrates the way in which Line 1 is illuminated. The remaining three plots show the evolution of T^{100} as a function of the LOB–OM distance for OM 0 (ARS_0 and ARS_1), OM 1 (ARS_2 and ARS_3) and OM 2 (ARS_4 and ARS_5) of the different storeys of Line 1.*

linear dependence appears no matter which LED Beacon is flashed and the line where it is located. In figure 3.18 the results obtained when the LED Beacon located in storey fifteen of *Line 1* is used to illuminate part of the line as illustrated in the top-left scheme are shown. A similar linear dependence appears when representing the estimate of T^{100} versus the different storeys of the line with a delay very close to that of the previous line.

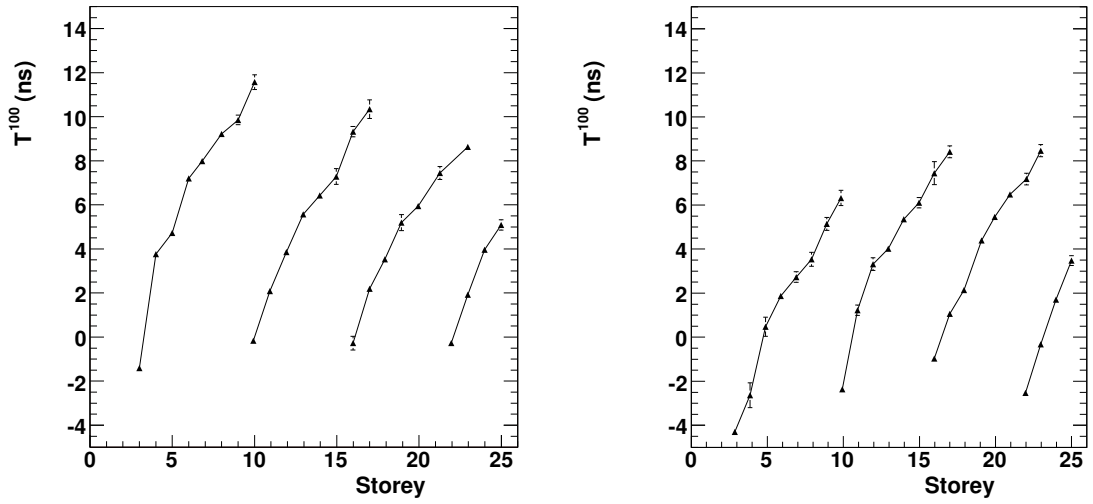

(a) *Line 1* **(b)** *Line 2*

Figure 3.19: *Averaged of the T^{100} for different storeys when the LED Beacons on the line are flashing. Each black line in the plots corresponds to a different flashing LED Beacon (different calibration run).*

These results can be summarized in figure 3.19 for *Line 1* and *Line 2*. These plots shows the averaged T^{100} parameter over the six ARSs of the OM triplet as a function of the storeys. Each of the lines on both plots illustrate the delay in the T^{100} parameter when a different LED Beacon were flashing. Thus, from left to right, the corresponding LED Beacon was the one located in storey 2, 9, 15 and 21. Note that each line begins with the storey next above the LED Beacon. As can be seen from the figure the linear delay appears all along the line. In some storeys the T^{100} can be estimated using two different beacons as can be seen at the end and beginning of two subsequent lines in the plots. The different time offsets obtained for the same OMs illuminated by different LED Beacons show that the explanation of this linear dependence must be only derived from geometrical or light intensity effects. It is evident that, apart from the distance, the delay depends as well on the deposited charged on the PMTs and not only on the distance. Figure 3.20 shows the averaged T^{100} estimate for different ARSs as a function of the mean Poisson charged collected on the PMTs for a different line (*Line 3*). Being the positioning accuracy in ANTARES detector about 50 cm, it is therefore expected that a possible explanation of this effect is related to the amount of light deposited on the photocathode of the PMTs. We will cover this in detail in the next section.

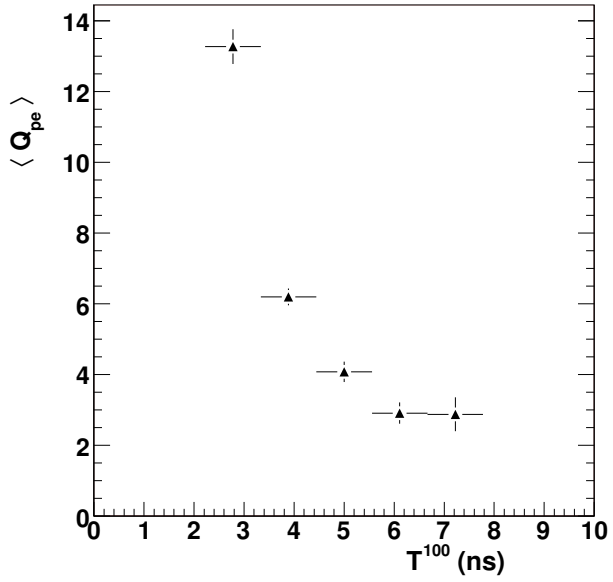

Figure 3.20: *Estimate of the T^{100} parameter computed from linear fits to the T^{100} displacement as a function of the average collected charge on the PMTs for Line 3.*

As remarked before, one of the particularities of this delay is that the value of the slope seems to be identical for all beacons and lines. In order to estimate a clear value for this slope we performed the analysis of several LED Beacon runs for which the alignment information was available, and computed the slope only for those cases in which the LED Beacon illuminates its own line. In this case, the mean value per storey is chosen, and no distinction between the two ARSs inside the OM is made. The parameter is shown this time as a function of the distance in metres. The resulting slope from the fits is represented in figure 3.21 and the parameters obtained by a Gaussian fit, are shown. The mean slope has a value of 0.11 ns/m which corresponds basically to 1.5 ns/storey assuming 14.5 m to be the distance between storeys within a line. As can be seen, the dispersion of this slope is very small, which confirms that the origin of this delay is independent of the LED Beacon. Furthermore, it seems that this delay is very stable and behaves as an empirical law. In the next sections we will inquire about the possible explanations for this delay, nonetheless, it is clear now that this delay should invoke fundamental effects not taking into account in the Monte Carlo simulation of the Optical Beacon system. The Optical Beacon simulation was performed with a software package called `Calibob` [144]. This software presumed that the time calibration with the Optical Beacon would be at the photoelectron level. On the contrary, the LED Beacons light pulses are beyond the photoelectron level and hence a dependence on the number of photons that arrive on the photocathode surface is expected.

It is also interesting to investigate the results when a part of a line is illuminated by an LED Beacon located in a different string. Figure 3.22 shows the T^{100} evolution when the difference between the arrival time measured at several OMs of *Line 1* and the LED Beacon on the second floor of *Line 2* are computed.

The following remarks can be made. Only OM 0 shows a linear displacement in the

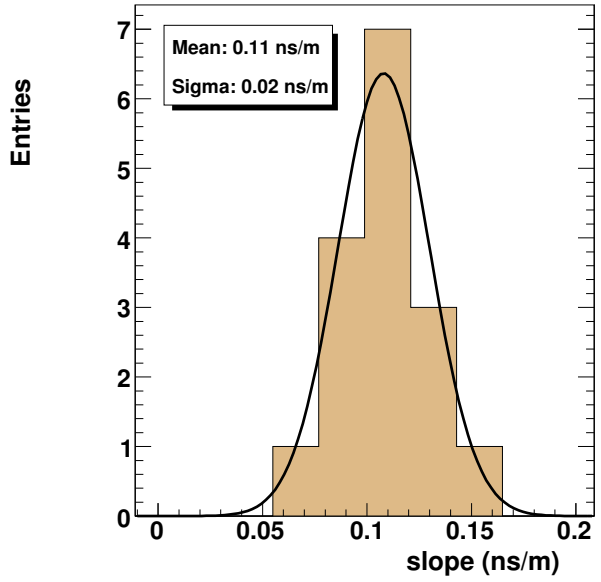

Figure 3.21: *Distribution of slopes computed from linear fits to the T^{100} displacement as a function of the LOB–OM distance.*

T^{100} estimate as in the previous case. As explained, this is likely because the OM 0 of all storeys along *Line 1* are facing toward *Line 2* and hence receives always the direct light coming from the LED Beacon in *Line 2*. On the other hand, due to the geometrical constrains of the storey, the two others OMs are facing in the opposite direction. These variations, however, become less significant as the storeys are located at higher positions with respect to the LED Beacon. In these cases the storeys receive the light from beneath and, therefore, the orientation of the OMs has a minor influence on the time difference distributions. As an example, figure 3.23 shows the time distributions for two OMs on the third storey of *Line 1* when they are illuminated by the OB in the second floor of *Line 2*. The OM 0 receives all the direct light, while the OM 2, facing in the opposite direction, records indirect scattered light. The long tail in the distribution is a consequence of light scattering. This is an important result since we are able to provide information about the geometrical orientation of a line with the Optical Beacon system, although it was not design to this end.

We can also plot the evolution of the width of the time difference distribution as a function of the distance of the storeys. As can be seen in figure 3.24 there is a correlation between the T^{100} parameter and the standard deviation. When there is a large width in the time difference distribution, the T^{100} estimate is also large.

It is important to mention that in the case of inter-line calibration, the delay effect is not as clear as in the case of a single-line calibration. As an example figure 3.25 shows the T^{100} evolution when the LED Beacon on the 15^{th} floor of *Line 2* is flashing and we computed the time residual distributions using the PMTs located on *Line 1*. As can be seen, in this case, the linear delay tendency is almost not present. It should be taken into account that the line shape reconstruction has an accuracy of 50 cm in the alignment correction, hence a possible mis-reconstruction can reproduced deviations of ~ 2.3 ns in the peak of the time residual distributions. Moreover, the accuracy of

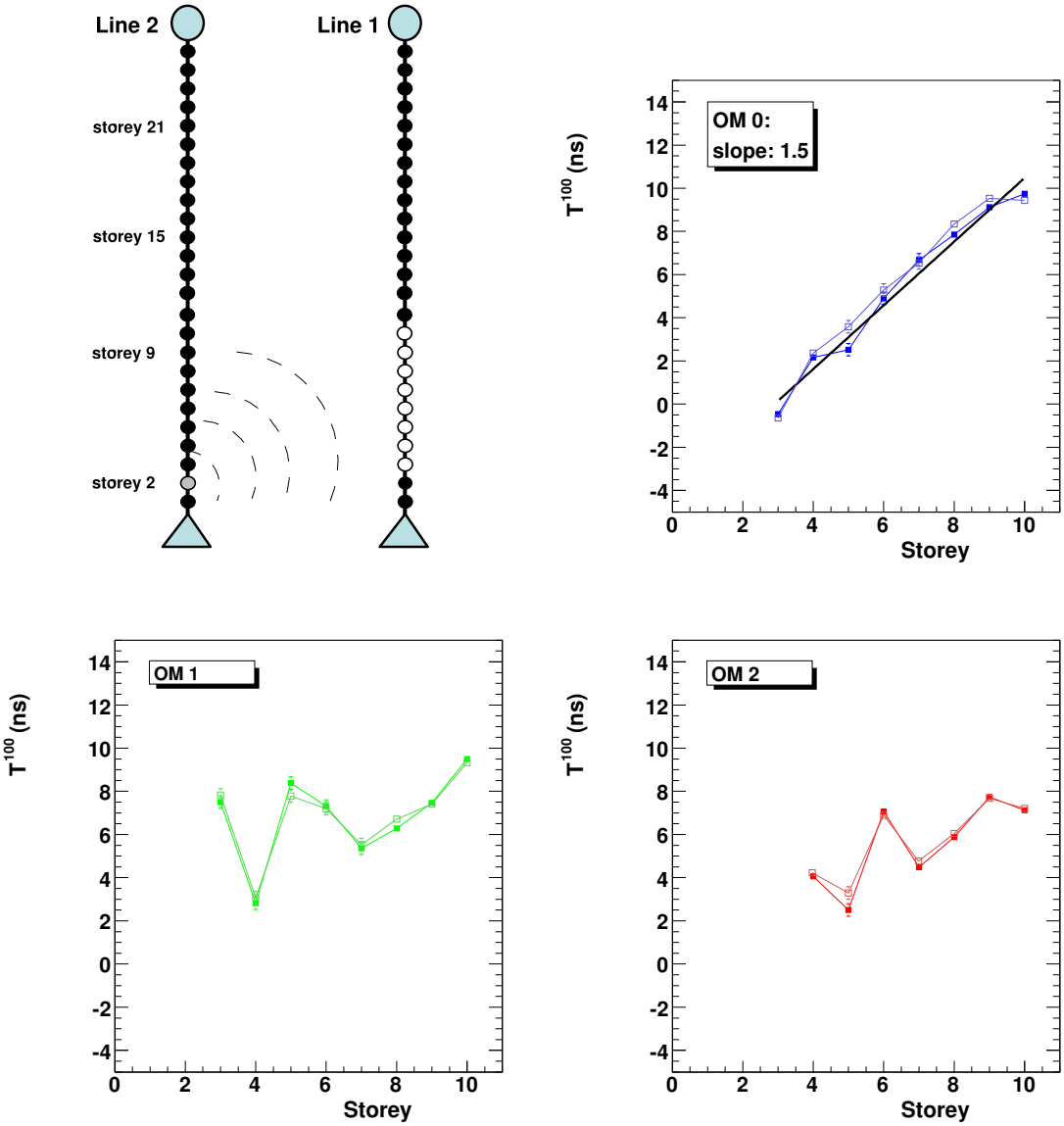

Figure 3.22: *The upper left drawing illustrates the way in which Line 1 is illuminated. The remaining three plots show the evolution of T^{100} as a function of the LOB–OM distance for OM 0 (ARS_0 and ARS_1), OM 1 (ARS_2 and ARS_3) and OM 2 (ARS_4 and ARS_5) of the different storeys of Line 1.*

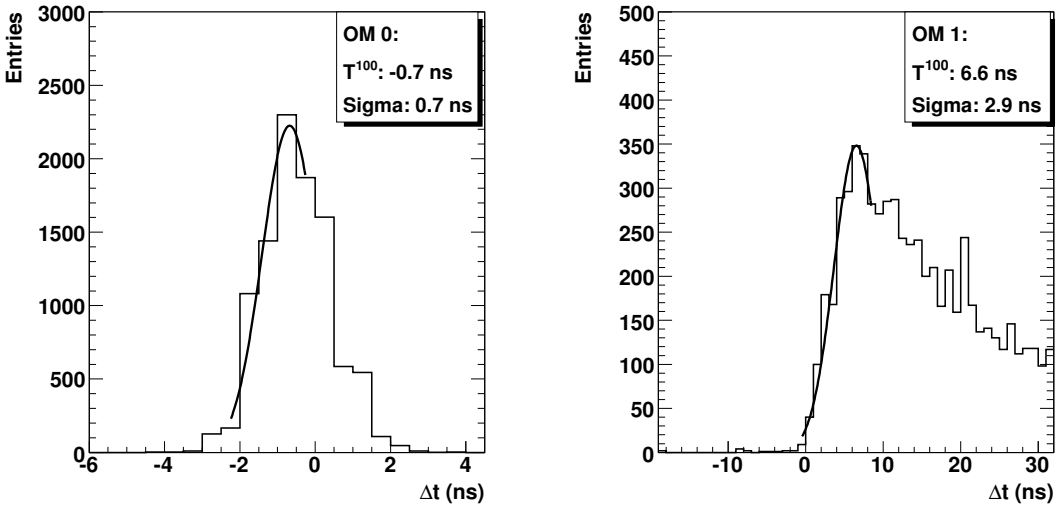

(a) OM 0 **(b)** OM 1

Figure 3.23: *Time difference distribution for two OMs of the third storey in Line 1 with respect to the LED Beacon located in Line 2 storey 2.*

the line reconstruction depends on the storey. The shape reconstruction make use of a mechanical model that described the line structure leaving only the water current velocity as a free parameter in the reconstruction. Since lines are anchored at the sea bed by the bottom end, it is not surprising that the reconstruction became less accurate at the higher storeys of the lines. This may have a negligible effect when a LED Beacon is used to illuminate its own line, since inclinations of the line have a minimal impact in the geometrical distances, but it may be important when the upper part of a line is illuminated by a LED Beacon from a different one.

Again these results can be summarized in figure 3.26. This figure shows the average delay in the T^{100} when the LED Beacons in *Line 1* illuminates *Line 2* (left) and when the LED Beacons in *Line 2* illuminates different parts of *Line 1* (right). This figure can be read as the figure 3.19 presented previously. It should be mentioned that being an average estimate of inter-line calibration, the error bars are larger compared to those in figure 3.19 since now the orientation of the OMs with respect to the source has an influence. An additional remark is that, as can be seen in figure 3.26(a), not only the delay becomes more negligible as we move to higher storeys along the line, which agrees with the fact that the line shape reconstruction is less accurate for the highest storeys, but also the value of the T^{100} in the OMs close above the beacon (initial point of the black lines in figure 3.26(a)) becomes lower at higher sections of the detector line. On the contrary, when *Line 1* receives the light from *Line 2* (figure 3.26(b)), the same tendency appears in the evolution of T^{100} as a function of the distance.

These results lead to the final conclusion that *Line 2* might be leaning toward *Line 1*. This inclination explains why the linear tend is not present. As mentioned above the accuracy in the line shape reconstruction is about 50 cm, and moreover, when water

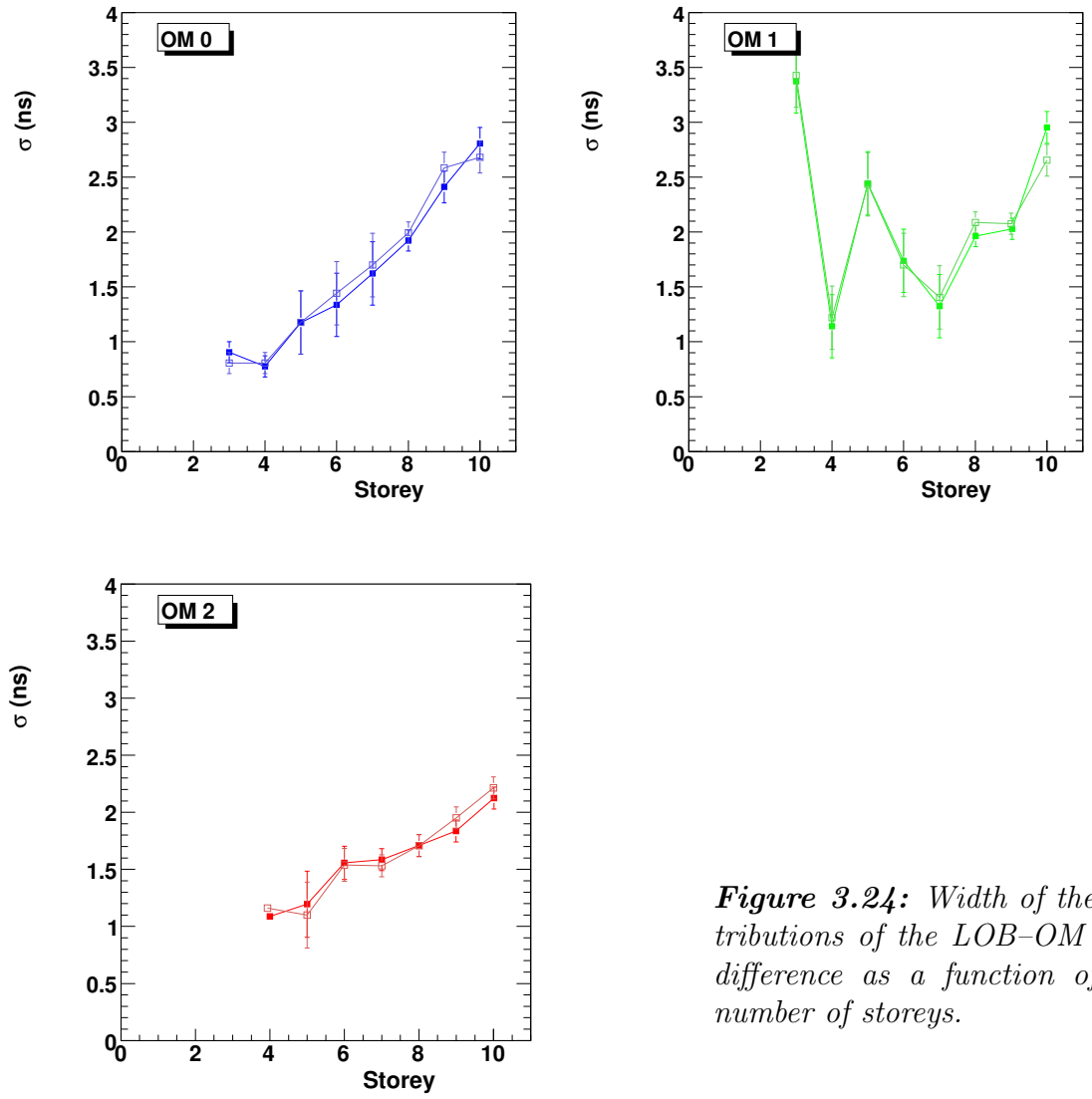

Figure 3.24: *Width of the distributions of the LOB–OM time difference as a function of the number of storeys.*

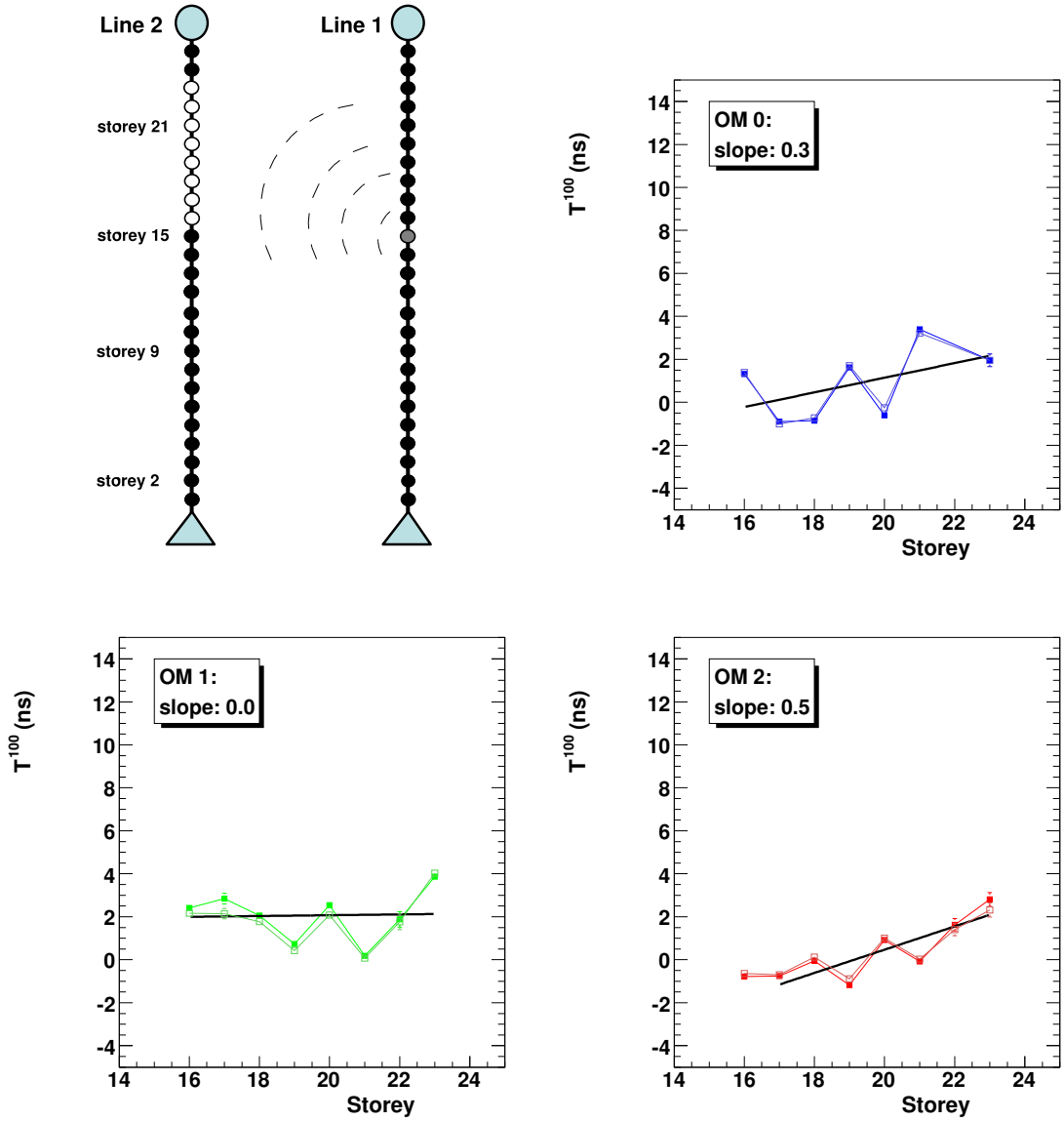

Figure 3.25: *The upper left drawing illustrates the way in which Line 2 is illuminated. The remaining three plots show the evolution of T^{100} as a function of the LOB–OM distance for OM 0 (ARS_0 and ARS_1), OM 1 (ARS_2 and ARS_3) and OM 2 (ARS_4 and ARS_5) of the different storeys of Line 2.*

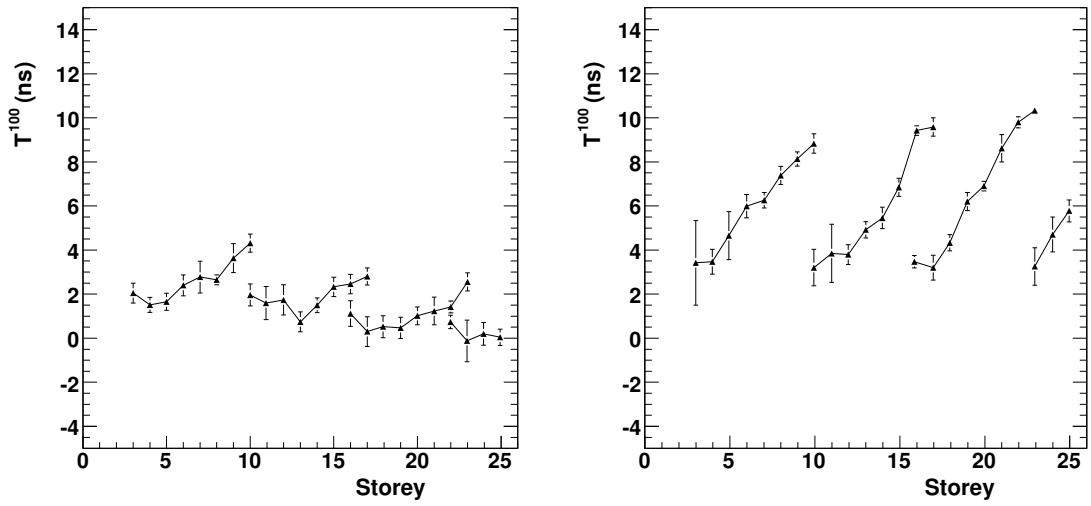

(a) *Line 1* illuminates *Line 2* **(b)** *Line 2* illuminates *Line 1*

Figure 3.26: *Averaged of the T^{100} for different storeys when the LED Beacons on the line are flashing. Each black line in the plots corresponds to a different flashing LED Beacon (different calibration run).*

currents are too low, the line shape reconstruction algorithm falls into a singularity around the vertical position, and the reconstruction is not well defined. In the future, the positioning information will be provided from both the line shape reconstruction and the acoustic positioning system which will prevent this kind of situations.

Concerning the Laser Beacon only a few storeys of the nearby strings can be illuminated. Figure 3.27 shows the evolution of the T^{100} parameter from a Laser Beacon run and the OMs of *Line 1* and *Line 2*. The low statistics makes it difficult to fit the rising edge of the time residuals distributions, and hence any conclusion derived from these results should be confirmed by the next lasers with an improved design.

As can be seen from the figures, there is also a slope in the evolution of the T^{100} estimate. It has to be mentioned that in this case, we used a different value for the speed of light in water accordingly with the wavelength of the laser light. We selected a value of 0.233 m/ns selected from figure 2.19. If this delay is confirmed with higher statistics by the future laser devices, with a adjustable intensity, it will mean that this effect is almost independent of the source of the signal (signal shape and wavelength). It should be mentioned that Laser Beacon is located at a farther distance ($\sim$ 109 m) from the OMs than the LED Beacon, hence scattering has a major impact since distances are of the order of the scattering length for the laser wavelength. As mentioned above, it is expected that this delay is related to some fundamental property derived from the light intensity of the beacons, nonetheless in the following subsections we will evaluate different issues that might explain the origin of this effect.

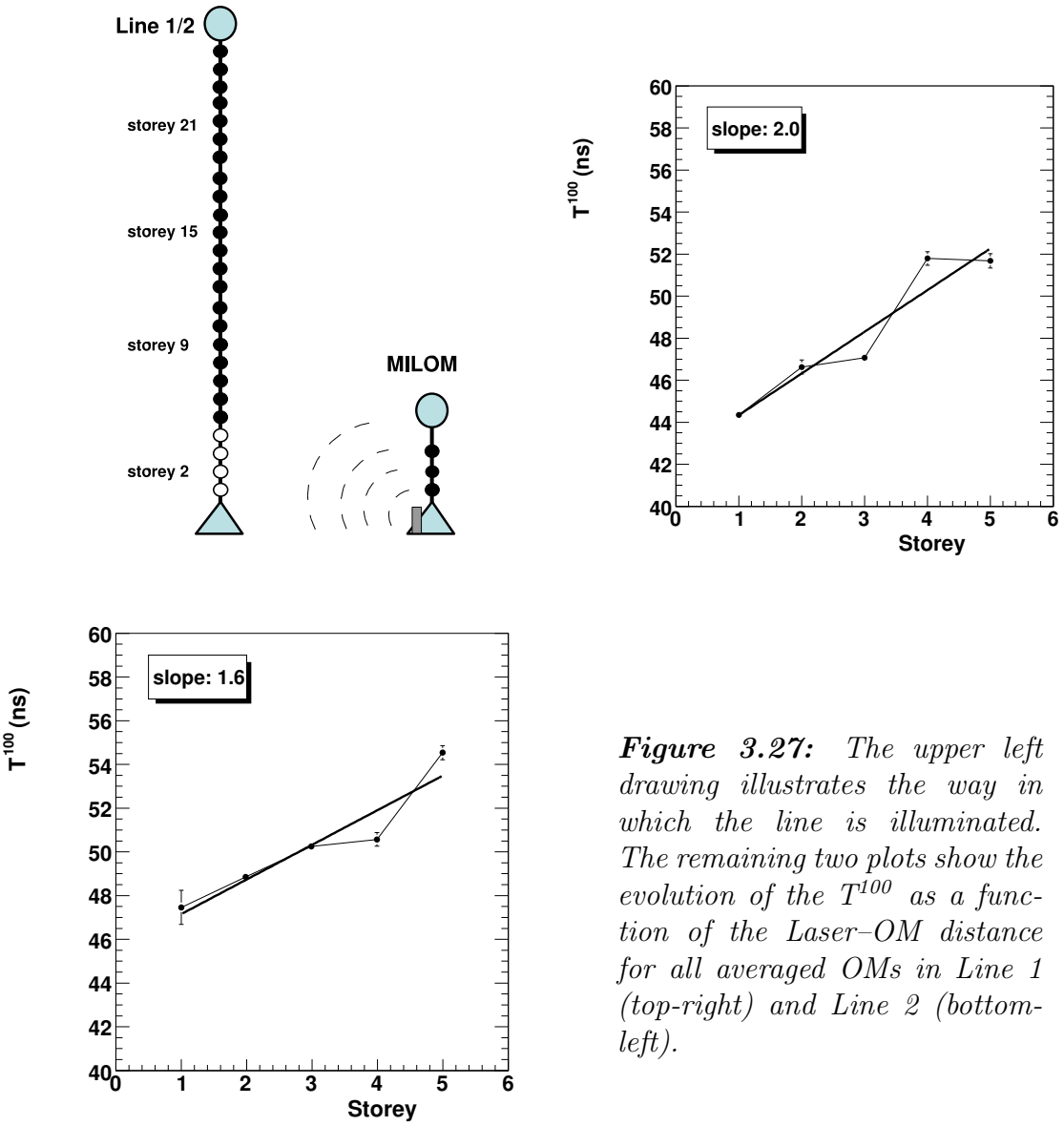

Figure 3.27: *The upper left drawing illustrates the way in which the line is illuminated. The remaining two plots show the evolution of the T^{100} as a function of the Laser–OM distance for all averaged OMs in Line 1 (top-right) and Line 2 (bottom-left).*

3.5.1 Walk effect

All signals discriminated by a fixed voltage threshold are affected by the so-called walk effect. This effect is caused by the variation in the amplitude of pulses recorded in the PMTs. The walk effect is illustrated in figure 3.28. Signals coincident in time at their maximum but with different amplitudes will cross the fixed voltage threshold L0, at different times. This effect translates into a correlation between the charge of the signal and the arrival time in the PMT and it induces a delay in the arrival time of photons as a function of the charge, however this effect should not be too large and hence is not expected to be the origin of the delay slope observed in the T^{100} estimate.

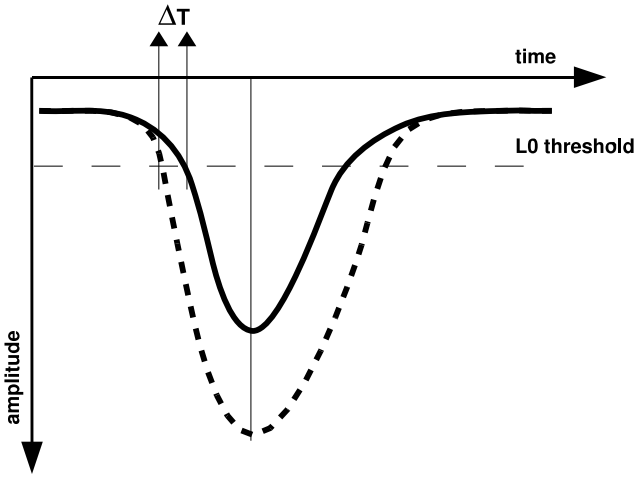

Figure 3.28: *The walk effect: two coincident signals (same time at their maximum amplitude) cross the L0 threshold at different times depending on their amplitudes.*

The walk effect has been studied during the assembly and calibration tasks in the different the dark-setups [145]. In order to take into account the walk effect in the arrival time determination of photons, two different corrections have been proposed. The first attempt was based on a parametrization of the effect using a functional formula. The solution applied in this thesis is based on [146] where physical description of the effect is considered to build the correction expression

$$\Delta T = \frac{\mathcal{F}}{\sqrt{\pi}} \left(\sqrt{-In(A_{HI}(t_{th}))} - \sqrt{-In(A_{LI}(t_{th}))} \right), \tag{3.4}$$

where $A(t)$ is the apodization function associated to the Gaussian function that describes the light pulse amplitude. The subindexes HI and LI indicate the high and low intensity respectively. The factor $\mathcal{F}$ is a scaling factor that accounts for the time difference between the highest and the lowest pulse intensity.

Before proceeding to the walk effect correction, another feature of the ARS needs to be corrected. It is the so-called cross-talk effect. The source of this effect is related to the ARS analog pipeline memory where the digitized charge and time of the signal are stored close-by. Extracted from this storage, the charge of the processed signal shows a small correlation with the digitized time [147]. Fortunately, this influence is not reciprocal, it only affects the charge of the signal and not the time, so an easy correction of the AVC is possible once the effect is measured and parametrized in the

dark-setups. This linear effect, measured during the calibration of the lines as well as during the data-taking in the sea, is described with one single parameter called XT_range. The correction equation used to transform from AVC values to corrected AVC values is

$$AVC_{corr} = AVC - XT\_range \, \frac{TVC - \frac{TVC_{max}+TVC_{min}}{2}}{TVC_{max} - TVC_{min}}. \tag{3.5}$$

Once the value of the AVC is corrected by the cross-talk effect, the conversion in photoelectrons is provided by equation 2.10. Afterwards, the hit charge can be represented as a function of the time residual as in figure 3.29 where this dependence is shown in a profile view. An example of the fit obtained using equation 3.4 is also shown.

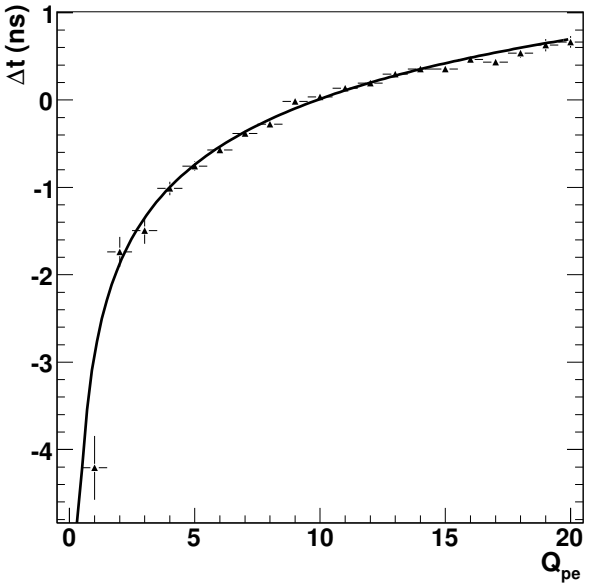

Figure 3.29: *Time delay due to the walk effect versus the charge in p.e. in a profile representation for a calibration run performed in the dark-setup for all averaged ARSs. The physical fit is also shown.*

The resulting fit of the profiles gives an $\mathcal{F}$ value of about 7 ns. The correction for the walk effect should not be larger than this value when comparing the lowest charged signal of a few photoelectrons and the signal with a charge equivalent to 20 p.e. The effect described in section 3.5 can be understood as a delay as a function of the number of photoelectrons that produce the hit. In this sense, the delay may be originated by a walk effect. However this effect is much steeper than the walk effect measured in the dark-setups, since delays larger than 6 ns are observed. We can represent the delay in the residual time, Δt, as a function of the charge once corrected by the cross-talk effect. Due to the impossibility of changing the light intensity during an on-going LED Beacon calibration run, all information recorded by the PMTs at different distances are combined to obtained such dependence (once you correct for the distance). Figure 3.30 shows the time delay as a function of the measured charge in units of photoelectrons. The solid line gives the result of the fit of equation 3.4. As can be seen, the fit is rather poor and $\mathcal{F}$ reaches values of 26 ns, which are too large for a walk effect. Hence, we can

conclude that the delays in T^{100} as a function of the distance should have a different origin.

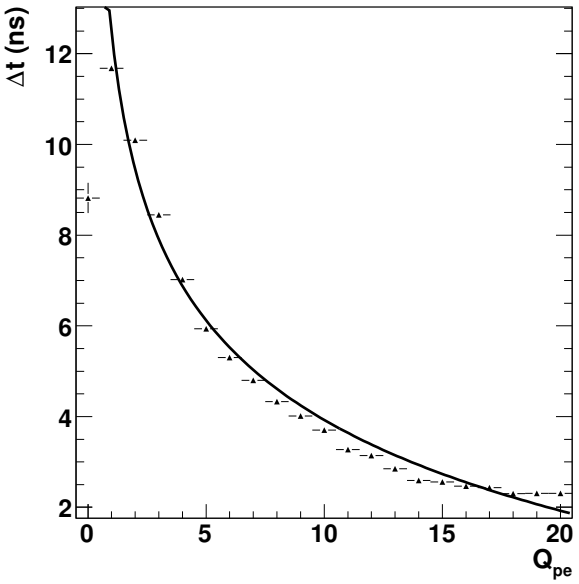

Figure 3.30: *Time delay in the sea water as a function of the charge in p.e. in a profile representation for all averaged ARSs. The physical fit is also shown.*

3.5.2 Geometrical effect

One of the most important issues concerning the delay of the T^{100} is its linear dependence as a function of distance. This linearity suggest a geometrical origin: either an incorrect value of the speed of light in water or an error in the estimate distances according to the line shape reconstruction might by the origin of the delay. This explanation differs from the one already suggested in which a dependence on the intensity of the light or photon field that reaches the PMTs was argued. In order to separate both possible explanations we have acquired data using different LED Beacon calibration runs with different intensities in order to see the influence of the intensity in the arrival times for a given storey. In figure 3.31 the T^{100} estimate for two OMs located at storey 16 (OM 3 was not working) of *Line 1* can be seen as a function of the voltage applied to the LED Beacon located in the storey beneath. Note that in this case, it is reasonable to separate the results per ARS and OM as the storey illuminated is always the same.

These plots show that the T^{100} decreases as the voltage increase. This tendency is not necessary linear, since there is no linear dependence between the voltage applied to the LED Beacon and the amount of light emitted. This excludes the discussion of a geometrical origin of the effect, since in this case the distance between the PMTs and the LED Beacon remains the same and the only difference comes from the variation of the LED Beacon intensity. Hence, the delay is presumably due to a non geometrical origin.

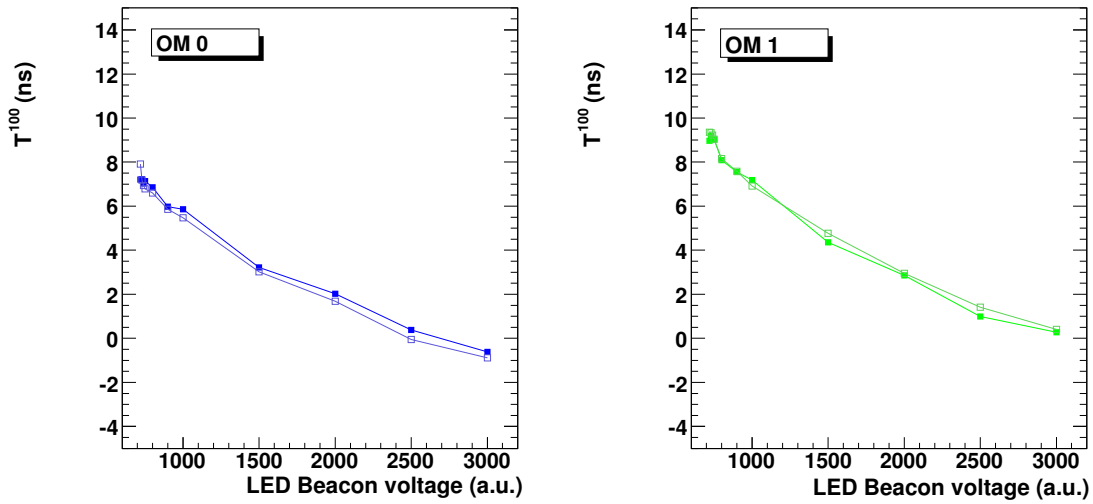

(a) OM 0 **(b)** OM 1

Figure 3.31: *Evolution of the T^{100} parameter in two OMs of storey 16 of Line 1 as a function of the voltage applied to the LED Beacon located in the storey underneath.*

3.5.3 Early photon effect

As mentioned before, the most probable explanation of the delay effect is derived from the high light regimes in which the Optical Beacon operates. As a consequence, a PMT is unable to resolve multiple photons arriving at the same time, contrary, only the arrival time of the earliest photons or pulse is recorded by the PMT. This time of arrival depends on the time distribution of the light pulse reaching the PMT which in turn depends on the time distribution of the pulse at the source and the transmission effects, that is scattering. This effect is, in fact, well described by the so-called order statistics distributions. If f is a density and F the distribution function and if $X_1, ..., X_n$ are ordered random variables with the density f then the i-th order statistic X_i is distributed according to the density

$$g_i^n(x) = \frac{n!}{(i-1)!(n-i)!} F(x)^{i-1}(1-F(x))^{n-i} f(x). \tag{3.6}$$

This expression can be simplified assuming the minimum order statistic, that is to say, selected a value of $i = 1$ in the prior equation

$$g_1^n(x) = n(1-F(x))^{n-1} f(x). \tag{3.7}$$

Figure 3.32 shows a simple Monte Carlo simulation in which this effect is illustrated. The solid line represents the initial density function from which a given number of events, n, are drawn. The histograms represent the distribution obtained when the smallest of the n numbers generated is kept for the case of a total number of 10 and 100. As can be seen, the change in the distribution is well described according to the

formula 3.7 as can be seen by the solid lines over the histograms. The expected value changes as a function of the number n of generated events and depends as well on the width of the original distribution as can be seen in figure 3.32 right.

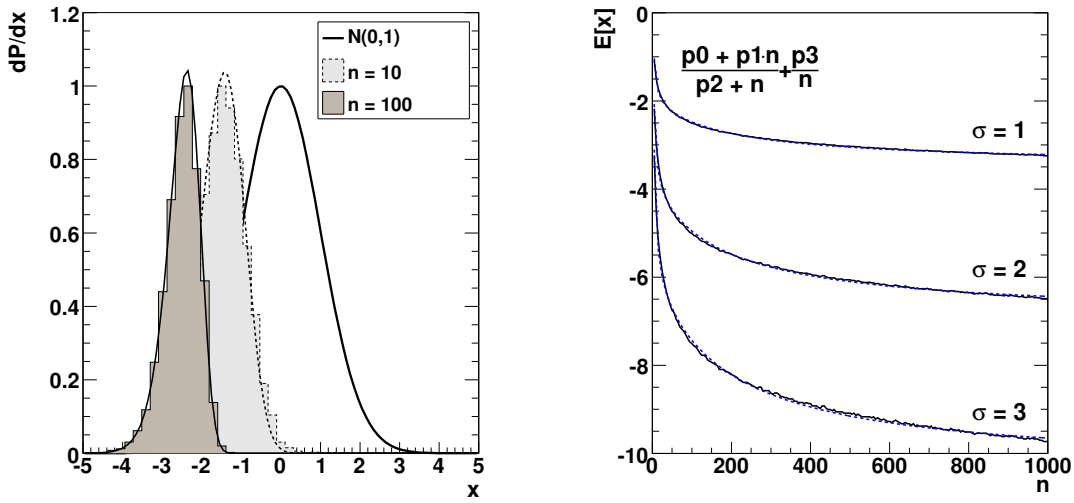

Figure 3.32: *Left: Monte Carlo that shows the effect of the order statistic in the emission of n photons. The fits given by equation 3.7 are also shown. Right: Expected value evolution as a function of n for different original width values.*

Unfortunately, there is no easy analytical expression for the evolution of the expected values in order statistics densities. In this figure the functional fit used to parametrize the expected value evolution is also illustrated. This fit is a polynomial function of the form

$$\frac{p_0 + p_1 n}{p_2 + n} + \frac{p_3}{n}, \tag{3.8}$$

where p_m $(m = 1, 4)$ are four free parameters. In our problem, we are considering the arrival time distribution of the earliest of n photons and the random variable x, is in our case, the time residual Δt. Hence the expected value is related to the T^{100} estimate. Being the number of photoelectrons n not known but a random Poisson variable, we can make the convolution of equation 3.7 with the Poisson probability, with μ the mean expected number of photoelectrons as a function of the distance

$$g_1^{\mu}(\Delta t) = \sum_{n=1}^{\infty} \frac{\mu^n e^{-\mu}}{n!} n(1 - F(\Delta t))^{n-1} f(\Delta t) = \mu e^{-\mu F(\Delta t)} f(\Delta t). \tag{3.9}$$

We can use equation 3.9 to fit the time residuals distributions[6]. In order to discard the non-relevant local minima during the fitting procedure, the range of the μ parameter is constrained using the information of the charge collected by the PMT.

[6]Note that in order that this distribution be properly normalized, a factor $1/(1 - \mu)$ should be included in the formula.

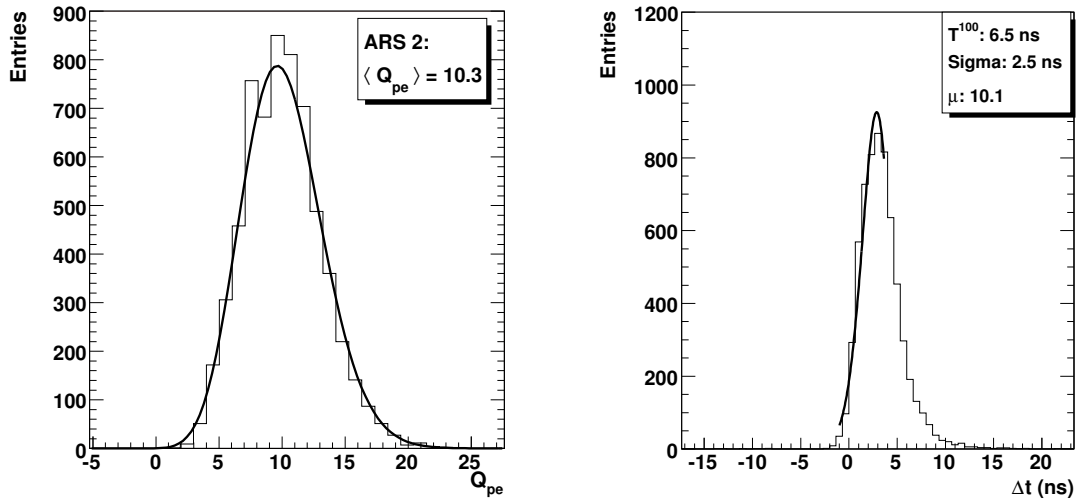

Figure 3.33: *Left: Distribution of the number of photoelectrons measured in one ARS of a PMT located 5 storeys above the LED Beacon. The Poisson fit is also shown. Right: Time residual distribution fitted according to equation 3.8. The parameter μ has been limited according to the charge distribution.*

Figure 3.33 shows the charge distribution measured for a PMT and the equivalent distribution of time residuals. The collected charge has been fitted to a Poisson distribution and the mean values is considered as the averaged charge processed by the ARS. Using the estimated value of the number of photoelectrons we fit the rising edge of the time residual distribution using equation 3.8. In our case, $f(\Delta t)$ is a Gaussian distribution and therefore $F(\Delta t)$ is the error function. As can be seen the equation fits rather well the rising edge of the distribution. However, this can only be done for not saturated OMs. We have also corrected for the rest of effects that might have an influence in the arrival time distribution of the photons, included the DNL correction. The correction for the walk effect has been done assuming a universal implementation for all ARS. With that series of corrections, we ensure that the remaining delay is only due to the early photon effect.

Figure 3.34 shows the parameter evolution T^{100} obtained when equation 3.8 is used to fit the time residual distributions. It should be remarked, that there is no correction in the arrival time distributions, we only changed the fit equation used and therefore the T^{100} is evaluated according to equation 3.8. As can be seen, in this case, there is no slope or delay as a function of the distance.

3.5.4 Discussion

The early photon effect is a problem that has its implication in the calibration using time-extended sources such as the LED Beacons but also in the transmission effects of the photons and in particular, in the light scattering. Delayed photons will suffer more scattering and therefore they are expected to arrive even later, hence when multi-

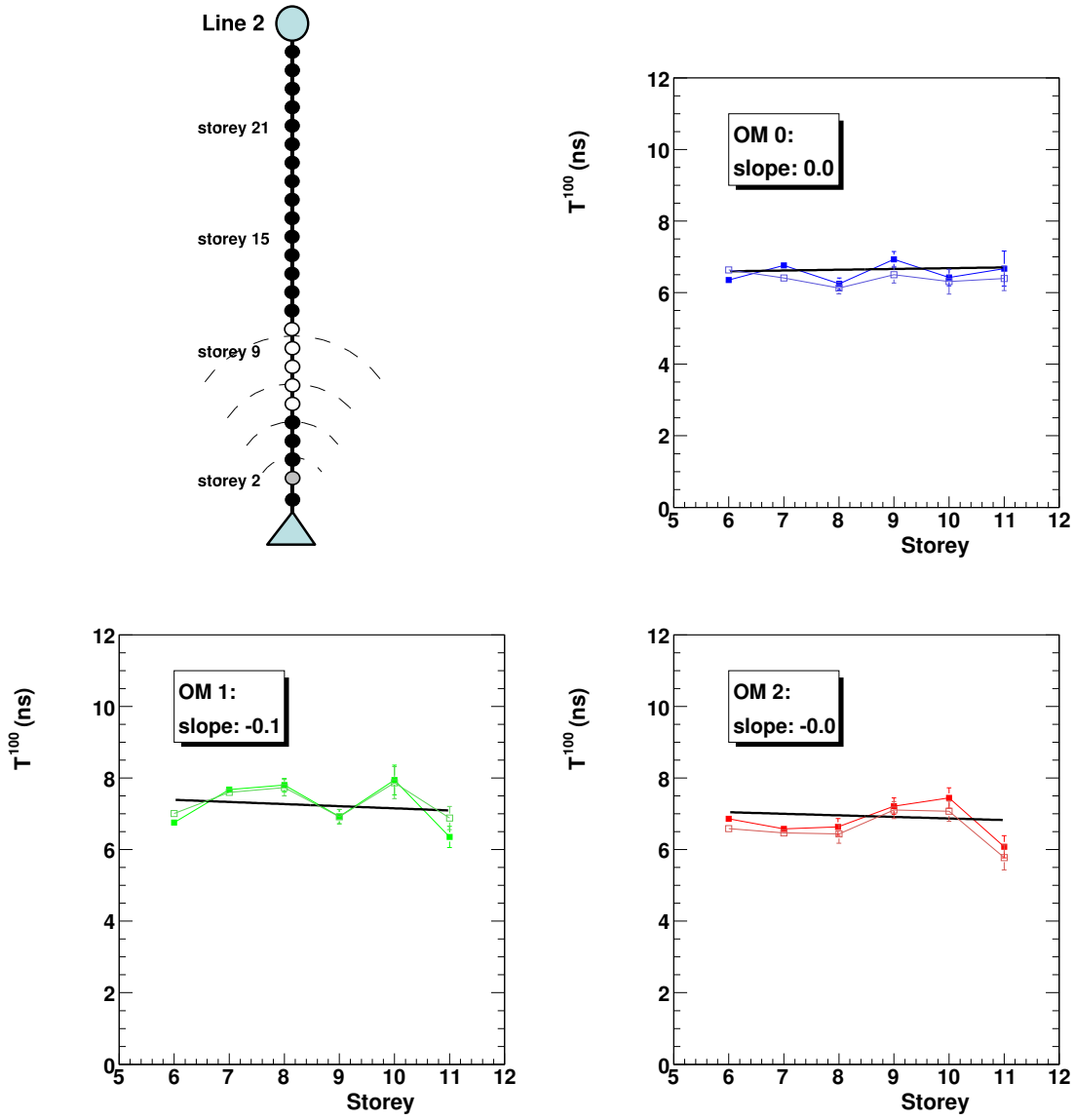

Figure 3.34: *The upper left drawing illustrates the way in which Line 2 is illuminated. The remaining three plots show the evolution of T^{100} as a function of the LB–OM distance for OM 0 (ARS_0 and ARS_1), OM 1 (ARS_2 and ARS_3) and OM 2 (ARS_4 and ARS_5) of the different storeys of Line 2.*

photon light pulses are generated it is expected a delay in the arrival time distribution as a function of the number of photons that reaches the PMTs. Unfortunately, this effect was not addressed by the Optical Beacon simulation software, in which only calibration at the photoelectron level was foreseen. The next step is the implementation of this effect in the software package and a detailed comparison between the Monte Carlo and the real data. This comparison will be useful to verify if this effect have some influence in the muon track reconstruction analysis. However, as the Cherenkov light is emitted at the photoelectron level, it is very unlikely that the order statistic applied to Cherenkov photon will have a significant effect.

3.6 Time correlations OM-OM

In this section the analysis of the time difference distributions between two signal recorded at different PMTs is treated. The reference signal selected as the readout signal for the Optical Beacon device in the previous section, is now one of the ARS hits of a given OM. In this case, the after-pulses described in the previous section, have a negative influence in the distributions as we will show. Figure 3.35 shows the time difference distribution where now $\Delta t = t_{\mathrm{ARS_{DEST}}} - t_{\mathrm{ARS_{REF}}}$, being ARS_{DEST} and ARS_{REF} the ARS_4 and ARS_0, respectively, of a given storey during a LED Beacon calibration run. As can be seen in the figure, the presence of after-pulse hits in saturated OMs yields the two symmetrical shifted peaks and a broader but more problematic bump in the central region.

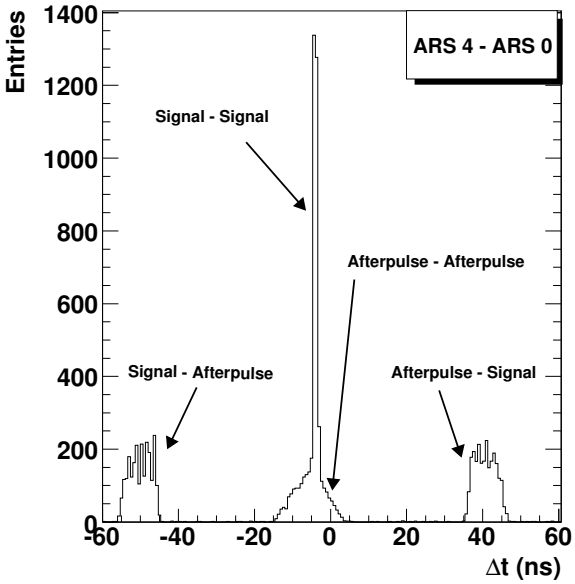

Figure 3.35: *Time differences between two OMs. The contribution of the after-pulse hits is indicated. The problematic region is the broader central peak originated when the time difference is between two equivalent after-pulse hits.*

The two symmetrical peaks can be rejected by the Optical Beacon trigger, the central region, however, can have negative effects in the fit of the time difference distributions (the central and narrow peak in figure 3.35). In order to filter this bump from

the distributions, we have done a clean up of the data considering only the saturated hits and eliminating the subsequent after-pulses. The procedure is the following: first we seek for one saturated hit in one ARS, then a time window about 40 ns is opened in the partner ARS, and if a hit is found within the window then it is rejected from the analysis. As an example, figure 3.36 shows the time difference distributions when the LED Beacon of the second storey is flashing after the clean-up procedure for the different ARSs in the third storey of *Line 2* using as the reference the ARS_0. Note that since the reference is given by the ARS_0, the difference between its time and that of the partner ARS_1 has no meaning and therefore is not presented in the plots.

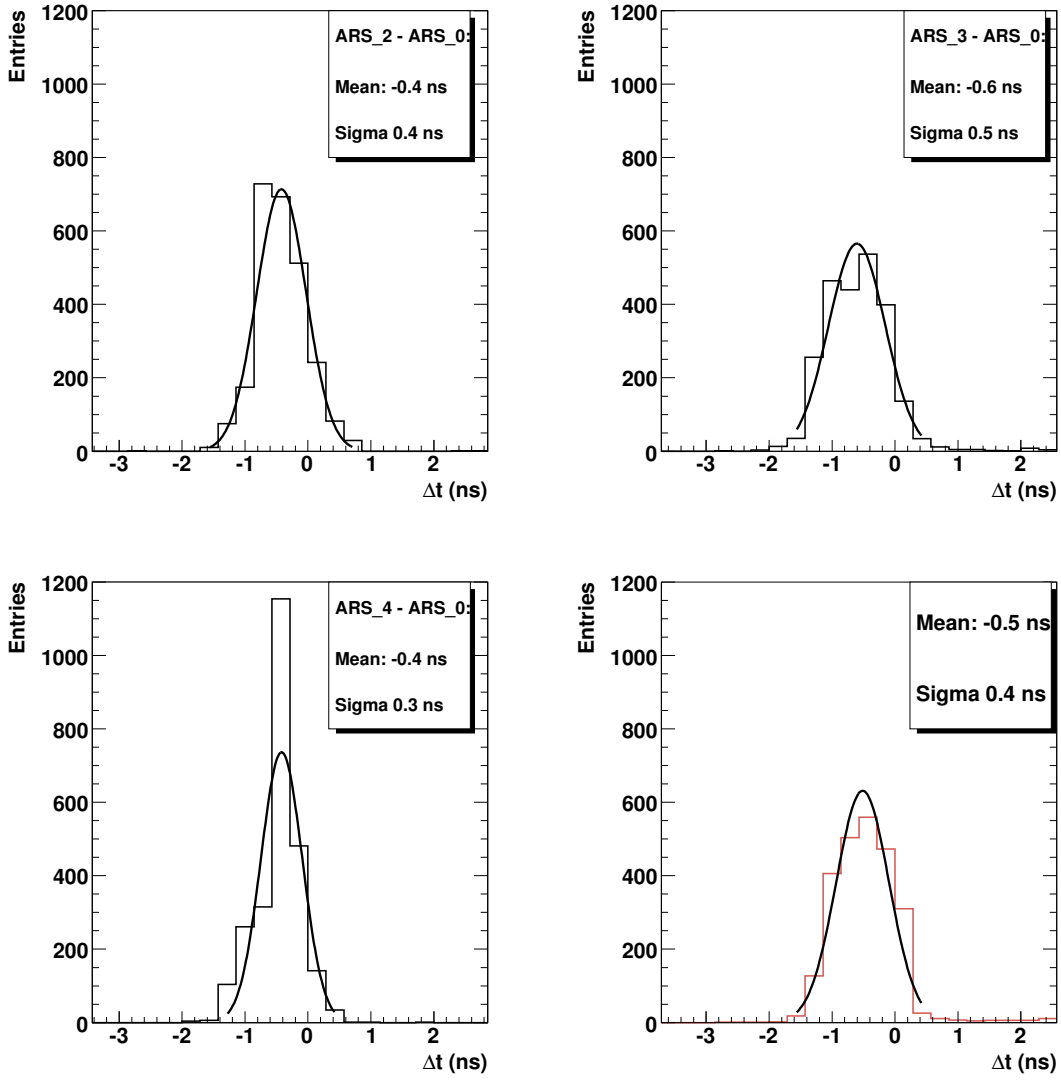

Figure 3.36: *Time differences using as a reference the ARS_0 of the third storey of Line 2 when the LED Beacon in the second storey is flashing and ARS_{DEST} are, clockwise, ARS_2, ARS_3, ARS_4 and ARS_5.*

The width of the distribution is now the contribution of the time resolution of the

two ARSs. Considering that at high light level there are negligible contributions from the TTS and optical uncertainties, the width of the distributions is then given by

$$\sigma = \sqrt{\sigma^2_{\mathrm{ARS_{DEST}}} + \sigma^2_{\mathrm{ARS_{REF}}}} = \sigma_{ARS}/\sqrt{2}. \tag{3.10}$$

As can be seen from figure 3.36, in this case the time residual distributions are Gaussian-like distribution, and therefore, symmetric. Hence, there is no need to fit only the rising edge, and the whole distribution has been fitted to a Gaussian distribution. Scattering will not distort the symmetry of the distributions, only the width, as explained before, will be affected by the photon propagation in water. Figure 3.37 shows a distribution of the fitted standard deviations for a series of nominal runs. In this distribution the result of the fit for storeys above an LED Beacon were used. The mean resolution is $\sim 0.40 \pm 0.09$ ns which is in agreement with 0.3 ns of resolution per ARS according to equation 3.10.

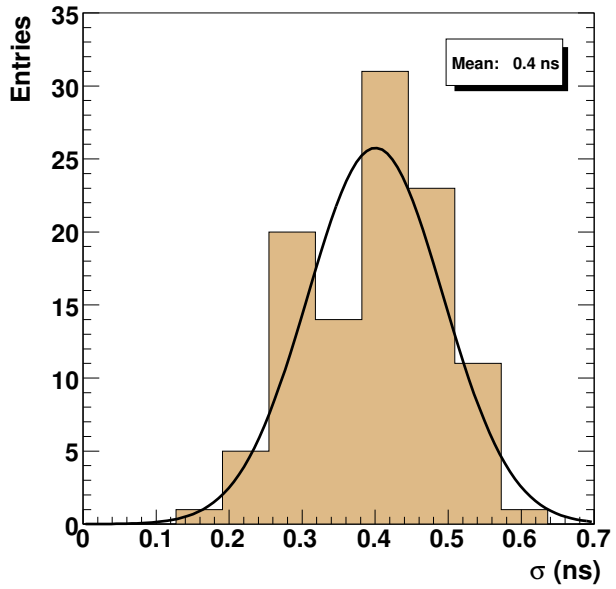

Figure 3.37: *Distribution of the standard deviations of the time difference distributions between two OM signals.*

The time difference distributions between OMs are a source of useful information since it can be used to discover and monitor any deviation of the relative calibration between OMs in the same storey. In particular, the full path addition should be null independently of the direction of the sum. Any deviation from this result should be studied in detail. Figure 3.38 shows the time difference distribution when different OMs of a given storey are used as the reference. In this case, the time differences are computed per OM and not per ARS. The two upper plots from figure 3.38 shows the time distribution when for OM 1 and OM 2, when OM 0 gives the reference time. Second line represents plots for OM 0 and OM 2 when OM 1 gives the reference time and the last two bottom plots, shows the time distributions for OM 0 and OM 1 when OM 2 gives the reference time.

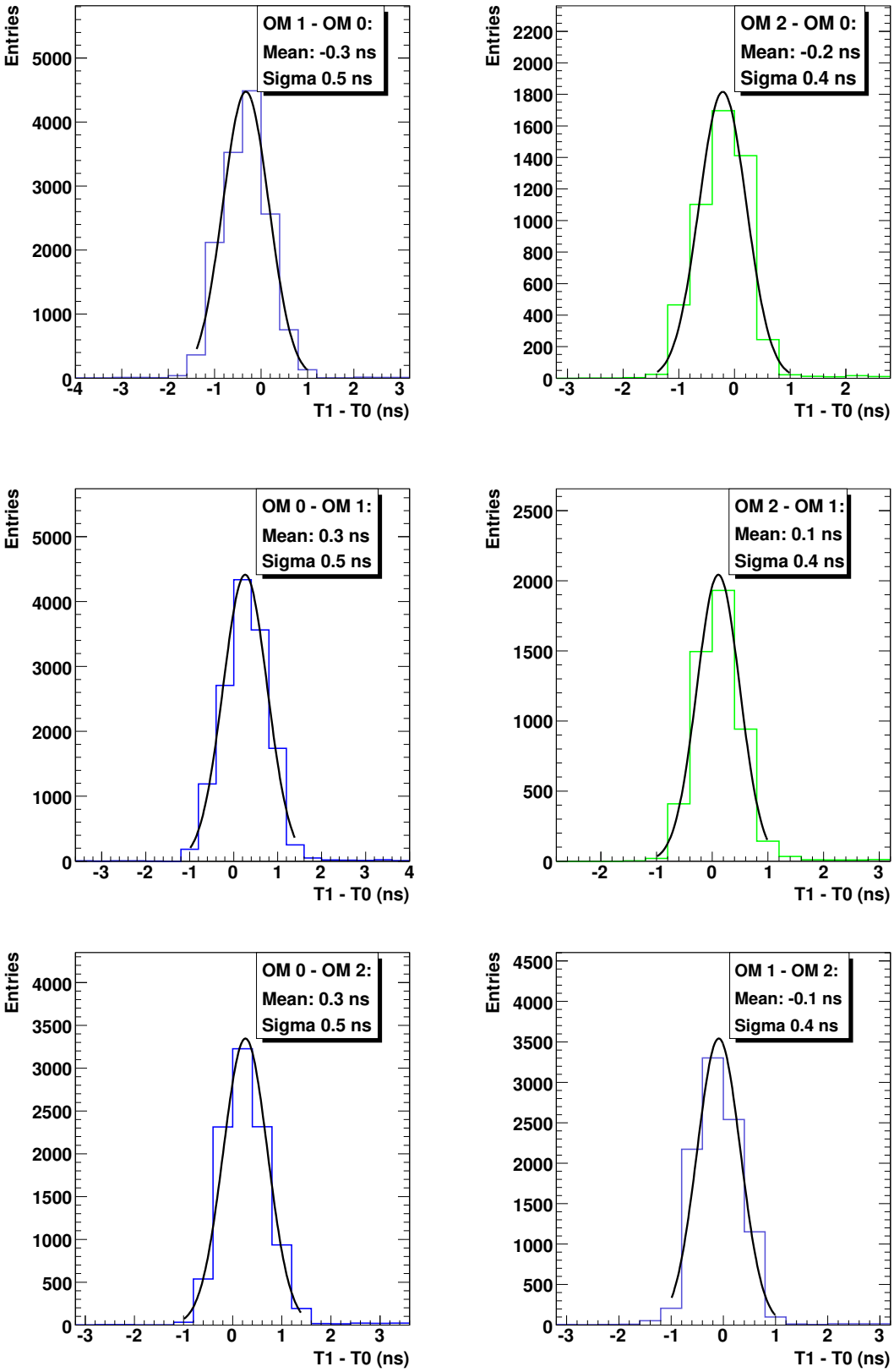

Figure 3.38: *Time differences per OM using as a reference one of the OMs of the third storey of Line 2 when the LED Beacon in the second storey. The difference is indicated in the label of the figures.*

We can verify if the distributions are correctly computed by summing all the differences using two paths, that is: $\Delta t_1 = (t_{OM\_2} - t_{OM\_1}) + (t_{OM\_1} - t_{OM\_0}) + (t_{OM\_0} - t_{OM\_2})$ and $\Delta t_2 = (t_{OM\_2} - t_{OM\_0}) + (t_{OM\_0} - t_{OM\_1}) + (t_{OM\_1} - t_{OM\_2})$. In both cases the total sum must be equals 0, in the case shown in figure 3.38 it can be seen that $\Delta t_1 = 0.1$ ns and $\Delta t_2 = 0.0$ ns. The information given by this procedure can be used for the time calibration of the OMs.

3.7 Measurement of the light attenuation length

As explained in the section 2.6 of previous chapter, the absorption and scattering phenomena are described mainly by the absorption length, λ_{abs}, and the volume scattering function, $\beta(\theta) = \widetilde{\beta}(\theta)/\lambda_{scat}$, which is defined as the radiant intensity $dI(\theta)$ from an infinitesimal volume element dV in a given direction θ, per unit of irradiance E on the volume, and per volume dV. This scattering function is described by the scattering length, λ_{scat}, and the normalized scattering angle function $\widetilde{\beta}(\theta)$. Assuming a specific shape of the scattering angle distribution we can describe the time distribution of photons at a distance R from the source by two parameters, the scattering length and the average cosine of the scattering angle distribution. In particular we can define $\lambda_{scat}^{eff}/(1 - \langle\cos\theta\rangle)$ as the effective scattering length which describes the main part of the scattering.

These two phenomena, scattering and absorption, can be described by the *effective attenuation length*. This parameter gives an indication of the fraction of photons emitted by the source that are detected at a given distance (including those that reach the PMTs although they have scattered on their way). The effective attenuation length results from the combination of the absorption length and the effective scattering length as shown in equation 2.7. For an isotropic source of photons with intensity I_0, the intensity I detected at a distance R from the source by a PMT with an active area A is given by

$$I = I_0 \frac{A}{4\pi R^2} e^{-R/\lambda_{att}^{eff}}. \tag{3.11}$$

The number of photoelectrons, Q_{pe}, measured by the PMTs in ANTARES should, therefore, have the same behaviour, since the photon field I is linearly related to the amplitude through the quantum and collection efficiencies of the PMTs. The measurement of the recorded amplitude on different PMTs located at different distances from the LED Beacon provides an estimate of the light attenuation length.

3.7.1 Analysis of the experimental data

In this analysis the following selection criteria are applied. First, only PMTs located in the same line in which the flashing LED Beacon is located are used for the analysis. This restriction minimizes the effects of the angular acceptance of the PMTs. Moreover, it prevents that any uncertainty due to the alignment information could have a big impact on the analysis. Concerning the hit selection, only those direct hits that populate the central region of the arrival time distribution have been used. We

select as the central region the hits within the time window $[\mathrm{T}^{100} - 3\sigma, T^{100} + 3\sigma]$, where T^{100} is the estimate of the mean of a Gaussian fit from 10% to 90% of the peak in the arrival time distribution (see figure 3.39 left). This selection is intended to eliminate the contamination from scattered hits. By rejecting the scattered hits the estimated parameter is in principle the effective attenuation length. If all the hits –including scattered hits– were considered, the estimated variable would be the absorption length, since only the absorbed hits would be missing from the distribution. However, due to the dead-times introduced by the front-end electronics, part of the distribution of the delayed scattered photons is rejected [133]. The exact combination of parameters that is actually being measured can only be established by means of a detailed Monte Carlo simulation, which is not available yet. Although this limits the accuracy with which we measure the exact attenuation length, the parameter thus obtained can be used to study the time variability of the optical properties and their dependence with the ocean depth. It should be emphasized, nevertheless, that with our hit selection we are including most of the forward hits, as we should, according to the definition of the attenuation length. The fraction of forward scattered photons that might be included in our hit selection only contributes with less than 30% to the total collected charge in the worst case, that is, when long tails of scattering are present.

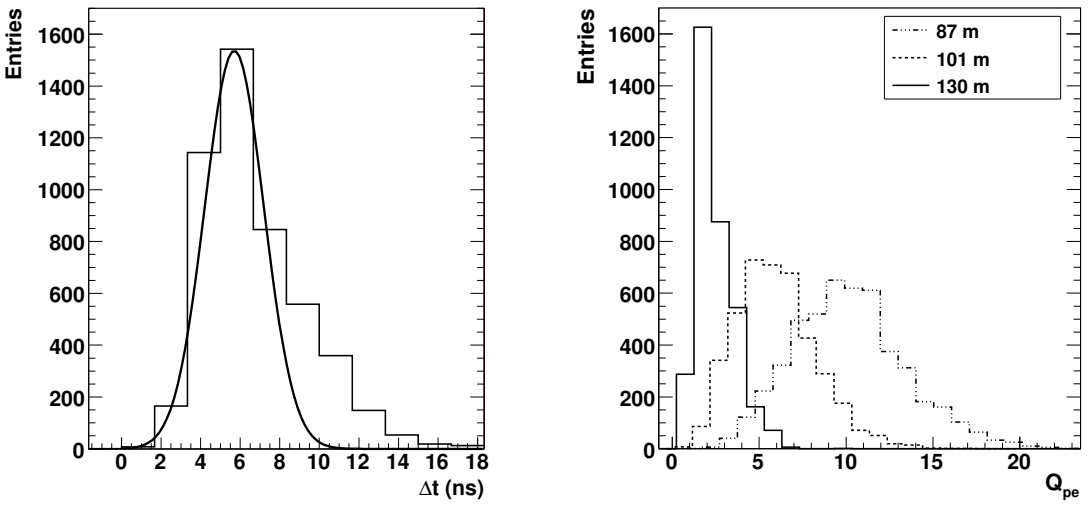

Figure 3.39: *Left: Arrival time distribution of the photons to a given ARS. The fit to the 10%-90% region of the rising edge is shown drawn to the complete region to show the area used for the amplitude distribution. Right: Different amplitude distributions for PMTs located at several distances from the LED Beacon.*

The amplitude distribution for the selected hits for PMTs located at different distances from the LED Beacon can be seen in figure 3.39 right. Different PMTs have to be used in order to measure the amplitude distribution at several distance. The different amplitude response of the PMTs may induce an error on the measurement of the attenuation length, which has to be taken into account in the estimate of the

systematic error (see section 3.7.2). In fact, we can envisage a future monitoring and correction of the changes in the amplitude response of the PMTs by means of the determination of the attenuation length.

The number of collected photoelectrons in a given channel should take into account not only the number of hits but also the amplitude of the hit. Therefore an estimate of the total collected amplitude is given by the following formula

$$\langle Q_{pe} \rangle = \sum_{i}^{N_{bins}} q(i) \times N_q(i), \tag{3.12}$$

where N_{bins} is the number of bins in the amplitude histogram, $q(i)$ is the charge of bin i and $N_q(i)$ the number of hits that populate this bin. It should be pointed out that $\langle Q_{pe} \rangle$ does not stand for an averaged amplitude but for the **total collected number of photoelectrons**.

If the LED Beacons were able to flash at the photoelectron level regime, it would be only necessary to count the number of direct hits in the time residual distributions as done in [128], since all hits will have the same amplitude. For higher amplitude levels, on the contrary, the averaged amplitude extracted from the amplitude distribution is a good estimate for the charge since the probability of having hits with no p.e. will be low according to the Poisson statistics [148]. In our case, however we should account for these events with no p.e. and therefore the total collected amplitude has to be compared.

3.7.2 Results

Figure 3.40 shows the different curves obtained when illuminating *Line 1* (left) and *Line 2* (right). The three straight lines on both show the results of the three flashing LED Beacons in each line.

The error bars have been derived by error propagation from equation 3.12 considering only a statistical origin. Other uncertainties, as the one due to the relative calibration of the different ARSs and to the PMT amplitude calibration are not included. An estimate of these errors is given below. A summary of the average values found with each LED Beacon in *Line 1* and *Line 2* using several calibration runs is presented in table 3.1. The complete list of calibrations runs used in this analysis is given in appendix B (the results of figure 3.40 are only a small fraction of those calibration runs). As can be seen from the table, no dependence on the LED Beacon position along the line, that is, on the depth, is observed.

An average value of $\boldsymbol{\lambda_{att}^{eff} = 45 \pm 1}$ **m** has been measured taking into account all the analysed calibration runs for the different LED Beacons. This value can be compared with previous measurements done in ANTARES and shown in table 3.2. These results have been done using experimental setups described in [128]. The collimation of the source used in the experimental setup of December 1997 prevents a direct comparison with the rest of values. However, a Monte Carlo simulation showed that an isotropic source would correspondingly yield $\lambda_{att}^{eff} = 44 \pm 1$ m [128], in full agreement with the result found in this study.

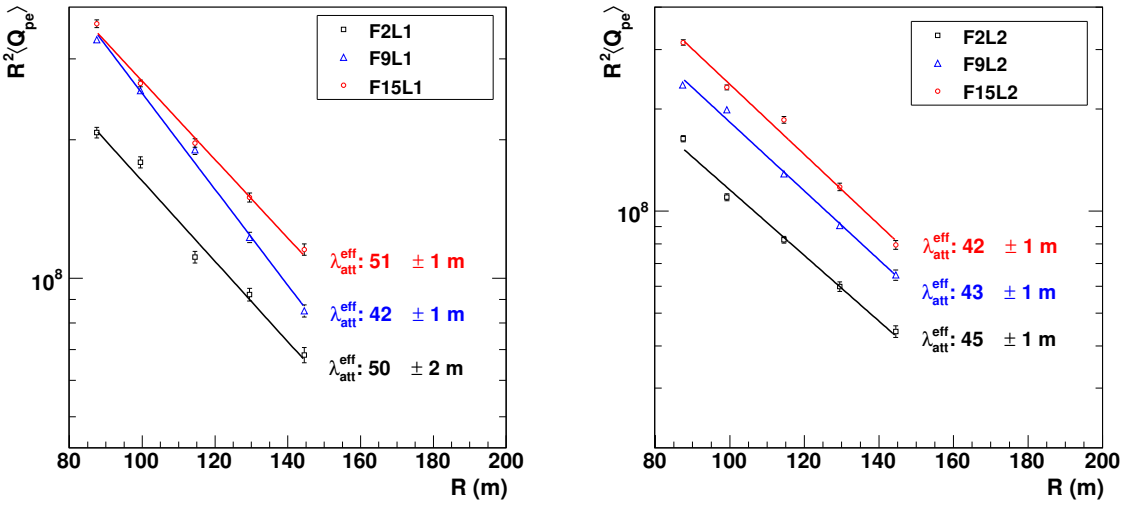

Figure 3.40: *Collected amplitude $\langle Q_{pe} \rangle$ times R^2 as a function of the distance R for three LED Beacons located along Line 1 (left) and Line 2 (right). The normalization depends on the LED Beacon intensity which is not the same for the different beacons.*

OB position	Line 1	Line 2
2^{nd} floor	51 ± 2 m	43 ± 1 m
9^{th} floor	41 ± 1 m	46 ± 1 m
15^{th} floor	47 ± 1 m	45 ± 1 m

Table 3.1: *Summary of the averaged effective attenuation lengths estimated from the analysed runs in our study (see appendix B).*

Period	λ_{att}^{eff} (m)
December 1997	41 ± 1 (collimated)
July 1998	60.6 ± 0.4
March 1999	51.9 ± 0.7
June 2000	46.4 ± 1.9

Table 3.2: *Summary of the measurements of attenuation length at 470 nm (statistical error only) using dedicated autonomous lines [128].*

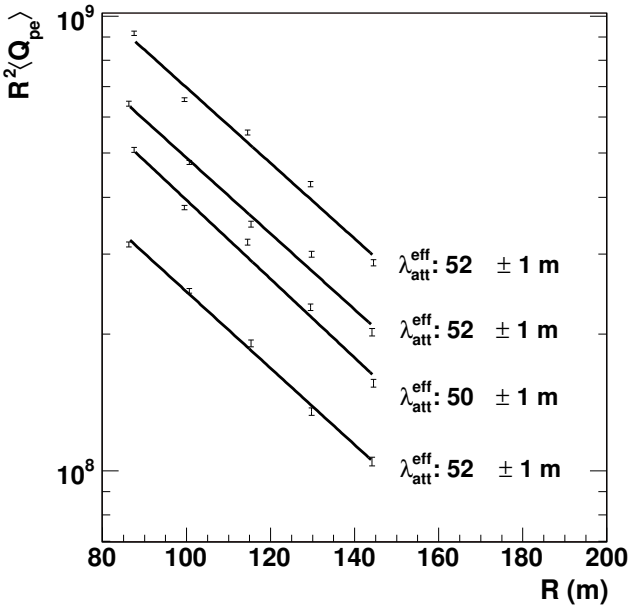

Figure 3.41: *Collected amplitude $\langle Q_{pe}\rangle$ times R^2 as a function of the distance R for the LED Beacon located in the 15^{th} floor of Line 1. Each line corresponds to a different LED Beacon intensity going from the highest intensity (top line) to the lowest (bottom line). The values of λ_{att}^{eff} obtained from the linear fit to the effective attenuation length are also shown.*

Several sources of systematic uncertainties may affect the results of this analysis. As already mentioned, the relative calibration of the ARSs for different PMTs and their efficiency, a possible slight anisotropy of the source, the use of different LED Beacons and therefore the reproducibility of identical conditions and the angular detection efficiency of the Optical Modules can influence the results. An accurate estimate of these systematic errors can only be carried out with the help of a Monte Carlo simulation, still under development. Nonetheless, a simple simulation has been used to estimate roughly the systematic error in our measurement. Assuming that the measurement of the distance based on the alignment information carries a relative error of at most 30 cm over 15 m and that the relative error on the charge measurement is $dQ/Q \leq 30\%$, an overall systematic error of 4 m is obtained for the measured value of the attenuation length, that is

$$\lambda_{att}^{eff} = 45 \pm 1(\text{stat.}) \pm 4(\text{syst.})\text{m}. \tag{3.13}$$

We have also studied the attenuation length using runs at different LED Beacon intensities. As explained before, during a nominal calibration run the LED Beacon is flashed at high intensity. In this case, we tried different intensities for the light emission of the LED Beacon and the same analysis was done leading to the results shown in figure 3.41.

Each line on the figure indicates different LED Beacon intensities which explains the different normalization. Bottom line correspond to the lowest LED Beacon intensity, upper line to the highest.

As expected, there is no indication that the estimated effective attenuation length depends on the LED Beacon intensity. The average value in this case is $\lambda_{att}^{eff} = 51 \pm 2$ m which differs by approximately 10% from the previous estimated value for the same LED Beacon three months earlier at full intensity. In order to study a possible seasonal variation, we computed the effective attenuation length using the LED Beacon located in the 15^{th} storey of *Line 1* in different periods of time. Figure 3.42 shows the evolution in time of the attenuation length. The lack of data during January 2007 was due to several detector maintenance and deploying operations.

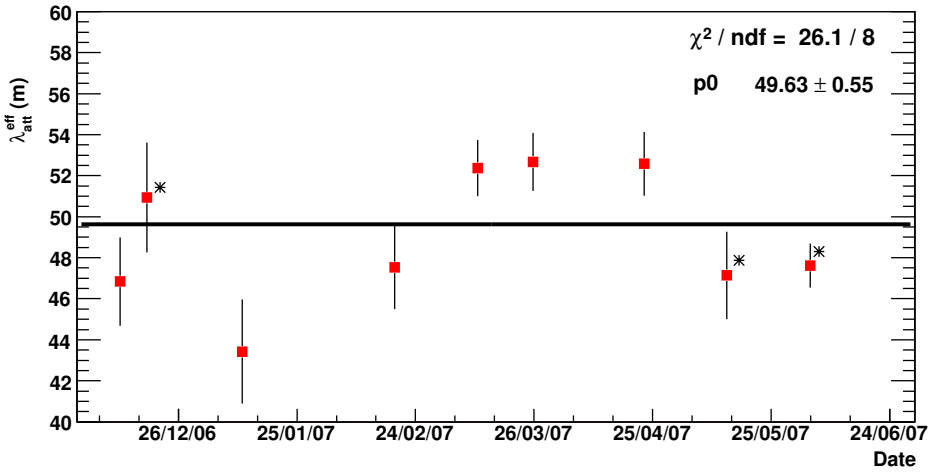

Figure 3.42: *Time evolution of the effective attenuation length estimate.*

Points labelled with (*) do not use the line shape reconstruction. No clear indication of a seasonal variation is observed. For instance, the shift during the March-April periods in the estimated effective attenuation length is of the order of 5% (around 2 standard deviations per point).

3.8 Conclusions

In this chapter we shown the results the first analysis done with the Optical Beacon system in under water conditions. This system has guaranteed the sub-nanosecond level in the time resolution, which is one the main results of the analysis. As a reminder, this time resolution was required in order to achieve the desired angular resolution with the ANTARES telescope. As we have shown, a $\sigma < 0.5$ ns is obtained at high light level when other uncertainties coming from the light propagation in water and the PMT response are negligible. During the analysis we discovered that different effects are involved in the Optical Beacon system, some related to the nature of the pulse shape,

which may induce different arrival times due to the light pulse width, and the number of arrival photons. This effect has been first addressed with the Optical Beacon system, and its influence in the muon track reconstruction is expected to be small due to the combination of the well-defined time emission of the Cherenkov photons and the low number of photoelectrons per PMT expected from the Cherenkov radiation[7]. We have also made the first measurement of one of the optical water properties with the Optical Beacon system. In particular, we have estimated the attenuation length in water. The average estimated value is in agreement with what was measured in the ANTARES site during the R&D phase.

- All the LED Beacons in *Line 1*, *Line 2* and the MILOM –with the exception of one LED Beacon in the MILOM that was damaged due to a water leakage– have been validated. The light emitted by the different LED Beacons reaches the nearby strings and its own line in a long range of storeys.

- We have developed a specific trigger, `triggerOB`, to filter and process the Optical Beacon events. This trigger has been successfully validated in underwater conditions.

- The readout signal of the Optical Beacons and the signals of the OMs that received the light have been analysed and the proper treatment of the data has been accomplished taking into account the DNL and considering the rising edge of the signal which gives the accurate measurement used in the time calibration.

- In the case of the closest OMs to the Optical Beacons the effects of the transit time spread, light propagation and the uncertainties in the OM positions are all negligible. In addition, the rising-edge of the read-out signal is very small and therefore the width of the time residual distributions is a direct measurement of the time resolution of the electronics in ANTARES. This accuracy has been verified to be less than **0.4 ns**, which is in agreement with the ANTARES specifications.

- For those OMs located along the same line in which the LED Beacon is flashing, it has been checked that there is a delay in the estimate of arrival time of about $\mathbf{0.11 \pm 0.02\ ns/m}$. This delay can be explained considering multi-photoelectron light pulses by the order statistic. Nonetheless, the resulting slopes are very stable and therefore it is possible to use them as an empirical rule to perform the time calibration of the OMs using, at the same time, the time coincidences given by the inter-storey OM calibration. When illuminating a different line from where the LED Beacon is located, we are able to give information about the orientation of the lines, moreover it will be possible to provide information about the inclination of the lines in those cases where the positioning system cannot resolve the line shape.

[7]This is the case for underwater experiments. In ice the time width is enlarged by scattering and the effect is not negligible [149].

- The inter-storey OM calibration reported a value of the electronics time accuracy which is in agreement with the previous measurement.
- The first study of the optical water properties using the Optical Beacon system has been performed. The information provided by the OMs along the same line of the flashing LED Beacon has been used in order to ensure the stability of the measurements. An average value of $\mathbf{45 \pm 1 \pm 4\ m}$ has been measured taking into account different LED Beacons located on *Line 1* and *Line 2*. No evidence of a water depth dependence or seasonal variations has been found.

Chapter 4

Search for point-like sources

– Now, we all know telescopes allow us to see distant objects. But what if we want to smell distant objects? Well now we can! Thanks to my new invention... the Smell-O-scope.
Professor Farnsworth, Futurama.

The main goal of a neutrino telescope is to look for astrophysical neutrinos and, in the absence of a signal, to constrain the predicted fluxes from different models of neutrino emission on several candidate sources. Although it is assumed that GRBs, flares and other transient sources may produce neutrino emission, in the point-like analysis that we present here, the whole sky is surveyed without any assumption about time correlation with observations of any other physical phenomena. In other words, the search for point-like sources is the seek of steady neutrino sources in the sky visible by ANTARES. Therefore, in this case, the time information is not used to enhance the signal to noise discrimination but only to convert the track reconstruction local parameters to celestial coordinates. In the following sections we will introduce a new method for the search for point-like sources based on the Expectation-Maximization (EM) algorithm, which is a widely used likelihood maximization algorithm for clustering analysis. The application to neutrino astrophysics will be described together with the difficulties which are faced when applied to low statistics, as it is our case.

4.1 Introduction

As already mentioned, since no further information is used apart from the neutrino track direction, an accurate angular resolution is crucial in order to confirm or reject the most optimistic models for point-like emission of neutrinos. As there is no time constraint in the data, atmospheric neutrinos turn out to be the most important source of physical background for this analysis since they are detected uniformly in time during the whole duty cycle of the detector. Superimposed to these background events, a small number of signal events could be present. These signal events would appear spread around a given location in the sky where a neutrino emitter is present depending on the detector pointing accuracy. Point source techniques try to identify and separate events coming from real sources from background events by identifying these signal events accumulations. In this sense, contrary to the diffuse flux analysis, the atmospheric

neutrino background does not represent a major problem since the probability of the background to show an excess of events in a given direction in the sky is small. Different searching algorithms have been developed within the ANTARES collaboration. They can be separated between binned and unbinned methods:

- **Binned methods**. They constitute a robust approach to the problem. In these methods the visible sky is divided following a given grid [150]. An excess of events in any bin of the grid is considered as a possible evidence of a point-like source along this direction. The significance of this bin is estimated by comparison to the distribution of the atmospheric background. These techniques require the selection of the initial size or shape of the bins which, in some cases, is based on Monte Carlo. A common difficulty of these techniques are the boundary effects inherent to the grid. In order to avoid this effect a shift of the whole grid is usually performed [151].

- **Unbinned methods**. They are more sensitive and powerful than the binned approach [152]. These methods rely on the maximization of the likelihood derived from a probability density function assigned to the signal events. This function can be drawn from the point spread function parametrized via Monte Carlo [153] or using a simple Gaussian-shape density [154]. The maximization procedure is also different depending on the algorithm.

The sensitivity of the search depends on the method applied. The EM technique that will be introduced in the following sections is an unbinned method that takes advantage of the clustering detection analysis. Being an unbinned method, it is a very powerful tool for point-like source searches and, in addition, is free from the Monte Carlo dependence that other methods used in ANTARES exhibit since no detector performance information is used. When comparing the EM algorithm to other methods, some advantages as well as some drawbacks can be mentioned:

- This method does not suffer strongly from the trial factor problem inherent to the binned techniques coming from the high number of bins in the grid. This makes the unbinned methods and specially the EM-based method, very sensitive in comparison to the binned approach.

- Unlike any other unbinned method devised in the ANTARES collaboration, this method, as applied in this thesis, requires only the data themselves and no further information about the detector performance is used in the analysis. Since it does not rely on the detector performance, it constitutes a robust approach to the point-like source search.

- Being an unbinned technique, the information is used in a continuous way, so the difficulty derived from the boundary nature of binned methods is not present. In addition, it is possible to incorporate additional information besides the event direction, such as the energy information of the event, which is relatively difficult for binned techniques.

- Due to its basic assumptions concerning the probability density functions and the fundamental concepts that underlie it, the EM algorithm can be easily extended to the search of other astroparticle sources and not only to neutrino astronomy [155].

- The EM algorithm is a well-known algorithm used in clustering analysis. The likelihood maximization procedure is achieved analytically. Hence, a method based on this algorithm constitutes a reliable technique for our particular aim of finding neutrino sources.

On the other hand, contrary to the binned algorithm, there is no analytical probability distribution associated to our problem. This means that there is no knowledge about the test distribution which is specially important when trying to obtain results at the 5σ confidence level and therefore, the tail behaviour of the likelihood distribution has to be extrapolated in order to overcome this difficulty.

Much progress has been made in the ANTARES collaboration concerning the energy reconstruction, nevertheless the stochastic nature of the muon energy loss prevents the energy reconstructed event by event to be a source of reliable information. This is specially true during the first years of operation of the detector in which a complete knowledge of the detector performance is not possible. Therefore the muon energy estimate is excluded for the analysis presented here and only the arrival angular information of the event provided by the muon track reconstruction strategy is used.

4.2 Monte Carlo data sample

The EM-based searching method uses a set of reconstructed events as input for the searching process. ANTARES is currently in the deployment stage, and therefore, no real data are still available. For that reason, in this work we have built a set of Monte Carlo data samples to be used as real data. However, it is important to point out that Monte Carlo samples will be used uniquely as data input and no further information or detector performance will be extracted from the simulation, apart from the background distribution as it will be explained later. In fact, the background distribution can also be obtained scrambling the real data.

The track direction is provided by the track reconstruction algorithm in local coordinates. In order to build the sample used for the clustering analysis, they are translated into equatorial coordinates, that is right ascension and declination (α, δ). Figure 4.1 shows an example of data sample corresponding to 1 year of data-taking in ANTARES. The natural time scale of cosmic neutrinos expected fluxes is in terms of years, one year data samples are commonly used although more than a year analysis will be also presented (see chapter 5).

A good estimate of the background is mandatory to produce realistic Monte Carlo data samples since most of the events are due to background and only a small fraction of signal events are added to the sample. The main contribution to the background comes from atmospheric neutrinos. As already mentioned, these neutrinos are produced in the upper layers of the Earth's atmosphere in the decays of particles produced by high

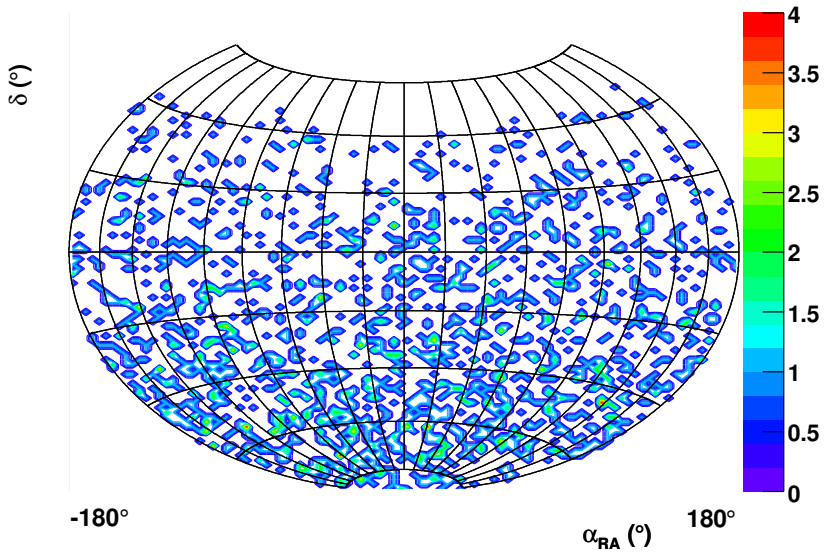

Figure 4.1: *Example of a one year data sample in equatorial coordinates.*

energy CR interactions and, therefore, these atmospheric neutrinos (and anti-neutrinos) are indistinguishable from cosmic neutrinos.

4.2.1 Background simulation

In order to build the data samples, we need to simulate a considerable number of neutrino events. Using the Monte Carlo production tools described in appendix A, we simulated a total of 95 neutrino files and 95 anti-neutrino files. The whole simulation was done by the Valencia and Bari groups of ANTARES [156]. Each file corresponds to 10^7 neutrinos generated from 10 GeV to 10^7 GeV (fluxes above 10^7 GeV are too small to be considered by a neutrino telescope like ANTARES). Table 4.1 shows a summary of the main characteristics of the Monte Carlo production.

Event Generator	Detector	Propagation	Reconstruction
GENHEN v5r6 $10^{10}\ \nu + 10^{10}\ \overline{\nu}$ upgoing, isotropic CTEQ6-DIS PDF $E^{-1.4}[10^2 - 10^7$ GeV]	GENDET v1r2 12-string octagonal layout	KM3 v2r1 GEASIM v4r9 partic-0.0075	RECO v4r4 AartStrategy

Table 4.1: *List of the programs and main parameters used for the Monte Carlo neutrino/anti-neutrino production.*

Neutrinos and anti-neutrinos were simulated with a 2π isotropic angular distribution

and only up-going events were considered. The generation flux follows a power law spectrum $E_\nu^{-1.4}$, although a proper weight that takes into account the atmospheric flux is also provided by the generation package. After reconstruction of the events only those that meet a goodness criteria are selected. These selection criteria, or quality cuts, are obtained from [153] and are the same cuts applied in section 2.9 when we showed the ANTARES main performance features. In order to select the number of background events contributing to the sample, an event rate corresponding to the Bartol model [157] was taken. After selecting the reconstructed track direction (θ, ϕ), the arrival time was randomized within a time window of one year and local coordinates were translated into equatorial coordinates by means of the positional astronomy library `slalib` [158]. The average number of expected events in one year was ~ 1319 ν and ~ 509 $\overline{\nu}$, which amounts to a total number of ~ 1828 neutrino events per year.

A second contribution to the physical background comes from atmospheric muons. Cosmic rays interactions in the upper shell of the Earth's atmosphere generate muons that can be misinterpreted as muons induced by astrophysical neutrinos. The Earth, however, will shield this muon flux and therefore it can be relatively easily rejected by accepting only up-going events. In some occasions, however the track reconstruction algorithm can mis-reconstruct a down-going muon event as up-going. This is specially likely in the case of multi-muons, which are bundles of parallel muons produced in the same cascade. However, a set of proper quality cuts can reduce considerably the number of atmospheric muons as can be seen in [119]. For point sources searches however, the number of atmospheric muon events that might be present in the data sample will be negligible compared to the main background contribution coming from atmospheric neutrinos and therefore are not included in the sample.

4.2.2 Signal simulation

In an ideal detector, all neutrinos coming from the source will almost point back directly to the source location except for the unavoidable angle between the neutrino track and the muon coming out from the neutrino-nucleon interaction. In a real detector, a contribution coming from the angular error due to the track reconstruction process is also present. This angular error smears the arrival direction of the neutrinos around the true source location. The angular distribution is known as the Point Spread Function of the telescope and is related to the angular resolution of the detector. Figure 4.2 shows the error distribution of the angle between the true neutrino direction and the reconstructed muon track for each declination band. In order to obtain the angular error distribution as a function of declination, it is necessary to weigh by a given neutrino spectrum.

Signal events are more difficult to simulate since there is no predictive model for point-like sources. However, an educated assumption is to characterize this neutrino flux as a power law of the form $\frac{d\Phi_\nu}{dE_\nu} \propto E_\nu^{-\gamma}$, being γ the so-called spectral index. The spectral index for cosmic neutrinos is expected to vary from 2 to 3 [17]. For the plot presented in figure 4.2 the angular error distribution has been weighed by a spectral index of 2. The procedure to simulate a source starts by selecting the source location and the number of signal events we want to simulate. Angular distances around

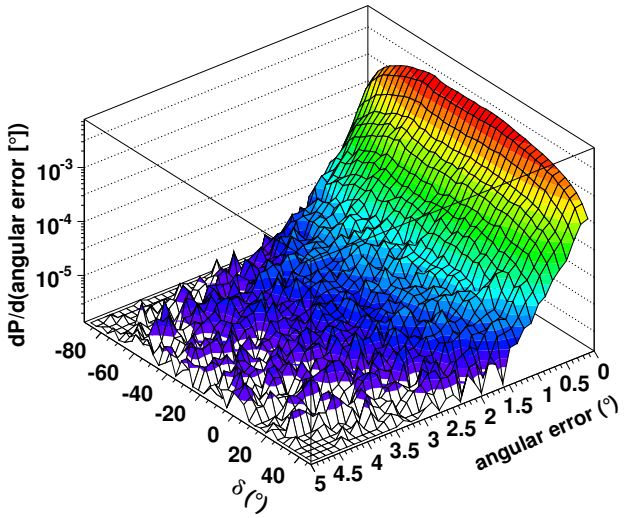

Figure 4.2: *Neutrino angular error distribution for different declination bands for a spectral index of 2.*

the source location are randomized according to the angular error distribution for the desired declination band. Although in this work the energy of the event is not explicitly used, the energy dependence is somehow included in the angular resolution since the latter depends on the source spectral index. Figure 4.3 shows the angular resolution, as defined in ANTARES: the median values of the angular error distributions as a function of the sine of declination (to show a more uniform dependence) for different spectral indexes. As expected, sources emitting with a harder spectrum give rise to more energetic neutrino events with a better angular resolution.

Note that the signal simulation we have just described applies only to point-like sources, that is, sources that cover a solid angle small compared to the ANTARES angular resolution.

4.2.3 Dependence on the track reconstruction strategy

The point-like search techniques can be applied independently of the track reconstruction strategy used, although there is an indirect influence through the data themselves. Different track reconstruction strategies can yield different data distributions. In the ANTARES collaboration there are two main strategies for a three-dimensional track reconstruction[1]: the *Carmona strategy* [150] and the *Aart strategy* [153]. The detector performance is therefore essentially affected by the reconstruction algorithm. Different effective areas will lead to different number of neutrino reconstructed events per year affecting the source searching algorithm sensitivity. In figure 4.4 the average effective areas[2] for both neutrinos and muons as a function of the declination can be seen. In order to compute the average effective area, we need to weigh by the neutrino

[1]Lately, new strategies have been developed with very promising results but not covered in this work.

[2]A detailed definition of average effective areas is given in section 5.2.1.

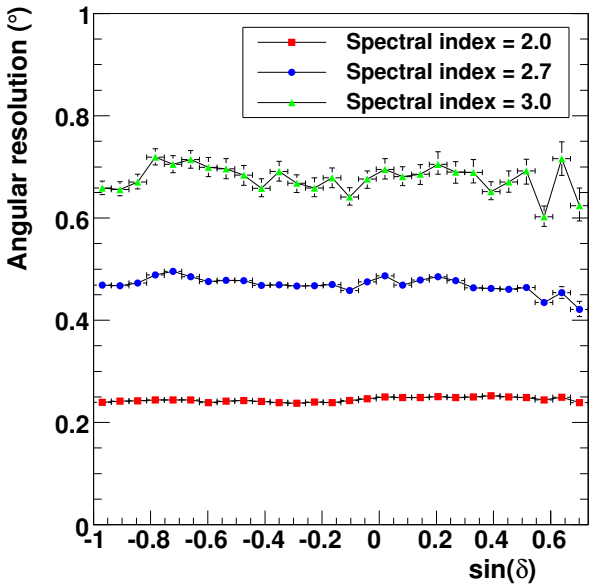

Figure 4.3: *Neutrino angular resolution for different spectral indexes shown as a function of the sine of declination.*

flux. In this case, results are shown for a spectral index of 2 and integrated from 10 to 10^7 GeV, which is the energy range of the Monte Carlo simulation.

The overall average effective area for the *Carmona strategy* is about 5% higher for muons and 1% for neutrinos with respect to the *Aart strategy*. The angular resolution will influence the source simulation since the angular error distributions are used to build the signal samples as explained in the previous section. Hence different angular resolutions will yield different signal shape simulations and different sensitivity in the point-like source analysis. Figure 4.5 shows the angular resolution, for a spectral index of 2, as function of the local coordinates, figure 4.5(a), and equatorial coordinates, figure 4.5(b), for both reconstruction strategies. As can be seen, the *Aart strategy* has a better angular resolution, about a 17% in the overall angular resolution and up to 25% for almost vertical muons and it is declination independent. In this work, due to its better angular resolution, we use the *Aart strategy* reconstruction.

4.3 Clustering analysis

The clustering analysis is the identification of groups of observations that are cohesive and separated from other groups. In this sense, the search for point-like sources can be understood as the identification of small cluster groups made up by signal events, originated independently of and spread over the atmospheric neutrino events that constitute the background. Clustering methods provide a tool for the search for structures in the data. Among the different clustering techniques, those called mixture model methods assume that data follow a global density function made up by the sum

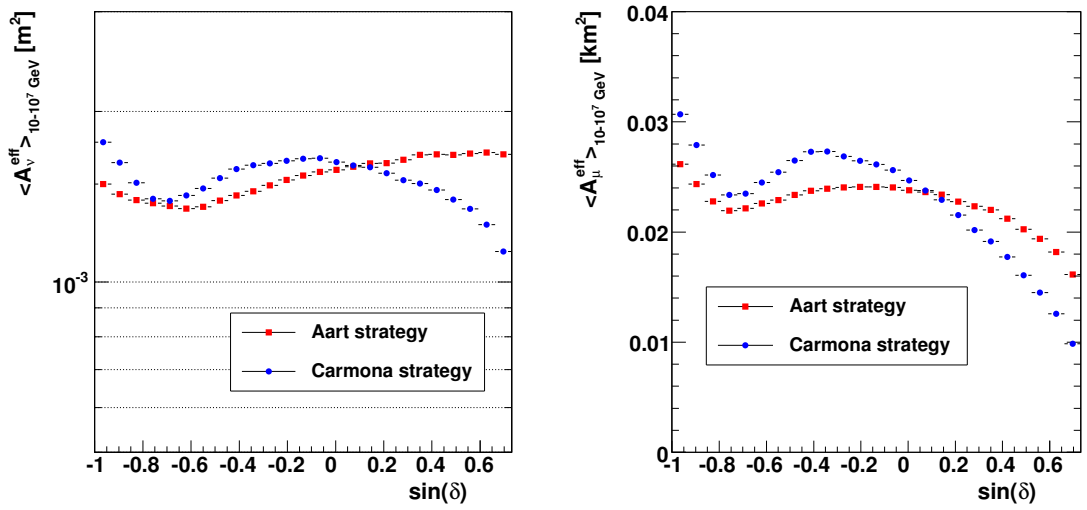

(a) Neutrinos **(b)** Muons

Figure 4.4: *Comparison of the energy averaged effective areas in the range 10-10^7 GeV as a function of the declination for two reconstruction strategies in the case of neutrinos and muons.*

of component densities. A common approach of these methods is to consider a simple parametric model for the density function.

4.3.1 The EM algorithm

The Expectation-Maximization (EM) algorithm [159] is a general approach to maximum likelihood estimation for finite mixture model problems. A mixture model is a distribution where different groups in the data are described by different density components. The total probability density function (p.d.f.) of the population can be expressed as

$$p(\mathbf{x}) = \sum_{j=1}^{g} \pi_j p(\mathbf{x}; \boldsymbol{\theta}_j), \tag{4.1}$$

where g is the number of mixture components, $\pi_j \geq 0$ are the mixing proportions that satisfy the unitary relation ($\sum_{j=1}^{g} \pi_j = 1$) and $p(\mathbf{x}; \boldsymbol{\theta}_j)$, $j = 1, ..., g$, are the *component density* functions which may depend on a parameter vector $\boldsymbol{\theta}_j$. To maximize the likelihood, there are three sets of values to estimate: the values of π_j, the components of $\boldsymbol{\theta}_j$ and the value of g. Several assumptions about the component density may be taken depending on the specification of the problem or the knowledge about the data generation. Most commonly, $p(\mathbf{x}; \boldsymbol{\theta}_j)$ are the multivariate normal (Gaussian) density parametrized by a mean vector and a covariance matrix $\boldsymbol{\Sigma}_j$, ($\boldsymbol{\theta}_j = \{\boldsymbol{\mu}_j, \boldsymbol{\Sigma}_j\}$)

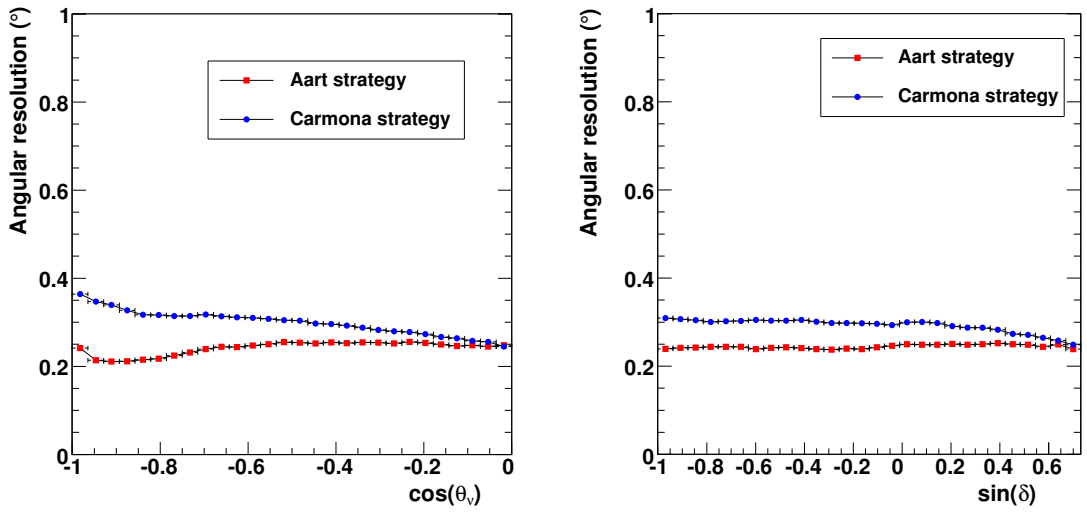

(a) Local coordinates **(b)** Equatorial coordinates

Figure 4.5: *Angular resolution between the reconstructed muon track and the true neutrino direction for two reconstruction strategies as a function of cos(θ_ν) and sin(δ).*

$$p(\mathbf{x};\boldsymbol{\mu}_j,\boldsymbol{\Sigma}_j) = \frac{\exp\{-\frac{1}{2}(\mathbf{x}-\boldsymbol{\mu}_j)^T\boldsymbol{\Sigma}_j^{-1}(\mathbf{x}-\boldsymbol{\mu}_j)\}}{\sqrt{\det(2\pi\boldsymbol{\Sigma}_j)}}. \tag{4.2}$$

In this case, the equations given by the maximum likelihood procedure based on the EM algorithm are well known as we will show later.

Having a data sample of n observations, the likelihood for a mixture model with g density components is given by

$$\mathcal{L}(\boldsymbol{\Psi}) = \prod_{i=1}^{n}\sum_{j=1}^{g}\pi_j p(\mathbf{x}_i;\boldsymbol{\theta}_j), \tag{4.3}$$

where $\boldsymbol{\Psi}$ stands for the set of parameters $\{\pi_1,...,\pi_g;\boldsymbol{\theta}_1,...,\boldsymbol{\theta}_g\}$. Normally, it is not possible to solve explicitly $\partial\mathcal{L}/\partial\boldsymbol{\Psi} = 0$ and an iterative approach must be employed. The EM algorithm is in this context, a general iterative procedure to maximize mixture model likelihoods.

The idea is to assume that the set of observations forms a set of *incomplete* data vectors $\{\mathbf{x}\}$. The likelihood given by this incomplete data set can be expressed by $\mathcal{L}(\boldsymbol{\Psi}) = p(\{\mathbf{x}\},\boldsymbol{\Psi})$. The unknown information that is missing in the data sample is, in fact, whether an observation belongs to a component or to another, in other words, the information about the clustering structure of the population is lacking.

Let now $\{\mathbf{y}\}$ denote a version of the *complete* data $\{\mathbf{x}\}$ formed by a new vector $\mathbf{y}_i = (\mathbf{x}_i,\mathbf{z}_i)$, where $\mathbf{z}_i = (z_{i1},...,z_{ig})$ is simply a class indicator vector given by the

following expression:

$$z_{ik} = \begin{cases} 1 & \text{if } \mathbf{x}_i \text{ belongs to group } k \\ 0 & \text{otherwise.} \end{cases} \tag{4.4}$$

With this complete data set the total density function is

$$g(\mathbf{y}; \mathbf{\Psi}) = g(\mathbf{x}, \mathbf{z}; \mathbf{\Psi}) = p(\mathbf{x}; \mathbf{z}, \mathbf{\Psi}) f(\mathbf{z}; \mathbf{\Psi}), \tag{4.5}$$

where $f(\mathbf{z}; \mathbf{\Psi})$ is the density function of the class indicator vector and the likelihood of this complete data set is $\mathcal{L}'(\mathbf{\Psi}) = g(\{\mathbf{y}\}, \mathbf{\Psi})$. We can obtain back the likelihood of the previous incomplete data set from $g(\{\mathbf{y}\}, \mathbf{\Psi})$ by integrating over all possible $\{\mathbf{y}\}$ in which the set $\{\mathbf{x}\}$ is embedded

$$\mathcal{L}(\mathbf{\Psi}) = p(\{\mathbf{x}\}, \mathbf{\Psi}) = \int \prod_{i=1}^{n} g(\mathbf{x}_i, \mathbf{z}; \mathbf{\Psi}) d\mathbf{z}. \tag{4.6}$$

The EM procedure consists in two main steps: the Expectation and the Maximization steps. After each iteration, the EM generates a sequence of estimates of $\mathbf{\Psi}$, $\{\mathbf{\Psi}^{(m)}\}$, from an initial estimate $\mathbf{\Psi}^{(0)}$. According to probability theory, after some computations, the log-likelihood of the incomplete data set, given the current parameter estimate, $\mathbf{\Psi}^{(m)}$, can be expressed by

$$\log(\mathcal{L}(\mathbf{\Psi}^{(m)})) = Q(\mathbf{\Psi}^{(m)}, \mathbf{\Psi}^{(m)}) + H(\mathbf{\Psi}^{(m)}, \mathbf{\Psi}^{(m)}), \tag{4.7}$$

where $Q(\mathbf{\Psi}, \mathbf{\Psi}^{(m)})$ =E$[\log(g(\{\mathbf{y}\}; \mathbf{\Psi}))|\{\mathbf{x}\}; \mathbf{\Psi}^{(m)}]$ is the expectation value of the complete data log-likelihood, conditional on the observed data $\{\mathbf{x}\}$, given by

$$Q(\mathbf{\Psi}, \mathbf{\Psi}^{(m)}) = \int \sum_i \log[g(\mathbf{x}_i, \mathbf{z}_i; \mathbf{\Psi})] p(\{\mathbf{z}\}|\{\mathbf{x}\}, \mathbf{\Psi}^{(m)}) d\mathbf{z}_1 ... d\mathbf{z}_n, \tag{4.8}$$

which is easily differentiable. $H(\mathbf{\Psi}, \mathbf{\Psi}^{(m)})$ is an entropy term representing the difference between the incomplete data likelihood and the expectation of the complete data likelihood. This entropy term is expressed as

$$H(\mathbf{\Psi}, \mathbf{\Psi}^{(m)}) = -\mathrm{E}[\log(\mathrm{g}(\{\mathbf{y}\}; \mathbf{\Psi})/\mathrm{p}(\{\mathbf{x}\}; \mathbf{\Psi}))|\{\mathbf{x}\}, \mathbf{\Psi}^{(\mathrm{m})}]. \tag{4.9}$$

The two steps of the EM algorithm can be easily summarized as follows:

- **E-step:** In the Expectation step we evaluate the expectation of the complete data log-likelihood, $Q(\mathbf{\Psi}, \mathbf{\Psi}^{(m)})$, for the current value of the parameter estimate $\mathbf{\Psi}^{(m)}$.
- **M-step:** The Maximization step is performed in order to find the set of parameters $\mathbf{\Psi} = \{\mathbf{\Psi}^{(m+1)}\}$ that maximize $Q(\mathbf{\Psi}, \mathbf{\Psi}^{(m)})$.

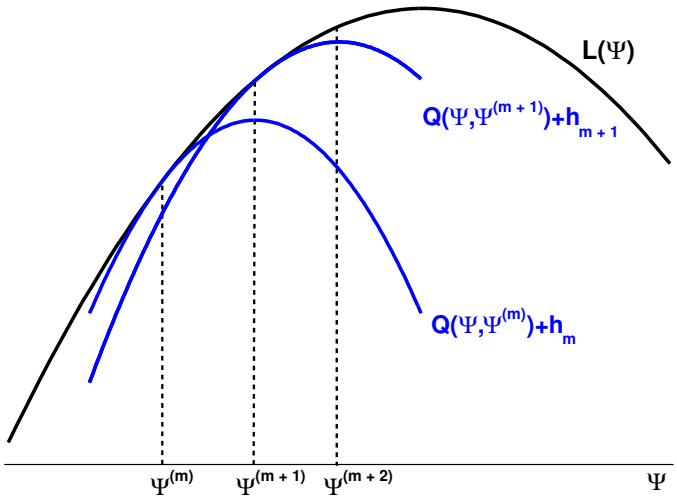

Figure 4.6: *Illustration of the EM mechanism where* $L(\boldsymbol{\Psi}) = log\mathcal{L}(\boldsymbol{\Psi})$ *and* $h_m = H(\boldsymbol{\Psi}^{(m)}, \boldsymbol{\Psi}^{(m)})$.

It is relatively easy to demonstrate, by means of Jensen's inequality, that the EM algorithm has a general convergence property. This means that we can always choose a set of parameters $\boldsymbol{\Psi} = \{\boldsymbol{\Psi}^{(m+1)}\}$ at iteration m such that

$$\mathcal{L}\{\boldsymbol{\Psi}^{(m+1)}\} \geq \mathcal{L}\{\boldsymbol{\Psi}^{(m)}\}. \tag{4.10}$$

In figure 4.6, an illustration of the EM iterative mechanism is shown. The key idea of the EM scheme is that the auxiliary function, $Q(\boldsymbol{\Psi}, \boldsymbol{\Psi}^{(m)})$ touches the log-likelihood function at the point $\boldsymbol{\Psi}^{(m)}$ and lies below everywhere else. More strictly, $Q(\boldsymbol{\Psi}, \boldsymbol{\Psi}^{(m)})$ differs from the log-likelihood of the incomplete data set at $\boldsymbol{\Psi}$ by the entropy factor $H(\boldsymbol{\Psi}, \boldsymbol{\Psi}^{(m)})$ [159] and therefore, successive maximizations in the expected value $Q(\boldsymbol{\Psi}, \boldsymbol{\Psi}^{(m)})$ lead to the maximization of the log-likelihood of the incomplete data set.

4.3.2 The EM algorithm for mixture models

Mixture models are a specific case in which the density function is made up by the sum of different component densities. In this case, the EM algorithm starts by assuming a density function for the complete data set. Taking into account equation 4.5 we can build the probability density function for $\mathbf{y}$ as

$$g(\mathbf{y}; \boldsymbol{\Psi}) = p(\mathbf{x}; \mathbf{z}, \boldsymbol{\Psi}) f(\mathbf{z}; \boldsymbol{\Psi}) = p(\mathbf{x}; \boldsymbol{\theta}_k)\pi_k, \tag{4.11}$$

thus, we can re-write it as

$$g(\mathbf{y}; \boldsymbol{\Psi}) = \prod_{j=1}^{g} [p(\mathbf{x}; \boldsymbol{\theta}_j)\pi_j]^{z_j}, \tag{4.12}$$

since z_j is zero except for $j = k$. For a set of n observations, the log-likelihood is given by

$$\log(\mathcal{L}'(\mathbf{\Psi})) = \sum_{i=1}^{n}\sum_{j=1}^{g} z_{ij} \log\left[p(\mathbf{x}_i|\boldsymbol{\theta}_j)\pi_j\right]. \tag{4.13}$$

where z_{ij} is the j-th component of the vector $\mathbf{z}_i$. The E-step of the EM iteration for mixture models computes the value of $\hat{\mathrm{z}}_{ij}$ where $\hat{\mathbf{z}}_i = \mathrm{E}(\mathbf{z}_i|\mathbf{x}_i, \mathbf{\Psi}^{(m)})$ is the expected value of $\mathbf{z}_i$ given the current estimation of parameters $\mathbf{\Psi}^{(m)}$ and is given by the following expression:

$$\hat{z}_{ij} \leftarrow \frac{\hat{\pi}_j^{(m)} p(\mathbf{x}_i|\boldsymbol{\theta}_j^{(m)})}{\sum_k \hat{\pi}_k^{(m)} p(\mathbf{x}_i|\boldsymbol{\theta}_k^{(m)})}. \tag{4.14}$$

For multivariate normal mixtures ($\boldsymbol{\theta}_i = (\boldsymbol{\mu}_i, \mathbf{\Sigma}_i)$), the E-step is given by the expression 4.14, where $p(\mathbf{x}_i; \boldsymbol{\theta}_j^{(m)})$ are the Gaussian components of the mixture model. Thus, in the M-step, the estimates of the means and probabilities have simple closed-form expressions obtained by differentiating Q with respect to the different parameters:

- Maximizing Q with respect to π_i (taking into account the unitary constraint $\sum_{j=1}^{g} \pi_j = 1$) leads to the equation

$$\hat{\pi}_j \leftarrow \frac{1}{n}\sum_{i=1}^{n} \hat{z}_{ij}. \tag{4.15}$$

- The re-estimate of the Gaussian mean is given by $\partial Q/\partial\mu = 0$:

$$\hat{\boldsymbol{\mu}}_j \leftarrow \frac{\sum_{i=1}^{n} \hat{z}_{ij}\mathbf{x}_i}{\sum_{i=1}^{n} \hat{z}_{ij}} = \frac{1}{n\hat{\pi}_j}\sum_{i=1}^{n} \hat{z}_{ij}\mathbf{x}_i. \tag{4.16}$$

- The computation of the covariance estimate $\hat{\mathbf{\Sigma}}_j$, however depends on the component density parametrization. Assuming a covariance value of $\sigma_{xy} = 0$, the variance vector $\boldsymbol{\sigma}$ is given by

$$\hat{\boldsymbol{\sigma}_j}^2 \leftarrow \frac{\sum_{i=1}^{n} \hat{z}_{ij}^2(\mathbf{x}_i - \hat{\boldsymbol{\mu}}_j)^2}{\sum_{i=1}^{n} \hat{z}_{ij}} = \frac{1}{n\hat{\pi}_j}\sum_{i=1}^{n} \hat{z}_{ij}^2(\mathbf{x}_i - \hat{\boldsymbol{\mu}}_j)^2. \tag{4.17}$$

Despite its awkward proof, the EM procedure can be in fact easily implemented. Nevertheless, this iterative process has some limitations. In principle, the general procedure of the EM algorithm is not optimized for data with a large amount of noise background, as is the case for point-like source searches. In addition, the convergence can be slow if poor initial parameter values are supplied. In the following section we will explore the performance of the EM algorithm applied to our problem.

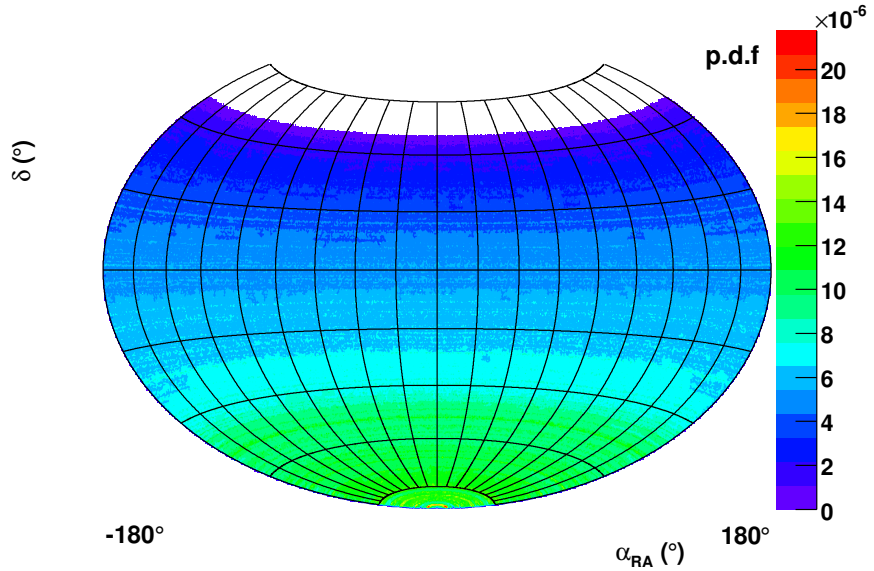

Figure 4.7: *Normalized probability density (p.d.f) for the atmospheric neutrino background in equatorial coordinates.*

4.4 The EM algorithm applied to point-like sources

One of the special features of point sources searches is that clusters of signal events are spread over a non-Gaussian distribution made up by the atmospheric background events. In order to start with the maximization iterative process, an estimation of the component density function model is required. In this case, the sources are supposed to follow Gaussian distributions of the form

$$P_S(\mathbf{x};\boldsymbol{\mu},\boldsymbol{\Sigma}) = \frac{1}{2\pi\sigma_\alpha\sigma_\delta}\exp\left(-\frac{(\alpha-\mu_\alpha)^2\cos^2\delta}{2\sigma_\alpha^2}\right)\exp\left(-\frac{(\delta-\mu_\delta)^2}{2\sigma_\delta^2}\right)\cos(\delta), \qquad (4.18)$$

where $\mathbf{x} = (\alpha, \delta)$ is the position of the event in equatorial coordinates and $\boldsymbol{\mu} = (\mu_\alpha, \mu_\delta)$, $\boldsymbol{\Sigma} = (\sigma_\alpha, \sigma_\delta)$ are the mean and covariance vector of the Gaussian distribution. This assumption turns out to be very sensible and it has been used in other source searching techniques as well [154]. It also has the great advantage that, in this case, the equations that lead to the likelihood maximization are well known. The background event distribution is also required in order to be able to reject the nuisance events from the signal events. A parametrized model can be applied; in this work, however, we are going to accept the background distribution as a well known distribution.

For an isotropically distributed background, the number of background events coming from a given direction will be proportional to the visibility of the source in that declination times the solid angle covered by this region. However, the atmospheric neutrino distribution is not isotropic in declination from the ANTARES location and hence, a dependency on that coordinate is expected. On the other hand, as can be

seen from figure 4.7, the background density is right ascension independent due to the Earth's rotation. In our case, the background distribution has been inferred from the Monte Carlo simulations, although it has to be noted that this background estimation from simulation induces no real Monte Carlo dependence since when real data will be available we will reproduce the background distribution by scrambling the azimuth angle and the arrival times of the events in a given declination band. In fact this is a common step in every searching algorithm since a knowledge of the background distribution is required to build the significances yielded by the method.

The mixture model for our point-like source problem can be expressed as

$$p(\mathbf{x}) = \pi_{BG} P_{BG}(\delta) + \sum_{j=1}^{g} \pi_{S_j} P_S(\mathbf{x}; \boldsymbol{\mu}_j, \boldsymbol{\Sigma}_j), \tag{4.19}$$

where both π_{BG} and π_{S_j} are the mixing proportions of the background component and the source distributions which satisfy the unitary condition. The parameter g is the number of clusters, in other words, the number of expected sources that might be present in the sample. Since it is very unlikely to detect more than one neutrino emitter, we set this parameter to 1, i.e. we assume that in our sample there is only contributions from the background and one single source located anywhere in the sky. Hence, equation 4.19 can be simplified to

$$p(\mathbf{x}) = \pi_{BG} P_{BG}(\delta) + \pi_S P_S(\mathbf{x}; \boldsymbol{\mu}, \boldsymbol{\Sigma}). \tag{4.20}$$

It is possible, however, to extend the analysis to more than one source in a very natural way by just applying the maximization equations derived in the previous section to the more general mixture model defined by formula 4.19.

4.4.1 Procedure to maximize the likelihood

The goal of the EM algorithm is to find the best estimate of the free parameters in equation 4.20 that maximize the likelihood. In our case, there is a set of 6 parameters to fit. The bare EM algorithm has some limitations when applied directly to the problem of the search for point-like sources such as a slow convergence and a variety of local minima due to the high background to signal ratio of the problem. These two limitations can be easily overcome by pre-selecting a number of candidate clusters and therefore a set of initial parameters for the EM iterative procedure. These clusters are selected by a simple clustering algorithm. A cone is drawn around each of the measured events on the sample. Those clusters with at least 3 events are considered to be useful for the EM algorithm[3]. The parameter that determines the size of these pre-clustering cones (`dismax`) has been selected to be 1.25°, which is large enough compared to the ANTARES angular resolution.

This parameter indirectly affects the average number of candidate clusters per sample as shown in figure 4.8 left. This average number of candidate clusters is about ~ 20

[3]In a full sky search a 2-event signal cluster is very unlikely to be detected. However, the minimum cluster size is reduced when looking at pre-defined locations in the sky as shown in the following chapters.

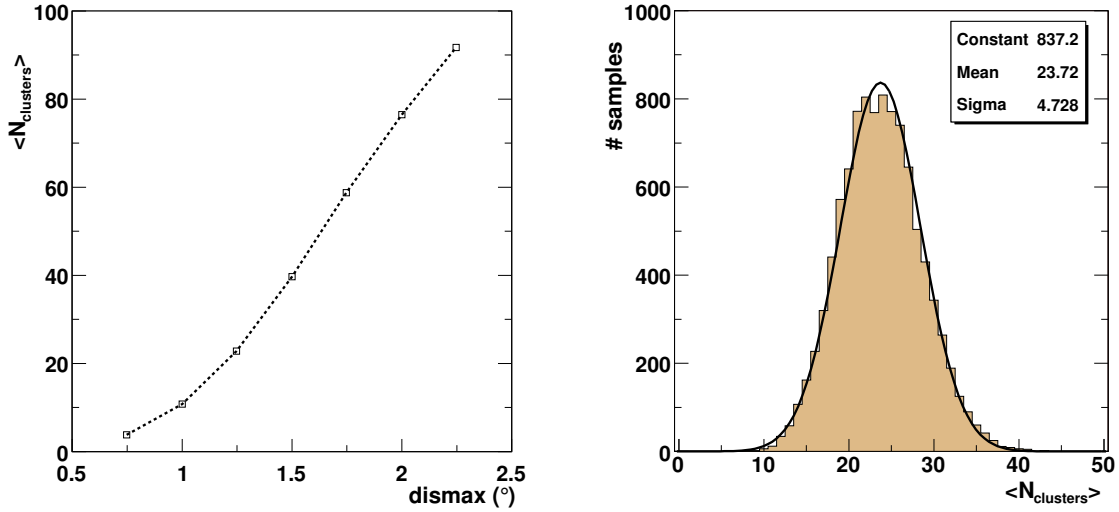

Figure 4.8: *Left: Average number of candidate clusters as a function of the initial cluster size* `dismax`*. Right: Number of clusters for 10^4 samples when a value of 1.25° is selected.*

for an initial cone size of 1.25° (see fig. 4.8 right). We have checked that the exact value of this parameter does not affect significantly the results in terms of discovery or sensitivities as far as reasonable values (typically from 1° to 3°) are selected as will be shown in next chapter. Once the candidate clusters are selected, we can obtain a set of initial parameters for the EM algorithm:

- Since π_{BG} and π_S are the mixing proportions they can be expressed in terms of the number of events in the sample. In this sense, for an experiment of n observed events, π_S can be expressed as $\pi_S = n_S/n$, where n_S is the number of events coming from the source. From the unitary relation π_{BG} is given by $\pi_{BG} = (n-n_S)/n$. Since the number of events coming from the source is unknown, a good approximation to the initial value is the number of events inside the candidate cluster.

- The initial values of the Gaussian means $\mu = (\mu_\alpha, \mu_\delta)$ are selected to be the coordinates of the barycentre of the cluster under study.

- $\sigma = (\sigma_\alpha, \sigma_\delta)$ are the covariance values of the Gaussian distribution. The width of the Gaussian should include the dependence on the angular resolution of the detector which also inherits the dependence on the source spectral index. The initial values are chosen to correspond to the `dismax` initial values (1.25°). However, since σ is not a fixed value it changes during the maximization process, and can evolve to a larger or smaller value. Assuming an axial symmetry in the Point Spread Function, we could constrain the two-dimensional widths by setting $\sigma_\alpha = \sigma_\delta$. In this work, however, we preferred to keep them as independent values

taking into account the situation in which, for instance, the detector angular resolution response in the δ-direction might be different with respect to the angular error in the α-direction.

For each candidate cluster the EM algorithm is performed until a convergence criterion is fulfilled. Then a criterion in the goodness of the maximization is applied by using a model selection criteria. Picture 4.9 shows a flow chart of the EM algorithm.

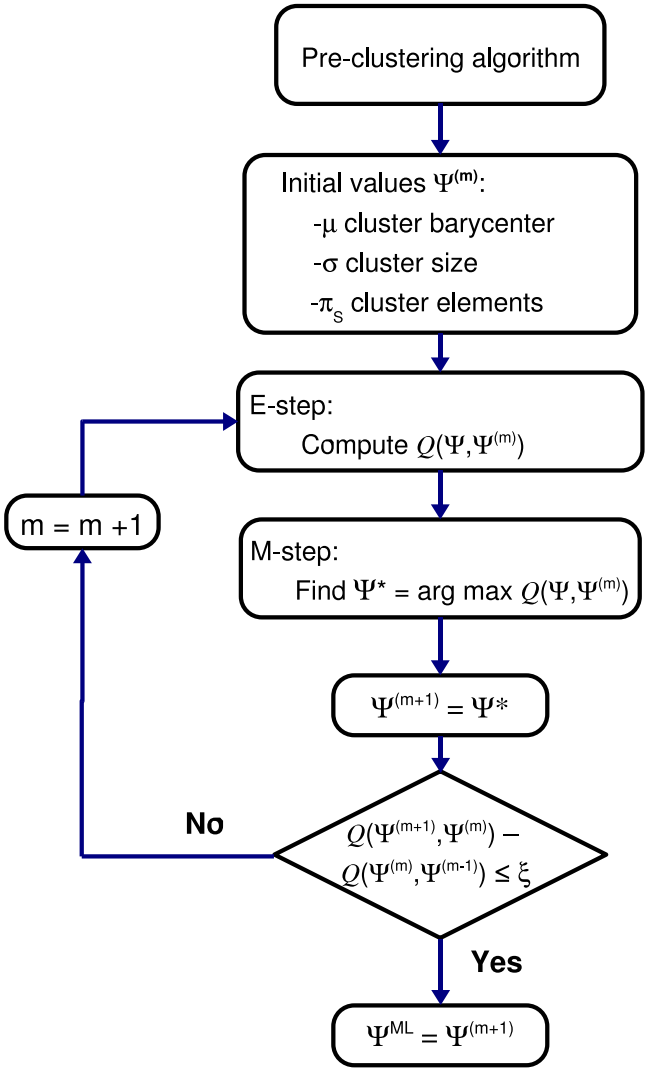

Figure 4.9: *Flowchart of the EM algorithm for the point like source searching analysis.* $\boldsymbol{\Psi}^{ML}$ *is the maximum-likelihood estimate and* ξ *is the termination threshold used by the convergence criterion.*

4.4.2 Model selection

A criterion is needed to confirm or reject the existence of a point-like source. The problem is then reduced to the comparison among several proposed models that lead to different statistical results. We need an observable discriminator that would depend on the data and on the model we are tackling. In this work, we used as a test statistics the so-called Bayesian Information Criterion (BIC) [160, 161] defined as

$$\mathrm{BIC}_k = 2\log p(\{\mathbf{x}\}|\mathbf{\Psi}_k^{\mathrm{ML}}, M_k) - \nu_k \log(n), \tag{4.21}$$

where M_k indicates one of the possible k models that we want to compare, $\mathbf{\Psi}_k^{\mathrm{ML}}$ is the estimate obtained by the algorithm for the set of parameters that define the k model, ν_k is the number of degrees of freedom in the algorithm for the M_k model, $\{\mathbf{x}\}$ is the data set and n the number of events in the data sample. The comparison of the different models can be performed using the ratios of their corresponding BICs. For our two model case (where M_0 is only-background model and M_1 the background plus source model) this amounts to using the following test statistic:

$$\mathrm{BIC} = 2\log p(\{\mathbf{x}\}|\mathbf{\Psi}_1^{\mathrm{ML}}, M_1) - 2\log p(\{\mathbf{x}\}|M_0) - (\nu_1 - \nu_0)\log(n). \tag{4.22}$$

Note that in our case the background model is assumed to be known and, therefore, no estimate of parameters is performed and $\nu_0 = 0$. Despite its name, the BIC can be used in an entirely frequentist manner. Indeed, the BIC value is just the **maximum likelihood ratio** with a penalty that takes into account the number of free parameters in the model weighed by the number of events in the data sample. In a Bayesian approach, the BIC of a model is an approximation to its integrated likelihood, $\mathrm{BIC}_k \approx 2\log \mathcal{L}_k$, where

$$\mathcal{L}_k = \int p(D|\mathbf{\Psi}_k, M_k) p(\mathbf{\Psi}_k|M_k) d\mathbf{\Psi}_k. \tag{4.23}$$

This likelihood is estimated by integration of the parameters $\mathbf{\Psi}_k$ assuming they are statistical variables and using the prior probabilities $p(\mathbf{\Psi}_k|M_k)$ and in a Bayesian approach we will take a decision just by examining the value of the BIC. In the classical approach, however, the parameters are found by maximization, avoiding prior probabilities and the concept that the true values of the parameters are statistical variables, which are typical constructs of the Bayesian approach.

The BIC is used in this framework as a discriminator whose sampling distribution can be obtained from Monte Carlo experiments or by data scrambling and tested by the **hypothesis testing theory**. In our case, the two models to test M_0 and M_1 are the only-background and background plus source model respectively. Once the BIC distribution for the only-background case is computed, we can make a decision about the acceptance or rejection of a model over the background hypothesis by the usual way used in model testing theory as illustrated in figure 4.10. The value α is the probability of rejecting M_0 if M_0 is true. It is called the **level of significance**. In a continuous p.d.f the parameter α can take any value. It is commonly accepted

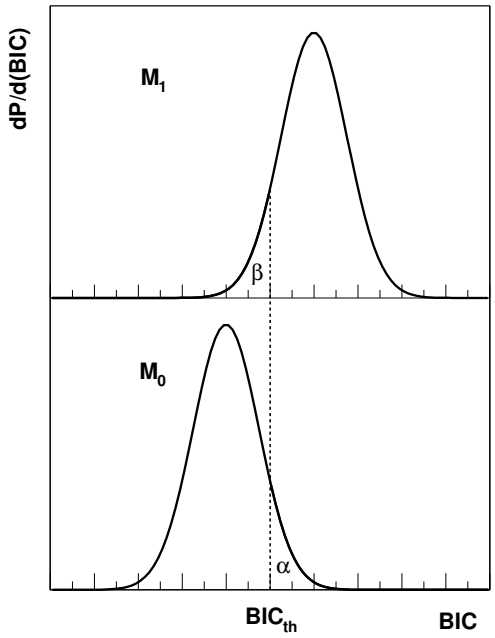

Figure 4.10: *Illustration of the BIC distribution for two different models (M_0 and M_1). The value α is the level of significance, and $1-\beta$ is the so-called power of the test of M_0 against M_1.*

to express the level of significance as a number of standard deviations of the normal probability distribution, although the BIC distributions under study do not follow the normal distribution as it will be shown in the following chapter. The expression of the level of significance given in terms of number of standard deviations (nσ) is

$$\alpha = \int_n^\infty \frac{dx}{\sqrt{2\pi}} \exp\left(-\frac{x^2}{2}\right), \tag{4.24}$$

which for the case of 3σ and 5σ corresponds to probabilities of 2.77×10^{-1} % and 5.73×10^{-5} % respectively. Alternatively, the complementary probability of β, (1 - β), is called the **power** of the test of M_0 against M_1. In this work it will be also referred to as the **discovery power** or **discovery potential** of the searching algorithm.

Chapter 5

Full sky blind survey

– Did you build the Smell-O-scope?
– No, I remembered that I'd built one last year. Go ahead, try it. You'll find that every heavenly body has its own particular scent. Here, I'll point it at Jupiter.
Fry and Professor Farnsworth, Futurama.

There are mainly two different procedures for the point source analysis. In this chapter we will explore the algorithm performance for a full sky survey. It is a *blind* search in the sense that no assumptions about the sources are made, in particular about the source location. All parameters in the component distributions are free and have to be estimated by the algorithm. In a blind search, the source may lie anywhere in the visible sky of ANTARES and, therefore, this analysis yields a lower sensitivity compared to the situation where constraints about the source position are applied, as it will be explained in the next chapter. We will also show the discovery potential of the EM-based technique for different declination bands, and the flux that is required so that with 50% probability the existence of a source can be claimed. Results will be shown according to the level of significance (3σ and 5σ) as explained in the previous chapter.

5.1 BIC distribution for the blind search

In this work, 10^4 Monte Carlo experiments have been simulated, each one corresponding to 1 year of data-taking. The EM-based searching algorithm is applied to the only-background samples in order to obtain the BIC distribution for the background case. Each sample is processed by the pre-clustering algorithm which will select a set of candidate clusters as input to the EM-based algorithm. Each cluster is analysed by the algorithm and at the end of the iterative procedure an estimate of all parameters that maximize the likelihood is obtained and each cluster is identified by the BIC value computed by the algorithm. Among them the highest BIC, which corresponds to the cluster that yields the maximum likelihood, is considered as the BIC value of the sample. For each Monte Carlo experiment, a value for the BIC statistics is obtained and the whole set of 10^4 experiments is used to make a sample of the BIC distribution required to infer the suitable **confidence level**. Figure 5.1 left, shows the BIC

distribution for 10^4 Monte Carlo identical, in average, experiments of only-background events.

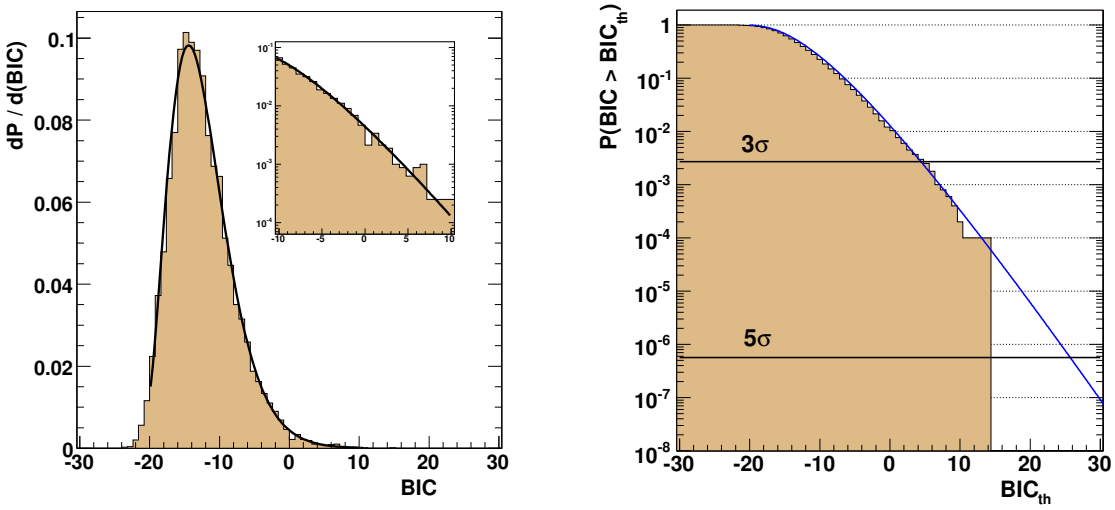

Figure 5.1: *Left: BIC distribution for 10^4 Monte Carlo experiments of only-background events. Right: Anticumulative distribution. The BIC values corresponding to 3σ and 5σ are indicated.*

One drawback of the unbinned methods is the lack of prior knowledge of the test distribution. In order to calculate the confidence level from the BIC value we must know its distribution. This leads us to use Monte Carlo experiments in order to obtain an approximation of the test distribution. Although this is completely satisfactory for the central range, it can be specially awkward in the tail region, since a large amount of experiments should be simulated in order to obtain an accurate knowledge of the tail behaviour. As an example, about 10^7 experiments will be required to reach a confidence level equivalent to 5σ. This huge amount of experiments is, for the time being, difficult to achieve due to computing and storage limitations. To overcome this problem we need to extrapolate the distribution to this problematic region. Figure 5.1 right shows the anti-cumulative distribution of the background BIC distribution. The threshold BIC_{th} is defined as the value where $P(\mathrm{BIC} > \mathrm{BIC}_{th}) = n\sigma$, being $n\sigma$ the desired confidence level equivalent to n Gaussian standard deviations. In figure 5.1 right the two solid lines indicate the confidence levels equivalent to 3σ (2.77×10^{-1} %) and 5σ (5.73×10^{-5} %). It can also be seen that the lack of statistics is crucial when inferring the BIC_{th} corresponding to a high confidence level like 5σ, and therefore an extrapolation of the background distribution toward the tail regime is required.

In order to make this extrapolation the asymptotic distribution behaviour is used. The asymptotic properties of the likelihood ratio test can be found in [162]. The likelihood ratio, and therefore the BIC distribution, can be asymptotically represented by a $\chi^2_{2\nu}$ distribution where ν denotes the degrees of freedom. As explained in chapter 3, the BIC value is closely related to the maximum likelihood ratio plus a penalization factor that accounts for the different number of degrees of freedom. Hence, it is expected

that the BIC distribution will follow the non-central $\chi^2_{2\nu}(r)$ with a non-zero mean, r. Figure 5.1 left shows the BIC distribution fit to a non-central χ^2, the inset is a blow-up of the tail section of the distribution. The right plot, shows the anticumulative extrapolation of the fit to the tail region and the corresponding values of BIC_{th} for confidence levels of 3σ and 5σ. As can be seen, $\mathrm{BIC}_{th}(3\sigma)$ is about 5 while $\mathrm{BIC}_{th}(5\sigma)$ is ~ 26. A discovery is made if the BIC value exceeds the BIC_{th} for a given confidence level.

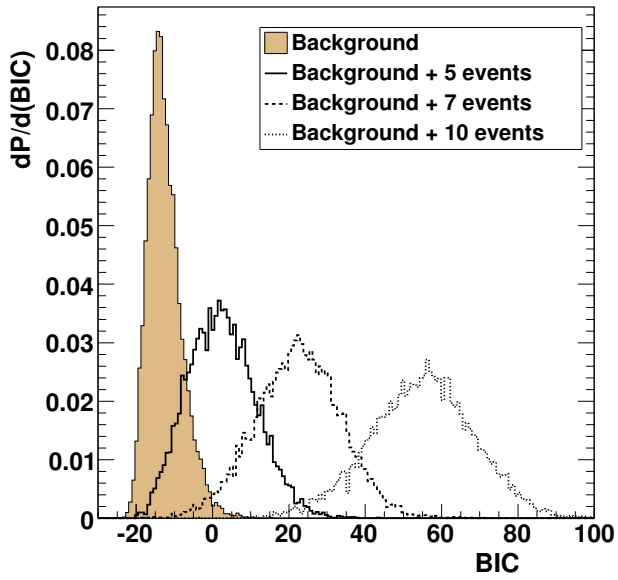

Figure 5.2: *BIC distribution of 10^4 Monte Carlo 1-year experiments events for only-background and background plus 5, 7 and 10 signal events from a source located at $\delta = -80°$.*

Once the BIC distribution for only-background experiments is obtained, the process is repeated adding different numbers of source events to the Monte Carlo samples. To this aim, we have to choose a source location, a spectral index and the desired number of events. As in the only-background case, the highest BIC among the analysed candidate clusters is selected as the sample BIC. Figure 5.2 shows the BIC distributions for different number of source events per year added to the sample for a source located at $\delta = -80°$ and simulated with a spectral index of 2 and compared to the case of only-background distribution (filled histogram). These distributions will enable to test the power of our algorithm as defined in previous chapter, and provide the probability of detecting a source under a given confidence level.

5.2 Discovery power

In order to claim the existence of a source we need to present the results in terms of a **discovery power or potential** as defined in section 4.4.2. A distinction must be made between the interpretation of the results for actually existing experimental data and for the forecast of results of future experiments, i.e. *prospective results*. In the latter case, the discovery power is defined as the percentage of success of discovering a point-like source over the atmospheric neutrino background. The discovery power is

easily inferred from the BIC distribution for a given confidence level. It is a common procedure in astronomy to claim the existence of a source with a 5σ confidence levels. In this work, results for 3σ will also be presented. The discovery potential is computed for a given source and for a series of different number of signal events added to the samples. In this way, we can build discovery plots like the one shown in figure 5.3, which represents the discovery power for a source located at $\delta = -80°$.

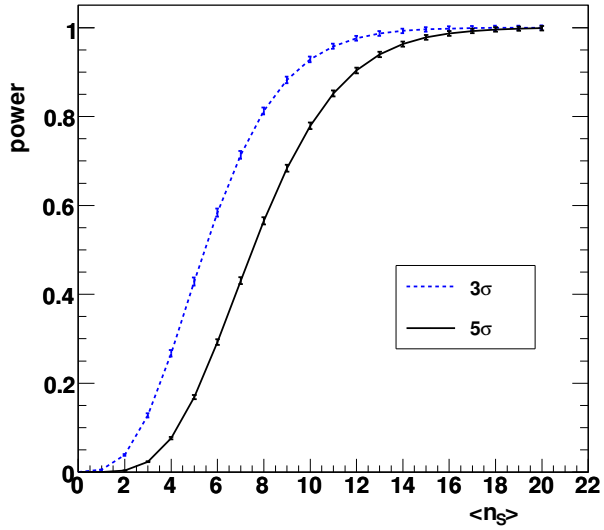

Figure 5.3: *Discovery power as a function of the mean number of observed (after the track reconstruction and selection cuts) events per year from a source located at $\delta = -80°$ for two confidence levels, 3σ and 5σ.*

The plot can be read as follows: Given a number of source events per year observed at the detector, the probability of detecting at a confidence level of 5σ is given by the solid line, whereas the dashed line accounts for the probability at a confidence level of 3σ. For instance a discovery power of p at 5σ means that the corresponding signal (plus background) will produce in $(100 \times p)\%$ identical experiments, in average, a fluctuation over the background whose BIC is equal or higher than a given BIC_{th} where in the case of only-background $P(\mathrm{BIC} > \mathrm{BIC_{th}}) = 5.73 \times 10^{-7}$, i.e. equivalent to five Gaussian standard deviations. The source distributions of the BIC for different values of n_S where shown in the previous section. This n_S represents a fixed number of events added to the simulated 1-year equivalent samples. On the contrary, the discovery potential is presented as a function of $\langle n_S \rangle$, which is the average number of source events observed per year that pass the selection quality cuts of the track reconstruction algorithm. This averaged number of events arises from the fact that a neutrino emission rate suffers from statistical variations following the Poisson statistics. Once the probability is computed as a function of n_S, this probability is properly weighted by the Poisson probability distribution. Being $P(n_S)$ the power for a source located at δ as a function of n_S the corresponding $P(\langle n_S \rangle)$ is given by

$$P(\langle n_S \rangle) = \sum_{n_S=0}^{\infty} P(n_S) \frac{\langle n_S \rangle^{n_S} e^{-\langle n_S \rangle}}{n_S!}. \tag{5.1}$$

The summation of this equation extends to infinity but in practice it can be truncated when the Poisson term becomes negligible. Equation 5.1 gives the discovery power as represented in figure 5.3. As expected, the probability increases as a function of the mean number of events observed from the source reaching the highest efficiency for a moderately large number of events. From figure 5.3 it can be seen that a source located at $\delta = -80°$ will be detected with a probability higher than 50% with a confidence level of $5\sigma(3\sigma)$ if an average of **8(6) source events** are observed in one year.

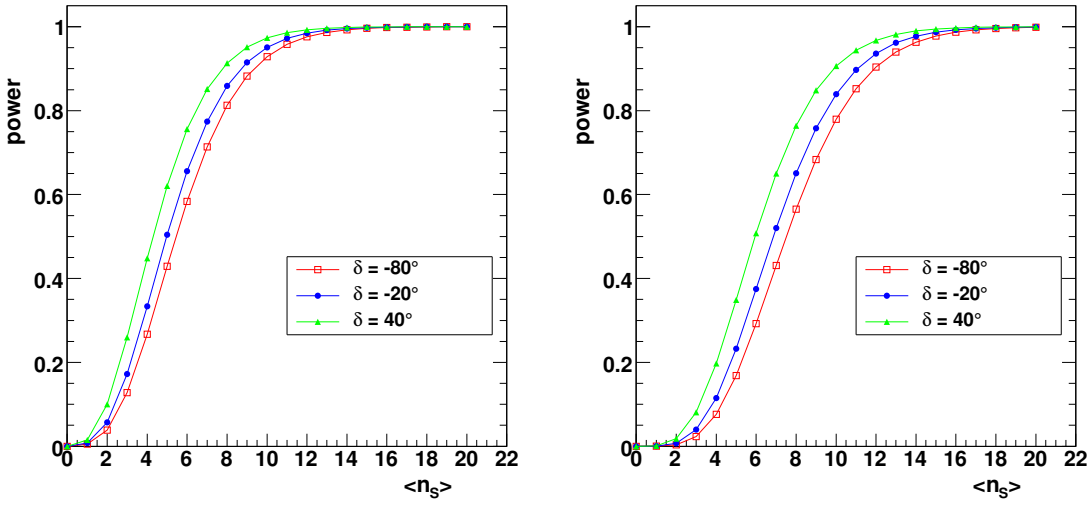

(a) 3σ level **(b)** 5σ level

Figure 5.4: *Discovery power for different sources at different declinations for two confidence levels: 3σ and 5σ.*

The discovery potential depends also on the source location in the sky due to the distribution of the background. Specifically it depends on declination since the atmospheric neutrino background is right ascension independent but with a strong dependence on declination. Figure 5.4 shows the probability of success for discovering a source located at different declinations bands for 3σ and 5σ confidence levels. Lower declination bands show a worse discovery potential, since the number of atmospheric neutrinos per solid angle is larger at these declinations. This declination dependence can be more clearly seen in figure 5.5. The left plot shows the probability of discovering a source when different number of observed events are added to the background samples for the whole declination band. The different curves represent 3, 5, 7, and 10 signal events per year. As expected, not only the potentiality increases as the number of events does, but also there is a declination dependence for each curve. This dependence, however is different for different values of n_S. When $n_S = 3$ the detector reaches the marginal extreme case in which it is impossible to claim the existence of a source on any declination and hence the declination dependence is almost flat. Identically, when 10 observed events are added to the sample, the detector will always identify the source and the extreme of 100% efficiency for all declinations is reached, which explains again

why the dependence is small for this case. Therefore, the declination dependence is more noticeable for the middle range with 5 and 7 observed events added to the sample. The right plot of figure 5.5 shows the required number of events per year observed from a source to yield a percentage for discovering the source of 50%. This probability is presented as a function of the declination band. Note that this number is larger for the declination bands near the celestial South Pole.

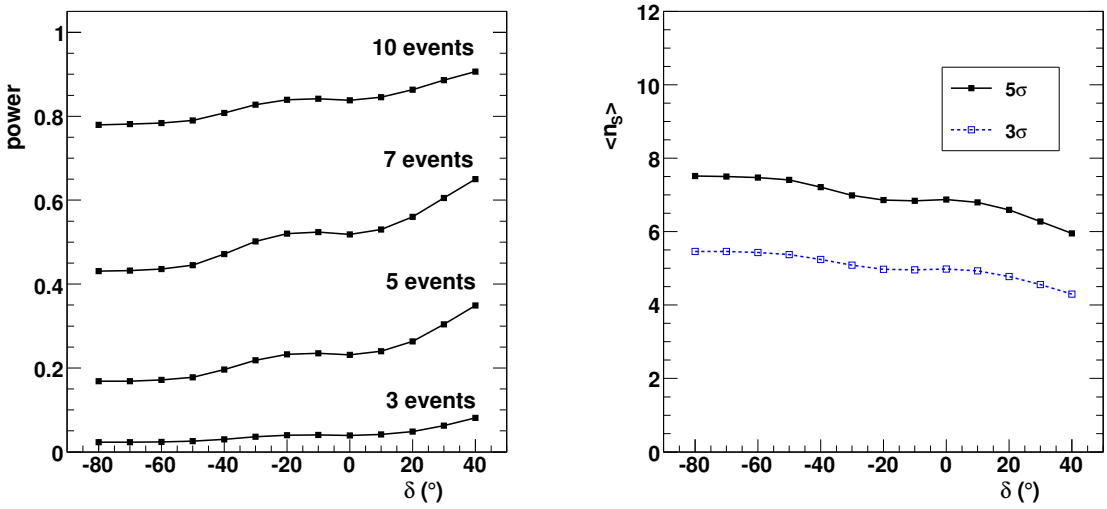

Figure 5.5: *Left: Probability of discovering for a 5σ confidence level as a function of the declination when 3,5,7 and 10 number of source events (on average) per year are observed. Right: Mean number of events required to yield a discovery power of 50% as a function of the declination.*

In the previous chapter, we mentioned that the `dismax` parameter controls the size threshold in the pre-clustering algorithm during the searching procedure. When introducing this parameter, it was also claimed that despite its influence in the number of candidate clusters to be processed, it has a negligible effect in the EM algorithm itself and in the resulting discovery potential provided that a reasonable value is selected.

This is closely related to the fact that the EM-based algorithm is an unbinned algorithm and the data are processed in a continuous way. In a binned method, only events that lie inside the cluster are used to build the significance. On the contrary, in our case, events selected as a cluster are only the starting seeds for the EM algorithm and hence, a threshold in the pre-clustering step does not introduce any bias in the EM methodology. As can be seen is figure 5.6, the discovery power for different number of source events included in the sample is the same in a reasonably wide region of the `dismax` parameter. This uniformity makes possible that the same value for `dismax` can be applied independently of the declination, even when the angular response of the detector is not identical for all declinations. As a result, the algorithm becomes less Monte Carlo dependent since no information about the estimated performance of the detector is used either in the pre-clustering step or in the EM-based algorithm.

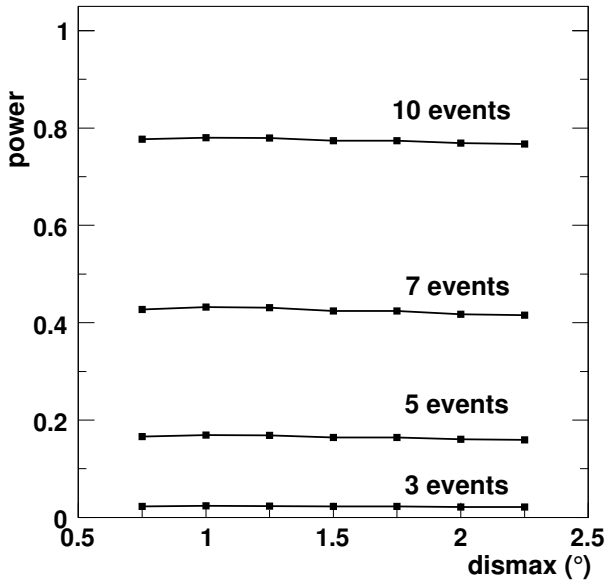

Figure 5.6: *Discovery power for 3, 5, 6 and 7 observed source events as a function of the* `dismax` *value for a confidence level of* 5σ.

5.2.1 Discovery flux

Results from the previous section were presented as a function of the average number of neutrino events detected in one year after the reconstruction and quality cuts. However, the discovery potential is more often shown in terms of the neutrino or muon flux. The neutrino or muon flux averaged over energy can be obtained from $\langle n_S \rangle$, the mean number of observed signal events, by means of the following formula:

$$\Phi_i^{limit}(\gamma,\delta) = \frac{\langle n_S(\delta)\rangle^{limit}}{\left\langle A_i^{eff}(\gamma,\delta)\right\rangle_{10-10^7\mathrm{GeV}} \cdot T(\delta)}, \tag{5.2}$$

where $i = \nu, \mu$, the parameter γ is the spectral index and $T(\delta)$ is the duty cycle of the detector which accounts mainly for the visibility or percentage per year that the given declination δ is visible from the ANTARES location (see figure 5.7). It is important to mention that $\left\langle A_i^{eff}(\gamma,\delta)\right\rangle_{10-10^7\mathrm{GeV}}$ is the *energy averaged effective area* whose definition is not as straightforward as the well-known effective area. This energy averaged effective area depends on the spectral index (contrary to the effective area) since it is weighed by the corresponding muon or neutrino flux. As just mentioned, in this work the visibility factor has been included in the duty cycle term, and hence the averaged effective area does not account for it. However, it may be possible to express the averaged effective areas including this factor.

The effective area can be expressed for neutrinos and for muons:

- **Neutrinos**

  The neutrino effective area (given by 2.12) gives the detector efficiency with respect to an incident neutrino flux and independently of it. The effective area is a function of three parameters: the neutrino energy, E_ν, and the two neutrino

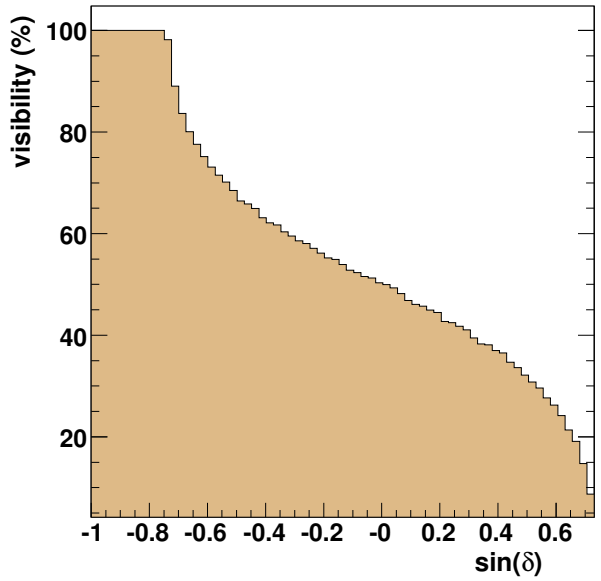

Figure 5.7: *Visibility factor as a function of declination showing the fraction of time that a source at a given declination is visible from ANTARES.*

track angles; θ_ν and ϕ_ν. However, the effective area is frequently presented as a function of only one parameter. In this case, the area is implicitly averaged over the two other parameters. Therefore, when representing the effective area as a function of the neutrino energy we are indicating that it is in fact averaged over $\cos\theta_\nu$ and ϕ. Being the neutrino generation uniform over these two parameters, the computation of effective areas as a function of the neutrino energy is straightforward. On the contrary, when presenting the effective area as a function of some angular direction of the neutrino track, for instance the declination, we need to average over the neutrino energy and therefore a neutrino flux must be introduced. Figure 5.8(a) shows the average effective area of neutrinos. The averaged effective area is computed in the generation energy range, i.e. between 10 GeV and 10^7 GeV.

- **Muons**

  As explained in chapter 2 the muon effective area is not a well defined concept. A proposal for its definition can be found in [163]. This definition leads to a muon effective area as a function of the neutrino parameters (E_ν, θ_ν, ϕ_ν). As in the neutrino case, an assumption about the muon flux is required in order to compute the averaged muon effective area. An additional complication arises since, whereas the neutrino flux is something well known and easily parametrized as a power law, the muon flux at the detector level is not. However, as explained in [150], the number of detected events is related to the muon flux by the muon effective area, hence we can use this relationship to extract the muon flux at the detector. Following a computation similar to that in the case of neutrinos, we obtain the average muon effective area shown in figure 5.8(b).

It is important to remark that averaged effective areas are, in fact, an average estimate of the exact effective area. For a given declination different pair of values of

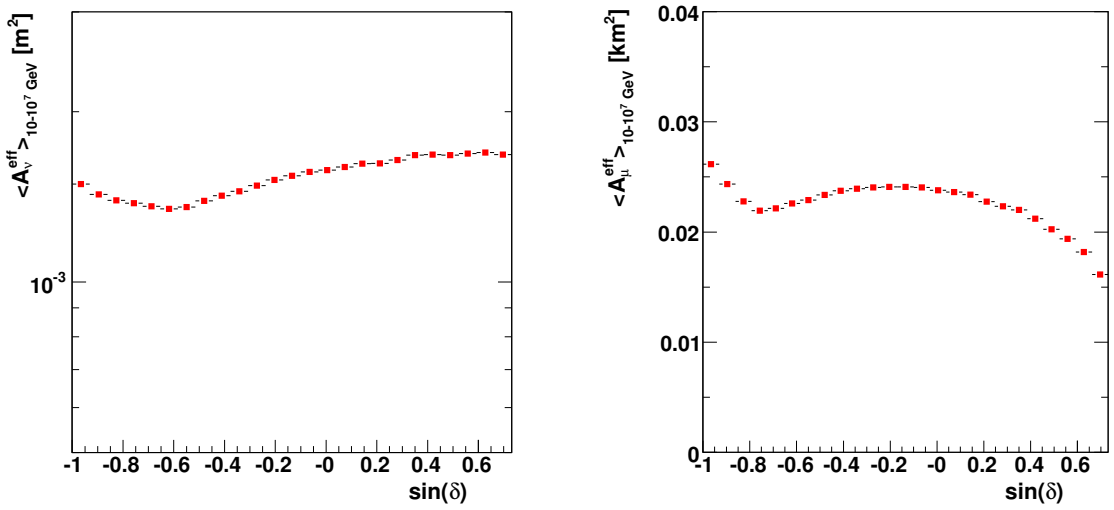

(a) Neutrinos **(b)** Muons

Figure 5.8: *Energy averaged effective areas between $10 - 10^7$ GeV*

the local arrival coordinates (θ, ϕ) are possible depending on the Star Time. Therefore, the *actual* effective area for a declination might be different from the averaged one for a specific arrival time. Although this may be important for GRBs analysis and flux estimations of events coming from transient sources, in the steady source analysis the averaged effective area is an accurate enough variable. In addition, the average result will match the real one as the number of events from the steady source increases.

Using the average effective areas it is possible to compute the corresponding energy averaged fluxes needed to claim the existence of a source at a given confidence level. Figure 5.9(a) shows the required neutrino flux for a power probability of 50% for two confidence levels (3σ and 5σ). When compared to plot 5.5 right, it can be noticed that declination dependence is now inverted due to the visibility factor. In fact, declinations below $-43°$ are 100% visible from ANTARES. An integrated neutrino flux of about 2×10^{-8} cm^{-2} s^{-1} is needed to claim the existence of a source located at $\delta = -80°$ with 50% and 5σ confidence level. Again, this calculation leads to the computation of the muon flux required to have a discovery probability of 50%. The corresponding result for muons is shown in figure 5.9(b).

In some occasions, it is more convenient to show the neutrino/muon differential flux. We can convert the integrated flux to a differential flux for a specific spectral index of 2 scaling by the factor that results after integration in energy. Figure 5.10 shows the neutrino differential flux for a discovery of 50% with two confidence levels assuming a spectral index of 2.

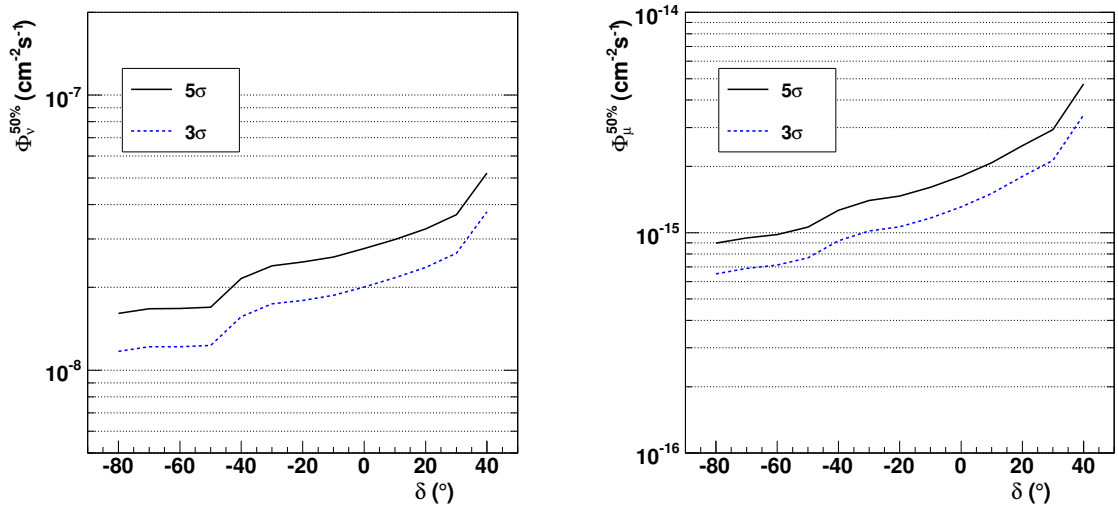

(a) Neutrinos **(b)** Muons

Figure 5.9: *Energy averaged flux required to yield a 50% of probability in discovering the source for two different confidence levels, 3σ and 5σ.*

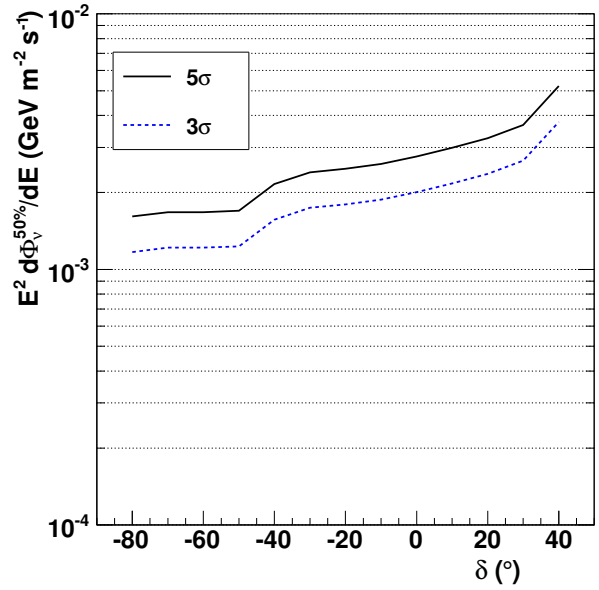

Figure 5.10: *Differential neutrino flux needed to reach a discovery potential of 50% at 3σ and 5σ confidence levels.*

5.3 Source position

One of the advantages of an unbinned method is that as a result, an estimate of the source location is obtained. Contrary to binned methods (in which the origin of the source is defined at the centre of each bin cell), maximizing the likelihood yields an estimate of the parameters $\hat{\alpha}_S$ and $\hat{\delta}_S$ which identify the source location in the sky. This location estimate can be used to test the pointing accuracy of ANTARES in detecting point-like sources. The parameter β_S in figure 5.11 is the pointing angular resolution defined as the median of the angular error between the true source location and the estimated coordinates. Figure 5.11 shows this parameter as a function of the number of signal events included in the sample. As expected, this angular resolution improves as the multiplicity of the cluster increases. The angular resolution when pointing to a source in the ANTARES detector is **less than 0.1**° when a number of 8 events are contributing to the signal cluster and for almost all declination bands within the ANTARES visible map ($\delta = -80°$ to $\delta = 40°$). This pointing angular resolution is, as expected, better than the track reconstruction angular resolution and for the best case, which includes an optimum detector performance and more than 10 observed signal events from the source, it can reach values of 0.06° for a spectral index of 2.

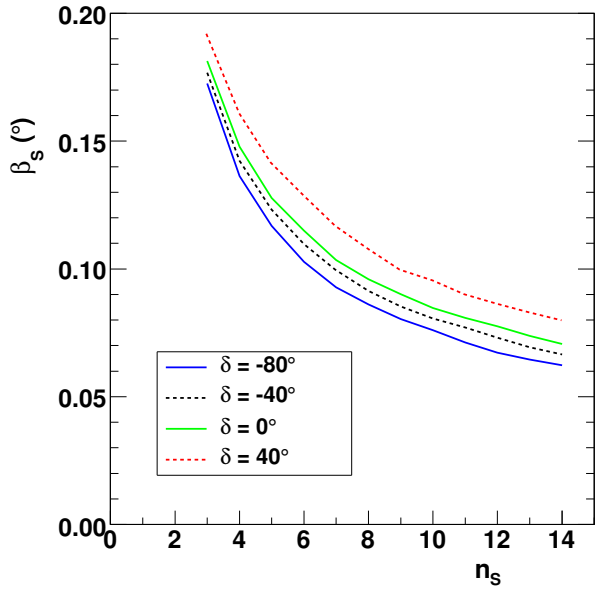

Figure 5.11: *Angular resolution for a point-like source as a function of the number of source events detected.*

Figure 5.12 shows the differences between the true right ascension and declination coordinates and the estimated ones with the EM-based algorithm. The left plots show the distribution when 4 source events are detected, and the right plots are for the case of 5 detected events. The number of entries correspond to the total number of source clusters simulated in 10^4 samples with the selected number of signal events. The Gaussian fit is shown. As expected, the result of this fit leads to the conclusion that the resolution is smaller as the number of events contributing to the signal or multiplicity increases.

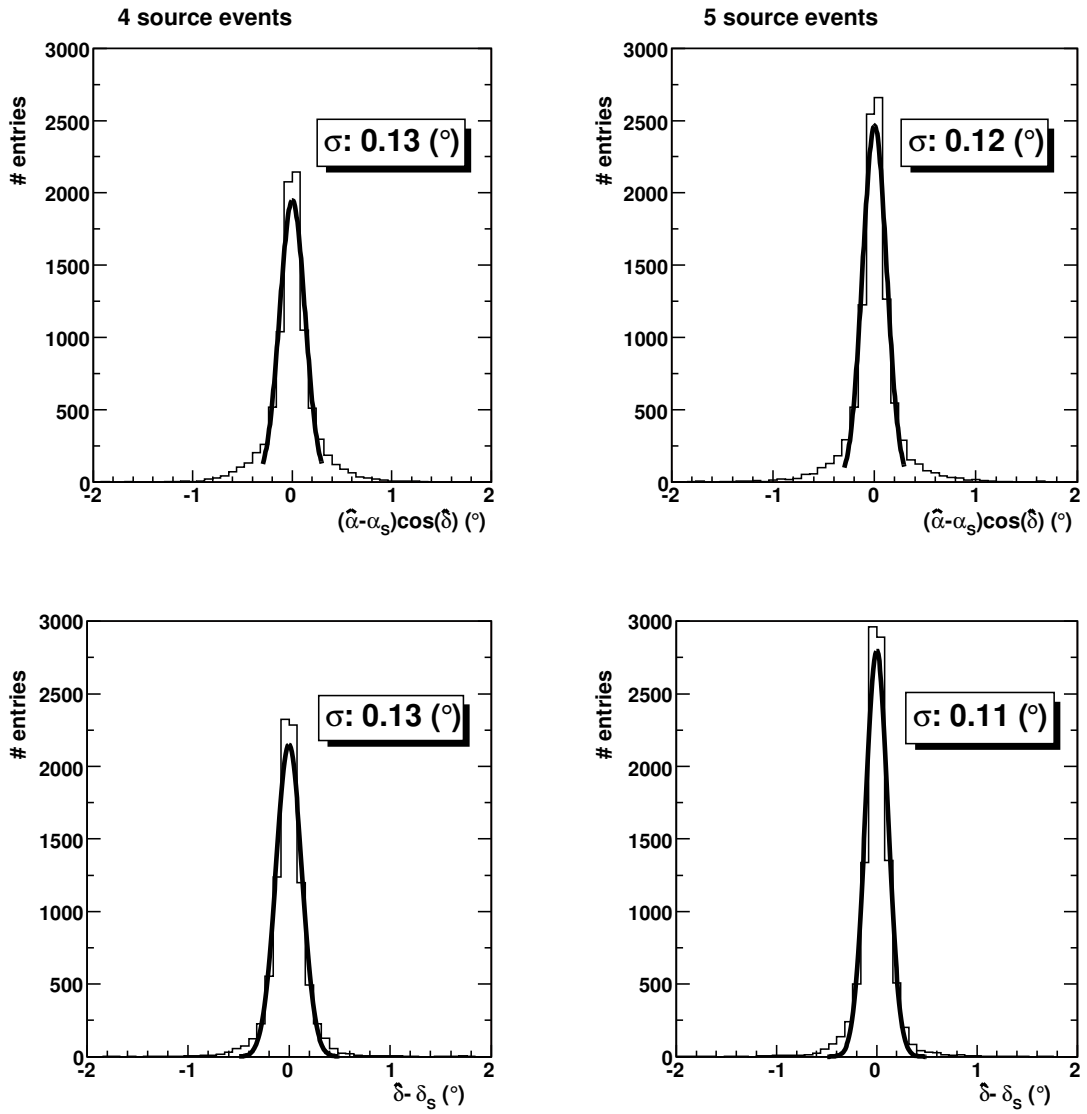

Figure 5.12: *Difference between the fitted and the true source location for 4 (left) and 5 detected events (right) emitted by the source.*

5.4 Spectral index

As mentioned before, in a blind survey of the sky, no assumptions about the source are made, not even on the spectral index of the neutrino flux emitted. However, in the work presented up to now, the signal simulation has been done assuming a spectral index of 2. There are sound theoretical arguments for this assumption. In addition,

the averaged effective area for spectral indexes greater than 2 is low and the derived fluxes required to claim the existence of such sources will be very high. However, in this section we will show how the EM-based searching algorithm performs when different values of γ are simulated. Specially we will see that no optimization of the algorithm has to be done, and the algorithm itself adapts to the shapes of the signal cluster.

5.4.1 Signal shape for different spectral indexes

Apart from the averaged effective area, which will increase the required muon or neutrino discovery fluxes, the track angular resolution will be also affected by the different γ values in the neutrino emission power law. As shown in chapter 3, from figure 4.3 it can be seen how the angular resolution varies according to different spectral indexes. A worse angular resolution will spread the signal shape over the atmospheric neutrino background, and therefore, it is reasonably expected that the searching performance will decrease as the angular resolution gets worse, or in other words, as the spectral index increases.

The EM-based algorithm constitutes a natural way to deal with these signal shape changes due to the different spectral indexes (or angular resolutions), since the widths of the Gaussian are let free during the process, contrary to what happens in the binned methods or even in other unbinned techniques. The algorithm itself will estimate the Gaussian which better fits the signal shape. Figure 5.13 shows three examples of how the algorithm performs for the different Gaussian widths of three different spectral indexes. As can be seen, different spectral indexes yield different Gaussian shapes. The softer spectral index is, the wider the spread the signal over the background. However, the final width estimation increases accordingly and no optimization or fine tuning of the initial parameters in the algorithm is required. The final BIC value for each cluster is also indicated in figure 5.13. More often, the BIC value will decrease as the signal shape spreads since it moves farther away from the Gaussian shape. On the contrary, it can be noticed that in the examples where $\gamma = 2.7$ and $\gamma = 3$ a better BIC value is obtained compared to the case of a harder index $\gamma = 2$. In this particular case, this apparently contradictory situation is due to the presence of background events near the signal cluster which contribute to increase the cluster significance.

Another example of how the EM algorithm adapts itself to different Gaussian shapes is shown in figure 5.14. It is clearly seen that when the spectral index increases so do the estimated Gaussian widths. The root mean square for those distributions are indicated in table 5.1.

	$\gamma = 2.0$	$\gamma = 2.7$	$\gamma = 3.0$
α_{RA}-direction	0.1	0.2	0.3
δ-direction	0.1	0.2	0.3

Table 5.1: *Root mean square for the estimated widths of the Gaussian shapes for different spectral indexes.*

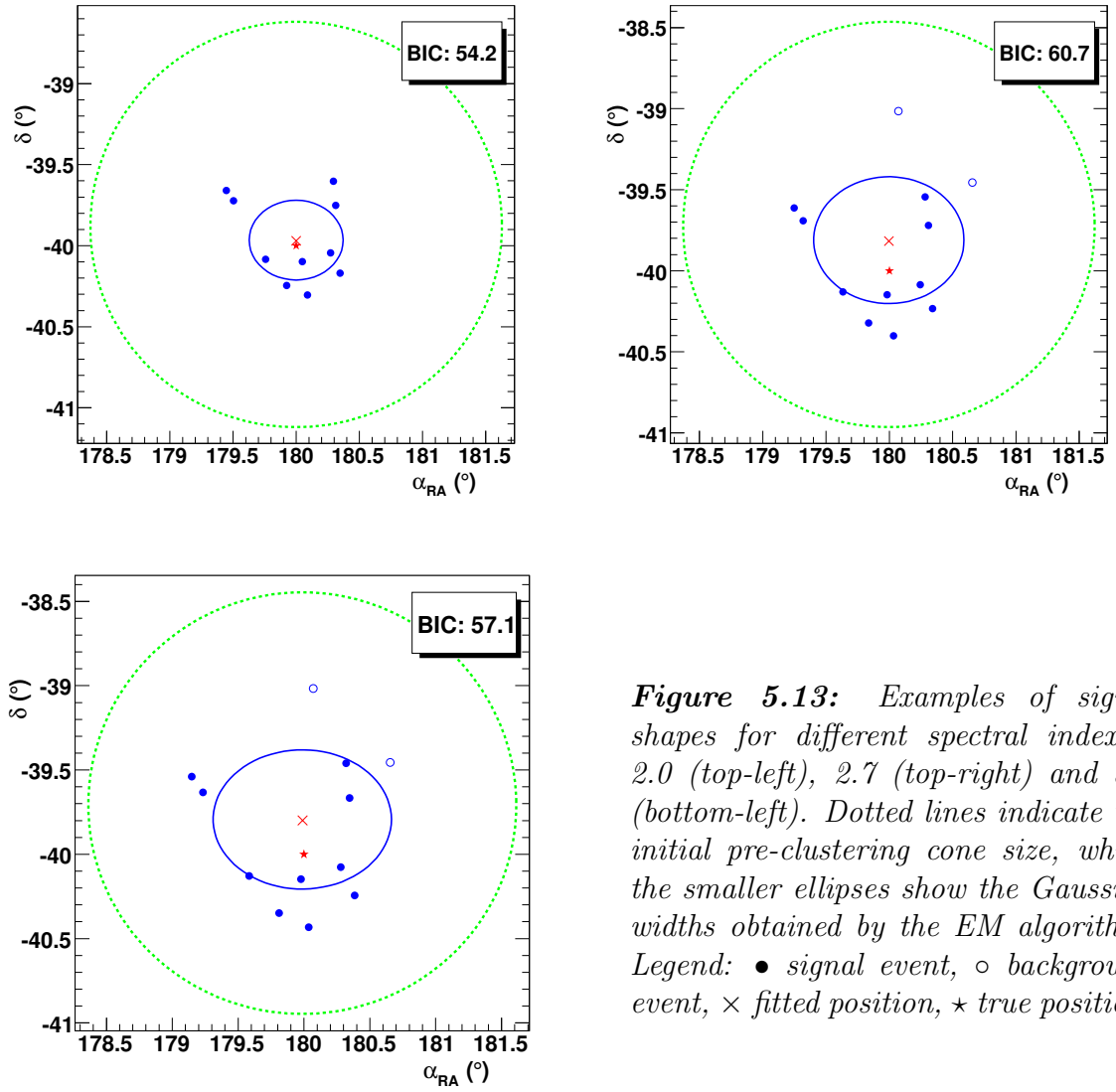

Figure 5.13: *Examples of signal shapes for different spectral indexes; 2.0 (top-left), 2.7 (top-right) and 3.0 (bottom-left). Dotted lines indicate the initial pre-clustering cone size, whilst the smaller ellipses show the Gaussian widths obtained by the EM algorithm. Legend: • signal event, ○ background event, × fitted position, ⋆ true position.*

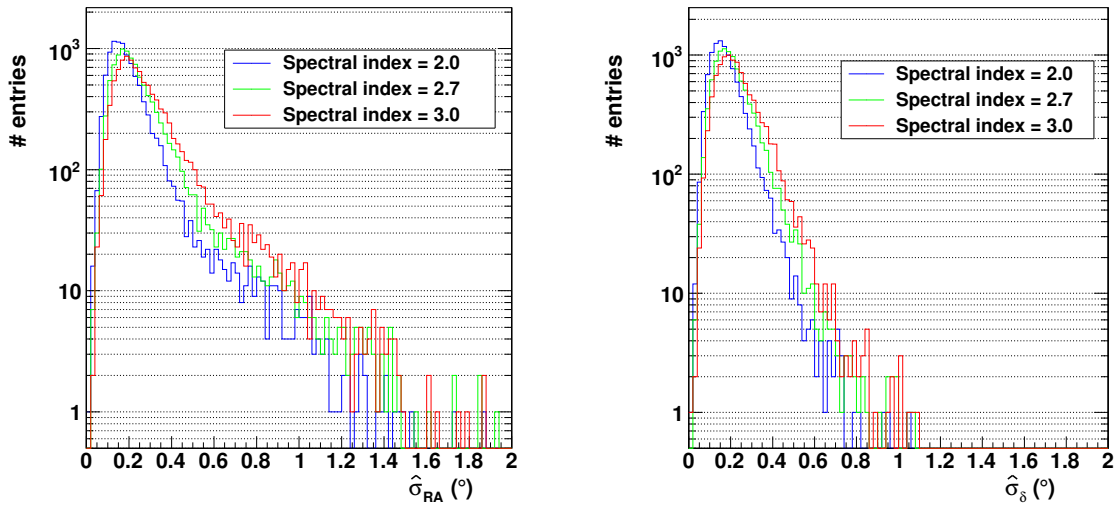

(a) α_{RA}-direction **(b)** δ-direction

Figure 5.14: *Widths of the Gaussian signal shapes estimated by the EM algorithm as a function of two galactic coordinates for three different spectral indexes.*

5.4.2 Discovery power for different spectral indexes

The EM-based algorithm fits naturally different signal shapes derived from different spectral indexes, hence it is expected that the discovery potential as a function of the number of events will not vary dramatically for different spectral indexes. Figure 5.15 shows the discovery power for a source located at $\delta = -80°$ for the three spectral indexes used in this work (2.0, 2.7, 3.0). As can be seen, there is no significant deviation from the *standard* case studied in previous sections ($\gamma = 2$), except the slight decrease expected for those spectral indexes greater than 2.

In figure 5.16, where the number of events needed for a 50% probability of discovery is shown, it is clearly visible that there is only a minor decrease for softer spectra ($\gamma = 2.7$ or 3). It is indeed, in terms of fluxes that these differences are dramatically important due to the differences in the averaged effective areas as a function of the spectral indexes. Figures 5.17(a) and 5.17(b) show the energy averaged effective areas for neutrinos and muons as a function of the declination. The differences reach several orders of magnitude when going from a spectral index of 2.0 to softer spectra.

These differences in averaged effective areas of the detector for different spectral indexes have implications in the estimated neutrino (muon) fluxes required to claim a neutrino source. Figure 5.18 shows the required fluxes for both neutrinos and muons, for the 5σ and 3σ confidence levels. As foreseen, the required neutrino (muon) fluxes to yield a discovery potential of 50% when the neutrino source emits following a spectrum softer than $\gamma = 2$, are essentially too low to be observable by a 0.1 km^2 neutrino detector like ANTARES.

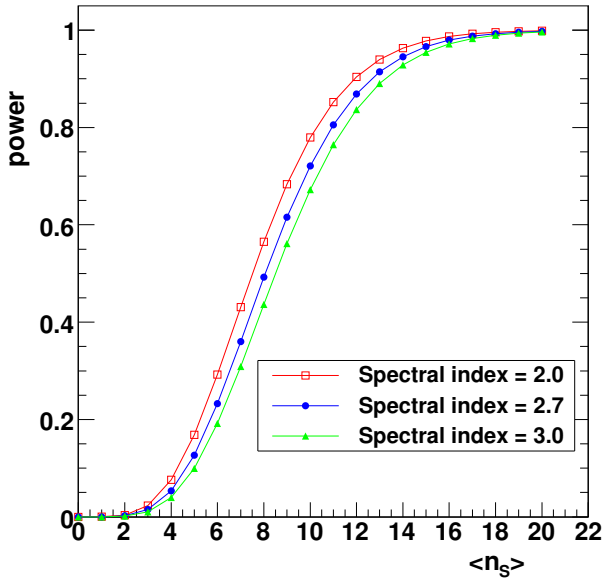

Figure 5.15: *Discovery power for a source located at $\delta = -80°$ as a function of the average detected number of source events for different spectral indexes.*

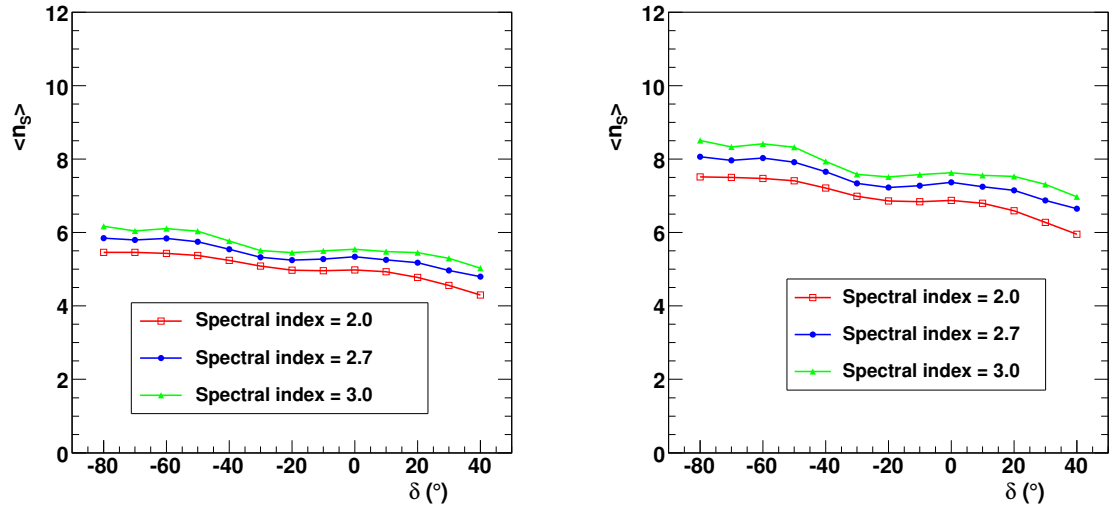

(a) 3σ (b) 5σ

Figure 5.16: *Average number of events that yields a discovery potential of 50% as a function of declination for different spectral indexes at two confidence levels.*

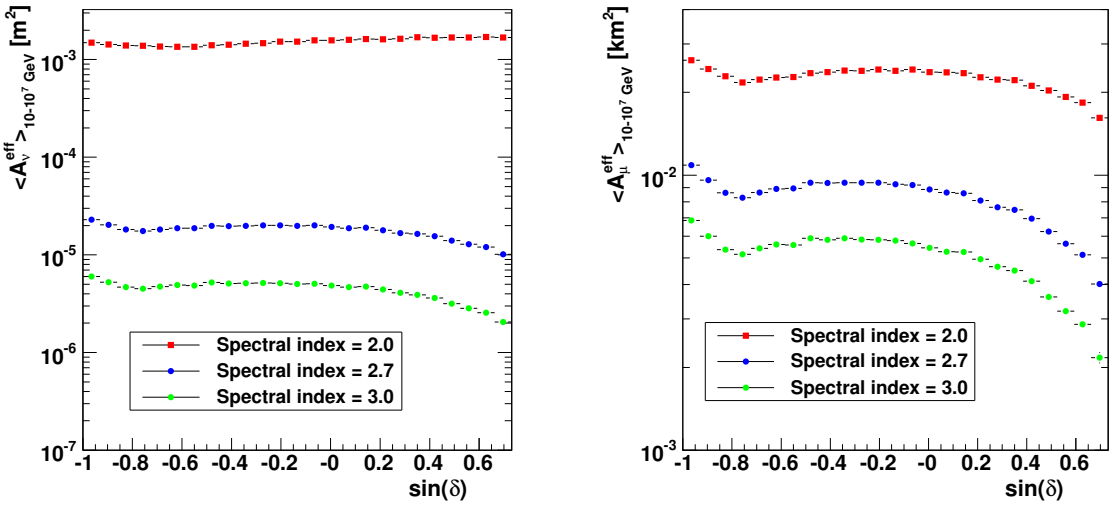

(a) Neutrinos **(b)** Muons

Figure 5.17: *Average effective area for (a) neutrinos and (b) muons as a function of the sine of declination for different spectral indexes.*

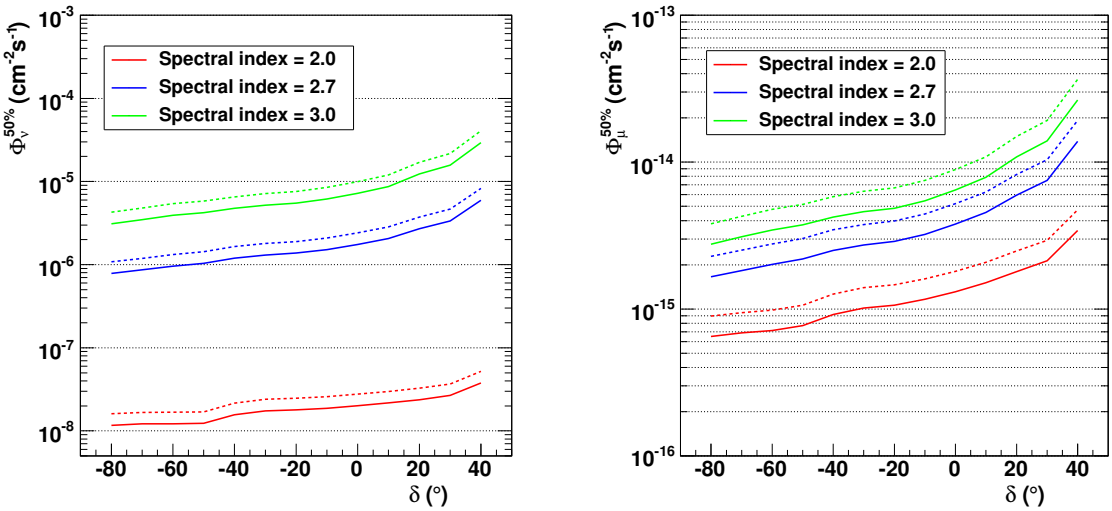

(a) Neutrinos **(b)** Muons

Figure 5.18: *Required neutrino (left) and muon (right) fluxes to claim the existence of a source with a 50% probability for different spectral indexes. Solid lines are for the 3σ confidence level and the dotted lines for 5σ.*

5.5 Sensitivity

The natural effective volume for a neutrino telescope to accomplish a neutrino source detection is 1 km^3 which will be achieved by future Kilometre-Scale detectors like IceCube and KM3NeT. However, a smaller detector with a lower effective volume can also yield interesting results by setting upper limits that might rule out some of the most optimistic models of neutrino emission from point-like sources. In this section, we will present the definition of flux upper limit for a blind survey of the sky, which differs significantly from the upper limit for fixed locations as will be explain in the next chapter. Being ANTARES an experiment that is being built, the data available are still being analysed. In this case, the experimental upper limit cannot be reported and the **sensitivity** of the experiment is used instead. The sensitivity is defined as the average upper limit that would be obtained by an ensemble of experiments with the same, in average, expected background and no true signal. The sensitivity is the average flux limit that guarantees (within a confidence level) that there is no source emitting with a higher flux. In this work, upper limits are computed using a procedure similar to that used with the discovery potential. In a binned technique, upper limits or sensitivities are computed using only the background-only simulated samples since the number of signal events confined in each bin essentially follows the Poisson statistics. The maximum average number of events statistically acceptable at a given confidence level can be derived using the Feldman and Cousins unified approach [164] or the classical Poisson statistics. For unbinned techniques, on the other hand, the methodology is somewhat different since we lack the prior information about how the test statistic for the signal is distributed. In an on-going experiment, we can select an observed value for our discriminator, BIC_{obs}, which corresponds to the highest of all observed BIC values in the sample. The probability that this BIC_{obs} is not coming from a source, or in other words, from the source BIC distribution, can be estimated using the mentioned source BIC distributions. When this probability reaches 90%(99%) it can be ensured that there is no source emitting a flux that would yield a BIC value higher than the one observed with a **confidence level of 90%(99%)**.

In the case of a future experiment, we must define which value of BIC_{obs} is selected. In other unbinned techniques, the median of the only-background BIC distribution is selected as BIC_{obs}, which constitutes a reasonable selection. In this work, however, we will perform differently by computing the upper limit for all the outcomes of background distribution. Each upper limit is then weighed by the corresponding BIC_{obs} weight in the background distribution. In this way we build the sensitivity of the experiment or the average upper limits. Selecting the number of events excluded with a probability of 90%(99%) we can build the sensitivity for two confidence levels.

Figure 5.19 left shows the sensitivity expected for ANTARES as a function of the mean number of observed events per year and for two confidence levels in a blind search, that is, making no assumptions about any preferable position of the source. This means that, in average, a source located at $\delta = -80°$ and emitting the equivalent, or higher, flux to **6(10) observed events** will be excluded with 90%(99%) C.L. by ANTARES. Using the conversion formula 5.2 we can obtain the excluded averaged energy integrated neutrino flux for the two confidence levels 90% CL and 99% CL.

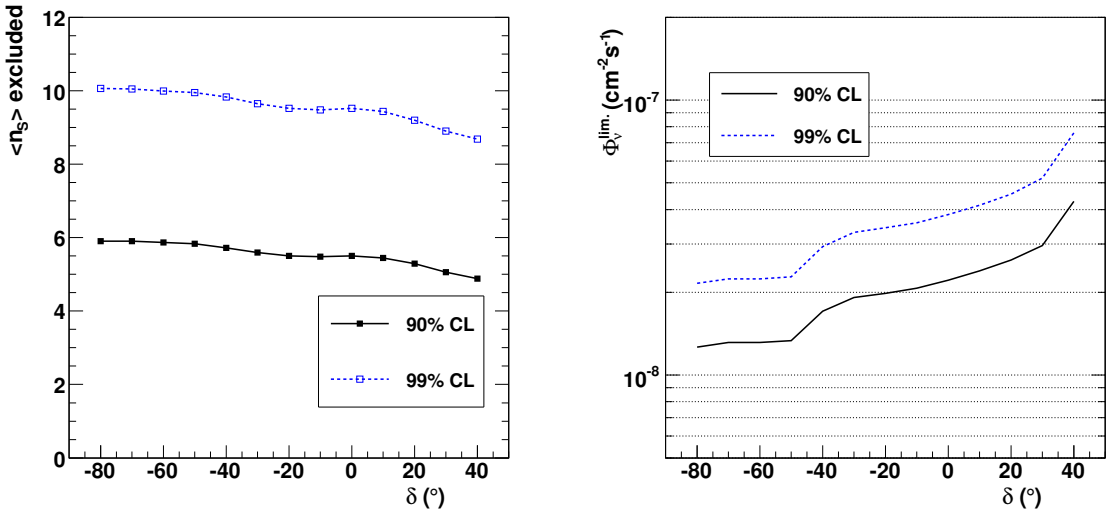

Figure 5.19: *Left: Average upper limits in terms of mean number of excluded events as a function of the declination for 90% and 99% C.L. Right: Same result presented in terms of the energy averaged neutrino flux (10 − 10^7 GeV).*

5.6 More than one year of data-taking

The results presented up to know have been obtained assuming only one year of data-taking. Obviously, after more than one year of operation the sensitivity of the detector will improve and so will the discovery potential to point-like sources. In this section we show the results of the EM-based algorithm applied to data samples whose time duration are equivalent to 2 and 5 years. Results will be presented also in terms of the average number of source events per year observed after track reconstruction quality selection. The sample simulation follows a similar procedure to that of the one year case except that obviously the number of atmospheric and source events has been increased accordingly. However, due to computing power and storage limitations, the number of samples that can be generated is limited. Hence for a 2-year simulation the number of samples is reduced from 10^4 down to 5×10^3 and to 2×10^3 when simulating 5 years of data-taking. Figure 5.20 shows the sky seen from ANTARES after 2 and 5 years of data-taking.

The EM-based algorithm has not been optimized for the case of several years of data-taking. This constitutes a proof of the robustness of the method, since no optimization is needed in order to adapt the analysis when more background is expected in the sample. In the next sections we will explore the potentiality of the algorithm when more than one year of data-taking is analysed. It should be mentioned that in the real experiment the best strategies to combine the data of different periods should be considered carefully. If a source search analysis has been performed using a 1-year equivalent sample, the data used in this case should be excluded from a more general 2 or 5-year analysis. This is part of the *unblinding* policy of the experiment that are not treated here, but that is a crucial step in the real detector analysis. In addition,

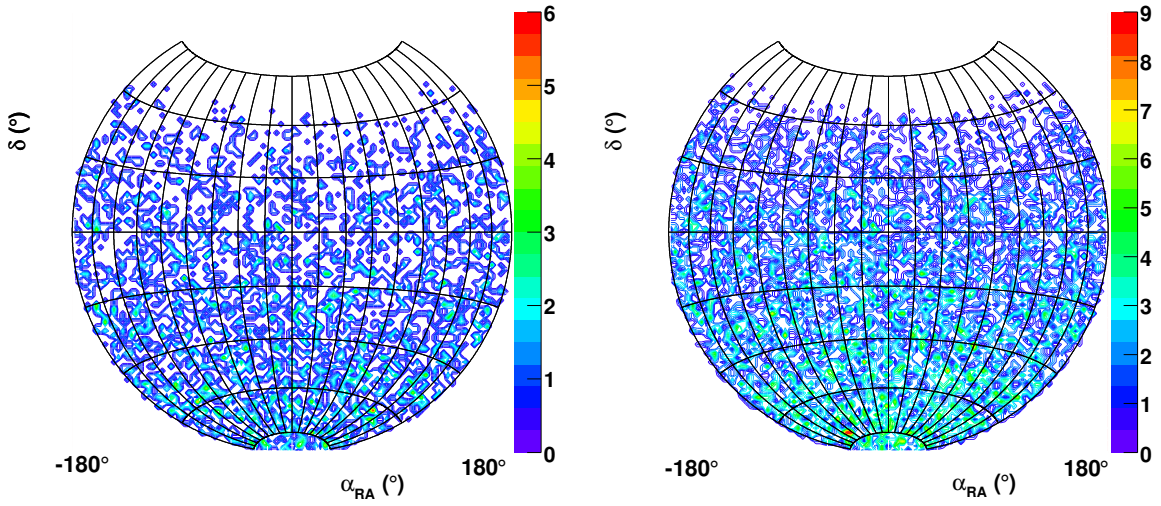

(a) 2 years **(b)** 5 years

Figure 5.20: *Sky maps for more than one year of data-taking. The samples are built using only-background events.*

the detector performance may change as a function of time due to different deployment stages of the detector or unexpected failures of some of its components, which should be taking into account when analysing longer periods of data.

5.6.1 Discovery potential for more than one year

The definition of the discovery potential is the same than in the case of one year. It should be noticed that $\langle n_S \rangle$ still indicates the average number of events per year. Figure 5.21 shows the discovery potential as a function of this variable for 2 and 5 years of data-taking for a source located at $\delta = -80°$. As can be seen, the discovery potential increases with the exposure time or duty cycle of the detector. About **5(3) observed events** per year are necessary to claim the existence of a source at a declination $\delta = -80°$ with a discovery power of 50% and a confidence level of $5\sigma(3\sigma)$ for a 2-year analysis, and about **3(2) observed events** per year in the case of 5-year data sample. We obtain an improvement with respect to the 1-year data of **30%(60%)** for 2(5) years for a 5σ confidence level. Table 5.2 summarizes the comparison of the discovery potential results of different periods of data-taking.

Figure 5.22 shows the required number of observed events from a source required to claim its existence with a probability of 50% as a function of the declination for 2 and 5 years. This limit means that in 50% of identical experiments, in average, a source will be identified if the shown number of signal events is observed. As can be seen for the 5-year case, the two lines representing the 3σ and 5σ confidence level are very similar. In addition, the dependence on declination is very small. The reason is that for 5-years we are reaching the highest performance of the method.

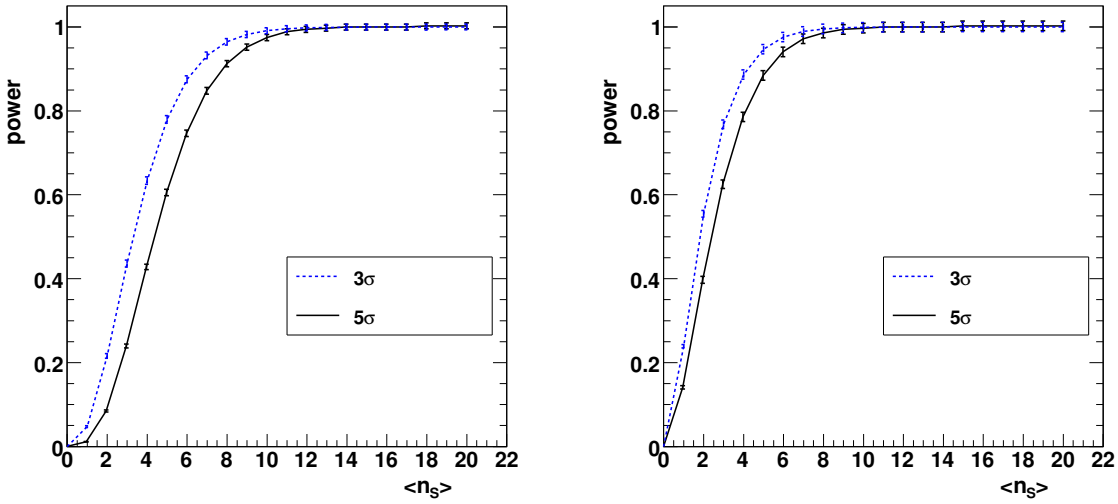

(a) 2 years **(b)** 5 years

Figure 5.21: *Discovery power for a source located at $\delta = -80°$ as a function of the observed number of events for different periods of data-taking.*

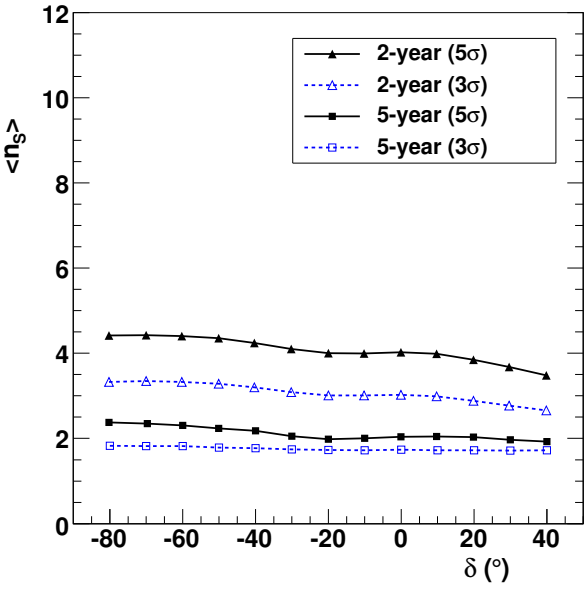

Figure 5.22: *Average number of observed events from a source required to claim the existence of the source with a probability of 50% as a function of the declination and for different periods of data-taking.*

Conf. level	1-year	2-year	5-year
3σ	5.5	3.2	1.7
5σ	7.5	4.5	2.5

Table 5.2: *Number of events per year required to reach a discovery power of 50% for a source located at $\delta = -80°$ for the indicated data-taking periods and confidence levels.*

As usual, we can convert the number of observed signal events to a neutrino or muon flux. This conversion is done using the same procedure described in previous sections. Figure 5.23 shows the energy averaged neutrino flux required to make a discovery with a 50% probability for a 2-year and a 5-year data sample.

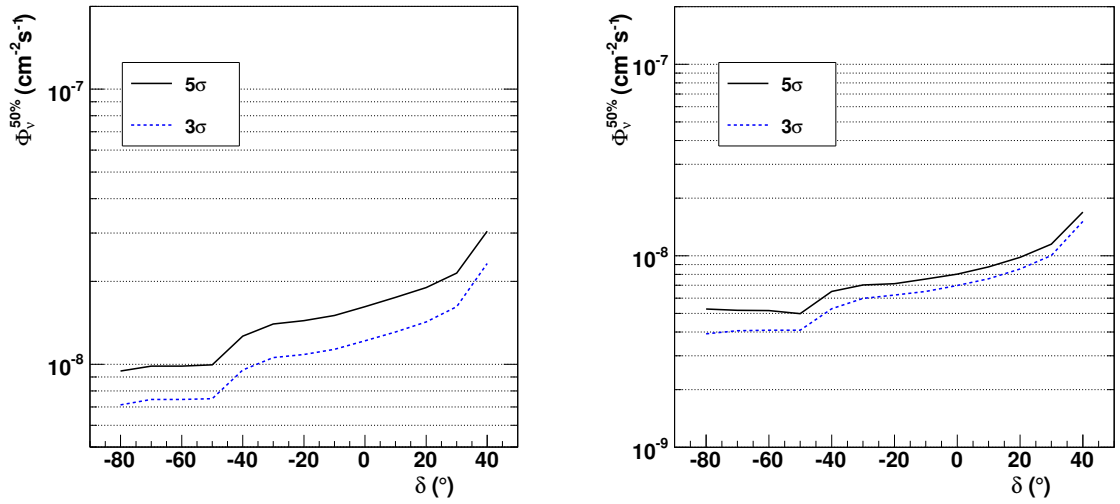

(a) 2 years **(b)** 5 years

Figure 5.23: *Energy averaged neutrino flux required to make a discovery with a probability of 50% for two confidence levels and different periods of data-taking.*

As can be seen, an increase of about **40%** is obtained in the case of 2 years of data-taking compared to one year, and this percentage increases up to **70%** in the case of 5 years, for a confidence level of 5σ.

The same situation arises when comparing the discovery potential in terms of the required muon flux. Figure 5.24 shows the energy average muon flux required to yield a discovery power of 50% for the analysis of the two different time equivalent data samples and for two confidence levels.

In this section we have shown that the ANTARES discovery performance can be significantly improved by increasing the exposure time of the detector. Not only the effective area will be improved, but also the capacity of the algorithm to identify a fluctuation of signal events over the background.

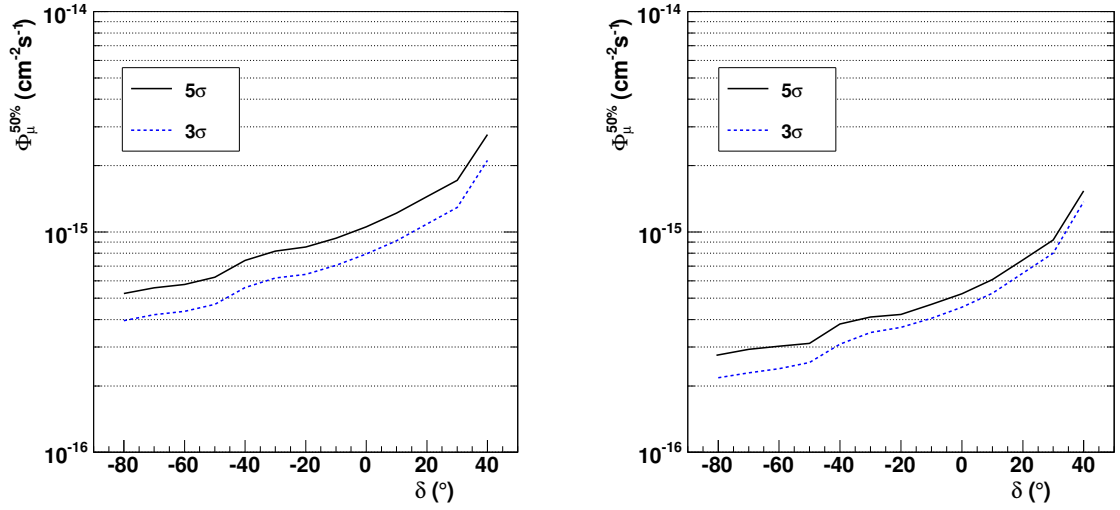

(a) 2 years

(b) 5 years

Figure 5.24: *Energy averaged muon flux required to make a discovery with a probability of 50% for two confidence levels and different periods of data-taking.*

Chapter 6

Fixed point-like sources search

– I've never seen a supernova blow up. But if it's anything like my old Chevy Nova, it'll light up the night sky!
Phillip J. Fry, Futurama.

In the previous chapter we performed and analysed the results coming from a blind survey of the whole sky in which no assumptions about the neutrino source were made, apart from the educated guess of a power law emission spectrum. However, the presence of a luminous source in other counterparts of astroparticle observations (gamma rays, X-rays, protons) might be used as an indication of the existence of a neutrino source in a given direction of the sky, since no direct observation of high energy astrophysical neutrino sources has been made up to now. This information can be used in order to constrain the search to specific regions of the sky in which there are presumptions of a neutrino emitter. Hence, a list of regions in the sky (declinations and right ascensions) can be elaborated providing a set of candidate neutrino sources based on theoretical predictions or on experimental data.

The analysis presented in this chapter shows how the EM-based algorithm can be applied to the search for point-like sources in a given series of fixed locations in the sky. In this case some constraints in the algorithm can be applied since we already select the direction in which the algorithm looks at. By specifying the direction of the source we are reducing considerably the chance of the background to imitate a signal cluster. For that reason, the results for a fixed search are better and present a greater discovery potential and sensitivities. This analysis can lead to an upper limit flux for some candidate sources, and we will be able to reject (or not) some models that predict the neutrino emission for a given list of candidate neutrino emitters.

6.1 BIC distributions for the fixed source search

For the analysis of the fixed point-like source search, we have simulated 10^4 Monte Carlo experiments equivalent to one year of data-taking in ANTARES. In this case, there is not a pre-clustering step, since a given direction is already introduced as input in the algorithm. However, the initial cone size, `dismax`, is used to select the starting event seeds for the EM algorithm. Another difference in this analysis compared to the

full sky survey or blind search, is that there is no need of a minimum cluster size since one single event may result in a sizeable significance.

Only one BIC per sample is produced, contrary to the blind search in which the highest BIC value was selected among all the BIC values of the candidate clusters. When constraining the position of the source to a given direction, the number of degrees of freedom is being limited. Hence, this situation will have a direct impact on the BIC distribution, both for the background-only case and when different signal events are added to the samples. Figure 6.1 shows the BIC distributions for the fixed source searches for a selected declination of -80°. The full histogram shows the BIC distribution for the only-background case, whilst the rest of histograms are the result when 1, 3 or 5 events are added to the sample. It is important to mention that the BIC distribution for the only-background case will be different depending on the declination that has been selected, which was not the situation for a full sky blind search.

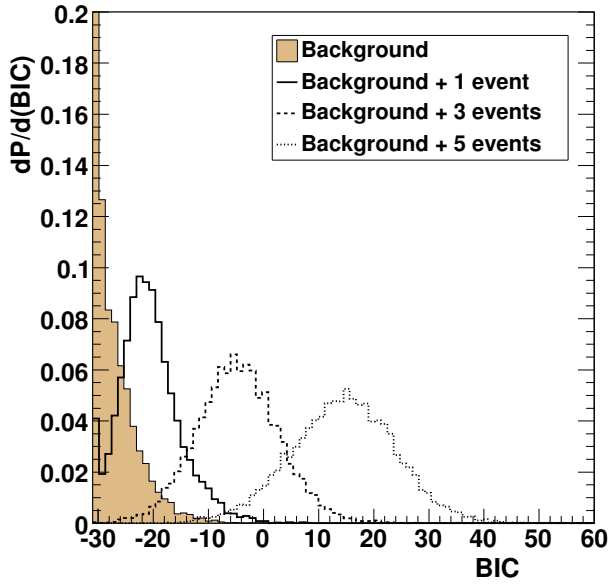

Figure 6.1: *BIC distribution for a selected direction in the sky of $\delta = -80°$ for the only-background case and when 1, 3 and 5 signal events are added to the sample.*

As can be seen from the figure, in the only-background BIC distribution there is a high population in the first bin. When no cluster or accumulation of events are present in the neighbourhood of the region that we are observing, the likelihood of the background plus source model equals the only-background likelihood and hence the algorithm ends with a null fit, yielding a value of the BIC of about -30 which corresponds to the last term of equation 4.22.

As explained in the previous chapter, the BIC distribution can be asymptotically expressed for high number of events as a $\chi^2_{2\nu}$ distribution with ν degrees of freedom. In this case, the degrees of freedom have been reduced since two parameters are fixed in the algorithm, i.e. the position of the source. Figure 6.2 shows the BIC distribution for the only-background case and a declination of $\delta = -80°$. The line is the fit from a $\chi^2_{2\nu}$ to the tail of the distribution. The inset shows the extrapolation in the cumulative distribution to the tail region of the BIC distribution. As can be seen, the value of 3σ

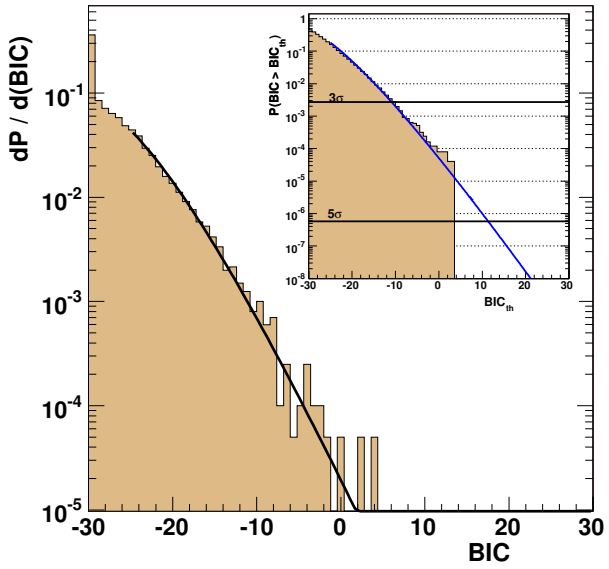

Figure 6.2: *BIC distribution for the background for a selected direction in the sky of δ= -80°. The inset shows the anticumulative distribution. The BIC values corresponding to 3σ and 5σ are indicated.*

can be directly extracted from the distribution, however for higher statistics like 5σ, we need the extrapolation of the fit in order to infer the BIC_{th} equivalent for 5σ, that is, the one that satisfies $P(\mathrm{BIC} > \mathrm{BIC}_{th}) = 5.73 \times 10^{-7}$. As can be seen from the inset, $\mathrm{BIC}_{th}(3\sigma) \approx -10$ and $\mathrm{BIC}_{th}(5\sigma) \approx 11$ for a declination of $\delta = -80°$.

6.2 Discovery potential

The discovery potential introduced in the previous chapter was applied to the whole sky region covered by ANTARES. In this section the definition of discovery potential is slightly different since it is applied to a given direction in the sky. This kind of search will be used when there are hints of a possible high energy neutrino source through observations by other cosmic messengers, or by theoretical predictions. Obviously, the reasons to search in a given direction of the sky should not be based on the data themselves since in that case the prior knowledge introduced would prevent any sensible probability estimation. A more interesting magnitude is the sensitivity or upper limits applied to fixed directions or candidate sources as we will explain in the next section.

The procedure to compute the discovery potential for the fixed source search is similar to the one described in section 5.2. Figure 6.3 shows the evolution of the discovery potential as a function of the mean number of observed events (after quality cuts) emitted by the source for three different sources with a confidence level of 5σ. As can be seen, a lower number of events are required to yield a given discovery potential compared to the full *blind* search.

Since for the steady sources the atmospheric neutrino background is right ascension independent, the location of the source along this coordinate is immaterial. Hence in this study we have selected only one source per declination band, and the right

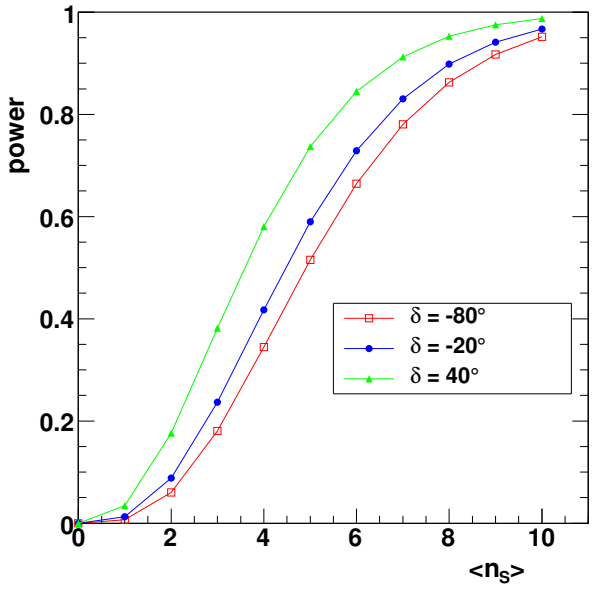

Figure 6.3: *Discovery power for three different declinations as a function of the average number of events emitted by the source for a confidence level of 5σ.*

ascension has been selected randomly. Figure 6.4 left shows the average number of observed events required to achieve a discovery potential of 50% for each declination band and for two confidence levels. Compared to the discovery potential for a full sky search, these numbers are much lower. As an example, if we observe a region of the sky located at $\delta = -80°$, a source will be identified with a probability higher than 50% and $5\sigma(3\sigma)$ confidence level, if an average of **5(3) source events** are observed. The reason for this low number is that the number of trials of the background to reproduce an excess equivalent to a cluster of a source signal is being limited since we are constraining our search to a specific direction of the sky. Hence, fewer number of events in the selected region will produce a sizeable increase in the significance.

In figure 6.4 right, the integrated neutrino flux (above 10 GeV) required to achieve a discovery potential of 50% can be seen. In this case we can see an improvement in the discovery performance of the detector when pointing at a specific region of the sky of $\sim 35\%$ for a confidence level of 5σ when compared to the search in which no assumption about the origin of the source is made. In the case that no evidence of a neutrino source emitter is obtained by the blind sky search, the next step would be to analyse the signals coming from specific direction in the sky corresponding to a set of candidate sources of neutrinos. Moreover, the method proposed here can be extended straightforwardly to the case in which several candidate sources for neutrino emissions are considered. In this case the combined signal expected by the set of candidate sources can be studied.

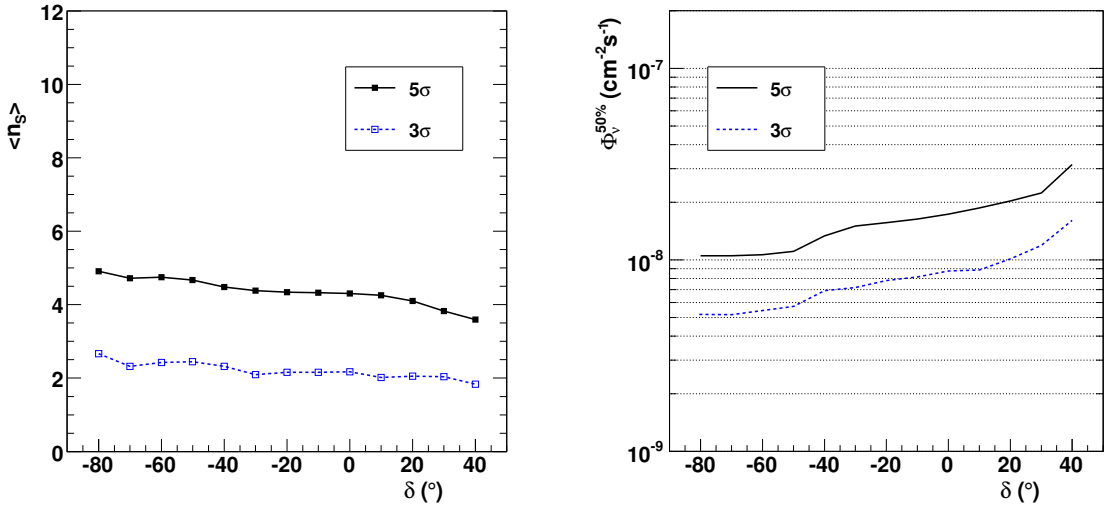

Figure 6.4: *Left: Number of events required to yield a probability of 50% in the discovery power as a function of the declination for two confidence levels. Right: Integrated neutrino flux ($10 - 10^7$ GeV) to yield a probability of 50% in the discovery power.*

6.3 Sensitivity to fixed directions

As explained in the previous chapter, if no excess of events in the sky is observed, we can set an upper limit on the expected neutrino flux on the whole sky. However, when the analysis is constrained to a specific direction in the sky, it can be used to set an upper limit on a given neutrino candidate source. In this section, we will introduce the sensitivity of ANTARES for the fixed direction analysis. As expected, the sensitivity of the detector to specific locations in the sky will be better that the one presented for a full sky survey.

The procedure to compute this average upper limit is similar to the one in the previous chapter. When no point source is added to the sample, the BIC follows the distribution for the only-background case. Then an observable value, BIC_{obs}, is selected and the upper limit is computed and weighed according to the only-background BIC distribution. The average value over an ensemble of identical, on average, experiments is called the sensitivity of the experiment. This sensitivity can be calculated using different confidence levels. Figure 6.5 left shows the sensitivity for 90% and 99% CL in the average number of events that can be excluded. This limit in the number of observed signal events can be extended to neutrino fluxes. In figure 6.5 can be seen the sensitivity of ANTARES in the integrated neutrino flux of the direct search for fixed positions in the sky in one year and for two confidence level.

The sensitivity presented here has an important role in the definition of the foreseen performance of an experiment. In fact, the comparison of the sensitivity for neutrino telescopes is generally shown in terms of fixed directions in the sky. In the next section, we will compare the ANTARES expected sensitivity to other existing and

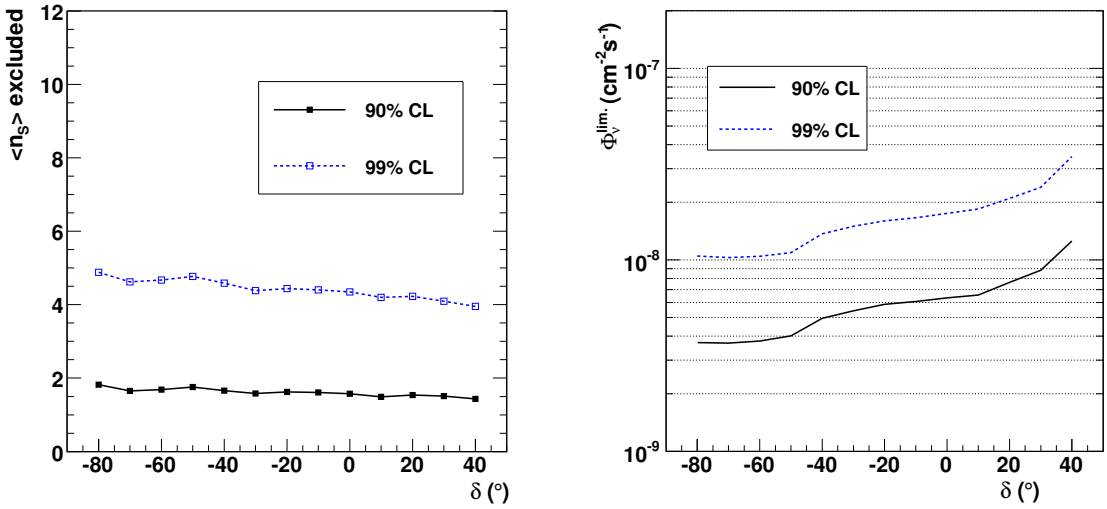

Figure 6.5: *Left: Average number of excluded events for 90(99)% CL as a function of declination. Right: Integrated neutrino flux (above $E_\nu = 10$ GeV) excluded for two confidence levels.*

future neutrino telescopes.

6.3.1 Comparison with other experiments

At present no claim of an astrophysical high energy neutrino source has been made. It is foreseen that the new generation of Kilometre-Scale neutrino detectors, such as IceCube at the South Pole or KM3NeT in the Mediterranean sea, will be able to increase the sensitivity for the detection of cosmic neutrinos below the theoretical models of neutrino emission. Hence a discovery of a point source is expected during the lifetime of these Kilometre-Scale detectors. In the meanwhile, experiments like ANTARES and AMANDA-II can provide very interesting upper limits and rule out some of the most optimistic models of neutrino emission as well as different candidate sources. In particular, ANTARES will be able to establish in the near future the best upper limit ever set on neutrino emission from the southern sky, which includes the promising region of the Galactic Centre. In this section we will review the expected sensitivity of ANTARES in comparison with several experimental results from other neutrino detectors. The different upper limits shown here are calculated for fixed directions in the sky and they correspond to several exposure times depending on the data analysed.

Figure 6.6 shows the sensitivity on the integrated muon flux over 10 GeV for the ANTARES experiment as compared with other experiments. The MACRO [165] results are computed with 1100 up-going muons for a live-time of 6.3 years with a search bin of 3°, and integrated above 1.5 GeV. The 90% C.L. upper limits from Super-Kamiokande-I [166] were derived from a set of 2359 up-going muon events in 4.6 years and with a

search cone of 4° integrated above 3 GeV. The AMANDA-II source limits in the muon flux are obtained from the data collected in the year 2000 consisting in 699 events in 0.5 years of data taken. These are the only neutrino induced muon limits published by AMANDA-II [167].

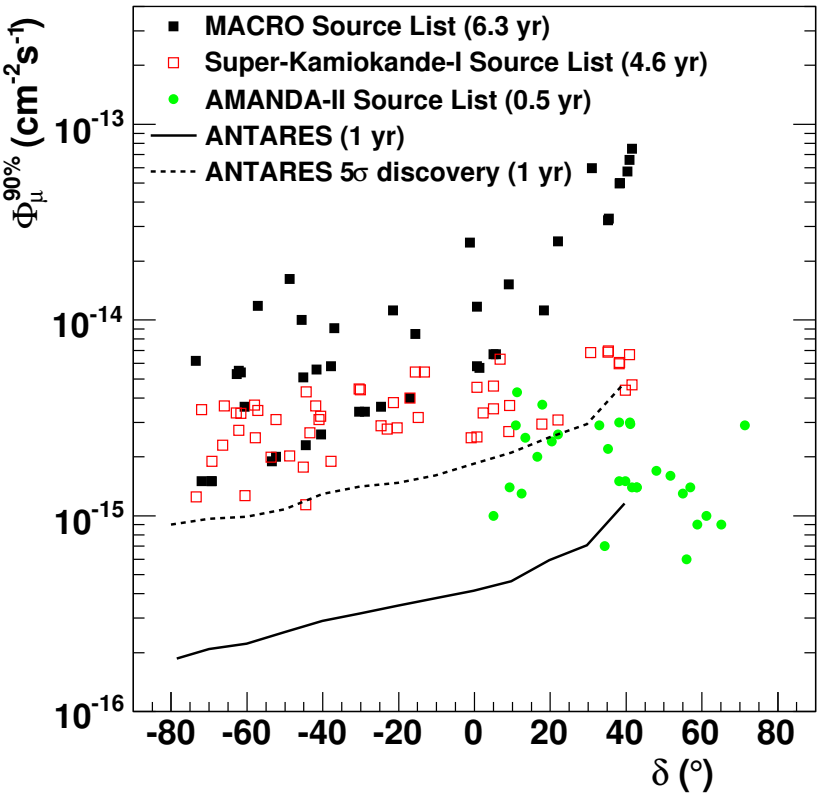

Figure 6.6: *Upper limits (90% C.L.) on the integrated muon flux as a function of the declination. Published limits from MACRO [165], Super-Kamiokande-I [166] and AMANDA-II [167] are shown. The expected ANTARES sensitivity and the discovery potential (5σ) for 1 year of live-time are also shown. See text for further details.*

As can be seen, the limits set by MACRO on a neutrino induced flux do not exclude the possibility that ANTARES will discover a source at 5σ confidence level. On the contrary, some of the limits set by Super-Kamiokande-I to a few number of sources exclude the possibility of a discovery by ANTARES from those sources. Nonetheless, the discovery of *any* source located in the same declination band is not excluded. It should be noted that ANTARES live-time has been calculated assuming a 100% efficiency of the detector during the data-taking, which means that no dead-times in the acquisition due to detector maintenance operation or high levels of optical background have been taking into account. Hence, it is foreseen that the sensitivity shown here will be achieved only after more than one year of data-taking.

It is more convenient to show the sensitivity in terms of a differential neutrino flux with spectral index of 2 for the sake of comparison. Figure 6.7 shows the sensitivity of ANTARES compared to other experiments. The MACRO results are presented now together with the analysis of AMANDA for the period between 2000 and 2004 corresponding to 4282 up-going muon tracks [99]. Also indicated is the limit that is expected to be set after one year of data-taking with the IceCube detector [168].

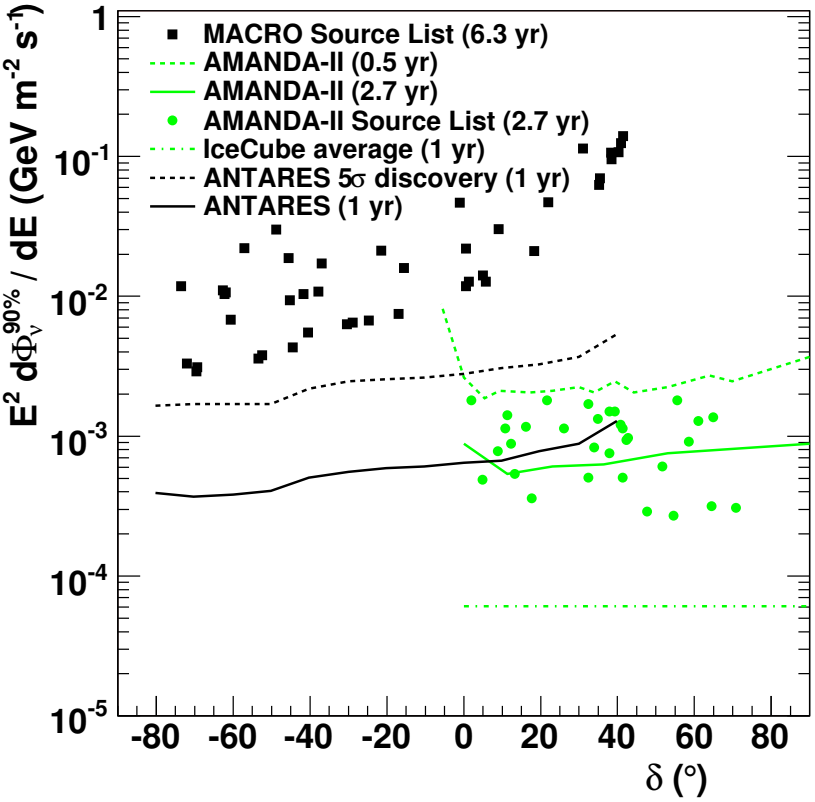

Figure 6.7: *Upper limits (90% C.L.) on the neutrino flux as a function of the declination. The Monte Carlo sensitivity of ANTARES for 1 year and the discovery potential with a confidence level of 5σ are shown together with the established limits from MACRO [165] and the upper limit for 1-year analysis of AMANDA-II [167]. More advanced results of AMANDA-II for five years are also shown [99] as well as the projected sensitivity of IceCube averaged over all declinations of the northern sky for one year [168].*

As can be seen, the good expected angular resolution of ANTARES makes possible to achieve an average upper limit in one year similar to the AMANDA-II upper limit for an equivalent live-time of 2.7 years. It should be mentioned, that ANTARES presented results are based on Monte Carlo whilst AMANDA-II are established limits. In particular, in the overlap region, the AMANDA-II limits for 2.7 years are better than those for ANTARES which, on the other hand, is able to study a larger range of declinations. Nevertheless, this plot shows in a clear way, the necessity of a global

covering of the whole sky. ANTARES is the perfect north counterpart of AMANDA-II telescope as the Mediterranean KM3NeT telescope will be of the future Kilometre-Scale detector IceCube.

6.4 Sensitivity after several years

The sensitivity of the ANTARES telescope to point-like sources will improve with the exposure time. In this section we present the expected sensitivity as a function of years of data-taking only for a given direction in the sky. In figure 6.8 the sensitivity of ANTARES for a source located at $\delta = -60°$ is shown together with the expected sensitivities of the Kilometre-Scale detectors IceCube and NEMO.

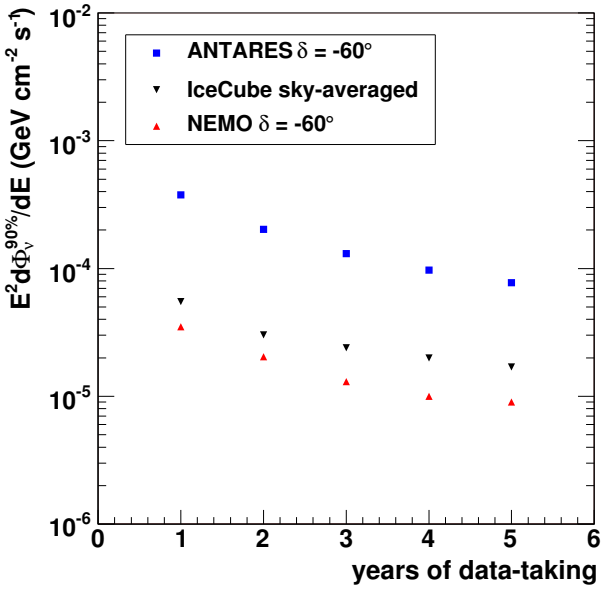

Figure 6.8: *Sensitivity for the ANTARES neutrino telescope as a function of the period of data-taking compared to the future Kilometre-Scale detectors, IceCube [168] and NEMO [169].*

The method followed by those telescopes is a binned technique in which a bin size of 1° was selected in the case of IceCube [168] and a search bin of 0.3°, due to its better angular resolution, for NEMO [169]. This explains the higher sensitivity of NEMO compared to IceCube. Obviously the sensitivity depends on declination, for simplicity here we only present the average upper limit for a given direction in the case of ANTARES and NEMO, and the expected sensitivity of IceCube averaged over its visible sky.

The improvement in the ANTARES sensitivity for 5 years with respect to the 1-year results is about **80%** for the given declination band. Moreover, as can be seen, the ANTARES average limit expected for 5 years of data-taking will be only about a factor **1.5** worse than the projected sensitivity for IceCube in one year of live-time.

Conclusions

– It worked! Eat it everyone who's never won a Nobel Prize! And that includes you, Amy.
Professor Farnsworth, Futurama.

The ANTARES collaboration is currently constructing and deploying a neutrino telescope in the Mediterranean sea. At the moment of writing these conclusions, 10 of the final 12 lines are already deployed and connected in December 2007. The detector design is optimized to detect high energy neutrinos from 100 GeV to 1 PeV. One of the main motivations to build a neutrino telescope is the observation of astrophysical point-like neutrino sources. Different theoretical models predict the production of high energy neutrinos in many astrophysical objects in the Universe. There are several astronomical scenarios where neutrino emission is foreseen, some of them are transient sources like supernova flares or Gamma Ray Bursts where the timing information of the neutrino event is a key issue in the analysis, or steady neutrino where an accumulation of signal events over the physical background is sought after. The search of point-like steady sources requires that the neutrino detector had a good angular resolution to enable the detection of the source. On the other hand, the aimed angular resolution of ANTARES (0.3° for muon events with $E_\mu > 10$ TeV) could only be achieved if an accurate determination of the arrival times of the Cherenkov photons to the photocathodes is performed.

This work is divided into two main parts. The first one contains the analysis of the Optical Beacon system. This system is devoted to the underwater time calibration of the photomultiplier tubes (PMTs). The relative time calibration is of utmost importance since an accurate determination of the arrival time of Cherenkov photons is a must for a good muon track reconstruction. Once the requirements concerning the timing resolution of the detector have been verified *in situ* with the Optical Beacon system, we can explore the capabilities of ANTARES identifying steady neutrino point-like sources assuming that the expected angular resolution will be achieved. Even though the available data are still not enough to start this analysis, the algorithm for the search of point-like sources described here has been carried out keeping in mind a prompt and straightforward application to real data. Therefore, with the higher potentiality of the unbinned techniques, this method has also the advantage that the model distributions have been built without any dependence on the knowledge of the detector performance or additional models resulting in a robust approach to the analysis.

The Optical Beacon system

In chapter 3, we have presented the first analysis of the Optical Beacon system. This system consists of a series of controlled sources of pulsed light located throughout the detector used for timing calibration in underwater conditions. In ANTARES, every active component of the detector is calibrated before the deployment in a dedicated dark-setup. The time offsets referred to common Optical Module are stored in a database which is accessible by the data acquisition program that uses the information in there to calibrate the out-coming raw data. However, it is possible that these values change in time due to several factors like the ageing of the components or other environmental reasons. To this end, the Optical Beacon system was conceived to monitor, and correct in case of necessity, the time offsets of the PMTs of the detector. We presented in this thesis, the first analysis of the Optical Beacon system in under water conditions. Some first outlooks were presented and can be summarized as follows:

- The Optical Beacon trigger, `OBtrigger`, was developed to process and subsequently analyse the events resulting from an Optical Beacon calibration run. This trigger has been tested for the first time in real conditions and good results have been obtained.

- The time residual distributions between the Optical Modules and the time registered at the Optical Beacon has shown that the ANTARES time electronics resolution is about $\sim$**0.4 ns**. This time resolution below the nanosecond level is one of the key elements to achieve the expected angular performance of ANTARES.

- Two subsequent fits are done to the rising-edge of the time residual distribution between the OMs and the reference time given by the Optical Beacon corrected by the geometrical distance between both. The result of these fits provide an estimate of the time offsets. This time offset estimate is dubbed as T^{100}. It has been verified that the linear calibration of the TVC does not worsen the estimation of the T^{100} and resolution parameters from the time residual distributions. Nevertheless, the *differential non-linearities* moves the Gaussian-like shape of the time residuals distributions and hinders the fit of the rising-edge of the distributions.

- The time offset estimate, T^{100}, has a dependence as a function of the distance. When performing a single line calibration, the delay of the T^{100} as a function of the distance has a value of **0.11 ns/m**. This delay is stable for all analysed lines and was not predicted by the Monte Carlo simulation.

- A geometrical factor have been decoupled by illuminating always the same storey with different light intensities. Variations in the T^{100} of about **12 ns** have been registered which cannot be explained by the walk effect measured in the dark-setup.

- A statistical effect has been proposed to be the origin of this delay. The earliest photons of multi-photoelectrons pulses dominates the arrival time on the photocathode surface and, therefore, a delay is expected as the charge recorded at the

PMT decreases. A density distribution that takes this effect into account has been proposed. With this density we are able **to explain** the delay in the T^{100} parameter.

- This delay in the T^{100} estimate is very stable and hence it can be considered as **empirically determined**. Using this value, and the time difference between OMs, we will be able to calibrate all the *time offsets* and verify any deviation from the measured values in the dark-setups. This procedure for timing calibration is being carried out although is not covered in this thesis.

- The time difference between the signal recorded by two different Optical Modules of the same storey has been also computed. The *after-pulses* resulted from saturated hits have been removed from the data. The width of the distributions is about $\sim$ **0.5 ns**, which is in agreement with the electronics resolution mentioned above.

In this chapter, we also presented the first study concerning the optical properties of the water with the Optical Beacon system. This system turns out to be an optimum instrument to measure some of the ocean water parameters. In particular we derived the attenuation length of water. Some of the results are summarized as follows:

- The photon field emitted by an isotropic source will depend on the distance and a parameter dubbed as the **attenuation length** by an exponential law. The number of photoelectrons measured by the PMTs should, therefore, have the same behaviour.

- By selecting the hits of the populated peak of the distributions of the time residuals we can infer a measurement of the light attenuation length by representing the collected charge of these hits as a function of the distance.

- The light attenuation length has been estimated using different LED Beacons and only the PMTs located on the same line. A simple Monte Carlo estimate for the systematic uncertainties has been done. The average value obtained is $\mathbf{45 \pm 1(stat.) \pm 4(syst.)\ m}$ and does not depend on the light intensity.

- There is no evidence of a seasonal variation for the moment, nonetheless a longer monitoring of the attenuation length will be performed.

Search of point-like sources

In chapter 4 we introduced a clustering algorithm and its application to the search of point-like sources. The Expectation-Maximization (EM) algorithm is a widely-used technique for the identification of accumulations of events. This technique has been adapted to our problem, the search of point-like sources over the atmospheric neutrino background. When adapting the EM algorithm to the search of point-like sources, we need to assume that the signal distribution over the background follows a Gaussian-like shape, which is a very reasonable assumption. Chapter 5 contains the results of

the analysis when a global sky search is performed. This searching analysis is usually referred to as a *blind* search since no prior information about the source is used, apart from the educated assumption that the neutrinos follow a power law emission with a spectral index of 2.

The main results of the analysis of the EM algorithm in a blind search are the following:

- The discovery potential or probability to detect a point-like source at a given confidence level increases with the average number of source events observed in the detector. A discovery potential of 50% means that in 50% of identical (in average) experiments, the source will have a significance higher than the one produced accidentally by background clusters. With this algorithm we have determined that the minimum number of required observed events to yield a discovery power of 50% for the two extreme visible declinations ($\delta = -80°$, $\delta = 40°$) are **7.5** and **6** events, respectively, for a confidence level of 5σ, and **5.5** and **4** for a 3σ confidence level.

- Due to the Earth's rotation the atmospheric neutrino background does not depend on right ascension. Hence, the discovery potential in terms of the average number of observed events depends only on the declination.

- The algorithm presented here constitutes a robust approach since neither a prior knowledge of the detector nor an optimization of the algorithm are needed. Only two initial parameters must be selected: the minimum number of events in the cluster candidate and the initial cone size for the pre-clustering search. Moreover, the results of the EM algorithm are independent of this initial size as long as a reasonable value is selected for this parameter.

- In terms of required muon/neutrino flux the declination dependence is inverted due to the visibility factor. The neutrino flux required to make a discovery of at least 50% of probability ranges from $\boldsymbol{E_\nu^2 d\Phi_\nu^{50\%}/dE_\nu = 1.7 \times 10^{-3}\ \mathrm{GeV\ m^{-2}\ s^{-1}}}$ for $\delta = -80°$ to $\boldsymbol{E_\nu^2 d\Phi_\nu^{50\%}/dE_\nu = 5.2 \times 10^{-3}\ \mathrm{GeV\ m^{-2}\ s^{-1}}}$ for $\delta = 40°$ with a confidence level of 5σ.

- Being an unbinned technique, we can estimate the source location. The angular resolution expected in ANTARES when pin-pointing a neutrino source will be **less than 0.1**$°$ with the EM algorithm if more than 6 signal events are observed.

- Different spectral indexes apart from 2, have been evaluated. The results in terms of the average number of observed signal events are very similar, only a $\sim$ **12%** worse for $\gamma = 2.7$ and $\sim$ **16%** for the case of $\gamma = 3.0$, which is an indication that the algorithm adapts itself very well to different shapes of the signal event distributions. Nevertheless, when presenting the results in terms of muon/neutrino fluxes the differences can reach up to **3 orders of magnitude** due to the low response of the detector to spectral indexes larger than 2. The conclusion is that neutrino sources emitting with a spectrum softer than 2 are unlikely to be detected with the effective area of ANTARES.

- In case no neutrino source is observed, it is possible, nonetheless, to set an upper limit on the muon/neutrino flux that would rule out some of the most optimistic models. An upper limit means that there is no source emitting with a flux higher than this limit within a given confidence level. In the case of future experiments an average upper limit, called sensitivity, is provided. The sensitivity in ANTARES for a complete blind search is $\boldsymbol{\Phi_\nu \simeq 2.5 \times 10^{-8}\ cm^{-2}\ s^{-1}}$, over 10 GeV.

- For longer periods of data-taking, the capabilities of the detector in searching point-like sources improve. For a confidence level of 5σ the improvement in the discovery potential flux is about **40%** for 2 years of data-taking, and about **70%** for 5 years.

In chapter 5 a different approach in the analysis of point-like sources is performed. Unlike the full blind search, in which no assumption about the source is made, in this case the position of the source is considered as known. This analysis is important to set upper limits on specific candidate sources when no discovery has been claimed in the full search analysis. The results are the following:

- Since the searching area is focused on the direction of the source, the trials of the background to mimic a signal accumulation are reduced. Hence, the discovery power is improved with respect to the blind search.

- The average number of observed events required to make a discovery of 50% ranges between **5 events** ($\delta = -80°$) and **3.5 events** ($\delta = 40°$) for a confidence level of 5σ.

- The average upper limit in this case has been compared to other experiments. The sensitivity of ANTARES (averaged over all declinations) is about $\boldsymbol{E_\nu^2 d\Phi_\nu^{50\%}/dE_\nu = 8.2 \times 10^{-4}}$ G

- The sensitivity will improve as we increase the period of data-taking. ANTARES will increase approximately **80%** its sensitivity in 5 years of data-taking.

Análisis de las Balizas Ópticas y búsqueda de fuentes puntuales con el telescopio de neutrinos ANTARES

Introducción

Astronomía de neutrinos

En los últimos años estamos siendo testigos de la consolidación de una nueva disciplina dentro de la astronomía y de la detección de rayos cósmicos, la astronomía de neutrinos. Ésta tuvo su origen con la detección de los primeros neutrinos provenientes de una fuente extra-terrestre, el Sol. Con la detección de los neutrinos provenientes de la supernova SN1987A por parte del experimento Kamiokande II, se ampliaron las posibilidades de esta nueva rama de la Física de Astropartículas. Ambos hechos fueron reconocidos por la comunidad científica y el año 2002 el Premio Nobel de Física fue otorgado a Raymond Davis y Masatoshi Koshiba por sus estudios pioneros en el campo de la Astrofísica y en particular en la detección de neutrinos cósmicos. Esta detección de neutrinos solares y de supernovas, se conoce como astronomía de neutrinos de baja energía. Nuevos experimentos, como ANTARES, pretenden extender dicha disciplina de manera que sea posible detectar neutrinos en un mayor rango de energía.

Una de las razones fundamentales para querer explorar el Universo usando los neutrinos como mensajeros cósmicos es que este tipo de astronomía ofrece un considerable potencial para el estudio de las regiones más lejanas o más densas del Cosmos.

La astronomía tradicional basada en fotones ha permitido realizar importantes descubrimientos en todas las longitudes de onda del espectro electromagnético. Sin embargo, este tipo de astronomía ha encontrado su limitación en el hecho de que fotones con energías del orden de TeV son absorbidos por el fondo cósmico de radiación de microondas. Esta incapacidad de poder observar el aspecto más energético del Universo ha propiciado que el interés científico se dirija hacia nuevos mensajeros cósmicos para explorar las regiones más densas y lejanas del Universo. De entre ellos, los neutrinos, al ser neutros y sólo interactuar débilmente, son los mejores candidatos debido a que no son desviados por los campos magnéticos y apuntan directamente a su fuente, además de no ser absorbidos en su trayecto.

Por otro lado, hoy en día el estudio de rayos cósmicos está proporcionando nuevos e interesantes descubrimientos, pero del mismo modo que ocurre con la astronomía

tradicional, la observación de rayos cósmicos está limitada por distintos aspectos físicos. Los protones, al ser partículas cargadas, son desviados por los campos magnéticos galácticos e intergalácticos, eliminando cualquier información sobre su origen, salvo para aquellos muy energéticos que procedan de fuentes no muy lejanas. Además, los protones y núcleos pesados interaccionan con el fondo de radiación de microondas que puebla el Universo en lo que se conoce como el efecto GZK. Esta interacción limita a su vez el recorrido libre medio de un protón de alta energía.

En este escenario, los neutrinos son los mejores candidatos para su uso como mensajeros cósmicos de alta energía debido a las características anteriormente descritas, si bien es cierto que la astronomía de neutrino también padece de ciertas desventajas. En primer lugar, el mismo hecho que convierte al neutrino en el mensajero ideal, es decir, su baja sección eficaz, lo hace muy difícil de detectar. Este obstáculo se ha superado usando grandes volúmenes naturales como medios de detección (hielo, agua e incluso la atmósfera). Así mismo, el interés principal de la astronomía de neutrinos se centra en la región de más alta energía (E_ν por encima de GeV-TeV), donde precisamente la sección eficaz de los neutrinos, así como el alcance y la resolución angular de los muones, es mayor, lo cual favorece su detección.

Actualmente, varios experimentos pioneros en la astronomía de neutrinos de alta energía han publicado sus primeros resultados. El experimento Baikal tiene el privilegio de ser uno de los precursores de la astronomía de neutrinos de alta energía al desplegar un detector en el fondo del lago Baikal en Siberia. Sin embargo, la escasa profundidad del lago y por ende, el limitado tamaño del detector, reducen su competitividad a la hora de buscar fuentes puntuales de neutrinos. Más interesante es el caso de AMANDA, un telescopio de neutrinos que usa el hielo del casquete polar de la Antártica como medio de detección. Si bien AMANDA no es el primero de los telescopios de neutrinos, sí es el primero con un área efectiva suficiente como para proporcionar límites a los flujos de neutrinos capaces de descartar algunos de los modelos de emisión de neutrinos más optimistas. Además, el diseño de AMANDA y los retos tecnológicos a los que se ha enfrentado, lo convierten en uno de los principales telescopios de neutrinos dentro del panorama actual, abriendo el camino para la construcción de un telescopio de un volumen efectivo diez veces mayor también situado en el polo sur, IceCube. Dicho telescopio será capaz de observar el cielo norte de una manera nunca vista hasta ahora. Por otro lado, el cielo sur será explorado por los telescopios de neutrinos situados el hemisferio norte y representados principalmente por ANTARES, de un área efectiva similar a la de AMANDA. Otros proyectos de telescopios de neutrinos en el Mediterráneo son NEMO y NESTOR. Todos ellos pertenecen a una generación de telescopios marinos cuya experiencia servirá para la construcción de un telescopio mayor en el mar Mediterráneo, KM3NeT, cuya observación del cielo visible será complementaria a la que realice el experimento IceCube.

Fuentes de neutrinos de alta energía

Los rayos cósmicos están constituidos principalmente protones y núcleos pesados cuya aceleración se produce en objetos cósmicos gracias, presumiblemente, al mecanismo de Fermi. La aceleración hadrónica permite a su vez la emisión de partículas

neutras, fotones de rayos gamma y neutrinos, como productos de desintegración de las partículas eléctricamente cargadas que han sido aceleradas previamente. En los modelos leptónicos en cambio, son los electrones las partículas aceleradas, en este caso la radiación sincrotrón es la responsable de la emisión de rayos X. La posterior colisión de estos fotones energéticos con electrones se conoce como proceso Compton inverso, y produce también rayos gamma de alta energía. Estos modelos no predicen la emisión de neutrinos. Es evidente que la aceleración leptónica se produce ya que las observaciones de rayos X así lo atestiguan. A su vez, la detección de los rayos cósmicos es una prueba de la aceleración de protones en objetos cósmicos e incluso recientemente han surgido indicios de las primeras correlaciones de rayos cósmicos con Galaxias de Núcleo Activo por parte del Observatorio Pierre Auger. Ambos modelos pueden coexistir pero sólo en los modelos hadrónicos se predice un flujo de neutrinos. En estos modelos los protones acelerados pueden interaccionar con la materia que rodea el medio acelerador produciendo piones (y otros mesones más pesados). La posterior desintegración de los piones neutros contribuirá también a la emisión de rayos gamma. Por otro lado, los piones cargados darán lugar a muones y un flujo de neutrinos. Adicionalmente, la desintegración de muones produce también neutrinos de la forma

$$\begin{aligned} p + X \longrightarrow \pi^{\pm}(K^{\pm}\cdots) + Y \longrightarrow \quad & \mu^{\pm} + \nu_{\mu}(\bar{\nu}_{\mu}) + Y \\ & \downarrow \\ & e^{\pm} + \bar{\nu}_{\mu}(\nu_{\mu}) + \nu_{e}(\bar{\nu}_{e}). \end{aligned} \tag{6.1}$$

De esta forma, la energía liberada por una fuente de rayos cósmicos está distribuida entre rayos cósmicos, fotones y neutrinos. Como consecuencia, es posible estimar un límite superior al flujo de neutrinos cósmicos a través de las observaciones de los rayos cósmicos. Este límite, deducido para fuentes genéricas, es comúnmente conocido como el límite de Waxman-Bahcall y viene dado por la siguiente expresión:

$$E_{\nu}^{2}\,\Phi_{\nu} < 4.5 \times 10^{-8}\ \text{GeV cm}^{-2}\ \text{s}^{-1}\ \text{sr}^{-1}. \tag{6.2}$$

Dicho límite se calcula suponiendo fuentes *transparentes*, esto es, aquellas que dejan escapar también los neutrones. De este modo, los mismos escenarios que dan lugar al flujo de rayos cósmicos son también los responsables de la emisión de neutrinos de alta energía. Por tanto, la detección y el estudio de dichos neutrinos ayudará a resolver muchas de las cuestiones aún abiertas sobre la naturaleza y el origen de los rayos cósmicos. Existen varias fuentes astrofísicas candidatas a emitir neutrinos de alta energía, entre ellas podemos destacar las siguientes:

- **Galaxias de Núcleo Activo.** Son galaxias con un núcleo brillante y compacto en su interior, presumiblemente un agujero negro. Entre ellas se incluyen varios tipos de objetos (Seyfert I y II, cuásares, radio galaxias, blazars...). Junto con las explosiones de rayos gamma, son los objetos astronómicos más brillantes del Universo y podrían explicar el espectro de los rayos cósmicos con energías en la región de 10^{11} GeV.

- **Explosiones de Rayos Gamma.** Probablemente sean las mejores candidatas a fuentes de rayos cósmicos. Estos fenómenos son, durante unos segundos, los más energéticos del Universo ($\sim 10^{51} - 10^{54}$ erg/s). Son breves explosiones de rayos gamma, a menudo seguidas de emisiones de rayos X, en el visible y en radio conocidas como *afterglows*. Los modelos que predicen la emisión de neutrinos en las explosiones de rayos gamma indican que un telescopio de un kilómetro cúbico de volumen efectivo sería capaz de detectar dicha señal.

- **Remanentes de supernova.** Son las más prometedoras fuentes de neutrinos de origen galáctico. Entre ellas, las clasificadas como remanentes de supernova *shell-type* son comúnmente asociadas a la parte del espectro de rayos cósmicos considerado de origen galáctico ($E_p < 10^7$ GeV).

- **Centro galáctico.** El centro galáctico ha sido objeto de especial interés científico debido a las observaciones realizadas por el telescopio de rayos gamma H.E.S.S. En ellas se aprecia que dicha región es una zona de gran actividad en rayos gamma ($E_\gamma > 10^2$ GeV). Una de las implicaciones de estas medidas experimentales es que existe una componente adicional al flujo de rayos cósmicos proveniente del centro de nuestra Galaxia. Esta supuesta contribución podría venir de la fuente HESS J1745-290 localizada en el centro gravitacional del centro galáctico y que coincide espacialmente con el agujero supermasivo Sagitario A* y el remanente de supernova SNR Sgr A East. La emisión de rayos gamma por parte de HESS J1715.290 también se ha estudiado asumiendo un posible origen relacionado con la aniquilación de materia oscura en el origen de la Galaxia, siendo ésta posibilidad casi descartada. El centro galáctico es una zona especialmente atractiva para un telescopio de neutrinos ubicado en el hemisferio norte como ANTARES.

Existen otras muchas fuentes candidatas que podrían emitir neutrinos. Entre ellas los microcuásares, pleriones, los púlsares, las magnetoestrellas o los sistemas binarios con una estrella de neutrones.

Además, es necesario mencionar otros posibles mecanismos que podrían dar lugar a un flujo detectable de neutrinos, como la desintegración del neutralino (uno de los candidatos a constituir la materia oscura), neutrinos de muy alta energía resultado de la interacción de los rayos cósmicos con el fondo de radiación de microondas que puebla el Universo (GZK neutrinos) o la emisión de neutrinos debido a la desintegración de partículas exóticas predichas en las teorías de gran unificación.

Por el momento, ninguna fuente de neutrinos de alta energía ha sido observada y por tanto la existencia de dichas fuentes es aún cuestión de controversia. Sin embargo, como se ha mencionado anteriormente, ciertas hipótesis relativas a los modelos de producción de rayos cósmicos garantizan la emisión de neutrinos en determinados escenarios, si bien los flujos detectables esperados son inciertos.

Telescopios de neutrinos

Como ya se ha mencionado, existe una distinción entre detectores de neutrinos extra-terrestres de baja energía y los experimentos dedicados a la observación de neutrinos por encima de los 100 GeV. En el segundo caso, la resolución angular que se puede obtener a altas energías ($E_\nu > 10$ TeV) nos permite usar el calificativo de *telescopio* para tales detectores. En los llamados de detección óptica, el principio de operación se basa en la detección de la radiación Cherenkov inducida por muones al atravesar un medio óptico adecuado como el agua o el hielo. Dichos muones son el resultado de la interacción de los neutrinos muónicos de alta energía con la materia que rodea al detector. Este principio permite el uso de grandes volúmenes naturales como el mar o el hielo polar como blancos de detección, idea inicialmente propuesta por Markov en 1960.

Dadas las relaciones geométricas de la emisión de radiación Cherenkov, su detección por medio de una serie de fotomultiplicadores permite la reconstrucción de la dirección del muon que induce la emisión. A altas energías, $E_\nu > 10$ TeV, el ángulo formado entre la dirección del muon y del neutrino es despreciable, por tanto, la traza reconstruida del muon es un buen indicador de la dirección original que llevaba el neutrino. Por otro lado, la luz recolectada por los fotomultiplicadores permite dar una estimación de la energía del suceso. En el análisis de fuentes puntuales es importante ser capaz de obtener la información de la dirección del neutrino que apunta directamente a la fuente emisora, por ello sólo las topologías que incluyan una traza leptónica larga son interesantes para el análisis, como en el caso de los neutrino muónicos. No obstante, ANTARES es capaz de detectar otras señales de neutrinos que no generan trazas, como los neutrinos electrónicos cuya interacción induce una cascada electromagnética que puede registrarse en el detector. También los neutrino tauónicos pueden reconstruirse, en particular la señal conocida como *double bang* (dos cascadas electromagnéticas dentro del volumen instrumentado del detector). Ésta es una señal inequívoca del paso de un neutrino tauónico. Por desgracia, la tasa de este tipo de sucesos en un kilómetro cúbico de detector es del orden de $1-3$ sucesos por año.

Las dificultades a las que se enfrenta la astronomía de neutrinos son importantes. Por una parte, los datos experimentales y las estimaciones teóricas indican que el flujo esperado de neutrinos a altas energías es muy bajo, por lo que áreas efectivas de km^2 son necesarias a la hora de diseñar un telescopio de neutrinos de alta energía. Las dificultades que conlleva la construcción de un telescopio de tales dimensiones en emplazamientos hostiles, como lo son el fondo marino o el hielo polar, convierten a estos experimentos en verdaderos retos tecnológicos. Por otra parte, el flujo de neutrinos atmosféricos supera al de la señal en varios órdenes de magnitud, lo cual supone una dificultad inevitable cuando se quiere buscar un flujo difuso de neutrinos cósmicos.

La detección de neutrinos de alta energía está en amplio desarrollo y diversas propuestas de detección, al margen de la anteriormente expuesta, han ido surgiendo a lo largo de los últimos años. La detección acústica de las interacciones de neutrinos con el hielo polar, o mediante ondas de radio y microondas, son nuevas iniciativas llevadas a cabo por nuevos diseños de telescopios de neutrinos de alta energía y que en el futuro complementarán el amplio abanico de experimentos de neutrinos.

El telescopio ANTARES

El experimento ANTARES (*Astronomy with a Neutrino Telescope and Abyss environmental RESearch*) es una colaboración interdisciplinaria en la que participan físicos, ingenieros, oceanólogos y astrónomos de Francia, Alemania, España, Holanda, Italia, Rumanía y Rusia. El emplazamiento elegido para desplegar el detector es el mar Mediterráneo, concretamente frente a la Costa Azul de Francia a 40 km de Tolón y a una profundidad de unos 2500 m. El Instituto Oceanográfico Francés (IFREMER) tiene parte de sus instalaciones en La Seyne sur Mer, donde se encuentra el centro de control del telescopio. Ésta es una ventaja para el experimento ya que le permite usar algunas de las infraestructuras del instituto para las diversas tareas relacionadas con el despliegue del detector y el estudio de las condiciones ambientales del emplazamiento. El telescopio está formado por 12 líneas distribuidas de forma octogonal sobre el fondo marino. La separación media entre líneas es de unos 70 m y éstas tienen una altura de aproximadamente 450 m de longitud. Las líneas están ancladas al fondo marino mientras que en el extremo opuesto una gran boya permite que se mantengan en posición vertical. Cada línea posee 25 pisos, cada uno de los cuales está compuesto por 3 módulos ópticos en cuyo interior se encuentra un fotomultiplicador (PM), creando una gran matriz tridimensional de 900 PMs. El volumen instrumentado comienza a unos 100 m sobre el fondo del mar y cubre unos 350 m. Todas las líneas están conectadas a la estación de control por medio del armario de conexiones o *junction box* el cuál también se encuentra sumergido en el fondo marino.

Los datos adquiridos por el detector, así como varios comandos de control y sincronización, se transmiten por medio de un cable electro-óptico submarino de unos 40 km de longitud. Este cable principal comunica la estación de control en la costa con el armario de conexiones situado en el fondo del mar. Dicho armario de conexiones se encarga de distribuir las señales desde, y hacia, las distintas líneas por medio de sendos cables electro-ópticos.

El detector ANTARES es un telescopio submarino de un área efectiva de 0.1 km^2. La experiencia y el conocimiento adquiridos en el desarrollo de los distintos componentes servirán en el futuro para el diseño y la construcción de un telescopio marino en el Mediterráneo de un kilómetro cúbico de volumen efectivo. Durante los años de desarrollo del proyecto se han hecho frente a varias dificultades de diversa naturaleza. Por un lado se llevó a cabo un exhaustivo estudio de los distintos componentes electrónicos y mecánicos del detector para asegurar su perfecta adaptación a las condiciones extremas que se dan en el fondo marino, tales como las altas presiones y la corrosión. Además, la verticalidad del detector genera grandes tensiones que pueden provocar roturas en los cables electro-ópticos de las líneas. A su vez, la elección del fondo oceánico como emplazamiento del detector conlleva un fondo óptico debido a las desintegraciones del ^{40}K presente en la sal marina junto con la bio-luminiscencia provocada por la emisión de luz por parte de organismos (generalmente bacterias) de las profundidades marinas. Todas estas condiciones derivadas del uso del agua oceánica como medio de detección hacen que el diseño y la construcción del detector hayan supuesto todo un reto tecnológico que finalmente se está resolviendo con éxito.

Durante la primera fase del proyecto ANTARES se estudiaron los parámetros am-

bientales relevantes del lugar de emplazamiento del detector y se realizaron pruebas sobre diversos componentes mecánicos y electrónicos del detector. Así mismo, se estudiaron y perfeccionaron las operaciones de despliegue y recuperación de las líneas. En la actualidad, ANTARES se encuentra en fase final de construcción del detector. Diez líneas definitivas, además de una línea de instrumentación, se han sumergido y se encuentran en operación. En Diciembre de 2007 cinco líneas se encontraban conectadas con el armario de conexiones y tomando datos desde un periodo de más de 10 meses. Los primeros muones atmosféricos fueron detectados durante las primeras semanas de operación y los primeros candidatos a neutrinos atmosféricos han sido observados. El despliegue de las dos líneas restantes y su conexión está planeada para el 2008.

Objetivos

Una de las principales características de ANTARES, y que lo distingue de otros detectores de neutrinos ya en operación, es la gran resolución angular que se espera alcanzar. Las propiedades ópticas del agua y el diseño de la electrónica de adquisición permiten que se pueda conseguir una resolución angular por debajo del grado, siempre y cuando dichos sistemas de adquisición electrónica tengan una resolución temporal por debajo del nanosegundo. Con las primeras líneas de ANTARES ya en funcionamiento, los sistemas de calibración del detector han podido ser testeados en condiciones reales. Entre ellos se ha podido verificar el sistema de Balizas Ópticas (*Optical Beacons*) para la calibración temporal del detector.

La gran resolución angular de ANTARES lo convierte en un experimento con gran potencial en el estudio de fuentes puntuales. La segunda parte de este trabajo está enfocada precisamente al estudio de ese potencial en la búsqueda de fuentes puntuales usando el algoritmo EM. Éste es un algoritmo de búsqueda de agrupaciones usado ampliamente en diversas ramas científicas. En este estudio hemos aplicado dicho procedimiento a la identificación de pequeñas agrupaciones de sucesos en determinadas direcciones, lo que pudiera indicar la presencia de un emisor de neutrinos cósmicos.

Calibración temporal con las Balizas Ópticas

El sistema de calibración temporal de las Balizas Ópticas consiste en una serie de fuentes pulsadas de luz dispuestas a lo largo del detector. Los fotones emitidos por las balizas se usan para estudiar la respuesta temporal de los fotomultiplicadores del detector. En ANTARES, todo elemento activo del detector ha sido calibrado en una sala oscura previamente a su inmersión. En dicha sala se miden los retrasos temporales en la medición de una señal simultáneamente enviada a todos los fotomultiplicadores. Las variaciones en los tiempos de llegada son almacenadas como variables de calibración. Aunque no se espera que los parámetros de calibración varíen una vez el detector ha sido sumergido, es posible, no obstante, que algunos de estos parámetros sufran pequeñas variaciones al cabo del tiempo debido al envejecimiento de algunos de los componentes o dependencia con determinados parámetros ambientales como la temperatura. Adicionalmente, este sistema de calibración *in situ* permite comprobar

posibles errores en las estimaciones de los tiempos de la sala oscura y en los casos que sea necesario corregirlos. Existen dos tipos distintos de balizas, ambas diseñadas para la misma finalidad:

- **Baliza LED**. Las Balizas LED constan de un prisma hexagonal cuyas caras disponen de 6 circuitos pulsadores cada uno con un LED. En total, una Baliza LED cuenta con 36 LEDs. En cada una de las caras, un LED apunta en dirección ascendente para iluminar los fotomultiplicadores que están por encima de la baliza. Los otros LEDs forman un grupo de cuatro con un LED central. Esta disposición se usa para reproducir una emisión angular uniforme de la baliza. En la parte interior del prisma hexagonal se haya un pequeño fotomultiplicador Hamamatsu H6780-03. Este fotomultiplicador tiene un tiempo de subida, *rise-time*, de 0.8 ns y un tiempo de tránsito, *transit time*, de 5.4 ns y se usa para determinar el tiempo de emisión de la luz de los LEDs. Un disco acrílico colocado en la parte superior del prisma hexagonal sirve de guía óptica para dirigir la luz al fotomultiplicador. Los circuitos de cada cara permiten la variación de la intensidad de la luz emitida por cada LED cuando se varía la alimentación del circuito de 0 V a 24 V. Además, también es posible emitir usando distintas combinaciones de LEDs. La parte inferior de la baliza alberga toda la electrónica y las unidades lógicas que controlan su funcionamiento siguiendo las órdenes externas enviadas por el sistema de *Slow Control*.

  Una vez montada la Baliza LED y sincronizados todos los tiempos de emisión de los circuitos pulsadores, ésta se introduce en un contenedor formado por un cilindro de cristal de borosilicato y una tapa extraíble. Todo el contenedor es transparente (excepto en la unión del cilindro con la tapa) lo que permite la emisión uniforme de la luz. Las Balizas LED están dispuestas en la parte superior de algunos de los pisos del detector, concretamente en los pisos 2, 9, 15, y 21 de cada una de las líneas de ANTARES.

- **Baliza Láser**. La Baliza Láser es un dispositivo que emite pulsos de luz de gran intensidad y de menos de 1 ns de duración (FWHM). Éste se encuentra alojado en la estructura mecánica que ancla la línea al fondo marino (*Bottom String Socket*) y apunta en dirección ascendente. El principal componente es un láser pulsado de Nd-YAG modelo NG-10120-120 que emite a 532 nm, después de doblar su frecuencia de la emisión original de 1064 nm. Es un láser muy compacto lo que permite que sea fácilmente ensamblado en un pequeño volumen. Cuando el funcionamiento del láser es en modo pulsado, éste emite después de que una señal cuadrada (TTL) llegue al dispositivo a través de la electrónica de la parte posterior. El tiempo de emisión del pulso de luz es medido por un fotodiodo integrado en la cabeza del láser.

  Como ya se ha mencionado, la Baliza Láser está emplazada en la parte inferior de algunas líneas, concretamente en las líneas 7 y 8. Una versión preliminar de la baliza fue sumergida junto con la línea de instrumentación MILOM. Los datos del láser analizados en este estudio se corresponden con dicho diseño de la Baliza Láser. Debido a su posición, el láser está apuntando hacia arriba por lo que

depósitos orgánicos o *biofouling* podrían cubrir parcialmente la superficie superior del láser provocando una disminución de la transparencia y una consecuente menor emisión de luz. Para evitar esta pérdida de transmisión, la Baliza Láser está provista de un cilindro de cuarzo colocado en la apertura del láser. Su diseño permite que la luz del láser se difunda a través de las paredes del mismo, evitando de esta manera la cara superior del cilindro, que es la zona de máxima opacidad. Por esa razón, la Baliza Láser está diseñada para iluminar las líneas adyacentes a su ubicación.

El capítulo 3 de esta tesis resume el primer análisis realizado en condiciones reales del sistema de Balizas Ópticas. Algunos de los resultados han permitido verificar que el diseño de la electrónica de ANTARES tiene una contribución a la resolución temporal del detector que está por debajo de los 0.5 ns. Esta gran resolución temporal se traduce en una buena resolución angular, debido a que la precisión en la determinación de los tiempos de llegadas de los fotones Cherenkov es crucial a la hora de reconstruir la dirección del muon y, por tanto, en la determinación angular de la dirección del neutrino original. Con las Balizas Ópticas también se han comprobado otros fenómenos como el efecto del *fotón primero* y se ha realizado un primer estudio sobre las propiedades ópticas del agua.

Fuentes puntuales

Uno de los principales objetivos de un telescopio de neutrinos es la identificación de posibles fuentes puntuales de neutrinos de alta energía. Existen numerosos modelos teóricos que predicen la emisión de neutrinos por parte de determinados objetos astronómicos. Gracias al telescopio ANTARES será posible confirmar, o rechazar, las estimaciones de los flujos que predicen algunos de los modelos teóricos que describen la emisión de neutrinos de dichas fuentes. Dado que hasta la fecha no existe ninguna evidencia o indicios de fuentes de neutrinos de alta energía, es especialmente interesante comprobar el potencial (o sensibilidad) del detector cuando se realiza una búsqueda *ciega*, esto es, cuando ninguna suposición sobre la localización de las fuentes candidatas se aplica a los datos.

En un detector ideal, y siempre que el ángulo entre el muon reconstruido y el neutrino sea despreciable, los sucesos provenientes de una fuente puntual de neutrinos apuntarán todos hacia dicha fuente. En la realidad, los sucesos tendrán un ligero desplazamiento debido a la resolución angular del detector y se presentarán en forma de agrupaciones, o *clusters*, alrededor de las coordenadas de la fuente. Cada suceso individualmente será indistinguible de otros sucesos del fondo físico (neutrinos atmosféricos, flujos difusos y muones descendentes mal reconstruidos), sin embargo, el conjunto o *cluster* puede ser identificable entre todos los sucesos que componen el fondo. Así pues, la búsqueda de fuentes puntuales consiste en la identificación de esas agrupaciones de sucesos sobre una distribución no uniforme de sucesos de fondo. El análisis de los datos para distinguir los sucesos de interés se basa, por tanto, en la identificación de la función de distribución de los mismos.

En este sentido, la búsqueda de fuentes puntuales es similar a un análisis de *clustering* o búsqueda de grupos de sucesos cohesivos y diferenciados del fondo. Para ello,

en este trabajo hemos empleado uno de los métodos generales usado en el análisis de acumulaciones, el algoritmo *Expectation-Maximization* (EM). El método EM es uno de los métodos llamados de *unbinning*, es decir, no se basa en la división del cielo en una cuadrícula para observar acumulaciones en algunos de sus bines. Por contra, los métodos *unbinning* tratan los datos de manera continua, de forma que no hay pérdida de información por los efectos de frontera a los que un *binning* aplicado a los datos da lugar. Por otro lado, y a diferencia de otros métodos de *unbinning*, el método propuesto en este trabajo no precisa de un conocimiento exhaustivo del comportamiento del detector y no depende de las incertidumbres en parámetros físicos como flujos o secciones eficaces.

El método EM es uno de los algoritmos de maximización de la verosimilitud (*likelihood*) en aquellos casos en los que sólo es posible una maximización numérica. En el esquema del EM, la muestra de datos es una muestra *incompleta*, es decir, carecemos de la información estructural de los datos (si son sucesos de fuente o fondo). Así pues, el primer paso del método es añadir una dimensión extra de información. En esa nueva capa de información, un vector nos dirá si el suceso pertenece a uno de los dos grupos, en nuestro caso, al fondo o a la señal. Una vez construida la nueva muestra *completa* de datos con una estimación inicial de esos vectores identificadores, podemos calcular la nueva verosimilitud y maximizarla analíticamente. En el caso de que supongamos que la señal sigue una distribución gausiana, las ecuaciones que permiten la maximización de la likelihood y que estiman los parámetros que dan la posición de la fuente y su normalización son conocidas.

En el capítulo 4 se presenta el método de manera general y posteriormente su aplicación a la búsqueda de fuentes puntuales. El capítulo 5 y 6 están dedicados al análisis en primer lugar cuando se realiza una búsqueda *ciega* y posteriormente cuando ciertas direcciones del cielo donde se espera que exista una fuente de neutrinos son seleccionadas. En ambos casos, el resultado del análisis se presenta en términos del potencial del experimento para detectar fuentes, y de la sensibilidad del detector o límites (en ausencia de señal) al flujo de neutrinos esperado.

Discusión de los resultados

Análisis de las Balizas Ópticas

El tiempo proporcionado por las distintas Balizas Ópticas, tanto LED como láser, sirve para calcular las diferencias de tiempo entre el tiempo esperado según la propagación de la luz en el agua y el tiempo real adquirido en los fotomultiplicadores del detector. En particular, esa diferencia de tiempo viene dada por $\Delta t = t_{DEST} - t_{REF} - d/c_{water}$ donde t_{DEST} y t_{REF} son, respectivamente, los tiempos de recepción en el PM y de emisión en la Baliza Óptica, d es la distancia entre la baliza y el fotomultiplicador y c_{water} es la velocidad de la luz en el agua para una determinada longitud de onda (según se trate de un LED o un láser). Las distribuciones de Δt proporcionan la información necesaria para la calibración del detector. En principio, la anchura de las distribuciones es una estimación de la resolución temporal adquirida por el detector.

En general, esta resolución viene dada por

$$\sigma^2 = \frac{\sigma^2_{TTS}}{N_{pe}} + \frac{\sigma^2_{water}}{N_\gamma} + \sigma^2_{OB} + \sigma^2_{elec}, \tag{6.3}$$

donde σ_{TTS} es la contribución a la resolución de la dispersión en tiempo de tránsito de los fotomultiplicadores, o TTS de sus siglas en inglés *Transit Time Spread*. Esta dispersión es inversamente proporcional a la raíz cuadrada del número de fotoelectrones inducido N_{pe}. La segunda contribución viene de las propiedades ópticas del agua, σ_{water}, no obstante, el tiempo de llegada estará dominado principalmente por los fotones más rápidos, debido a que dichos fotones son los que llegan directamente de la fuente los efectos en la resolución de la transmisión óptica en el agua son despreciables al aumentar el número de fotones emitidos. La dispersión en tiempo de tránsito de la fuente, σ_{OB}, es también despreciable debido al rápido *risetime* del fotomultiplicador interno de las Balizas LED. Así pues, iluminando los fotomultiplicadores con gran intensidad, gran parte de las componentes a la resolución pueden eliminarse de la ecuación 6.3 quedando como única contribución la resolución de la electrónica de adquisición del detector, σ_{elec}. Para conseguir una resolución angular por debajo del grado, en ANTARES se precisó que la electrónica no debería contribuir con más de 1 ns en la resolución temporal. Con el primer análisis de las Baliza Ópticas a alta intensidad hemos comprobado que dicha resolución es cierta, lo que garantiza la buena respuesta angular del detector.

Por otro lado, la posición del pico en las distribuciones de tiempo es una estimación de los retardos temporales, T^{100}, en la adquisición de cada fotomultiplicador. Como se ha mencionado previamente, antes del despliegue de las líneas, cada instrumento activo es calibrado en una sala oscura adecuada a tal efecto. La estimación del parámetro T^{100} para cada distribución temporal sirve para corregir dichos valores en caso de que se haya producido una desviación con respecto a las mediciones de la sala oscura.

Medida de la longitud de atenuación

El objetivo principal del sistema de Balizas Ópticas es la calibración temporal del detector *in situ*. No obstante, este sistema permite observar y estudiar las propiedades ópticas del agua que son relevantes para la posterior reconstrucción de muones y cascadas. Usando las Balizas Ópticas somos capaces de estimar algunos de los parámetros ópticos del agua, tales como la longitud de atenuación. En esta parte de la tesis se estudia la dependencia de la energía depositada en los PMs por cada pulso de luz de una Baliza LED con la distancia entre ambos. Esta relación debe seguir una ley exponencial que nos ayudará a inferir la longitud de atenuación. Eliminando los fotones dispersados, que en las distribuciones de tiempo de llegada se corresponden con los fotones tardíos, podremos escoger los fotones directos y por tanto dar una estimación de la longitud de atenuación en el agua.

Búsqueda de fuentes puntuales

Para la búsqueda de fuentes puntuales hemos usado una técnica de *unbinning* basada en la identificación de agrupaciones de sucesos o *clusters*. El método de EM

es un algoritmo ampliamente usado en diversas áreas cuya problemática común es el análisis de *clusters*. Evidentemente, dicho algoritmo ha de aplicarse al caso particular de la búsqueda de fuentes puntuales, donde una de las peculiaridades es la poca estadística de los *clusters* y el considerable fondo sobre el que están diseminados. Es necesario, pues, seleccionar previamente al algoritmo, un conjunto de parámetros iniciales para acelerar así el proceso de convergencia. Un sencillo algoritmo de *pre-clustering* es el encargado de seleccionar una serie de agrupaciones candidatas las cuáles, a su vez, serán evaluadas por el algoritmo EM. Una de las limitaciones de los métodos *unbinning* es que no tienen una manera directa y analítica de calcular las probabilidades. Para ello es necesario recurrir al Monte Carlo. Debido a que los datos de ANTARES aún están siendo analizados, en este estudio hemos simulado 10^4 muestras equivalentes a un año de toma de datos del detector completo basándonos en el Monte Carlo. En un telescopio de neutrinos, la contribución principal a los datos es la de neutrinos y antineutrinos atmosféricos. Otras fuentes de fondo como muones atmosféricos mal reconstruidos o sucesos debidos al flujo difuso de neutrinos pueden ser despreciados. De hecho, los muones mal reconstruidos pueden eliminarse si se eligen adecuadamente los cortes de selección en los algoritmos de reconstrucción de trazas. Por ello, las muestras de Monte Carlo utilizadas cuentan sólo con la contribución de los neutrinos atmosféricos al fondo. Esta dependencia con la simulación puede, en cualquier caso, ser eliminada cuando el detector esté plenamente operativo. En este caso, y gracias a su respuesta uniforme en ascensión recta, debido a la rotación de la Tierra, podremos sortear el valor de dicha coordenada en los sucesos de llegada para poder generar varias muestras equivalentes a un cierto periodo de toma de datos. Para estudiar las prestaciones en cuanto a búsqueda, sin embargo, se añaden sucesos de señal correspondientes a una fuente puntual para lo cual es necesario el Monte Carlo para simular la señal. La distribución de dichos sucesos tendrá una dependencia en energía y por tanto en el índice espectral. La significancia del método se estima a través de la teoría de testeo de hipótesis, donde en nuestro caso la variable discriminante u observable es el llamado *Bayesian Information Criterion* o BIC. El BIC es una aproximación al factor de probabilidad, y consiste en la **verosimilitud maximizada** menos una penalización que tiene en cuenta los grados de libertad del modelo.

La distribución de BIC se calcula para el caso en el que el algoritmo se aplica a un conjunto de muestras únicamente de fondo. Esta distribución se compara entonces con aquellos resultados en los que varios números de sucesos de señal se añaden a las muestras. De este modo somos capaces de separar las acumulaciones de señal reales de aquellas que fortuitamente ha producido el fondo de sucesos. Se define como **potencial de descubrimiento** al porcentaje de éxito en descubrir una fuente cuyo valor del BIC sea mayor que el de una fluctuación del fondo para una probabilidad dada, expresada generalmente en términos de desviaciones estándar de una gausiana. Por ejemplo, una probabilidad de descubrimiento p a 5σ significa que la señal (junto con el fondo) producirá en $(100\times p)\%$ experimentos idénticos (en promedio) una fluctuación sobre el fondo cuyo valor del BIC es igual o mayor que un cierto valor umbral, BIC_{th}, donde en el caso de sólo fondo se cumple que $P_{BG}(\mathrm{BIC} > \mathrm{BIC_{th}}) = 5.73 \times 10^{-7}$, es decir, equivalente a cinco desviaciones estándar gausianas. El criterio usado habitualmente para decidir si una fuente es detectable se basa en que la probabilidad p de encontrar

dicha fuente sea de al menos 50% cuando la probabilidad de que el fondo produzca un exceso equivalente es menor que 3σ ó 5σ.

La técnica desarrollada aquí demuestra una eficacia mayor que las técnicas de *binning* y comparable con otras técnicas de *unbinning* con la ventaja adicional de que no introduce ninguna información del detector como parámetro en el algoritmo. Los principales resultados de este trabajo se presentan asumiendo un índice espectral $\gamma = 2.0$, siendo ésta una estimación razonable de dicho parámetro. Para índices espectrales mayores el área efectiva a un flujo de neutrinos decae considerablemente de manera que el potencial de detección es mucho menor. No obstante, parte de esta tesis se dedica al estudio de la detección de fuentes puntuales con índices espectrales mayores. En particular, se han simulado señales provenientes de fuentes con un índice espectral de 2.7 y 3. Es importante señalar que ninguna optimización es necesaria a la hora de simular fuentes de distinto índice espectral de emisión. En esta parte se demuestra que la prestación del algoritmo, y por tanto los resultados en función del número de sucesos de señal necesarios para una detección (no en función del flujo) son casi independientes del índice espectral simulado.

El potencial de descubrimiento se muestra en función del promedio de sucesos de señal añadido en las muestras para distintas declinaciones. Existe una dependencia en función de la declinación por un lado debida a la dependencia del fondo de neutrinos atmosféricos en dicha coordenada y a la respuesta angular del detector a distintas declinaciones. La tabla 6.4 es un ejemplo de los sucesos necesarios para tener una probabilidad de descubrimiento de 50% con un nivel de confianza de 3σ y 5σ para algunas declinaciones:

$\delta(^\circ)$	3σ	5σ
-80°	5.5	7.5
-20°	5	6.9
$+40^\circ$	4.2	6

Como se puede apreciar, las declinaciones más bajas son aquellas que presentan un peor potencial de descubrimiento. También es posible presentar los resultados en términos del flujo necesario para realizar un descubrimiento. Para transformar un número de sucesos de una fuente en un flujo equivalente de neutrinos (o muones) es necesario disponer del valor promediado en energía del área efectiva en el rango de sensibilidad del detector en función de la declinación además de un factor que tenga en cuenta la visibilidad de la fuente (porcentaje de tiempo que la fuente se encuentra bajo el horizonte).

El cálculo de las áreas efectivas promediadas en energía se realiza mediante la convolución del espectro de neutrinos (muones) con el área efectiva para neutrinos (muones). El flujo de neutrinos se puede deducir fácilmente asumiendo que es isótropo y con un índice espectral que puede variar entre 2 y 3. Por el contrario, el flujo de muones en el detector es una magnitud desconocida que se debe deducir mediante el Monte Carlo. La visibilidad de una región del cielo se calcula utilizando funciones astronómicas que nos permiten convertir las coordenadas ecuatoriales (δ, AR) en coordenadas locales

(θ, ϕ) dentro del sistema de referencia del detector. La visibilidad sólo depende de la declinación de la fuente y de la latitud del detector. En el caso de ANTARES, todas las fuentes con declinaciones menores de -42° son visibles el 100% del tiempo y a partir de ese valor la visibilidad disminuye hasta $\delta = +48^\circ$ donde termina el cielo visible de ANTARES.

Cuando se muestran los resultados del potencial de descubrimiento en función de la declinación para flujos de neutrinos o muones, la dependencia con la declinación se invierte, siendo las declinaciones más bajas las que necesitan emitir un menor flujo de neutrinos para ser detectadas debido al factor de visibilidad.

El número medio de sucesos requerido para un descubrimiento puede reducirse si se incrementa el tiempo de observación. Si el tiempo de exposición del detector aumenta de uno a dos años, el número de sucesos por año necesario para un descubrimiento del 50% a 5σ se reduce en un factor $\sim \mathbf{2.2}$. El factor aumenta a $\sim \mathbf{6.3}$ si el tiempo de exposición son cinco años.

Los resultados en función del potencial de descubrimiento indican que sólo fuentes muy potentes podrán ser detectadas por ANTARES. Aún en el caso de que el descubrimiento de una fuente de neutrinos no fuera posible, ANTARES será capaz de establecer un límite máximo al flujo de neutrinos predichos por varias teorías y rechazar así algunas de las previsiones más optimistas. La sensibilidad es el promedio de los límites de flujos en un conjunto de muestras idénticas en promedio. En el capítulo 5 de esta tesis se presenta la sensibilidad del detector cuando se realiza una búsqueda *ciega*. Debido a que el fondo atmosférico de neutrinos es uniforme en ascensión recta, la sensibilidad aparece en función de la declinación. Cualquier flujo de neutrinos en una cierta banda de declinación será detectado por ANTARES si está por encima de dicha sensibilidad.

Fuentes seleccionadas

En una búsqueda *ciega*, es decir cuando se busca una fuente puntual en cualquier parte del cielo visible, las probabilidades de que el fondo genere accidentalmente un exceso no son despreciables. Por el contrario, podemos hacer uso de ciertas hipótesis a priori sobre qué objetos astronómicos son candidatos a emitir neutrinos. Es posible utilizar una lista de fuentes candidatas y realizar una búsqueda de agrupaciones de sucesos en cada una de las direcciones de dichas fuentes. En este caso, al restringir la búsqueda a una zona específica del cielo las probabilidades de que fondo pueda producir un exceso en esa dirección determinada y sea confundido con la señal de una fuente puntual, se reducen considerablemente.

En esta parte del análisis, el algoritmo EM se usa para calcular la verosimilitud restringiendo dos de los grados de libertad en los modelos que describen la densidad de probabilidad. En concreto los ángulos que determinan la posición de la fuente puntual en el cielo vienen fijados por la suposición de que en esa región del espacio existe una fuente de neutrinos. En el caso de que sólo los sucesos de fondo estén presentes en la muestra, es posible que ningún suceso aparezca en la región del espacio que estamos observando y el algoritmo no pueda estimar un valor de la normalización del *cluster*. Por ese motivo, la distribución del test estadístico para el caso de sólo fondo presenta un pico en su primer valor debido a los casos en que la estimación de la normalización

es nula. Al margen de este detalle, el resto del análisis es idéntico al presentado anteriormente. Dado que el fondo es uniforme en ascensión recta, la localización de la fuente a lo largo de esta coordenadas es irrelevante. Por ello, el estudio se ha realizado con una fuente por banda de declinación generando aleatoriamente entre 0 y 2π la posición en ascensión recta. La tabla 6.4 resume brevemente algunos de los resultados en términos del número de sucesos necesarios para hacer un descubrimiento al 50% en algunas bandas de declinación.

$\delta(^\circ)$	3σ	5σ
-80°	2.5	5
-20°	2.1	4.5
$+40^\circ$	2	3.5

Evidentemente, el potencial de descubrimiento en búsquedas prefijadas aumenta con respecto a una búsqueda *ciega* gracias a la información adicional sobre la posición de la fuente.

El análisis de ciertas fuentes candidatas es especialmente interesante en el caso de que ninguna fuente sea observada mediante la búsqueda global o *ciega*, ya que en esta situación, cuando se conoce la posición de una posible fuente candidata de neutrinos de alta energía, se puede utilizar el método EM para establecer un límite superior sobre el flujo emitido por dicha fuente. Del mismo modo que en las búsquedas, la sensibilidad de este tipo de límite es superior a la de los límites sobre todo el cielo. Cada límite obtenido es únicamente aplicable a una dirección o posible fuente a diferencia del límite aplicado a todo el cielo. En este estudio el valor promedio de los límites, o sensibilidad, se ha comparado con los límites establecidos por otros experimentos. Así, se encuentra que la sensibilidad alcanzable por ANTARES es mejor que los límites establecidos por otros detectores, en el rango en que sus regiones de visibilidad se solapan. Sin embargo, hay que señalar de nuevo que los resultados obtenidos para ANTARES corresponden solamente a la simulación Monte Carlo de un detector ideal, y no a datos reales.

Tanto en el caso de los límites para todo el cielo como en el caso de los límites para fuentes puntuales, al incrementar el tiempo de observación se incrementa su sensibilidad. Sin embargo, este aumento no es equivalente al incremento de tiempo y así se tiene que los límites son aproximadamente un factor 1.7 mejores tras 2 años de toma de datos y aproximadamente un factor 3 tras 5 años de toma de datos.

Conclusiones

El telescopio de neutrinos ANTARES se encuentra en fase de construcción. En la actualidad, 10 líneas se encuentran instaladas en el fondo de mar y para el 2008 todo el detector estará operativo. A partir de ese momento se podrán comenzar los estudios de búsqueda de fuentes puntuales. Primero, sin embargo, se debe comprobar que todos los elementos activos del detector están bien calibrados tanto temporalmente, como en carga en el caso de los fotomultiplicadores. Dentro de la calibración temporal, el

sistema de Balizas Ópticas es crucial a la hora de comprobar la resolución del detector y los tiempos de retraso de cada fotomultiplicador. Gracias a este sistema se puede comprobar que el diseño de la electrónica de ANTARES cumple con los requisitos que garantizan una resolución angular por debajo del grado.

Calibración temporal con las Balizas Ópticas

Utilizando el sistema de Balizas Ópticas hemos analizado por primera vez las distribuciones de los tiempos de llegada de los fotones emitidos por dichas fuentes luminosas a los fotomultiplicadores. Primeramente se ha estudiado la señal digitalizada por los chips de adquisición de los Módulos Ópticos y también la señal recogida en el fotomultiplicador y fotodiodo de las balizas. Después, se han calculado las diferencias de tiempo entre la señal adquirida en los Módulos Ópticos, y la señal registrada como tiempo de emisión en la baliza. Las conclusiones más importantes de este análisis son la siguientes:

- En este análisis se ha comprobado la eficacia del *trigger* desarrollado para procesar los eventos producidos en un *run* de calibración de las Balizas Ópticas. Gracias al `triggerOB` podemos procesar y analizar los datos de calibración del detector.

- Se han estudiado las distribuciones de los tiempos de llegada de los fotones en los fotomultiplicadores. Para distancias cortas, la anchura de dichas distribuciones son una medida directa de la resolución temporal de la electrónica de adquisición en ANTARES. Se ha comprobado que la resolución temporal es $\sim$ **0.4 ns**, tal y como se requería para conseguir la resolución angular deseada.

- Se ha comprobado como las diferencias no lineales en la electrónica del TVC generan que las distribuciones temporales se alejen ligeramente de la forma gausiana. No obstante, la calibración temporal de los TVC no causa grandes diferencias en la estimación de los tiempos de retardo, T^{100}, y de las resoluciones. Para obtener una estimación de los T^{100} de los fotomultiplicadores, se ha ajustado doblemente el flanco de subida de las distribuciones a una gausiana. La media del ajuste, T^{100}, se considera que es una clara estimación del valor que se ha desviado con respecto a los valores de la sala oscura de calibración.

- Cuando se realiza una calibración usando las balizas para iluminar a su propia línea se puede apreciar un retraso en la estimación del parámetro T^{100} con respecto a la distancia del fotomultiplicador a la baliza. Este retraso es estable para todas las líneas analizadas con un valor de aproximadamente **0.11 ns/m**. Dicho retraso no estaba predicho por el Monte Carlo dedicado a la simulación de las Balizas Ópticas.

- Para excluir un posible un origen geométrico (valores erróneos en la estimación de la velocidad de la luz o el posicionamiento) en el retraso del parámetro T^{100}, se han estudiado las distribuciones de tiempo cuando se ilumina un piso a distinta intensidad de luz obteniendo similares resultados. Así pues, dicho retraso tienen

un origen en su dependencia con la intensidad de luz depositada y no con la distancia.

- Cuando un pulso de luz de más de un fotoelectrón llega al fotocátodo de un PM, el tiempo de llegada viene determinado por el primer fotón debido a la incapacidad del PM de resolver pulsos de multi-fotoelectrones. Como consecuencia, cuando los pulsos de luz son de gran intensidad se produce una desviación en la estimación de los T^{100} que depende de la cantidad de luz emitida. Así pues, es posible corregir el retraso en la estimación del T^{100} construyendo una distribución de probabilidad que tenga en cuenta este efecto y donde la información de la cantidad de fotones se obtenga directamente de la carga depositada en el PM.

- También se ha estudiado las diferencias de tiempo entre Módulos Ópticos dentro de un mismo piso. En este caso ha sido necesario eliminar de los datos aquellos pulsos retrasados (*afterpulses*) provocados por una segunda integración de la carga cuando la señal depositada en el fotomultiplicadores es grande. Esta limpieza permite conservar la forma gausiana en la distribución de las diferencias temporales.

- La anchura de las distribuciones entre Módulos Ópticos da una resolución de aproximadamente $\sim$ **0.5 ns**, lo cual está de acuerdo con la medida de la resolución electrónica mencionada anteriormente.

- La información obtenida por las diferencias temporales entre Módulos Ópticos es de mucha importancia, ya que cualquier desviación sirve para calibrar los valores medidos en la sala oscura. Es más, el retraso en el caso de diferencias entre la baliza y el fotomultiplicador es tan estable que puede ser considerado una **regla empírica** completando así la información necesaria para calibrar los fotomultiplicadores. Actualmente, dicho procedimiento de calibración se está llevando a cabo aunque no esté cubierto en este estudio.

En este primer análisis de las Balizas Ópticas también hemos sido capaces de dar una primera estimación a uno de los parámetros ópticos del agua. Con ello se ha comprobado que el sistema de balizas no sólo permite la calibración temporal del detector, sino que también es posible llevar a cabo un estudio y vigilancia de ciertas propiedades de la transmisión de luz en el agua.

- La atenuación de la luz en el agua emitida por una fuente isótropa sigue una ley exponencial que depende de la distancia a la fuente y de un parámetro conocido como la **longitud de atenuación**. Por tanto, el número de fotoelectrones registrado en el fotomultiplicador tendrá, a su vez, la misma dependencia. Seleccionando los *hits* de las distribuciones temporales que pueblan la parte central podemos dar una medida de la longitud de atenuación representando la carga depositada por dichos *hits* en función de la distancia.

- La longitud de atenuación se ha estimado usando varias balizas y usando sólo los fotomultiplicadores de la misma línea. El valor medio es de $\boldsymbol{\lambda_{att} = 45 \pm 1 \pm 4}$ **m**

y no depende de la intensidad de la luz emitida. Posible variaciones estacionales podrán ser controladas por el sistema de balizas, aunque de momento no existe indicaciones a tal efecto.

Búsqueda de fuentes puntuales de neutrinos

En primer lugar hemos realizado una búsqueda *ciega* de fuentes puntuales en todo el cielo visible. Las búsquedas *ciegas* se caracterizan porque no se realiza ninguna suposición sobre la fuente, su posición o flujo emitido. El algoritmo EM se ha aplicado a este tipo de búsquedas para una muestra equivalente a un año de toma de datos y una señal con índice espectral de 2. Los resultados más importantes obtenidos en las búsquedas son los siguientes:

- La probabilidad de descubrir una fuente puntual a un cierto nivel de confianza aumenta rápidamente con el número de sucesos observados en la dirección de la fuente. Con el algoritmo EM hemos determinado que el número de sucesos mínimo necesario para detectar una fuente con una probabilidad de 50% varía entre **7.5** y **6**, siendo éstos los valores de dos extremos del mapa de visibilidad ($\delta = -80°$, $\delta = 40°$) respectivamente, y para un nivel de confianza de cinco desviaciones estándar (5σ). Los números descienden a **5.5** y **4** para un nivel de confianza equivalente a 3σ.

- Debido a la rotación de la tierra el fondo de neutrinos atmosféricos depende únicamente de la declinación. A su vez, la resolución angular del detector tiene cierta dependencia en esta coordenada, por ello, es evidente que el potencial de descubrimiento también tenga una dependencia en dicha coordenada pero no en la ascensión recta.

- La probabilidad de descubrimiento también se puede presentar en términos del flujo neutrinos/muones necesario para realizar una detección de una fuente puntual. El flujo de neutrinos necesario para descubrir una fuente con una probabilidad de 50% en una declinación de $\delta = -80°$ es de $\boldsymbol{E_\nu^2 d\Phi_\nu^{50\%}/dE_\nu = 1.7 \times 10^{-7}\ \mathrm{GeV\ m^{-2}\ s^{-1}}}$ para un nivel de confianza de 5σ.

- El algoritmo EM trata la información de forma continua, de manera que es posible estimar un valor para la posición de la fuente a diferencia de las técnicas de *binning*. Evidentemente, la resolución de ANTARES para identificar fuentes depende del número de sucesos observados de dicha fuente. Teniendo en cuenta un funcionamiento óptimo del detector, se pueden alcanzar valores **menores que 0.1**° en la determinación de la posición de una fuente gracias al algoritmo EM cuando más de 6 sucesos de señal son observados.

- El algoritmo EM presentado en este estudio demuestra ser un método robusto para la búsqueda de fuentes puntuales. Ninguna optimización ha sido necesaria y ningún ajuste hacia un tipo determinado de emisión de la fuente se ha tenido en cuenta. De hecho, se ha estudiado la respuesta del algoritmo a señales de neutrinos con índice espectral distinto de 2 sin ninguna adaptación en el método.

Como resultado se puede observar que la probabilidad de descubrimiento, cuando se expresa en función del número de sucesos, no varía notablemente siendo aproximadamente un $\sim$ 12% peor. No obstante, la diferencia en términos de flujo de neutrinos llega a alcanzar los **3 órdenes de magnitud** debido a que el área efectiva de ANTARES tiene una gran dependencia en la energía y por tanto en el índice espectral. Así pues, el área efectiva para índices espectrales mayores que 2 es tan pequeña que un flujo de neutrinos con dicho índice será practicamente indetectable en ANTARES.

- En el caso de que ninguna fuente de neutrinos sea detectada en una búsqueda *ciega* o global, siempre será posible estimar cuál es el límite superior al flujo de neutrinos que podría estar emitiendo una fuente de neutrinos. En este estudio presentamos un promedio de límites superiores conocido como la *sensibilidad* del detector. La sensibilidad de ANTARES a una fuente localizada en cualquier parte del cielo en términos del flujo de neutrinos es $\mathbf{\Phi_\nu \simeq 2.5 \times 10^{-8}\ cm^{-2}\ s^{-1}}$, integrado sobre 10 GeV.

- Al aumentar el tiempo de toma de datos se mejora sensiblemente la probabilidad de descubrimiento lo cual viene relacionado por el aumento del tiempo de exposición del detector. Para un nivel de confianza de 5σ la mejora en el flujo de descubrimiento es de aproximadamente un **40%** cuando el tiempo de exposición aumenta a 2 años, y sobre un **70%** para tiempos de adquisición de 5 años.

Por último, podemos restringir la búsqueda de fuentes puntuales a ciertas direcciones del cielo donde haya indicios o evidencias de la existencia de una fuente emisora de neutrinos. Los resultados más importante para esta parte del análisis son los siguientes:

- Dado que la búsqueda se centra ahora a una región específica del cielo, la probabilidad del fondo de imitar una fuente de neutrinos se ve reducida considerablemente. Así pues el poder de descubrimiento incrementa con respecto a una búsqueda *ciega*.

- El número de sucesos de señal observados necesarios para hacer un descubrimiento del 50% varía entre **5** para una declinación de $\delta = -80°$ y **3.5** para $\delta = 40°$, asumiendo un nivel de confianza equivalente a 5σ.

- La sensibilidad de ANTARES para la búsqueda de fuentes fijas es aproximadamente $\boldsymbol{E_\nu^2 d\Phi_\nu^{50\%}/dE_\nu = 8.2\times 10^{-4}\ GeV\ m^{-2}\ s^{-1}}$ (promediada para todas las declinaciones).

- Al aumentar el tiempo de exposición del detector su sensibilidad mejorará, así pues en 5 años ANTARES bajará su sensibilidad aproximadamente un **80%**.

Resumen

Bibliography

[1] K. S. Hirata et al. Observation of ^{8}B solar neutrinos in the Kamiokande-II detector. *Phys. Rev. Lett.*, 63:16, 1989.

[2] K. S. Hirata et al. Observation of a neutrino burst from the supernova SN1987A. *Phys. Rev. Lett.*, 58:1490, 1987.

[3] A. M. Hillas. In *Cosmology, galaxy formation and astroparticle physics on the pathway to the SKA*, Oxford, United Kingdom, 2006. astro-ph/0607109.

[4] V. L. Ginzburg and V. S. Ptuskin. On the origin of cosmic rays: Some problems in high-energy astrophysics. *Rev. Mod. Phys.*, 48:161, 1976.

[5] A. M. Hillas. Can diffusive shock acceleration in supernova remnants account for high-energy galactic cosmic rays? *J. Phys. G: Nucl. Part. Phys.*, 31:39, 2005.

[6] E. G. Berezhko and L. T. Ksenofontov. Composition of cosmic rays accelerated in supernova remnants. *JETP 89*, 3:391, 1999.

[7] D. Kazanas and A. Nicolaidis. In *Proceedings of the 27th International Cosmic Ray Conference*, Hamburg, Germany, 2001. astro-ph/0103147.

[8] J. R. Hörandel. Models of the knee in the energy spectrum of cosmic rays. *Astropart. Phys.*, 21:241–265, 2004. astro-ph/0402356.

[9] F. Halzen et al. The highest energy cosmic ray. *Astropart. Phys.*, 3:151, 1995.

[10] B. Peters. Primary cosmic radiation and extensive air showers. *Nuovo Cimento*, 22:800, 1961.

[11] J. Abraham et al. Correlation of the highest-energy cosmic rays with nearby extragalactic objects. *Science*, 318:938–943, 2007.

[12] K. Greisen. End to the cosmic ray spectrum? *Phys. Rev. Lett.*, 16:748, 1966.

[13] G. T. Zatsepin and V. A. Kuzmin. Upper limit of the spectrum of cosmic rays. *Sov. Phys. JETP Lett.*, 4:78, 1966.

[14] P. Mantsch for the Pierre Collaboration. In *Proceedings of the 29th International Cosmic Ray Conference*, Pune, India, 2005.

[15] M. Takeda et al. Extension of the cosmic ray energy spectrum beyond the predicted Greisen-Zatsepin-Kuz'min cutoff. *Phys. Rev.*, 81:1163, 1998.

[16] T. Abu-Zayyad et al. (HiRes Collaboration). Measurement of the flux of ultrahigh energy cosmic rays from monocular observations by the high resolution Fly's Eye experiment. *Phys. Rev. Lett.*, 92:151101, 2004. astro-ph/0208243.

[17] E. Fermi. On the origin of cosmic rays. *Phys. Rev.*, 75(8):1169, 1949.

[18] E. Fermi. Galactic magnetic fields and the origin of cosmic radiation. *Astrophys. J.*, 119:1–6, 1954.

[19] A. Dar and A. De Rújula. A theory of cosmic rays. 2006. hep-ph/0606199.

[20] D. V. Semikoz and G. Sigl. Ultra-high energy neutrino fluxes: New constraints and implications.

[21] F. Halzen. In *Proceedings of the International Workshop on Energy Budget in the High Energy Universe*, Kashiwa, Japan, 2006.

[22] R. J. Protheroe and T. Stanev. Extremely high energy neutrinos, neutrino hot dark matter, and the highest energy cosmic rays. *Phys. Rev. Lett.*, 78:2420, 1996.

[23] J. J. Beatty et al. In *Proceedings of the 26th International Cosmic Ray Conference*, volume 5, pages 61–64, Salt Lake City (Utah), USA, 1999.

[24] F. Gahbauer et al. In *Proceedings of the 27th International Cosmic Ray Conference*, Hamburg, Germany, 2001.

[25] M. Boezio et al. The space experiment PAMELA. *Nucl. Phys. B*, 134:39–4, 2004.

[26] M. Aguilar et al. (AMS Collaboration). The Alpha Magnetic Spectrometer (AMS) on the International Space Station: Part I - results from the test flight on the space shuttle. *Phys. Rep.*, 366:331–404, 2002.

[27] T. Antoni et al. Electron, muon, and hadron lateral distributions measured in air-showers by the KASCADE experiment. *Astropart. Phys.*, 14:245–260, 2001.

[28] T. Antoni et al. A large area limited streamer tube detector for the air shower experiment KASCADE-Grande. *Nucl. Instr. and Meth. Phys. Res. A*, 533:387–403, 2004.

[29] O. Ravel et al. Radio detection of cosmic ray air showers by the CODALEMA experiment. *Nucl. Instr. and Meth. Phys. Res. A*, 518:213–215, 2004.

[30] F. W. Stecker et al. Observing the ultrahigh energy universe with OWL eyes. *Nucl. Phys. B (Proc. Suppl.)*, 136:433–438, 2004.

[31] G. Agnetta et al. In *Proceedings of the 29th International Cosmic Ray Conference*, Pune, India, 2005.

[32] J. N. Bahcall and E. Waxman. High energy astrophysical neutrinos: The upper bound is robust. *Phys. Rev. D*, 64:023002, 2001.

[33] F. A. Aharonian. *Very High Energy Cosmic Gamma-Ray Radiation.* World Scientific Publishing, 2004.

[34] C. E. Fichtel and J. I. Trombka. Gamma-ray astrophysics: New insight into the Universe. Technical report, 1997. NASA-RP-1386.

[35] N. Gehrels and P. Michelson. GLAST: The next-generation high energy gamma-ray astronomy mission. *Astropart. Phys.*, 11:277–282, 1999.

[36] T. C. Weekes et al. Observation of TeV gamma rays from the Crab nebula using the atmospheric cerenkov imaging technique. *Astrophys. J.*, 342:379–395, 1989.

[37] R. Mirzoyan et al. The first telescope of the HEGRA air cherenkov imaging telescope array. *Nucl. Instr. and Meth. Phys. Res. A*, 351:513–526, 1994.

[38] J. A. Hinton. The status of the H.E.S.S. project. *New Astron. Rev.*, 48:331–337, 2004.

[39] J. Albert i Fort et al. In *Proceedings of the 29th International Cosmic Ray Conference*, Pune, India, 2005.

[40] J. Holder et al. In *Proceedings of the 29th International Cosmic Ray Conference*, Pune, India, 2005. astro-ph/0507451.

[41] R. Enomoto et al. Design study of CANGAROO-III, stereoscopic imaging atmospheric cherenkov telescopes for sub-TeV gamma-ray. *Astropart. Phys.*, 16:235–244, 2002.

[42] F. Halzen. Astroparticle physics with high energy neutrinos: from AMANDA to IceCube. *Eur. Phys. J.*, C46:669–687, 2006. astro-ph/0602132.

[43] F. Aharonian et al. Detection of TeV gamma-ray emission from the shell-type supernova remnant RX J0852.0-4622 with H.E.S.S. *Astron. & Astrophys.*, 437:L7, 2005. astro-ph/0505380.

[44] M. D. Kistler and J. F. Beacom. Guaranteed and prospective galactic TeV neutrino sources. *Phys. Rev. D*, 74:063007, 2006. astro-ph/0607082.

[45] O. Reimer and M. Pohl. No hadronic TeV γ-rays from SNR RX J1713.7-3946. *Astron. & Astrophys.*, 390:L43, 2002.

[46] H. Muraishi et al. Evidence for TeV gamma-ray emission from the shell-type SNR RX J1713.7-3946. *Astron. & Astrophys.*, 354:L57, 2000.

[47] R. Enomoto et al. The acceleration of cosmic-ray protons in the supernova remnant RX J1713.7-3946. *Nature*, 416:823, 2002.

[48] F. Aharonian et al. (H.E.S.S. Collaboration). A detailed spectral and morphological study of the gamma-ray supernova remnant RX J1713.7-3946 with H.E.S.S. *Astron. & Astrophys.*, 449:223, 2006.

[49] J. Alvarez-Muñiz and F. Halzen. Possible high-energy neutrinos from the cosmic accelerator RXJ1713.7-3946. *Astrophys. J.*, 576:L33, 2002. astro-ph/0205408.

[50] M. L. Costantini and F. Vissani. Expected neutrino signal from supernova remnant RXJ1713.7-3946 and flavor oscillations. *Astropart. Phys.*, 23:477–485, 2005.

[51] D. Horns, F. Aharonian, A. Santangelo, A. I. D. Hoffmann, and C. Masterson. Nucleonic gamma-ray production in Vela X. *Astron. & Astrophys.*, 451:L51, 2006.

[52] D. Guetta and E. Amato. Neutrino flux predictions for galactic plerions. *Astropart. Phys.*, 19:403, 2003. astro-ph/0209537.

[53] F. Aharonian et al. (HEGRA Collaboration). *Astrophys. J.*, 614:897, 2004.

[54] IceCube Collaboration. In *Proceedings of the 29th International Cosmic Ray Conference*, Pune, India, 2005. astro-ph/0509330.

[55] F. Aharonian et al. (H.E.S.S. Collaboration). Discovery of very high energy gamma-rays from the galactic centre ridge. *Nature*, 439:695, 2006. astro-ph/0603021.

[56] F. Aharonian et al. (H.E.S.S. Collaboration). Very high energy gamma rays from the direction of Sagittarius A*. *Astron. & Astrophys.*, 425:L13–17, 2004.

[57] F. Aharonian et al. (H.E.S.S. Collaboration). Very high energy gamma rays from the composite SNR G0.9+0.1. *Astron. & Astrophys.*, 432:L25–29, 2005.

[58] F. Aharonian et al. (H.E.S.S. Collaboration). H.E.S.S. observations of the Galactic Center region and their possible dark matter interpretation. *Phys. Rev. Lett.*, 97:221102, 2006. astro-ph/0610509.

[59] S. Chaty. In *Proceedings of Rencontres de Moriond, Very High Energy Phenomena in the Universe*, La Thuile, Italy, 2005. astro-ph/0506008.

[60] S. Migliari, R. Fender, and M. Méndez. Iron emission lines from extended X-ray jets in SS 433: Reheating of atomic nuclei. *Science*, 297:1673, 2002.

[61] F. Aharonian et al. (H.E.S.S. Collaboration). Discovery of very high energy gamma rays associated with an X-ray binary. *Science*, 309:746, 2005.

[62] J. Albert et al. (MAGIC Collaboration). Variable very high energy gamma-ray emission from the microquasar LS I+61 303. *Science*, 312:1771, 2006. astro-ph/0605549.

[63] D. F. Torres and F. Halzen. LS I+61 303 as a potential neutrino source on the light of MAGIC results. 2006. astro-ph/0607368.

[64] F. Aharonian, L. Anchordoqui, D. Khangulyan, and T. Montaruli. Microquasar LS 5039: a TeV gamma-ray emitter and a potential TeV neutrino source. *J. Phys.: Conf. Ser.*, 39:408.

[65] W. Bednarek, G. F. Burgio, and T. Montaruli. Galactic discrete sources of high energy neutrinos. *New Astron. Rev.*, 49:1, 2005. astro-ph/0404534.

[66] A. Loeb and E. Waxman. The cumulative background of high-energy neutrinos from starburst galaxies. *JCAP*, 0605:003, 2006. astro-ph/0601695.

[67] R. V. E. Lovelace. Dynamo model of double radio sources. *Nature*, 262:649, 1976.

[68] K. Mannheim. High-energy neutrinos from extragalactic jets. *Astropart. Phys.*, 3:295, 1995.

[69] F. Halzen and E. Zas. Neutrino fluxes from active galaxies: A model independent estimate. *Astrophys. J.*, 488:669, 1997.

[70] R. J. Protheroe. High energy neutrinos from blazars. *ASP Conf. Ser.*, 121:585, 1997.

[71] J. K. Becker, P. L. Biermann, and W. Rhode. The diffuse neutrino flux from FR-II radio galaxies and blazars: A source property based estimate. *Astropart. Phys.*, 23:355–368, 2005. astro-ph/0502089.

[72] T. J. Galama et al. Discovery of the peculiar supernova 1998bw in the error box of GRB980425. *Nature*, 395:670, 1998.

[73] K. Z. Stanek et al. Spectroscopic discovery of the supernova 2003dh associated with GRB030329. *Astrophys. J.*, 591:L17, 2003.

[74] J. Hjorth et al. A very energetic supernova associated with the gamma-ray burst of 29 March 2003. *Nature*, 423:847, 2003.

[75] E. Waxman and J. N. Bahcall. High energy neutrinos from cosmological gamma-ray burst fireballs. *Phys. Rev. Lett.*, 78:2292, 1997.

[76] S. Razzaque, P. Mészáros, and E. Waxman. Neutrino signatures of the supernova - gamma ray burst relationship. *Phys. Rev. D*, 69:023001, 2004.

[77] D. Guetta et al. Neutrinos from individual gamma-ray bursts in the BATSE catalog. *Astropart. Phys.*, 20:429, 2004. astro-ph/0302524.

[78] R. Engel, D. Seckel, and T. Stanev. Neutrinos from propagation of ultra-high energy protons. *Phys. Rev. D*, 64:093010, 2001. astro-ph/0101216, and references therein.

[79] E. Waxman. Extra galactic sources of high energy neutrinos. *Phys. Scripta*, T121:147, 2005. astro-ph/0502159.

[80] H. Dannerbauer et al. Follow-up near-infrared spectroscopy of ultraluminous infrared galaxies observed by ISO. *Astron. & Astrophys.*, 441:999, 2005.

[81] V. Springel et al. Modeling feedback from stars and black holes in galaxy mergers. *Astron. Soc.*, 361:776, 2005.

[82] G. 't Hooft. Magnetic monopoles in unified gauge theories. *Nucl. Phys. B*, 79:276, 1974.

[83] A. M. Polyakov. Particle spectrum in quantum field theory. *JETP Lett.*, 20:194, 1974.

[84] E. W. Kolb and M. S. Turner. *The Early Universe*. Perseus Publishing, 1990.

[85] E. N. Parker. The origin of magnetic fields. *Astrophys. J.*, 160:383, 1970.

[86] D. Bakari et al. Magnetic monopoles, nuclearites, Q-balls: A qualitative picture. 2000. hep-ex/0004019.

[87] A. M. Polyakov. Particle spectrum in quantum field theory. *JETP Lett.*, 20:194, 1974.

[88] G. T. Horowitz. Spacetime in string theory. *New J. Phys.*, 7:201, 2005. gr-qc/0410049.

[89] T. Mohaupt. Introduction to string theory. *Lect. Notes Phys.*, 631:173, 2003.

[90] C. Rovelli. Loop quantum gravity. *Living Rev. Rel.*, 1:1, 1998. gr-qc/9710008.

[91] G. Amelino-Camelia et al. On the fate of Lorentz symmetry in loop quantum gravity and noncommutative spacetimes. 2002. gr-qc/0205125.

[92] M. C. González-García and Y. Nir. Neutrino masses and mixing: Evidence and implications. *Rev. of Mod. Phys.*, 75:354, 2003.

[93] J. G. Learned and S. Pakvasa. Detecting nutau oscillations as PeV energies. *Astropart. Phys.*, 3:267, 1995.

[94] T. Kashti and E. Waxman. Astrophysical neutrinos: Flavor ratios depend on energy. *Phys. Rev. Lett.*, 95:181101, 2005.

[95] J. F. Beacom et al. Measuring flavor ratios of high-energy astrophysical neutrinos. *Phys. Rev. D*, 68:093005, 2003.

[96] The Baikal Collaboration. The Baikal neutrino project: Status report. *Nucl. Phys. B (Proc. Suppl.)*, 91:438, 2001.

[97] M. P. Kowalski. In *Proceedings of the 28th International Cosmic Ray Conference*, Tsukuba, Japan, 2003.

[98] V. Aynutdinov et al. In *Proceedings of the 29th International Cosmic Ray Conference*, Pune, India, 2005. astro-ph/0508675.

[99] A. Achterberg et al. Five years of searches for point sources of astrophysical neutrinos with the AMANDA-II neutrino telescope. *Physical Review D*, 75:102001, 2007.

[100] The IceCube Collaboration. IceCube: A kilometer scale neutrino observatory. NSF Proposal, 2001. `http://pheno.physics.wisc.edu/IceCube/proposal.html`.

[101] G. Hill et al. In *Proceedings of the Neutrino 2006 Conference*, Santa Fe, USA, 2006.

[102] The KM3NeT Consortium. Design Study for a Deep Sea Facility in the Mediterranean for Neutrino Astronomy and Associated Sciences. KM3NeT FP6 Proposal, 2006. `http://www.km3net.org`.

[103] E. Migneco. NEMO Collaboration. In *Proceedings of the NO-VE 2006 Conference*, Venice, Italy, 2006.

[104] G. Aggouras et al. Recent results from NESTOR. *Nucl. Instr. and Meth. Phys. Res. A*, 567:452–456, 2006.

[105] The ANTARES Collaboration. A Deep Sea Telescope for High Energy Neutrinos. Proposal for a 0.1 km^2 detector, 1999. astro-ph/9907432.

[106] *European Roadmap for Research Infrastructures*. ISBN 92-79-02694.

[107] *Toward New Research Infrastructures for Europe*. The ESFRI List of Opportunities.

[108] G. A. Askaryan et al. Excess negative charge of an electron-photon shower and the coherent radio emission from it. *JETP*, 14:441, 1962.

[109] I. Kravchenko et al. RICE limits on the diffuse ultrahigh energy neutrino flux. *Phys. Rev. D.*, 73:082002, 2006.

[110] S. W. Barwick et al. Constraints on cosmic neutrino fluxes from the Antarctic Impulsive Transient Antenna experiment. *Phys. Rev. Lett.*, 96:171101, 2006. astro-ph/0512265.

[111] P. W. Gorham et al. In *Proceedings of the First International Workshop on Radio Detection of High Energy Particles*, Los Angeles, USA, 2000.

[112] S. L. Glashow. Resonant scattering of antineutrinos. *Phys. Rev.*, 118:316, 1960.

[113] R. Gandhi et al. Ultrahigh-energy neutrino interactions. *Astropart. Phys.*, 5:81, 1996.

[114] J. Pumplin et al. New generation of parton distributions with uncertainties from global QCD analysis. *JHEP*, 07:012, 2002. hep-ph/0201195.

[115] P. A. Cherenkov. Visible radiation produced by electrons moving in a medium with velocities exceeding that of light. *Phys. Rev.*, 52:378, 1937.

[116] A. M. Markov. In *Proceedings of the Rochester Conference*, New York, USA, 1960.

[117] E. Bugaev et al. Propagation of τ-neutrinos and τ-leptons through the Earth and their detection in underwater/ice neutrino telescopes. *Astropart. Phys.*, 21:491, 2004.

[118] A. Margiotta. Simulation of muons from atmospheric showers in the ANTARES detector using HEMAS. ANTARES Internal note, 2004. ANTARES-Soft/2004-002.

[119] J. d. D. Zornoza. *Sensitivity to Diffuse Fluxes and Energy Spectrum Reconstruction in the ANTARES Neutrino Telescope*. PhD thesis, Universitat de València, Spain, 2005.

[120] A. Romeyer. *Étude de la sensibilité du détecteur ANTARES à un flux difuss de neutrinos cosmiques de haute énergie*. PhD thesis, Université Deni Diderot - Paris VII, France, 2003.

[121] A. Okada. On the atmospheric muon energy spectrum in the deep ocean and its parametrization. *Astropart. Phys.*, 2:393, 1994.

[122] V. Agrawal et al. Atmospheric neutrino flux above 1 GeV. *Phys. Rev. D*, 53:1314, 1996.

[123] The ANTARES Collaboration. Conceptual Design Report of the 0.1 km^2 detector. ANTARES Internal document, 1999.

[124] P. Amram et al. *Nucl. Instr. and Meth. Phys. Res. A*, 484:369, 2002.

[125] J. A. Aguilar et al. The ANTARES optical module. *Nucl. Instr. and Meth. Phys. Res. A*, 555:132–141, 2005.

[126] J. A. Aguilar. Study of the performances of several layouts and geometries for the future ANTARES neutrino telescope. Master's thesis, Universitat de València, Spain, 2004.

[127] P. Amram et al. Background light in potential sites for the ANTARES undersea neutrino telescope. *Astropart. Phys.*, 13:127–136, 2000. astro-ph/9910170.

[128] J. A. Aguilar et al. Transmission of light in deep sea water at the site of the ANTARES neutrino telescope. *Astropart. Phys.*, 23:131–155, 2004. astro-ph/0412126.

[129] R. C. Millard and G. Seaver. An index of refraction algorithm for seawater over temperature, pressure, salinity and wavelength. *Deep Sea Res.*, 37:121, 1990.

[130] X. Quan and E. Fry. Empirical equation for the index of refraction of seawater. *Appl. Opt.*, 34:18, 1995.

[131] J. A. Aguilar et al. The data acquisition system for the ANTARES neutrino telescope. *Nucl. Instr. and Meth. Phys. Res. A*, 570:107, 2006. astro-ph/0610029.

[132] F. Feinstein. (ANTARES Collaboration). The analogue ring sampler: A front-end chip for ANTARES. *Nucl. Instr. and Meth. Phys. Res. A*, 504:258–261, 2003.

[133] J. A. Aguilar. Talk in ANTARES Collaboration meeting, 2005. Ravenna, Italy.

[134] R. Brun and F. Rademakers. ROOT: An object oriented data analysis framework. *Nucl. Instr. and Meth. Phys. Res. A*, 389:81, 1997. http://root.cern.ch.

[135] R. Gurin and A. Maslennikov. ControlHost: Distributed Data Handling Package. CASPUT Inter-University Computing Consortium Rome, 1995.

[136] A. Romeyer. *Étude de la sensibilité du détecteur ANTARES à un flux diffus de neutrinos cosmiques de haute énergie*. PhD thesis, Université Denis Diderot - Paris VII, France, 2003.

[137] J. A. Aguilar et al. First results of the instrumentation line for the deep-sea ANTARES neutrino telescope. *Astropart. Phys.*, 26:314, 2006. astro-ph/0606229.

[138] M. Ageron et al. The ANTARES Optical Beacon system. *Nucl. Instr. and Meth. Phys. Res. A*, 578:498, 2007.

[139] T. Fields and D. Jankowski. Simple scheme for light collection from large-area plastic scintillators. *Nucl. Instr. and Meth. Phys. Res.*, 215:131, 1983.

[140] J. S. Kapustinsky et al. A fast timing light pulser for scintillation detectors. *Nucl. Instr. and Meth. Phys. Res. A*, 241:612, 1985.

[141] F. Salesa. Integration and first results of the Optical Beacon calibration system of the ANTARES neutrino telescope. Master's thesis, Universitat de València, Spain, 2006.

[142] J. A. Aguilar and M. de Jong. The Optical Beacon trigger. ANTARES Internal note, 2005. ANTARES-Soft/2005-002.

[143] S. Karkar. *Détection de microquasars et calibration en temps du télescope à neutrinos ANTARES*. PhD thesis, Université de la Méditérranée - Aix Marseille II, Marseille, France, 2004.

[144] S. Navas. Timing calibration with an Optical Beacon. ANTARES Internal note, 1999. ANTARES-Cali/1999-001.

[145] J. S. Ricol. *Étude de la détection de monopôles magnétiques au sein du futur télescope à neutrinos ANTARES et caractérisation des performances du traitement des impulsions des photomultiplicateurs*. PhD thesis, Université de la Méditérranée - Aix Marseille II, Marseille, France, 2002.

[146] G. Lambard. Walk effect correction. ANTARES Internal note, 2004. ANTARES-Cali/2006-004.

[147] S. Loucatos. Private communication.

[148] V. Balkanov et al. In situ measurements of optical parameters in lake Baikal with the help of a neutrino telescope. *Applied Optics*, 38:33, 1999.

[149] J. Ahrens et al. Muon track reconstruction and data selection techniques in AMANDA. *Nucl. Instr. and Meth. Phys. Res. A*, 524:169–194, 2004.

[150] E. Carmona. *Study of the event reconstruction and expected performances for the point-like sources of the future ANTARES neutrino telescope*. PhD thesis, Universitat de València, Spain, 2003.

[151] A. Chilingarian et al. In *Proceedings of the 29th International Cosmic Ray Conference*, Pune, India, 2005.

[152] J. A. Aguilar for the ANTARES Collaboration. In *Proceedings of the 30th International Cosmic Ray Conference*, Mérida, México, 2005. astro-ph/0710.0252.

[153] A. Heijboer. *Track reconstruction and point source searches with ANTARES*. PhD thesis, Universiteit van Amsterdan, 2004.

[154] The High Resolution Fly's Eye Collaboration and G. R. Farrar. Search for point sources of ultra-high energy cosmic rays above 40 EeV using a maximum likelihood ratio test. *Astrophys. J.*, 623:164, 2005. astro-ph/0412617.

[155] J. A. Aguilar and J. J. Hernández-Rey. The Expectation-Maximization algorithm applied to the search of point sources of astroparticles. *Astropart. Phys.*, 2007. doi:10.1016/j.astropartphys.2007.12.002.

[156] J. A. Aguilar. Talk in ANTARES Collaboration meeting, 2003. CERN, Geneva.

[157] V. Agrawal, T. K. Gaisser, P. Lipari, and T. Stanev. Atmospheric neutrino flux above 1 GeV. *Phys. Rev.*, D53:1314, 1996. hep-ph/9509423.

[158] SLALIB - Positional Astronomy Library. `http://www.starlink.rl.ac.uk/star/docs/sun67.htx/sun67.html`.

[159] A. P. Dempster, N. M. Laird, and D.B. Rubin. Maximum likelihood from incomplete data via the EM algorithm. *J. Royal Statistical Soc. Series B*, 38:1–38, 1977.

[160] G. Schwarz. Estimating the dimension of a model. *Ann. Stat.*, 6:461–464, 1978.

[161] D. M. A. Haughton. On the choice of a model to fit data from an exponential family. *Ann. Stat.*, 16:342–355, 1988.

[162] M. Kendall and A. Stuart. *The advanced theory of statistics*, volume 2. Charles Griffin & Co. Ltd, 1978.

[163] D. J. L. Bailey. *Monte Carlo tools and analysis methods of understanding the ANTARES experiment and predicting its sensitivity to Dark Matter.* PhD thesis, University of Oxford, United Kingdom, 2002.

[164] G. J. Feldman and R. D. Cousins. Unified approach to the classical statistical analysis of small signal. *Phys. Rev.*, D57:3873, 1998.

[165] M. Ambrosio et al. Neutrino astronomy with the MACRO detector. *Astrophys. J.*, 546:1038–1054, 2001.

[166] K. Abe et al. High energy neutrino astronomy using upward-going muons in Super-Kamiokande-I. *Astrophys. J.*, 652:198–205, 2006.

[167] J. Ahrens et al. Search for extraterrestrial point sources of neutrinos with AMANDA-II. *Physical Review Letters*, 92:071102, 2004.

[168] J. Ahrens et al. Sensitivity of IceCube detector to astrophysical sources of high energy muon neutrinos. *Astropart. Phys.*, 20:507–532, 2004.

[169] P. Sapienza for the NEMO Collaboration. In *Proceedings of the 20th European Cosmic Ray Symposium*, Lisbon, Portugal, 2006. astro-ph/0611105.

[170] D. J. L. Bailey. Genhen: Extension of Genneu for high energy neutrino interactions. ANTARES Internal note, 2000. ANTARES-Soft/2000-005.

[171] D. J. L. Bailey. Genhen v3r1: Further optimisation for large energy ranges. ANTARES Internal note, 2000. ANTARES-Soft/2000-006.

[172] D. J. L. Bailey. Genhen v5r1: Software Documentation. ANTARES Internal note, 2002. ANTARES-Soft/2002-004.

[173] G. D. Barr. *The separation of signal and background in nucleon decay experiment.* PhD thesis, University of Oxford, United Kingdom, 1987.

[174] G. Ingelman et al. LEPTO 6.5: A Monte Carlo generator for deep inelastic lepton-nucleon scattering. *Comput. Phys. Common*, 101:108, 1997. hep-ph/9605286.

[175] P. Lipari and T. Stanev. Propagation of multi-TeV muons. *Phys. Rev. D*, 44:3543, 1991.

[176] P. Antonioli et al. A three-dimensional code for muon propagation through the rock: MUSIC. *Astropart. Phys.*, 7:357–368, 1997.

[177] D. J. L. Bailey. KM3 v2r1: User Guide. ANTARES Internal note, 2002. ANTARES-Soft/2002-006.

[178] J. Brunner. ANTARES Internal documentation. `http://antares.in2p3.fr/internal/software/geasim.html`.

[179] S. Navas. A Comparison between GEASIM and KM3 generators. ANTARES Internal note, 1999. ANTARES-Soft/1999-002.

[180] F. Cassol. Recontruction re-organisation: RECO version 2.0. ANTARES Internal note, 1999. ANTARES-Soft/1999-004.

[181] F. Cassol. RECO version 2.1: code and scripts. ANTARES Internal note, 1999. ANTARES-Soft/1999-005.

Appendix A

The ANTARES Monte Carlo

In this appendix we will review the ANTARES Monte Carlo tools. The simulation chain can be itemized in four steps:

- **Physic generator**. Neutrino induced events are generated using the `GENHEN` package [170, 171, 172]. This package supports the three neutrino flavours and both interaction channels (neutral current NC, and charged current CC). The neutrino energy and zenith angle are randomized following a given input distribution. Secondly, the target nucleon is selected and the interaction vertex is created in a large cylindrical generation volume (typically 25 km in radius) that includes the instrumentation volume inside. The `GENHEN` program simulates the neutrino interaction and the propagation of the muon to the *can*, the instrumentation volume of the detector. Quasi elastic and resonant scattering interaction constitute only about 10% of cross-section and are simulated with `RSQ` package [173] at energies below 100 GeV when this kind of processes plays a major role. Charged current deep inelastic scattering which dominates the neutrino interaction rate, are generated using the `LEPTO` [174] software. The parametrization of the quark distribution are extracted from the CTEQ collaboration fit to experimental data. The parametrization CTEQ6-DIS [114] is used in this work. If the neutrino vertex interaction is inside the instrumentation volume or *can*, all final particles are stored for further Cherenkov light emission simulation. If the interaction point lays outside, only the muon is propagated to the *can* surface. In this case, several cuts are applied to the muon energy and direction in order to avoid the full simulation of events with a negligible probability of producing a detectable signal in the detector. This propagation of the muon to the *can* surface is performed mainly[1] by `MUSIC` [176].

- **Track simulation and Cherenkov light emission**. All particles that reach the *can* surface are stored for a full track simulation inside the instrumentation volume. The `KM3` [177] and `GEASIM` [178] are used for this purpose. The `KM3` software was previously devised for track simulation in water or ice. The version

[1] Other packages such as `PropMu` [175] are used to propagate atmospheric muons from sea level to the detector.

used in ANTARES has been modified to adapt to the ANTARES subtleties. Both packages simulate the passage of the muon through the *can* and most of the relevant physical processes. However, there are some difference between both [179]. `GEASIM` does not simulate the scattering of the Cherenkov light, and in addition the full track simulation results in long execution times. The `KM3` makes a track simulation in steps of one metre. In order to provide a fast simulation of light scattering, a set of *scattering tables* are created beforehand using `GEANT3`. The composition and density of water are fitted to the values of the experimental site. On the other hand, the main drawback of the `KM3` software is that the hadronic cascade, which can add up a 30% of light at lower energies, is not included in the simulation. Therefore, for a realistic track simulation both packages are used together. At each step of the track simulation, the Cherenkov cone produced by charged particles is computed. The hit probability for all Optical Modules which lay inside the cone is calculated and converted into a photoelectron number following the Poisson statistic. Several elements are taking into account to evaluate this hit probability such as the wavelength dependent absorption length, the transmission coefficients of the glass sphere and the silicone gel and the quantum efficiency and orientation of the photomultiplier with respect to the the direction of the photons. Together with the signal produced by Cherenkov photons, `KM3` also simulates the optical background hits produced by the β-decays of ^{40}K (see section 2.6 for further details). Bioluminescence is difficult to predict and therefore has not yet been added to the Monte Carlo. However, the bioluminescence will affect only a reduced region of the detector in a given time and will be easily recognizable and rejected by the filtering criteria.

- **Digitalization**. The front-end electronics, the detector response and digitalization are also simulated in the Monte Carlo. As mentioned in section 2.7.1, the read-out ASIC in ANTARES is the ARS. The behaviour of the ARS response can be approximated by setting a few parametres like the integration, dead time and saturation, which enable a rather realistic and simple simulation.

- **Event reconstruction**. The are different event reconstruction algorithm, depending on the nature of the event we want to reconstruct: down-going atmospheric muons, very low energy events or multi-string reconstruction. All reconstruction strategies are implemented inside a code named `RECO` [180, 181], a software which inherits the basic algorithms and classes from `POSIDONIA`, the first reconstruction program used on ANTARES. For the main topic of this thesis, the search of point-like sources, we are mainly interested in those reconstructions strategies devoted to high energy neutrino events track reconstruction. There basically two strategies: the *Carmona strategy* and the *Aart strategy*. For further details about these two reconstruction strategies, the reader is invited to see [150] for an extensive description of the *Carmona strategy*, and for a more deep discussion on the *Aart strategy* see [153].

Appendix B

LED Beacon calibration runs

The following table contains the list of LED Beacon calibrations runs used for the analysis of the optical properties of water:

RunNumber	LED Beacon	Date
25218	F2L1	11-12-2006 19:54:03
25281	F2L1	18-12-2006 11:33:26
25494*	F2L1	11-1-2007 12:13:19
25219	F9L1	11-12-2006 20:09:25
25282	F9L1	18-12-2006 11:48:27
25499*	F9L1	11-1-2007 17:44:08
25220	F15L1	11-12-2006 20:22:45
25297	F15L1	18-12-2007 16:37:09
25500*	F15L1	11-1-2007 18:00:13
25222	F2L2	11-12-2006 20:50:10
25301	F2L2	18-12-2006 17:28:10
25502*	F2L2	11-1-2007 18:29:42
25223	F9L2	11-12-2006 21:03:22
25302	F9L2	18-12-2006 17:41:42
25503*	F9L2	11-1-2007 18:42:24
25224	F15L2	11-12-2006 21:17:25
25303	F15L2	18-12-2006 17:55:04
25504*	F15L2	11-1-2007 18:54:55
27269[a]	F15L1	20-4-2007 19:21:01
27268[a]	F15L1	20-4-2007 19:00:09
27266[a]	F15L1	20-4-2007 18:39:28
27301[a]	F15L1	23-4-2007 11:23:39

LED Beacon calibration runs

27673*	F15L1	14-5-2007 10:22:31
28076*	F15L1	4-6-2007 12:41:31
26839	F15L1	26-3-2007 10:21:32
26550	F15L1	12-3-2007 10:00:39
26090	F15L1	19-2-2007 10:09:05

Table B.1: *List of runs used in the estimate of the attenuation length. Runs tagged with (*) do not include the alignment provided by the line shape reconstruction. The label (^{a}) indicates that runs have been performed using LED Beacon intensities different from the nominal value.*

In most of these runs the positions of the PMTs have been calculated using the information provided by the line shape reconstruction. However, runs tagged with (*) do not use this information. In these cases, the values measured during the calibration in the dark-setup were used instead.